Optomechanics with Semiconductor Nanomembranes

The quest for the pure node

Danish National Research Foundation Centre for Quantum Optics (QUANTOP) Niels Bohr Institute
Graduate School of Science
Faculty of Science
University of Copenhagen

PhD Thesis

Andreas Næsby Rasmussen

May 2013

Principal academic supervisor: Eugene S. Polzik
External supervisor: Anja Boisen

Contents

Part I.

Optomechanics

1. Introduction

1.1. Abstract

In this thesis our work with micromechanical membrane structures made out of gallium arsinide is described. The interaction of coherent light with the membranes was found to have a strong coupling to the motional degrees of freedom, and exceptionally high *cooling* of the mechanical modes was shown. The cooling effect was determined to be caused by a *photothermal* effect, that is due to local heating of the membrane by the laser light. This heating induces a slow change in the shape and motion of the membrane. Because this expansion is not instantaneous, the membrane moves before the force of the local heating has reached equillibrium. This delay makes the force viscous, and removes energy from the membrane motion. This is denoted vibrational cooling. A very strong vibrational cooling down to an effective 4 K from room temperature is shown for the (4,3) mode of a large GaAs membrane. Additionally the GaAs membrane is shown to have had a record mechanical quality factor of $Q_m > 2 \times 10^6$ at room temperature, which is a remarkable result for a GaAs membrane.

Another source of vibrational cooling was discovered, and the use of *deformation potential* coupling to the vibrations is described. This effect is due to the coherent excitation and subsequent relaxation of electrons and holes in the membrane, which couples to the lattice spacing, and thus to the vibrational modes of the membrane. This method has the potential of enabling coherent coupling to the vibrational modes. New GaAs membrane systems created with thin quantum wells for confinement of the electron-hole excitations were investigated using vibrational methods and techniques measuring photoluminescence. These devices did not show a high mechanical quality factor and a next generation of GaAs membrane system was proposed. This setup has two quantum wells for better confinement and additional tunability added by an electrical degree of freedom, and the current work on these samples is described in this thesis. As work is going on with this next generation of GaAs micromembranes, it is hoped, that a strong deformation potential cooling of vibrations will be shown in the immediate future.

As part of characterizing the possibilities in these GaAs heterostructures, it was realized that a better characterization setup was needed, and the design and characterization of a Michelson interferometer is described. The device is shown to be able to reliably and quickly measure the minute Brownian motion of a sample SiN membrane and is an optimal instrument for the next generation of the optomechanical investigations in the group.

Resumé

I denne tese er beskrevet vores arbejde med mikromekaniske membranstrukturer. Disse systemer er primært fremstillet af galium arsenid (GaAs). Interaktionen mellem kohærent lys og disse membraner viste sig at føre til en stærk kobling til den mekaniske frihedsgrad af disse membraner. En usædvanlig kraftig *køling* af de mekaniske frihedsgrader blev bevist. Kølingen viste sig at være resultatet af en *fototermisk* effekt, der skyldes den lokale ophedning, laserlyset inducerer. Den lokale ophedning starter en relativ langsom udvidelse, en ændring af formen og bevægelse af membranen. Da udvidelsen ikke er øjeblikkelig, men der snarere er en forsinkelse, har membranen flyttet sig til en ny konfiguration før den fototermiske kraft har opnået en ligevægt. Denne forsinkelse er grunden til, at der udføres arbejde ved at flytte energi fra membranens bevægelse, og man siger, at kraften er *viskos*. Dette fænomen kaldes vibrationel køling. En kraftig vibrationel køling blev vist for (4,3) tilstanden af membranen, og det svarer til en køling til en effektiv temperatur på 4 K fra stuetemperatur. Dette er et usædvanlig godt resultat for en GaAs membran.

En anden metode til at opnå vibrationel køling blev også opdaget i løbet af dette projekt. Den såkaldte *deformations potentiale* kobling til vibrationerne af membranen er introduceret. Denne effekt skyldes kohærent eksitation og efterfølgende henfald af elektroner og huller i membranen, og da dette kobler med krystalstrukturens dimensioner, kobler det også til de vibrationelle tilstande. Nye GaAs membran systemer blev undersøgt. Disse er lavet med tynde *kvantebrønde* for at indfange elektron-hul eksitationerne, og disse systemer blev undersøgt ved vibrationelle metoder og metoder der målte det udsendte fotoluminisens. Disse prøver udviste ikke en høj mekanisk kvalitetsfaktor og endnu en ny generation af GaAs membraner blev foreslået. Dette nye design inkorporerer to kvantebrønde for at opnå en bedre indfangning og har yderligere en mulighed for at tilpasse tilstandene ved en elektrisk frihedsgrad, der er tilføjet. Det igangværende projekt med modellering og design af disse systemer er beskrevet i denne tese. Det er håbet, at med denne næste generations af GaAs mikromembraner, det snart er muligt at fremvise kraftig deformations potentiale køling af vibrationer

Undervejs i processen med at karakterisere mulighederne i disse GaAs heterostrukturer, blev det klart, at en bedre opstilling til karakterisering var nødvendig. Dette var motivationen for at designe og undersøge et Michelson interferometer, og dette er også beskrevet. Det har været muligt at måle den meget lille termiske bevægelse, hurtigt og pålideligt, for en SiN prøve. Det er vist, hvordan interferometret er et optimalt instrument for den næste generation af optomekaniske eksperimenter der, vil blive foretaget i gruppen.

1.2. Acknowledgements

I would like to thank every *Quantop* member for a very nice and helpful mood and level of ambition, Koji and Tolga for some long working hours which payed off, as well as Eugene specifically for giving me the opportunity to prove my worth as an experimentalist.

I would like to thank Ataç İmamoğlu for the possibility of visiting the impressive group in ETH Zürich, and would like to thank Emre Togan, Javier Miguel Sánchez, Andi Reinhard, and Yves Delley specifically, but also the rest of the Quantum Photonics Group, for a very warm welcome, a helpful atmosphere, and good friendship during my time in Zürich.

Finally I want to thank my friends and family for not killing me in the process, and not letting me kill them.

1.3. Publications

Here is listed publications that have been contributed to as well as conferences presented at.

Peer reviewed

[Usami11]
Optical cavity cooling of mechanical modes of a semiconductor nanomembrane
Koji Usami, Andreas Naesby, Bo Melholt Nielsen, Jin Liu, Søren Stobbe, Peter Lodahl, and Eugene S.Polzik,
Nature Physics (2011), Vol. 8, Feb. 2012, doi:10.1038/nphys2196

[Liu11]
High-Q optomechanical GaAs nanomembranes
J. Liu, K. Usami, A. Naesby, T. Bagci, E. S. Polzik, P. Lodahl, and S. Stobbe,
Appl. Phys. Lett. 99, 243102 (2011); doi:10.1063/1.3668092

[Xuereb12]
Exciton-mediated photothermal cooling in GaAs membranes
André Xuereb, Koji Usami, Andreas Naesby, Eugene S Polzik, and Klemens Hammerer
New Journal of Physics 14 (2012) 085024

Peer reviewed related

[Taylor11]
Laser Cooling and Optical Detection of Excitations in a LC Electrical Circuit
J. M. Taylor, A. S. Sørensen, C. M. Marcus, and E. S. Polzik
Phys. Rev. Lett. 107, 273601 (2011)

Conference contributions

[Naesby10]
CONT 2010
A. Naesby
Quantum Opto-Nanomechanics, HCØ, København 2010

[Naesby11]
Optoelectronic cooling of mechanical modes in a semiconductor nanomembrane
A. Naesby
CLEO 2011, Münich, Germany

[Miguel-Sánchez12]
Semiconductor quantum well based nanomembranes: From mechanical cooling towards polariton optomechanics
J. Miguel-Sánchez, A. Naesby, E. Togan, D. Pinotsi, A. Reinhard, T. Volz, A. Imamoglu, B. Besga, J. Esteve, J. Reichel, I. Wilson-Rae, K. Usami, and E. Polzik
ICPS 2012, ETH Zürich, Switzerland

[Naesby12]
Optical cavity cooling of mechanical modes and possibility of bulk cooling of a semiconductor nanomembrane
A. Naesby
QNLO 2012, Sønderborg, Danmark

Additionally attended the 2011 Gordon conference on Optomechanics in Galveston, Texas, USA, but did not present.

Our main work was published in [Usami11] where my contribution was second to Koji. All the experiments and a lot of the analysis was performed by Koji and I, with the inital help of Tolga. My contribution to the manuscript and the development of our narrative was also substantional. My contribution to [Liu11] was mainly helping Jin with figures and discussions. The work in [Xuereb12] was mainly Andrés with a lot of discussions between André, Koji, Klemens, Eugene, and I.

1.4. Motivation

The field of optomechanics has been thriving in the last couple of years, and this work represents a venture into the field and the work that we have done to contribute to this field. In a nutshell, optomechanics is about coupling the electric field intensity and phase of light to the motion of a mechanical system. If this is achieved a vast variety of possibilities have been suggested and quite a few of them have been shown already.

A couple of good review articles for the field are in [Florian Marquardt09, Aspelmeyer10].

Among possibilities for optomechanics are the use of optomechanical systems for measuring minute forces, minute concentrations of particles, gravitational wave detectors for indication of ripples in the space-time as a result of supernovae explosions, but also for opening up the possibility of making a 'macroscopic' mechanical system show quantum behaviour. This has been a dream objective for a long time, and in last year or two this has been achieved in different groups. This is a remarkable feat that opens up the possibility of e.g. using microoscillators as a 'bus' between quantum information systems such as flying qubits, i.e. photons, and storage medium such as ions or superconducting qubits.

The reason that the field has been gaining momentum during the last decade is probably a combination of interest and the new micro/nano fabrication methods that the semiconductor industry has helped introducing. It is possible to make much more complex and smaller structures and this is beneficial for getting a strong effect of light interaction due to the small dimension and mass of the oscillators. It is also a field where people of different background enter and is on comparable 'light'-footing, and this leads to surprises. In our case this was seen with a simple GaAs membrane that was thought to be a simple little feat to characterize, but ended up showing a lot of new physics and intriguing complex behaviour that required more than what was expected. It was also even more fortunate that the system, that was manufactured as a by-product, had remarkable physical characteristics with a lot of knowledge gained both on the fabrication side, but also on the modeling of the physics.

This opens up the possibilities for how to make the proposed electronic recombination cooling effects even more pronounced and this is then the path onward for this project. Showing this force as dominating would undoubtably require a more detailed understanding of the microscopic processes in the oscillator, while still being possible to approach from a 'top-down' perspective and maintain an understanding.

Outline

The thesis is separated into five parts. The project is introduced in part. **I** and the basic optomechanical theory for describing the systems and the vibrational cooling of them. Then in part. **II** the basic mechanical model for these membrane structures are described along with some methods for finding the mechanical modes, including Finite Element methods. Then in part. **III** the main vibrational cooling experiment is described. The strong cooling of mechanical modes is proven to be due to photothermal cooling, and new methods for vibrational cooling are proposed. The *deformation potential* cooling is introduced and newer heterostructure systems are proposed and investigated. While a lot of interesting physics was found, it was found hard to vibrationally characterize higher frequency systems, and a new setup was designed. In part. **IV** the design and implementation of a Michelson interferometer for high frequency characterization was discussed. The device is proven

to be able to measure and characterize modes of brownian motion for SiN sample systems, and it is explained how the characterization of high frequency GaAs samples are feasible in the near future. In part. **V** an outlook is presented for some future possibilities in these systems, and the thesis is concluded.

My contribution

In the course of this PhD the author has contributed with substantional experimental work at the Niels Bohr Institute for the various optomechanical experiments described herein. Additionally a lot of characterization work has been done at DTU Nanotech in collaboration with the Nanoprobes group of Anja Boisen. The author was also so fortunate as to have the possibility of visiting the Quantum Photonics group of Ataç İmamoğlu at ETH Zürich. Here extensive experimental work was done on the nanomembrane structures and new characterization setups were built and used.

Extensive theoretical modeling of the systems have also been performed by the author with tools such as Comsol for finite element modeling.

2. Optomechanics

What is a typical optomechanical setup? In the case of a cavity system, a coupling is obtained between the state of light and a motional degree of freedom in a cavity. Such a system is sketched in **fig. 2.1b** where a cavity is created between two mirrors, where one is allowed to move. If the mirror moves, the light mode between the mirrors will change and thus change the light intensity. This can in turn couple to the motion of the mirror. This describes an archtypical optomechanical system.

In this chapter the basic optomechanical model will be described, and the possibilities for vibrational cooling with light will be derived.

2.1. Optomechanical model

In this section the model for the optomechanical system will be derived, ultimately ending with the Hamiltonian being assembled and the dynamics outlined. An obvious mechanism for coupling the light to the motion of a macroscopic object can be achieved via radiation pressure of the incoming light. The collision and absorption of a single incoming photon will yield a momentum difference for the object, Δp, of [Loudon00]

$$\Delta p = 2\hbar k = \frac{2E}{c} \tag{2.1.1}$$

with $\hbar k$ being the photon momentum, E being the energy and c being the speed of light, as is illustrated in fig. 2.1a. The exerted force of a photon flux $(\Delta N/\Delta t)$ is thus

$$F = \frac{\Delta p}{\Delta t}\Delta N = \frac{2P_{in}}{c} \tag{2.1.2}$$

with ΔN then being the amount of photons hitting in the time Δt and P_{in} is the optical power. In the case of reflection the object has recieved a 'kick' of $\hbar k$, and the photon is reflected back with a momentum of $-\hbar k$.

This will not be a very large force for the light powers that are easily attainable in a lab. According to **eqn.** (2.1.2), for a light power of 1 mW the force will be, $2 \times 1\ \text{mW}/(3 \times 10^8\ \text{m/s}) \approx 7 \times 10^{-12}$ N. This is not a strong effect on e.g. a 1 inch mirror. However for micro- or nanometer sized structures. it can still have a strong effect. An often used method for enhancing this effect is to trap the light between two mirrors to form a cavity, where one of the mirrors is allowed to move. A single photon is reflected back and forth in the cavity and thus can hit the movable mirror many times. The higher the reflectivity, the higher the photon lifetime, and the stronger the force on a freely moving mirror. If the photon is absorbed it will still transfer the momentum $\hbar k$ in an inelastic collision, but will not hit the mirror more times.

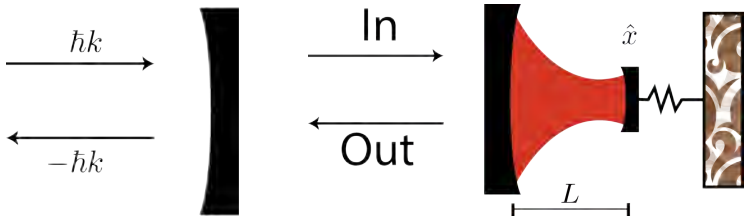

(a) Radiation pressure momentum transfer

(b) Archtypical optomechanical system. One mirror is allowed to vibrate and thus modulate the cavity resonance frequency. The direction of propagation of a beam is denoted x and the length of the cavity is called L.

Figure 2.1.: Radiation pressure force and Optomechanical systems.

The cavity resonance

An example of a Fabry-Pèrot cavity built with a large fixed mirror and a small movable one is illustrated in **fig. 2.1b**. A light induced force can then lead to a displacement of the movable mirror and change the cavity length. Now going from the picture of single photon events that was used above, to the description of fields in the cavity, the resonance condition is written as

$$n\lambda = 2L \tag{2.1.3}$$

if L is the length of the cavity, n is an integer, and λ is the wavelength of light. The wavelength can be written $\lambda = 2\pi c/\omega_c$ with ω_c being the cavity resonance angular frequency and c being the speed of light. By use of this and **eqn.** (2.1.3) it is clear how $2L = n\lambda = n2\pi c/\omega_c$ and thus

$$\omega_c = 2\pi \frac{c}{2L} n \tag{2.1.4}$$

and this is then the resonance condition for fixed mirrors. Another resonance could be found by elongating or shortening the cavity $n\lambda/2$. While **eqn.** (2.1.4) is true in the case with fixed mirrors, if the light is allowed to induce a force on a movable mirror, the coupling would introduce a new equilibrium condition. This coupling can be due to various mechanism, but for now the actual physics is ignored. The light field is just modeled as coupling to the motion of one of the mirrors. If the equilibrium position is changed from the case with no light it is costumary to introduce a shifted cavity resonance. Some groups prefer to denote the coupled system of the mirror and field as a resonator with the resonator resonance ω_R. In this work the shifted ω_c' and unshifted ω_c angular frequencies are used.

Now assuming that the end mirror move a short amount δx, the length of the cavity will change from L to $L+\delta x$, and then the resonance condition, **eqn.** (2.1.4) will change, so that the resonance angular frequency becomes

$$\omega_c' = 2\pi \frac{c}{2(L+\delta x)} n \tag{2.1.5}$$

In this expression L can be moved as

$$\omega_c' = 2\pi \frac{c}{2L} \frac{1}{1+\frac{\delta x}{L}} n \tag{2.1.6}$$

and again the cavity resonance **eqn.** (2.1.4) can be identified as $2\pi cn/(2L)$, to reduce to the simpler expression

$$\omega_c' = \omega_c \frac{1}{1+\frac{\delta x}{L}} \tag{2.1.7}$$

and this is then the explicit expression for the δx dependence of the shifted cavity resonance ω_c'. The form, as well as the choice of denoting the displacement δx, hints that a linearization might be the possible. Indeed if the displacements from equillibrium is assumed small compared to the length of the cavity, $\delta x \ll L$, **eqn.** (2.1.7) can be linearized as

$$\omega_c' \approx \omega_c \left(1 - \frac{\delta x}{L}\right) \tag{2.1.8}$$

which is then the simple linear expression for the change in cavity resonance by a small displacement δx. The small displacement approximation is a very good approximation for the case of realistic coupling strengths and for realistic mirror motion due to the coupling. The correspondance between the length of the cavity and the cavity angular resonance is illustrated in **fig. 2.2**.

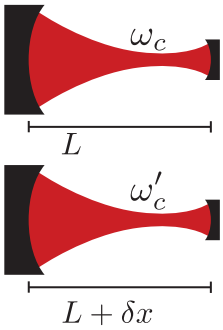

Figure 2.2.: The cavity length L of a Fabry-Perot with a small movable mirror is shown above. It has the cavity angular frequency ω_c. If the light field couples sufficiently to the motion of the movable mirror through e.g. radiation pressure it can induce a small displacement δx and the cavity length will be $L+\delta x$ as shown in the lower sketch. The corresponding angular frequency is denoted ω_c'.

The Hamiltonian

Now in order to make progress towards writing up an equation of motion the Hamiltonian should be stated. The Hamiltonian for the cavity and the phononic system can be written

$$\hat{H} = \hbar\omega_c'\hat{a}^\dagger\hat{a} + \hbar\omega_m\hat{b}^\dagger\hat{b} \tag{2.1.9}$$

where $\hat{a}^\dagger$, $\hat{a}$ are the creation and annihilation operators of the light field in the cavity, and $\hat{b}^\dagger$, $\hat{b}$ are the creation and annihilation operators for the phononic vibrational degree of freedom. Here ω_c' is the shifted cavity resonance and ω_m is the resonance of the motional degree of freedom. Note that the coupling between the phonon and position of the mirror is hidden in ω_c'. This is the standard form for a quantum harmonic oscillator which is not in the ground state. Now with the assumption

of small displacement δx from equillibrium, which enables the linearization of the cavity resonance, the Hamiltonian can be written

$$\hat{H} = \hbar\omega_c \left(1 - \frac{\delta x}{L}\right) \hat{a}^\dagger \hat{a} + \hbar\omega_m \hat{b}^\dagger \hat{b} \tag{2.1.10}$$

and from this expression the naming convention of ω_c' and ω_c should make sense.

The position of the movable mirror can be ascribed the position operator $\hat{x}$. Since the displacement from equilibrium is assumed to be small δx can be replaced by the position operator $\hat{x}$ in **eqn.** (2.1.10) [Law95, Marquardt07]. The Hamiltonian can then be written as

$$\hat{H} = \hbar\omega_c \left(1 - \frac{\hat{x}}{L}\right) \hat{a}^\dagger \hat{a} + \hbar\omega_m \hat{b}^\dagger \hat{b} \tag{2.1.11}$$

Position and momentum operators

From the identification of the position operator $\hat{x}$ it is possible to write up the standard creation and annihiliation operators for a harmonic oscillator. The phononic operators are [Ballentine98]

$$\hat{b} = \sqrt{\frac{m\omega_m}{2\hbar}} \left(\hat{x} + \frac{i}{m\omega_m}\hat{p}\right) \tag{2.1.12}$$

$$\hat{b}^\dagger = \sqrt{\frac{m\omega_m}{2\hbar}} \left(\hat{x} - \frac{i}{m\omega_m}\hat{p}\right) \tag{2.1.13}$$

where $\hat{x}$ and $\hat{p}$ are the two quadrature operators for the position and momentum. By rewriting the ladder operators an expression for the momentum operator becomes

$$\hat{x} = \sqrt{\frac{\hbar}{2m\omega_m}}(\hat{b} + \hat{b}^\dagger) \tag{2.1.14}$$

the expression for the position operator has then been found. The squareroot in **eqn.** (2.1.14) is denoted the *zero point fluctuations* of the system, x_{zpf}. $\hat{x}$ can then be written

$$\hat{x} = x_{zpf}(\hat{b} + \hat{b}^\dagger) \tag{2.1.15}$$

Thus x_{zpf} basically denote the amount of vibration that is available with no excitation. x_{zpf} can be understood as related to the RMS variation of the motion. For typical experimental values for membranes[1]

$$x_{zpf} = \sqrt{\frac{\hbar}{2m\omega_m}} \sim 10^{-15}\ \text{m} \tag{2.1.16}$$

with m being the effective motional mass of the system. For a discussion of the effective motional mass, see **sec. 4.2**

[1] Typical effective motional mass of 10 pg and a resonance frequency of $\omega_m/(2\pi) \approx 1$ MHz. This is roughly the order of magnitude of a typical Norcada membrane which several groups use.

Coupling strength g_0

Now that an expression for $\hat{x}$ has been found, a nice expression for the coupling strength g_0 between the cavity field and the phononic degree of freedom can be identified from the Hamiltonian. Around the resonance condition ω_c can be written as the series expansion

$$\omega_c = \omega(x) = \omega_c \big|_{x=0} + \left(\frac{\partial \omega_c}{\partial x} \bigg|_{x=0} \right) x + \dots \tag{2.1.17}$$

where ... refer to higher order terms. Truncating at the first order spatial derivative the Hamiltonian can be written

$$\hat{H} = \hbar\omega_c \hat{a}^\dagger \hat{a} + \omega_m \hat{b}^\dagger \hat{b} + \hbar \frac{\partial \omega_c}{\partial x} \hat{a}^\dagger \hat{a} x \tag{2.1.18}$$

Inserting x from **eqn.** (2.1.15)

$$\hbar \frac{\partial \omega_c}{\partial x} \hat{a}^\dagger \hat{a} x = \hbar \frac{\partial \omega_c}{\partial x} \cdot x_{zpf} \hat{a}^\dagger \hat{a} (\hat{b} + \hat{b}^\dagger) \tag{2.1.19}$$

and then the coupling rate can be identified as

$$g_0 \equiv \frac{\partial \omega_c}{\partial x} \cdot x_{zpf} \tag{2.1.20}$$

Full Hamiltonian

Rewriting yields the full Hamiltonian

$$\hat{H} = \hbar(\omega_c + g_0 \hat{x}) \hat{a}^\dagger \hat{a} + \hbar\omega_m \hat{b}^\dagger \hat{b} \tag{2.1.21}$$

and again insertion of the position operator, $\hat{x}$, yields

$$\hat{H} = \hbar \left[\omega_c + g_0 x_{zpf} (\hat{b} + \hat{b}^\dagger) \right] \hat{a}^\dagger \hat{a} + \hbar\omega_m \hat{b}^\dagger \hat{b} \tag{2.1.22}$$

In these eqns. (2.1.21, 2.1.22) the coupling is apparent. It enables the manipulation of the vibrational degree of freedom through the application of a photoinduced light force, and at the same time the cavity enables a simple readout of the vibrations as these modulate the cavity transmission/reflection. This is then the Hamiltonian for the typical optomechanical setup.

2.2. Vibrational cooling

The coupling between the vibrational degree of freedom and the cavity mode enables the manipulation of the mechanical behaviour. In this section it is shown how this coupling is used to either excite or dampen the vibrations of the cavity mirror.

In a classical picture cooling can be understood in the following way. The photoinduced force is what displaces the movable mirror from the equilibrium, and this force is proportional to the light field intensity. Then the force on the movable mirror is a function of the mirror displacement just as the field intensity is. This is illustrated in **fig. 2.3** where the photoinduced force is

illustrated as a function of mirror position around the cavity resonance. In an experiment one would position the movable mirror in such a way that the cavity is slightly off resonance while still having a finite transmission, which corresponds to a finite force on the mirror. If the mirror is positioned on the slope of the resonance, the small fluctuations of the mirror from this position will lead to an increase and decrease of the force on the mirror due to the changing force, [Florian Marquardt09].

However if the fluctuations just led to varying force on the mirror, no work would necessarily be done, but there is a time lag involved as well. This means that the system takes some time to react to a change in configuration due to the finite lifetime of the photons in the cavity. As the mirror moves the conditions for the light field in the cavity changes, but because of the long lifetime of photons in the cavity, it takes some time before a new equilibrium can be achieved. The lifetime is proportional to the finesse of the cavity, and thus the better cavity, the more pronounced time lag. If it moves closer to the resonance from the outset, the force will be smaller than 'expected' as the cavity field is not quick enough to respond, and likewise when it moves back away from the resonance. This lag — or viscous behaviour — enables the extraction of work from the mirror. Depending on which slope the system is kept at, the slope is of a different sign. This enables the extraction of work and the injection of work. This is termed *cooling* and *heating* as the mechanical modes will be changed in a manner analogous to changing the bulk temperature of the mirror. The cooling/heating cycle is indicated in **fig. 2.3**. The critical point is that the change in cavity length does not instantaneously turn into a change in the light-induced force on the moving mirror, and the force then does not follow the slope that it would if the cavity field reacted instantaneously. This is why the cycle encloses an area in **fig. 2.3** and does not just follow the Lorentzian peak.

In the experiment the system would be kept stable at a configuration by an electronic circuit adding feedback to the movable mirror. One talks about *locking* the cavity on a position on the cavity resonance, and thus this piece of equipment is denoted a cavity lock.

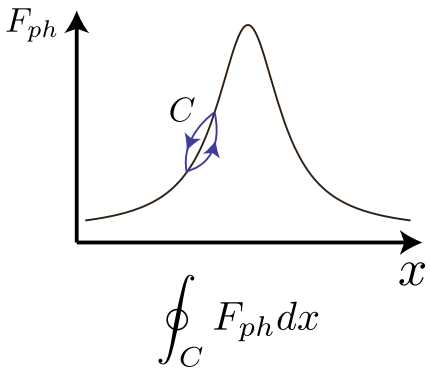

Figure 2.3.: The photoinduced force F_{ph} around the cavity resonance. The cooling cycle C is indicated. The membrane vibration makes the cycle on the red-detuned side of the optical resonance, and the area inside the cycle indicate the vibrational energy that the cooling removes.

Equation of motion

Now going from the Hamiltonian in **eqn.** (2.1.21), the equations of motion for the displacement operator can written. Using the Heisenberg equation for the displacement operator as

$$\frac{\partial \hat{x}}{\partial t} = \frac{i}{\hbar}[\hat{H}, \hat{x}] \tag{2.2.1}$$

the equation of motion can be determined. Insertion of the position operator, $\hat{x}$, from **eqn.** (2.1.14) and the Hamiltonian from **eqn.** (2.1.11) can yield the equation of motion. For a standard harmonic oscillator (HO) the Hamiltonian can be written as

$$\hat{H}_{HO} = \frac{m\omega_m}{2}\hat{x}^2 + \frac{\hat{p}^2}{2m} \tag{2.2.2}$$

with m being the mass and $\hat{x}$ and $\hat{p}$ being the position and momentum operators. By the use of the Heisenberg equation the equation of motion for $\hat{x}$ and $\hat{p}$ is found [Scully97]

$$\frac{\partial \hat{x}}{\partial t} = \frac{\hat{p}}{m} \tag{2.2.3a}$$

$$\frac{\partial \hat{p}}{\partial t} = -m\omega_m^2\hat{x} \tag{2.2.3b}$$

which then describes the motion of a particle in a harmonic potential. Here $m\omega_m^2$ can be identified as the spring constant K. In a similar manner this can be done for the coupled optomechanical system, but this will not be shown here. Instead the derivation will be shown by going back to the assumption that the coupling between light and mirror motion can be seen as linear for small fluctuations around equilibrium and then can be described as a harmonic oscillator. It is again natural to write up the equation of motion for an oscillator with mass m as (neglecting at first the light field in the cavity)

$$m\frac{\partial^2 x}{\partial t^2} + Kx = 0 \tag{2.2.4}$$

with K being the spring constant of the restoring force. In order to include damping by influence of connection to a thermal bath, a damping term $\beta_m \frac{\partial x}{\partial t}$ is introduced and then the fluctuation-dissipation theorem stipulates that a corresponding Brownian Langevin noise term $F_{th}(t)$ describing the thermal force must be added [Coffey96, Kampen07]. The equation of motion becomes

$$m\frac{\partial^2 x}{\partial t^2} + \beta_m\frac{\partial x}{\partial t} + Kx = F_{th}(t) \tag{2.2.5}$$

This thermal Langevin force $F_{th}(t)$ has a mean zero $\langle F_{th}(t)\rangle = 0$, and show no correlation between stochastic events. This is expressed by the fluctuation-dissipation theroem in that the force autocorrelation can be written

$$\langle F_{th}(t)F_{th}(t+\tau)\rangle = 2k_BT\beta_m\delta(\tau) \tag{2.2.6}$$

with k_BT being the thermal energy. The factor of 2 comes from the derivation of the two-time autocorrelation function as described in [Kampen07]. In order to relate the decay rate of the mechanical mode to the damping term, $\beta_m \frac{\partial x}{\partial t}$ **eqn.** (2.2.5) is rewritten as

$$\frac{\partial x}{\partial t} + \gamma_m\frac{\partial x}{\partial t} + \omega_0^2 x(t) = \frac{F_{th}}{m} \tag{2.2.7}$$

where $\gamma_m = \beta_m/m$ is the decay rate of the mechanical mode, and $K = m\omega_m^2$ is the spring constant. Thus in terms of the decay rate γ_m instead of the damping term β_m, **eqn.** (2.2.5) is written

$$m\frac{\partial^2 x}{\partial t^2} + m\gamma_m\frac{\partial x}{\partial t} + Kx = F_{th}(t) \tag{2.2.8}$$

and the corresponding autocorrelation is

$$\langle F_{th}(t)F_{th}(t+\tau)\rangle = 2k_B T\gamma_m m\delta(\tau) \tag{2.2.9}$$

which then describe the thermally dampened harmonic oscillator system. So far this is only the model for a harmonic oscillator with damping included due to a stochastic thermal force. Adding a photoinduced force on the mechanical degree of freedom transfers the problem to an optomechanical setup. A force due to a light field, F_{ph}, can be simply introduced to yield

$$m\frac{\partial^2 x}{\partial t^2} + m\gamma_m\frac{\partial x}{\partial t} + Kx = F_{th}(t) + F_{ph} \tag{2.2.10}$$

The system is indicated in **fig. 2.4a**. Here the F_{ph} is a general light induced force that is proportional to the light power at the position of the mirror that is allowed to move around equilibrium. The mirror is allowed to excibit thermal fluctuations and these are included as a Langevin force F_{th}.

Regarding the explicit form of F_{ph} in **eqn.** (2.2.10) it is not always as simple as the stochastic force used to model F_{th}. For the case of radiation pressure photoinduced force the Markovian expression **eqn.** (2.2.9) is a fitting way of describing F_{ph}. This is because of the Markovian form of the radiation pressure. Because it stems from photon collisions, and the interaction time involved in a reflection event can be called instantaneous, there is no need for any delay. Therefore the autocorrelation follow $\langle F_{ph}(t)F_{ph}(t+\tau)\rangle \propto \delta(\tau)$. However for a different photoinduced force, the Markovian form of F_{ph} is not realistic. An example of such a force is the photothermal force, where the slow spreading of heat due to the incident light field couples to the motion of the mechanical degree of freedom as shown in [Metzger04]. As this thermal time scale is on the order of milliseconds another form of F_{ph} that the Markovian description is required.

The critical part is that the photonic force F_{ph} shows a delay between the thermal induced vibration and the F_{ph} reaching equilibrium $F(x_n)$. This is illustrated in **fig. 2.4b**. In this figure the contact with a thermal reservoir is modeled as thermal kicks perturbing the system at random times. In the top part of **fig. 2.4b** these kicks are illustrated. The system is started in the initial situation at zero and at random times it gets a kick from the environment. Consequently it moves toward the final situation of the value one. In the bottom part of **fig. 2.4b** is illustrated the delayed response of the optomechanical system.

After a kick at a time t_1 the photon induced force follows with an exponential delay[2] with a time constant of τ. The delay function in the limit of large number of photons hitting the mirror has the form

$$h(t) = 1 - e^{-t/\tau}, \quad \text{for} \quad t \geq 0 \tag{2.2.11a}$$
$$= 0, \quad \text{for} \quad t < 0 \tag{2.2.11b}$$

where it has been chosen to define $h(t)$ as being zero for negative time to ensure causality.

[2] The exponential behaviour makes sense as radiation pressure reacts with exponential behaviour due to the cavity, and the thermal heat flow of photothermal force does as well.

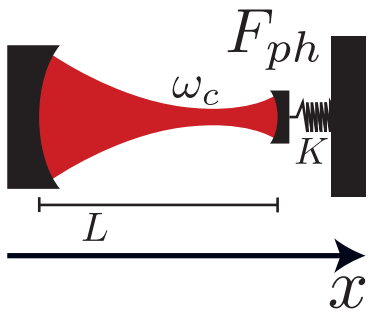

(a) Archtypical optomechanical system.

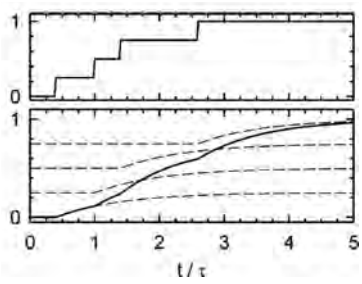

(b) Delayed force with characteristic exponential time dependence on the time lag τ. The top illustrates the position of the mirror, while the bottom illustrates the induced force. Reproduced from [Metzger08a]

Figure 2.4.: Archtypical optomechanical system and delayed force characteristic.

Delay Function

This delay function in **eqn.** (2.2.11) is worth a little more discussion. The exponential decay form makes sense for a number of different systems. For a fast interaction process such as radiation pressure the interaction with a single photon is a lot quicker than the lifetime of the cavity field for realistic cavities. This means that a change in position of the movable mirror by a 'kick' from a photon changes the cavity resonance condition effectively instantaneously compared to the cavity lifetime, κ^{-1}, and the cavity light field then adjusts to the new cavity condition with an exponential time dependence [Siegman86].

Now for a slower process such as photothermal cooling where the time is due to heat diffusion the delay process can be a lot longer. A delay time was found in [Metzger08a] of $\tau \approx 0.5$ ms due to the slow bending that thermal diffusion cause. Since 0.5 ms is longer than the photon lifetime of a low finesse cavity, the response of the cavity to a photoinduced 'kick' will be following the behaviour of the movable mirror completely, and this makes τ the dominant timescale. Because the local heating diffusion and consequent bending also follow an exponential time dependence [Greiner95], **eqn.** (2.2.11) is equally applicable for this case. For the case of a cavity with a higher finesse the photon lifetime can be made comparable to this delay time and then there can be an interplay of the radiation pressure and photothermal cooling effects simultaneously. It could be interesting to e.g. be able to tune the dominance of one effect compared to another.

For now the realization that different physical processes would follow the exponential decay time dependence allows for the application of **eqn.** (2.2.11) in the following derivation.

Photoinduced force

Here the photoinduced force will be approximated for small displacements around the equillibrium and the equation of motion transformed to frequency space. From this the effective parameters

describing the cooling and heating can be derived.

The field intensity inside the cavity is position dependent and this means that the photothermal photoinduced force will be position dependent as well with $F_{ph} = F_{ph}(x(t))$. Thus for the time t the mirror will be at position $x(t)$ and the photoinduced force will be

$$F_{ph}(x(t)) = F(x_0) + \int_0^t dt' \frac{dF(x(t'))}{dt'} h(t-t') \tag{2.2.12}$$

where the delay function $h(t)$ from **eqn.** (2.2.11) enters as a convolution with the time derivative of the force. Here $F(x)$ is introduced as the contribution to the photoinduced force at the different positions, and thus no suffix is introduced. The choice of the lower limit of the integral is just chosen to start at $t' = 0$ but as the delay function was defined to be zero for negative arguments it might be starting at $t' = -\infty$ here. It turns out however to be convenient to choose $t' = 0$. $F_{ph}(x_0)$ corresponds to the static displacement due to the light field in the cavity, and this does not enter into the dynamics of the motion. This explicit expression of $F_{ph}(x(t))$ can then be inserted into the equation of motion, **eqn.** (2.2.10). Using the chain rule the derivative in **eqn.** (2.2.12) is written as

$$\frac{dF(x(t'))}{dt'} = \frac{\partial F\left(x(t')\right)}{\partial x} \frac{\partial x(t')}{\partial t'} \tag{2.2.13}$$

and as long as the fluctuations around the equilibrium due to the photoinduced force are "small", $F(x(t'))$ can be approximated around the equilibrium point x_0 as

$$F\left(x(t')\right) \approx F(x(t_0)) + \left(x(t') - x(t_0)\right) \frac{\partial F(x(t'))}{\partial x}|_{x=x(t_0)} \tag{2.2.14}$$

where the partial derivative is evaluated for x being at the fixed position $x(t_0)$. Here [Metzger08a] is followed and the derivate is written as $\nabla F = \frac{\partial F(x(t'))}{\partial x}|_{x=x(t_0)}$. The spatial derivative ∇F is identified as the photo-induced *rigidity*. It makes sense to denote it the rigidity because of the usual form of Hooke's law $F = -kx$. Taking the spatial derivative it is clear how $\partial_x F = -k$ and thus it is basically the induced spring constant of the system.

The approximated expression for the second term in **eqn.** (2.2.14), then becomes

$$\left(x(t') - x(t_0)\right) \frac{\partial F(x(t'))}{\partial x}|_{x=x(t_0)} \approx \left(x(t') - x(t_0)\right) \nabla F \tag{2.2.15}$$

and subsequently the expression for dF_{ph}/dt', in **eqn.** (2.2.13), becomes

$$\frac{dF(x(t'))}{dt'} \approx \nabla F \frac{\partial x(t')}{\partial t'} \tag{2.2.16}$$

and this expression can finally enter into **eqn.** (2.2.12) to yield

$$F_{ph}\left(x(t)\right) \approx \int_0^t dt' \nabla F \frac{\partial x(t')}{\partial t'} h(t-t') \tag{2.2.17}$$

Now F_{ph} is inserted into the equation of motion, **eqn.** (2.2.10), and the Laplace transform[3], is used to transform to frequency space. The transformed symbols are here denoted by the $\tilde{o}(\omega)$ for a

[3]With the Laplace transform defined as $\tilde{x}(\omega) = \int_0^\infty dt x(t) e^{i\omega t}$. The Laplace transform of convolutions is used in the reformulations as noted in [Metzger08a]. It is convenient to use the Laplace transform with $= i\omega$ here instead of using the Fourier transform. The main motivation is again the limits of time in the integration over the delay function.

function $o(t)$ in ω space. The transformation enables the equation of motion to be rewritten in ω space as

$$-\omega^2 m\tilde{x}(\omega) + im\omega\gamma_m\tilde{x}(\omega) + K\tilde{x}(\omega) = F_{th}(\omega) + i\omega\tilde{x}(\omega)\nabla F\tilde{h}(\omega) \tag{2.2.18}$$

In this equation the terms with ω factors stem from transforming derivatives in $x(t)$. Because $x(t)$ denote the small fluctuations of the membrane from equilibrium, x_0, the transformed $\omega = \omega_m$ corresponds to the frequency of the membrane mode. Thus ω_m will be identified as such in the following.

Now the Laplace transform of the function $h(t)$, which was given in **eqn.** (2.2.11), is

$$\tilde{h}(\omega) = 1/i\omega(1 + i\omega\tau) \tag{2.2.19}$$

and inserting this in **eqn.** (2.2.18) the equation of motion in frequency space can be written as

$$-\omega_m^2 m\tilde{x}(\omega) + K\tilde{x}(\omega) = F_{th}(\omega) + im\omega_m\gamma_m\tilde{x}(\omega) + \nabla F\frac{\tilde{x}(\omega_m)}{1 - i\omega_m\tau} \tag{2.2.20}$$

and this can be restructured as

$$-m\omega_m^2\tilde{x} + i\omega_m m\gamma_m^{\text{eff}}\tilde{x} + K^{\text{eff}}\tilde{x} = \tilde{F}_{th} \tag{2.2.21}$$

with the newly coined effective damping

$$\gamma_m^{\text{eff}} = \gamma_m\left(1 + Q_m\frac{\omega_0\tau}{1 + \omega_m^2\tau^2}\frac{\nabla F}{K}\right) \tag{2.2.22}$$

where the mechanical quality factor is defined as $Q_m = \omega_0/\gamma_m$, and ω_0 is the mechanical angular frequency for the center of mass of the movable mirror $\omega_0^2 = K/m$. Again it is noted how γ_m is the intrinsic mechanical decay rate, and that γ_m^{eff} is the effective decay rate due to the coupling. Additionally the effective spring constant is introduced as

$$K^{\text{eff}} = K\left(1 - \frac{1}{1 + \omega_m^2\tau^2}\frac{\nabla F}{K}\right) \tag{2.2.23}$$

From the effective spring constant the shifted vibrational resonance is found as $(\omega_m^{\text{eff}})^2 = K^{\text{eff}}/m$ and so

$$(\omega_m^{\text{eff}})^2 = \omega_0^2\left(1 - \frac{1}{1 + \omega_m^2\tau^2}\frac{\nabla F}{K}\right) \tag{2.2.24}$$

Thus the simple model includes the shift of the resonance frequency as well as the damping of vibration as the light induced force changes. In **fig. 2.5a** is shown an indication of how the ω_m^{eff} decrease with increasing input power, while the damping γ_m^{eff} increases. This can be seen to follow from **eqn.** (2.2.22) as the effective damping rate of a mechanical mode scale with the photoinduced rigidity ∇F for a given cavity configuration and as this scale with input power γ_m^{eff} will increase. Likewise in **eqn.** (2.2.24) is shown how the effective mode angular frequency decrease with increasing ∇F because of the minus sign. This is also dependent on the timescale of the delay τ and the mechanical angular frequency of the mechanical mode in question. For a given cavity configuration this means that the detuning of the cavity from resonance does change, and it is assumed that the cavity is kept at a fixed detuning, with the mechanical degree of freedom then being a

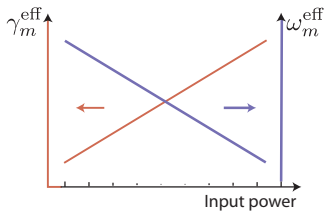

(a) Damping (red) and frequency shift (blue).

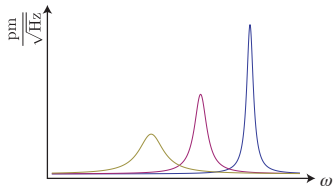

(b) Cooling effects in the spectra. The blue trace shows the lowest cooling power while the greenish shows the most cooling power.

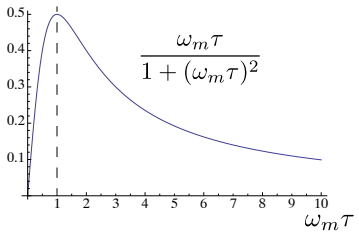

(c) The cooling term $\omega_m\tau/(1+(\omega_m\tau)^2)$ in **eqn.** (2.2.22). The maximum for $\omega_m\tau = 1$ is indicated.

Figure 2.5.: Optomechanical damping and frequency shift as a function of input power.

small perturbation of this configuration. In **fig. 2.3** a sketch of the optical resonance for the cavity was shown. The cavity resonance angular frequency is denoted by ω_c. If the cavity is detuned off resonance and kept at a fixed detuning, it is customary to talk about that the cavity is *locked* at this detuning. Considering a cavity made of a fixed mirror and a movable mirror, the cavity could be locked on one of the sides of the resonance, and a small change x of the position of the movable mirror would then change the cavity field intensity. From the sketch **fig. 2.3** it is clear that the direction of x and which side of the resonance is what determines the sign of ∇F for a small x.

Again going back to **eqn.** (2.2.22), it is seen how γ_m^{eff} has a maximum for $\omega_m\tau = 1$ and this in turn shows how τ is important for judging the effectiveness of cooling processes. For a typical mechanical resonance around 1 MHz the optimal time constant would then be $\tau = 1\ \mu$s. The $\omega_m\tau/(1+(\omega_m\tau)^2)$ dependence is indicated in **fig. 2.5c**.

2.2.1. Mirror temperature and cooling

In order to estimate the energy in the vibrational mode the equipartition theorem [Greiner95] is utilized. It states that in thermodynamical equilibrium with no illumination the average power in the vibrational equillibrium is given as

$$\frac{1}{2}K\int_0^\infty dt|x(t)|^2 = \frac{1}{2}k_BT \tag{2.2.25}$$

with k_B being Boltzmann's constant and T temperature of the thermal reservoir for the system. The time t here is again chosen in a way that will be convenient later on. It is chosen so that the light induced force starts affected at $t = 0$, but could also be starting at $t = -\infty$. Thus the vibrational behaviour is linked to the temperature of the system, under the assumption that the parameters such as the rigidity K, the effective mass m and so on can be measured independently of the measurement of the vibrational information. However this is for no illumination and it is necessary to perform the integral $\int_0^\infty dt|x(t)|^2$ explicitly to include the photo-induced force.

Assuming that the thermal excitation is spectrally "white" and that the damping rate $\gamma_m \ll \omega_0$ expressions for the thermal noise spectrum of the movable mirror $|\tilde{x}(\omega)|^2$ and the thermal driving force $\tilde{F}_{th}$ is determined in [Metzger08a]. When the photo-induced force is included the spectral force density of $\tilde{F}_{th}$ is unchanged as it is only dependent on the intrinsic mechanical damping γ_m and effective spring constant K^{eff}. The $|x(t)|^2$ is again related to the effective temperature, T^{eff}, by the equipartition theorem as

$$\frac{1}{2}K^{\text{eff}}\int_0^\infty dt|x(t)|^2 = \frac{1}{2}k_B T^{\text{eff}} \tag{2.2.26}$$

The effective temperature of a vibrational mode can then be found to be

$$\frac{T^{\text{eff}}}{T} = \frac{\gamma_m}{\gamma_m^{\text{eff}}} \tag{2.2.27}$$

or by insertion of γ_m and γ_m^{eff} from **eqn.** (2.2.22) this can be expressed differently as

$$\frac{T^{\text{eff}}}{T} = \frac{1}{1 + Q_m \frac{\omega_0\tau}{1+\omega^2\tau^2}\frac{\nabla F}{K}} \tag{2.2.28}$$

Again the cooling effect is shown in **fig. 2.5**. This corresponds to the membrane behaving just like if it was connected to a thermal reservoir with temperature $T = T^{\text{eff}}$. In the framework here described, there is nothing to hinder the cooling of the vibrational mode to the ground state as long as the cavity decay rate is large enough. This is however not the full story. For example shot noise is neglected in this model, which leads to increased noise. Motivated by such considerations led to the development of a quantum model for cooling, published simultaneously by two groups in [Wilson-Rae07, Marquardt07]. This is briefly noted in **sec. B.1**.

2.2.2. Cooling vs. damping

In the treatment above the intrinsic damping, γ_m, due to thermal Langevin noise is unchanged when a light field is introduced, but it introduces a new effective damping, γ_m^{eff}. As mentioned in [Pinard00, Grassia00, Courtya01] this distinction is what enables the "cold damping" or cooling of the mechanical mode, while not changing the bulk temperature of the mirror. This is in contrast to the case where an added random noise term to the thermal Langevin force would lead to an increased damping of the motion, but not change the energy in the vibration.

There is then a difference between damping and cooling of a mechanical mode. As illustrated in **fig. 2.6** damping broadens the peak while the area under it remains the same, reflecting the unchanged power. In the case of cooling this area is decreased. It is also possible to heat as mentioned, and in that case the peak will broaden and the area beneath will increase.

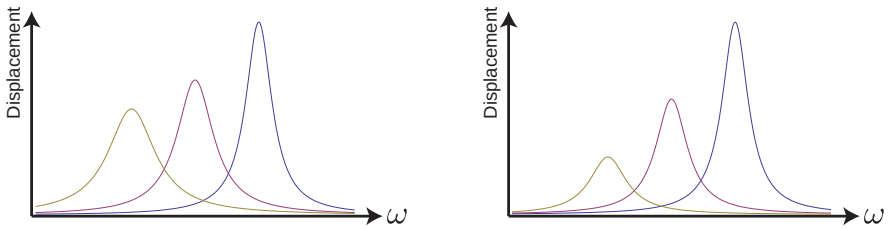

(a) Damping where the power in the peak is unchanged.

(b) Cooling where the power in the peak is decreased.

Figure 2.6.: Damping versus cooling for increasing force.

In this approach cooling [Mertz93] corresponds to the coupling to a reservoir with different temperature, that changes the vibrational motion of a mechanical mode to an effective temperature to what it would be if the bulk temperature of the system was the temperature of the cold reservoir. This is in contrast with the case of pure damping where the damping is not accompanied with an effective temperature change, but only add energy and noise.

2.2.3. Expected vibration

The expected vibrational amplitude can be estimated using the equipartition theorem [Greiner95] as noted above. This states how the temperature of a system is related to the average energies, and stems from an assumption that in equillibrium the energy will be distributed among all degrees of freedom. In the case of a harmonic oscillator this means that the potential energy and the kinetic energy will be equal. If the potential energy is $E_{pot} = \frac{1}{2}kx^2$ for a harmonic oscillator at position x with spring constant k, and it has the kinetic energy $E_{kin} = \frac{1}{2}mv^2$, for m denoting the mass and $v = \partial x/\partial t$. In thermal equillibrium the average total energy is then

$$\langle E \rangle = \langle E_{kin} \rangle + \langle E_{pot} \rangle = \frac{1}{2}k_B T + \frac{1}{2}k_B T = k_B T \tag{2.2.29}$$

where k_B is the Boltzmann constant, and $\langle ... \rangle$ denote the average. For the more complicated case of a vibrating membrane system, it is necessary to include damping and integrate up small pieces of the vibrating system to get the energy [Saulson90, Kippenberg07]. In this way can be written

$$\frac{1}{2}K \int_0^\infty dt|x(t)|^2 = \frac{1}{2}k_B T \tag{2.2.30}$$

for a system which is connected to a thermal bath with temperature T, and where K is the total spring constant of the mechanical system. From **eqn.** (2.2.30) the RMS thermal amplitude of the brownian fluctuations of a vibrational system with the mechanical angular resonance ω_m, can be determined as

$$\sqrt{\langle x^2 \rangle} = \sqrt{\frac{k_B T}{m\omega_m^2}} \tag{2.2.31}$$

For a clamped membrane structure it can be shown [Thompson08] that the effective motional mass is $m = 1/4 m_{\text{phys}}$. Insertion of mechanical parameters for the system yields the expected RMS displacement that would be measured.

For the typical Norcada SiN membrane of 50 nm × 500 μm × 500 μm the mass is about 40 ng, and thus the motional mass will be 1/4 of that, about 10 ng. These membranes show a fundamental mechanical resonance frequency of about 740 kHz, and thus from **eqn.** (2.2.31) the RMS displacement can be estimated as

$$\sqrt{\langle x^2 \rangle} = \sqrt{\frac{k_B \times 300 \text{ K}}{10 \text{ ng} \times (2\pi \times 740 \text{ kHz})^2}} \approx 4.4 \text{ pm} \tag{2.2.32}$$

In the following the membrane thickness is denoted, t, the lateral dimension, l, the thickness of an optional aluminum coating being t_{al} and m_{phys} and m being the physical mass and the motional mass respectively. The fundamental mechanical resonance is ν_0.

t [nm]	l [μm]	t_{al} [nm]	m_{phys} [ng]	m [ng]	ν_0 [kHz]	$\sqrt{\langle x^2 \rangle}$ [pm]
50 nm	500 μm	0	41 ng	10 ng	740 kHz	4.4 pm
50 nm	1000 μm	0	165 ng	41 ng	412 kHz	12 pm
100 nm	500 μm	0	82 ng	21 ng	$\sim$	$\sim$
200 nm	500 μm	0	165 ng	41 ng	$\sim$	$\sim$
100 nm	1000 μm	200	622 ng	156 ng	270 kHz	3.0 pm

Which clearly shows that the range for all these SiN membranes are a couple of picometer in RMS displacement amplitude.

2.3. Avenues of optomechanical coupling

By introducing the light field and the photoinduced force that this include, the effective equation of motion **eqn.** (2.2.21), shows that a manner of control is added over the behaviour of the mechanical degree of freedom. As shown in **fig. 2.5** the mechanical modes can be cooled by a change in the input power. This is because ∇F scale with the input power for a given cavity configuration. This enables the cooling of mechanical modes. What is not shown in the figure, is that it works both ways, in that the sign if ∇F enters into the equations for γ_m^{eff}, **eqn.** (2.2.22). From the definition of $\nabla F = \frac{\partial F(x(t'))}{\partial x}|_{x=x(t_0)}$ it is clear that the sign of ∇F is given by the spatial derivative of the photoinduced force, and depending on the configuration of the Fabry-Pèrot cavity this can be either for elongation of the cavity, increasing x, and for shortening of the cavity, which corresponds to decreasing x. It is customary to denote the higher frequency side (shorter cavity) of the cavity resonance as the blue side or likewise red side (longer cavity) for the other side. Thus for a cavity configuration where the elongation leads to a positive ∇F, γ_m^{eff} will increase and the cooling will increase. If an elongation leads to a negative ∇F , which is the case for the blue side, then a heating of the mechanical mode will occur, meaning that the decay rate and spectrum of the mode will correspond to that of a membrane at a higher bulk temperature [Arcizet06, Kippenberg08].

Thus a change in the configuration between the mechanical system and the cavity field mode enables the manipulation of the mechanical energy in the mechanical modes and of the coupling between the optical input and the mechanical mode. This is the basic takeaway for optomechanics and achieving control over the coupling between the light field and the mechanics, is a step twoards manipulation of the mechanical behaviour and coupling to other systems.

This coupling of light to the mechanical motion have led to the quest for reaching the so-called ground state of a mechanical mode, by cooling the mechanical motion with light and cryogenic equipment. This is a fascinating possibility as it would enable the mechanical mode to show true quantum behaviour with an average vibrational phonon mode number of unity, leading to a new avenue for showing standard quantum optics experiments. Not only is it new to show this behaviour in mechanical systems, but it is also the biggest scale of massive samples where quantum effects have been shown, with quantum optics experiments usually involving single trapped ions or atomic ensembles and so on. The ground state cooling have now been achieved in several groups [O/'Connell10, Teufel11, Chan11], and will probably be replicated by others soon. These groups start out with samples already at really low bulk temperature in dilution refrigerators, and this gives a nice head start as the vibrational modes are at the cyrogenic bulk temperature without photoinduced cooling.

Regarding the ground state cooling, it should be noted that what is achieved is not the ground state as an equillibrium. Rather one should think about it as a thermal state with a probability of being in the ground state. If the effective temperature of a mechanical mode is sufficiently low it starts to make sense to identify the vibrational mode as being described by a finite number of phonons occupying the mode. The phonon occupancy is given by [Chan11]

$$n_{phon} = \frac{k_B T^{\text{eff}}}{\hbar \omega_m} \tag{2.3.1}$$

with k_B being Boltzmann's constant. For $T^{\text{eff}} \to 0$ the phonon number approaches zero. The cooling process then effectively removes phonons from the mechanical mode in the quantum model for cooling as noted in **sec. B.1**. The ground state that is achieved is then the situation where a measurement of the vibrational occupation, through the decay rate of the mode, would result in a value around or lower than a single phonon occupying the mode. This is still a fascinating situation and enables modeling the mechanical mode as a few level system. Standard quantum optics experiments that would usually be available for systems such as trapped ions are then possible for the optomechanical system. Reaching the ground state cooling have not been the main focus

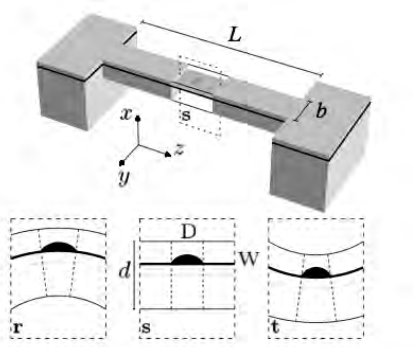

Figure 2.7.: Proposed system for coupling an embedded QD to the mechanical motion of the structure. The bending changes the local stress at the QD and changes the energy levels of it. Reproduced from [Wilson-Rae04].

of this work, and rather the interest is in the design and application of functional devices using optomechanical physics for manipulation. That is not to say that the cooling of mechanical modes have not been a goal, but the quest for the ground state requires a different mindset and preparation than what have been this project. It is interesting to combine the cooling of vibrational modes with

coupling to other systems and there have been a lot of proposals for coupling the mechanical mode of an oscillator to e.g. a *Quantum Dot* (QD) embedded inside, [Treutlein12] and experiments have shown the coupling of mechanical degrees of freedom to QD states [Bennett10]. Specifically the proposed system in [Wilson-Rae04] is indicated in **fig. 2.7**. It is a model system for coupling the mechanical motion to the quantum nature of the QD operating as a simple two level atom, and utilizing this coupling to cool the mechanical motion.

The focus has been on mechanical systems made out of Galium Arsenide (GaAs). These structures are so-called direct-band semiconductors, which enable the excitation of carriers directly by illumination [Harrison10]. This enables a lot of control of the internal state of the structure, and complicated structures combining GaAs with neighboring, in the sense of the periodic table, elements such as aluminum or indium, enables the trapping of excitations in e.g. QDs or *quantum wells*. Additionally the material can be doped with different elements, enabling the control of the potential in the structure by applying an external bias. This tunability enables an easy access to a large parameter space for different physics and applications and this prospect is what has motivated the work on functional materials.

Part II.

Mechanical modeling

3. Mechanical modeling

In this chapter the model of mechanical modes of membrane structures is presented as an interlude before the experimental work. First the basic approach to model the mechanical modes from the wave equation directly is described and the distinction between the plate approximation and the membrane approximation is introduced. Then in **chap. 4** a finite element method, FEM, is used with the commercial software Comsol to model more complex structures than is possible using the traditional approaches.

3.1. Mechanical model for membrane

Assuming that u describe the transverse displacement field in the z direction, that is $u = u_z(x, y)$, the model of the equilibrium configuration for a bend plate or membrane is significantly simplified if the displacements are much smaller than the thickness of the membrane. This is not a necessary requirement and if the requirement is loosened to only be that the displacement is much less than the lateral dimension of the plate, $u \ll l$, the large deflection of a plate can be calculated. From standard elasticity theory [Landau86, Soedel04] an expression of the minimization of the pure bending energy and general stretching energy can be found as

$$D\Delta^2 u - h\frac{\partial}{\partial x_\beta}\left(\sigma\frac{\partial u}{\partial x_\alpha}\right) = P \tag{3.1.1}$$

where Δ denote the biharmonic operator, $\Delta = \nabla^2$, and α and β denote the spatial axis. The *flexural rigidity* D is

$$D = \frac{Eh^3}{12(1-\gamma^2)} \tag{3.1.2}$$

The first bending term can be written as Du/l^4 by evaluating the biharmonic, while the second stretching term can be evaluated as Thu/l^2 with T being the tensile stress. In elasticity theory it is customary to denote a *membrane* as a thin plate subject to large external stretching forces applied at the edge. That is also called a clamped membrane in alternative to a free membrane.

In the case of a clamped membrane the tensile stress T is dominating the internal stress, and there is negligible contribution to the stress by the longitudinal stresses caused by bending of the membrane. Thus there is basically the case where the energy is dominated by the bending energy, which would be the case for the bending of a plate, and the stretching energy for a clamped membrane.

The bending energy per area is then Eh^3ul^{-4} while the stretching energy per area is $Thul^{-2}$. For a specific system these can then be compared. Work on membrane structures with the dimensions

in the few micrometers are described in **chaps. 7, 8** and for these *nanomembranes* the ratio can be estimated as

$$\frac{Eh^3\frac{u}{l^4}}{Th\frac{u}{l^2}} = \frac{Eh^2}{Tl^2} \approx 1000 \times \frac{(110\times10^{-9})^2}{(10^{-5})^2} = 10^{-4} \tag{3.1.3}$$

where the thickness $h = 110$ nm and $l = 10$ μm. The Young's modulus $E = 86$ GPa for GaAs while the tensile stress is a lot smaller, and certainly not the 800 MPa of the high stress SiN used for the Norcada clamped membranes. Here it is set to MPa range so that the E/T ratio is 10^3. From **eqn.** (3.1.3) it is clear how the bending part is dominating even though $E \gg T$ because of the geometrical aspect ratio, $h^2/l^2 \approx 1\times10^{-4}$. Thus there are these two different approximations applicable for different systems. For a clamped membrane the equation is

$$hT\Delta u + P = 0 \tag{3.1.4}$$

where the pressure P can be expressed by the dimensions and the second time derivate of displacement field as $P = \rho h\frac{\partial^2 u}{\partial t^2}$. The membrane equation then becomes

$$hT\Delta u + \rho h\frac{\partial^2 u}{\partial t^2} = 0 \tag{3.1.5}$$

Now assuming that u has the time dependence as $e^{-i\omega t}$ the $\frac{\partial^2 u}{\partial t^2} = -\omega^2 u$ and likewise with $e^{ik_x x}$, $e^{ik_y y}$ being the spatial dependence the $\Delta u = (k_x^2 + k_y^2) = k^2$. Then the membrane equation can be rewritten as $hTk^2 + \rho h(-\omega^2) = 0 \Leftrightarrow \omega = k\sqrt{\frac{T}{\rho}}$ which is the well known membrane dispersion relation. In **fig. 3.1** this linear dependence is indicated. Similarly for the bending plate equation

$$D\Delta^2 u = P \tag{3.1.6}$$

which can be written

$$\frac{\partial^2 u}{\partial t^2} - \frac{D}{h\rho}\Delta^2\rho = 0 \tag{3.1.7}$$

and thus

$$\omega = \sqrt{\frac{Eh^2}{\rho(1-\gamma^2)}}(k_x^2 + k_y^2) = \sqrt{\frac{Eh^2}{\rho(1-\gamma^2)}}k^2 \tag{3.1.8}$$

where it is noted how the plate equation scales with k^2 while the membrane scales with k. In **fig. 3.1** the different dispersion functions are shown for the plate bending equation and the membrane stretching equation.

Now for the bending plate equation approximation the fundamental frequency can be calculated by assuming the fundamental drum mode has a wavelength equal to half of the lateral dimension $l = \lambda/2$ and so

$$\omega_m = \sqrt{\frac{Eh^2}{\rho(1-\gamma^2)}}\left(\left(\frac{2\pi}{\lambda}\right)^2 + \left(\frac{2\pi}{\lambda}\right)\right) \tag{3.1.9}$$

$$\nu_m^{1,1} = \frac{2}{2\pi}\sqrt{\frac{Eh^2}{\rho(1-\gamma^2)}}2\left(\frac{2\pi}{l}\right) \tag{3.1.10}$$

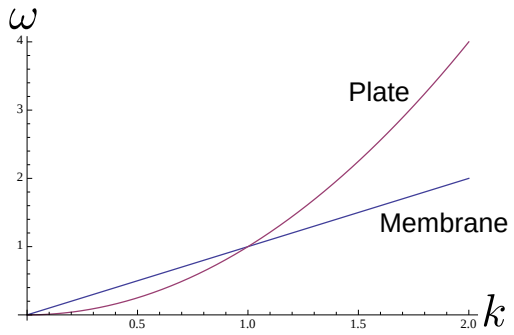

Figure 3.1.: Membrane k, versus bending plate k^2 approximation.

and for a tethered nanomembrane with parameters

h	l	$\nu_m^{1,1}$
110 nm	10 μm	8.45 MHz

which is in the same order of magnitude as measured for these structures as shown in **chaps. 7, 8**. To compare with another example from the literature the GaAs optomechanical tethered micromembranes in [Cole11] is found to be

h	l	$\nu_m^{1,1}$
10 μm	200 μm	1.92 MHz

which fits very nicely with the reported value. In conclusion it is worth noting how two different models are describing the membrane samples, whether the membrane approximation or the plate approximation is the most fitting, changes the behaviour considerably.

3.2. Vibrational modes of membrane

Here the standard model for the vibrational modes of a membrane is derived [Timoshenko08].

Rectangular plates vibrational

The basic model for rectangular plates can be derived by writing up the wave equation in rectangular coordinates, x, y

$$\frac{\partial^2 z}{\partial x^2} + \frac{\partial^2 z}{\partial y^2} = \frac{1}{v^2}\frac{\partial^2 z}{\partial t^2} \tag{3.2.1}$$

where v is the speed of sound in the medium. By assuming a product solution we can assume a solution of the form

$$z(x, y, t) = X(x)Y(y)T(t) \tag{3.2.2}$$

which can be inserted into the wave equation, **eqn.** (3.2.1), yielding

$$YT\frac{d^2X}{dx^2} + XT\frac{d^2Y}{dy^2} = \frac{1}{v^2}XY\frac{d^2T}{dt^2} \tag{3.2.3}$$

By dividing through with XYT and multiplying with v^2 we find

$$\frac{v^2}{X}\frac{d^2X}{dx^2} + \frac{v^2}{Y}\frac{d^2Y}{dy^2} = \frac{1}{T}\frac{d^2T}{dt^2} \tag{3.2.4}$$

which has a solution only if both sides are equal to a constant k^2. Setting the RHS of **eqn.** (3.2.4) equal to a constant yield the harmonic solution

$$T(t) = A\cos\omega t + B\sin\omega t \tag{3.2.5}$$

where the constant have been identified as the angular frequency. Likewise for the LHS of **eqn.** (3.2.4)

$$\frac{v^2}{X}\frac{d^2X}{dx^2} + \frac{v^2}{Y}\frac{d^2Y}{dy^2} = -\omega^2 \tag{3.2.6}$$

and this is equal to

$$\frac{1}{X}\frac{d^2X}{dx^2} = -\frac{\omega^2}{v^2} - \frac{1}{Y}\frac{d^2Y}{dy^2} = -k_x^2 \tag{3.2.7}$$

The same proceedure can be followed for the $Y(y)$ dependent term which should also equal a constant

$$\frac{1}{Y}\frac{d^2Y}{dy^2} = k_x^2 - \frac{\omega^2}{v^2} = -k_y^2 \tag{3.2.8}$$

and identifying

$$k_x^2 + k_y^2 = \frac{\omega^2}{v^2} \tag{3.2.9}$$

the solution for x and y is

$$X = C\cos k_x x + D\sin k_x x \tag{3.2.10}$$
$$Y = E\cos k_y y + F\sin k_y y \tag{3.2.11}$$

Now we limit the model to clamped rectangular membranes and thus set the boundary conditions to be zero displacement at the boundary. Thus

$$z(0, y, t) = z(x, 0, t) = 0 \tag{3.2.12}$$

which requires $E = G = 0$ in eqns. (3.2.10,3.2.11). Similarly, the conditions

$$z(L_x, y, t) = z(x, L_y, t) = 0 \tag{3.2.13}$$

gives rise to

$$\sin k_x L_x = \sin k_y L_y = 0 \tag{3.2.14}$$

so that $L_x k_x = m\pi$ and $L_y k_y = n\pi$ where m, n are integers. The wavenumbers can then be identified

$$k_x = \frac{m\pi}{L_x}, \quad k_y = \frac{n\pi}{L_y} \tag{3.2.15}$$

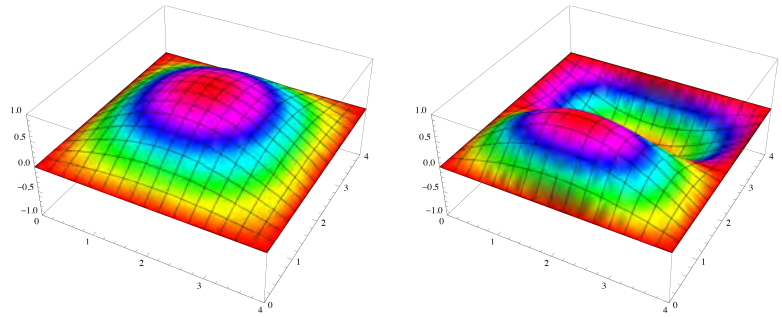

(a) (1,1) mode. (b) (1,2)

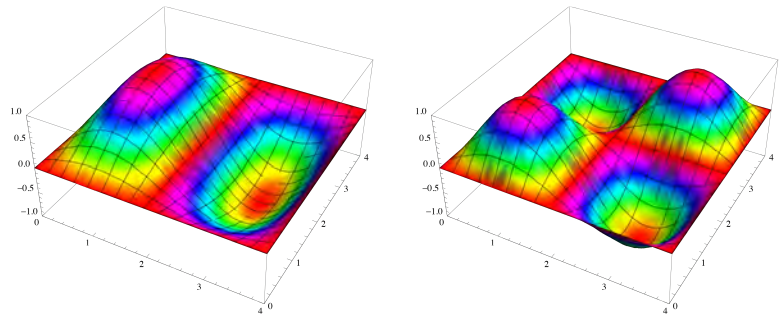

(c) (2,1) (d) (2,2)

Figure 3.2.: The first 4 mechanical modes of a symmetric membrane following **eqn.** (3.2.17).

which now enable the solution of the eigenfrequencies ω_m. Inserting the wavenumbers into **eqn.** (3.2.9) give

$$\omega = v\pi\sqrt{\left(\frac{m}{L_x}\right)^2 + \left(\frac{n}{L_y}\right)^2} \tag{3.2.16}$$

Inserting the solutions of the x, y parts into **eqn.** (3.2.9) makes it possible to rewrite the solution **eqn.** (3.2.2) as

$$z_{mn}(x, y, t) = \left(A_{mn}\cos\omega_{mn}t + B_{mn}\sin\left(\omega_{mn}t\right)\right)\sin\left(\frac{m\pi x}{L_x}\right)\sin\left(\frac{n\pi y}{L_y}\right) \tag{3.2.17}$$

where A_{mn} and B_{mn} is the constants depending on the initial conditions. Example mechanical modes are illustrated in **fig. 3.2**.

The formula for the vibrational frequencies **eqn.** (3.2.16) is used a lot when identifying a peak in the vibrational spectrum and trying to find other modes. The problem is that the speed of sound in the prefactor $v\pi$ is very dependent on the intrinsic stress and thus the value for bulk is not appropriate in most cases. However once one of the mechanical modes have been identified, **eqn.** (3.2.16) is a powerfool tool for finding other modes.

4. Finite Element Modeling

In this chapter the use of FEM for determining the eigenmodes is described of more complicated structures than described in **chap. 3**. The applicability in describing heat transfer and the mechanical Q_m is discussed as well. In the end it is concluded that FEM is a great tool for mapping out the different mechanical modes, but the determination of e.g. the Q_m from first principles is not trivial.

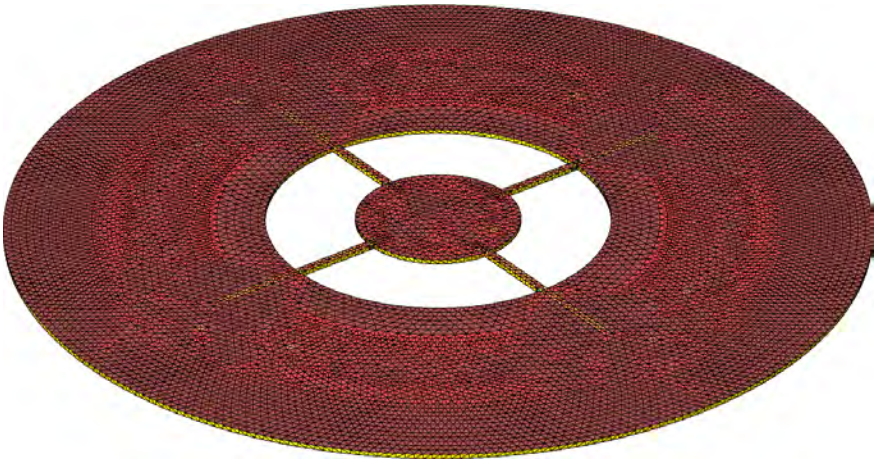

Figure 4.1.: Example Finite Element grid for solving a differential equation, e.g. finding the mechanical eigenmodes. In this example the grid have been made coarse to make the structure of the grid visible. The color indicate the quality of the grid, based on a Comsol algorithm.

4.1. Mechanical eigenvalues

The commercial software package Comsol is used for FEM. It is not necessary to perform FEM when identifying mechanical modes of the simple rectangular membranes, as these behave very much like the simple model, but for a more complicated structure, the interactions of different modes need to be included, and for example the edges not being sharp but rather softened round structures lead to different mechanical modes showing up in the spectra. Thus the FEM is useful in conjunction with the measurements to identify modes.

The *Finite Element - Frequency domain* approach is especially suitable for the needs of this project, as the eigensolutions is always ordered with the lowest energy ones first. This makes it easy to numerically find the lowest energy mechanical modes, without having to model all the degrees of freedom of the system. An example of the grid that the FEM method uses for a tethered nanomembrane structure is shown in **fig. 4.1**.

In **fig. 4.4** the (1,1) and a higher order mode of a non-rectangular membrane are shown. This is the shape of the big GaAs membrane studied in **chap. 5** and it is illustrated how the mode shape is nontrivial.

Because of the way the wave equation is set up, the problem can be reduced to only being dependent on the Young's Modulus and the density of the material (except of course the geometry and boundary conditions), but this is unfortunately not enough to simply get the right values for the mechanical eigenfrequencies [Eichenfield09]. This is because of the way the tension enters and is related to Youngs modulus. The speed of sound in the structure is approximated by

$$v = \sqrt{\frac{E}{\rho}} \tag{4.1.1}$$

with E being Young's modulus, and ρ being the density. The formula for the eigenfrequencies for a simple square clamped membrane was found above as

$$\nu_m = \frac{v}{2}\sqrt{\frac{i^2+j^2}{L^2}} \tag{4.1.2}$$

with L being the sidelength, and i, j denoting the mode indices. As this simple equation is simply related to the E and the tension is dependent on the stress deposited during fabrication, it is clear that values from the literature for e.g. bulk GaAs, is not applicable to estimate the eigenfrequencies in a quantitatively manner. Thus only the order and identification of eigenmodes should be found using the FEM. When the apropriate mode has been identified in experiment, the corresponding E can be changed in the FEM and then the actual frequencies can be estimated.

4.2. Effective mass contribution

The motional mass of the mechanical systems is what enters into the equation of motion, instead of the total mass, as only the effective motional part of the system should enter into the dynamics. The motional mass for a clamped membrane can be found as [Gillespie95, Pinard99, Thompson08]

$$m_{\text{eff}}^{n,m} = \rho h \int_0^w \int_0^w \sin^2\left(\frac{n\pi x}{w}\right)\sin^2\left(\frac{m\pi y}{w}\right) dxdy \tag{4.2.1}$$

$$m_{\text{eff}}^{1,1} = \frac{1}{4}\rho h w^2 = \frac{1}{4}m \tag{4.2.2}$$

with m being the membrane mass, w denoting with sidelength of the membrane and h denoting the thickness. The density is ρ and n, m denote the mode index. It is implicit in this definition of the effective mass that the inclusion of the coupling to a light field would require the inclusion of an overlap integral between the light field and the acoustic mode. If no overlap is taken into account it is actually the effective mass when a point-like light beam is sampling an antinode of the mechanical mode. For a higher order mode the effective mass would then correspond to the antinode with largest displacement. It is customary for more involved geometries than clamped membranes to introduce an effective mass that is including the effective coupling g_m for a given mode m. This

makes a lot of sense in a case where the motional mass involved in an acoustic mode is spread out accross a complicated structure, as in the optomechanical crystal [Eichenfield09] case. Following [Pinard99, Schließer09] a definition of the effective mass for a particular mode, m, coupling can be found as

$$m_{\text{eff},m} \equiv \frac{m_m}{\langle w, u_m^0 \rangle^2} \tag{4.2.3}$$

with u_m^0 being the mechanical displacement field for the mode m with moving mass m_m and w being a weighting function. This weighting function is introduced to map the displacement field $u = u(r,t)$ into a scalar displacement z. Thus a definition including the overlap has been introduced in this effective definition of the 'detected' mass into $m_{\text{eff},m}$

For more complicated structures than a membrane it not easy to find the motional mass of a given mode and work towards a numerical method was done.

It is possible in FEM to extract the so-called motional participation factor (MPF) from the eigenmodes. This is done by a renormalization of the eigensolutions in terms of the so-called mass matrix, and expresses in what manner a certain mode might respond to an actuation in a given direction. Technically the eigenmodes $\mathbf{U}_n$ are orthogonalized with respect to the mass matrix M so that [Com]

$$\mathbf{U}_n^T M \mathbf{U}_n = \mathbf{1} \tag{4.2.4}$$

for a mode n and the participation factor for a mode n in the direction p, $r_{n,p}$ is given as

$$r_{n,p} = \mathbf{U}_n^T M \mathbf{d}_p \tag{4.2.5}$$

where $\mathbf{d}_p$ is a vector containing unity displacement in the 3 directions of the coordinate system of the sample. It is clear that this motional mass participation should be compared to the probe optical field size on the membrane. If it experimentally makes sense to approximate the probe field size as a point compared to the acoustic mode size then the MPF can be used as an indication of the optomechanical coupling. This is a good aproximation for a big structure like the GaAs membrane used in **chap. 5** where the optical beamsize was about 80 μm in $1/r^2$ measurement. Compared to the transverse dimensions of roughly 1 by 2 mm this is well approximating a point. In the opposite regime the nanomembranes investigated in **figs. 7, 8** are the size of a couple of μm, and the probe beam size is very much the same size as the structure. If the nanomembrane is the only structure vibrating and coupling to the optical field, the MPF in the longitudinal direction would be a good indicator of the optomechanical coupling. However for quite a few of the mechanical modes a large part of the surrounding underetched area is also contributing to the displacement, and thus a calculation of the overlap with the optical beam would be necessary. In **fig. 4.2** an example sketch of the 4.84 MHz mechanical mode is shown with a probe beam indicated. It is clear that the big area around the tethered membrane, which is denoted the underetched, contributes to the measured motion with a large probe beam while a smaller probe beam will only sample the motion of the nanomembrane. In **sec. B.2.1** is shown the FEM of the 20 lowest energy mechanical modes of these nanomembranes, and it is found that a lot of the modes show a large displacement of the underetched area.

Examples of the calculated of the participation factor are shown in **fig. 4.3** where it is shown how the participation is different for different modes, and that it is not trivially a monotonous decline in participation for higher energy modes.

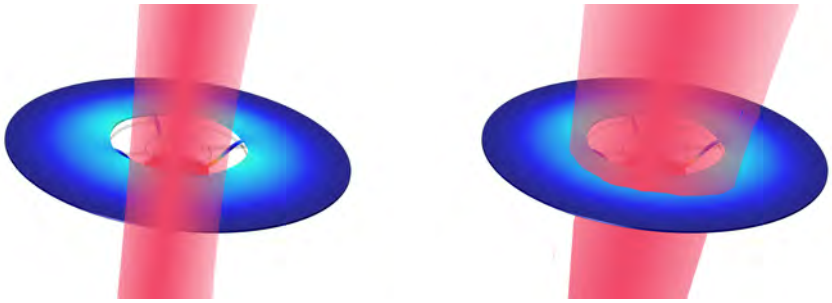

(a) (b)

Figure 4.2.: Illustration of an example beam overlap for the nanomembranes with a beamsize comparable with the nanomembrane and one bigger.

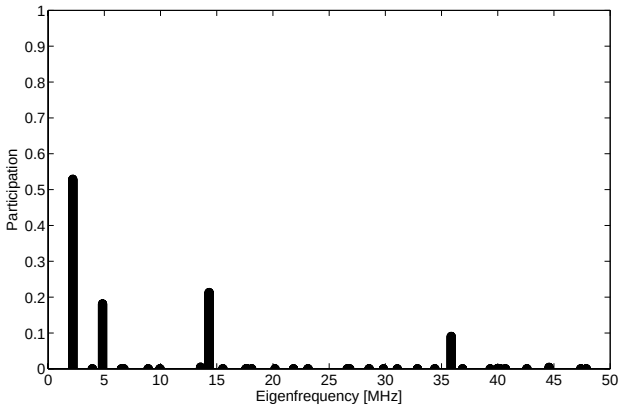

Figure 4.3.: Participation factor of the mechanical modes of the nanomembranes studied in **sec. 7.2**. Clearly the modes with 2.19 MHz, 4.84 Mhz, 13.6 MHz, 14.3 MHz MHz dominate.

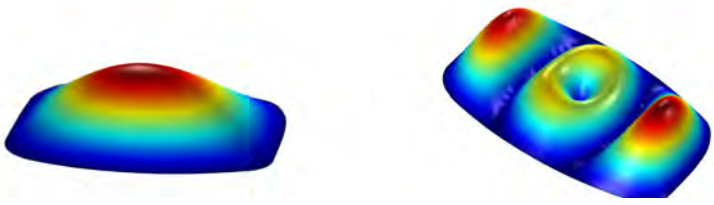

(a) The (1,1) mode. (b) Higher order mode

Figure 4.4.: Examples of FEM mechanical modes for a GaAs membrane. The nontrivial shape leads to nontrivial mechanical mode shape.

So in one convention the effective mass include the overlap between the light field and the mechanical mode, while in another convention this is included as an explicit overlap term that is integrated over. The effect is illustrated in **fig. 4.5** where a probe beam at the side of a membrane only show a small overlap with the (1,1) mechanical mode. For three different positions of center, corner and the side (as shown in **fig. 4.5**), the overlap is shown in **fig. 4.6**. It is clear how the different modes will have different contribution to the measured signal, and this needs to be included when the effective mass of a mode is discussed.

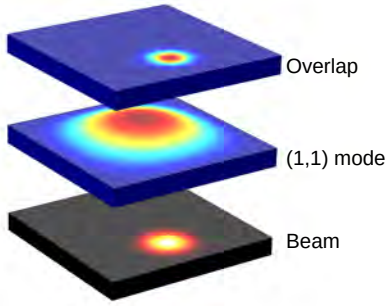

Figure 4.5.: Overlap with beam for the (1,1) mode.

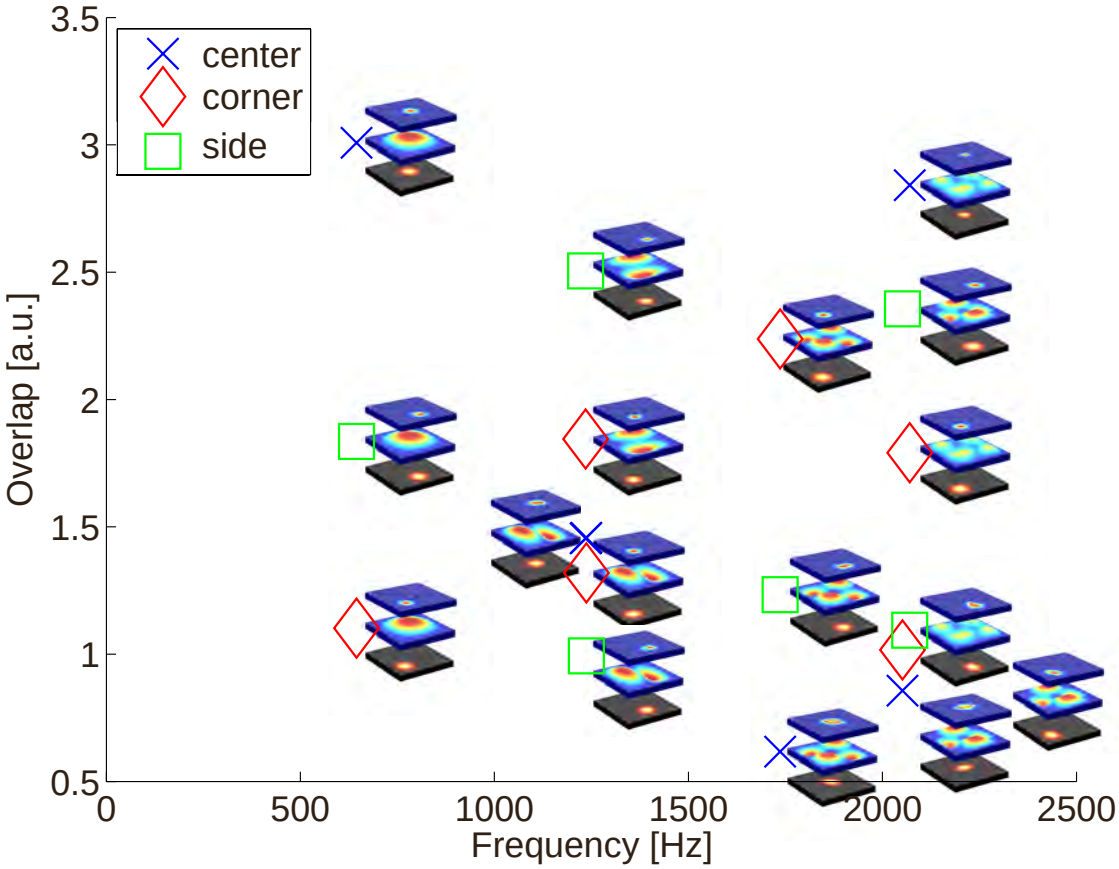

Figure 4.6.: Overlap with beam

4.3. FEM modeling of mechanical quality factor

In the FEM no loss is included unless specifically input. This is possible through inclusion of the various loss mechanisms that actually occur in the materials. However these are manyfold, and complicated to model. An estimate of the dominating loss mechanism would be very nice to have.

What is needed is to model the extend the excitation can reach if allowed to travel in the area surrounding the sample. Consider a mechanical system suspended by tethers. It is then necessary to include a large surrounding system where an excitation can travel and dissipate without reaching the edge and reflecting. It is problematic to achieve this computationally but what is done instead of creating a large structure, is include an absorption of the excitation in the material outside the sample. A technical way of implementing this is to include an imaginary term in the Young's modulus for the material [Eichenfield09, suppl. inf.] that is increasing as the distance from the sample increases. This is akin to the *Perfectly Matched Layer* [Taflove05] which is well known from studying electromagnetics where it is needed to not have reflections. The Young's modulus is included as $E_{reservoir} \rightarrow E_0(1+i\eta)$ where E_0 is the standard material E and $\eta = \eta(z)$ is then the function of distance z from the sample that includes absorption. The mechanical Q_m is then estimated using $Q_m = \Re(\nu_m)/(2\Im(\nu_m))$.

The η function needs to be small enough around the sample to not effect the power dissipated at the tethers which would change the estimated Q_m, but at the same time big enough and varying appreciably so that the radiated excitation propagates a significant distance in the surrounding system but attenuated so that nothing reflects and reenters the sample area. Thus the surrounding system should be made very big, and η varied until the above requirements are met. Then the absorption is increased until there is a clear change in Q_m as estimated using the above relation, which then fixes the η, and thus Q_m.

In **fig. 4.7** examples of these excitations are shown. It is seen how the excitations propagating in the surrounding material with and without enough η function are shown. The procedure of optimizing the η is done for all eigenfrequencies of interest.

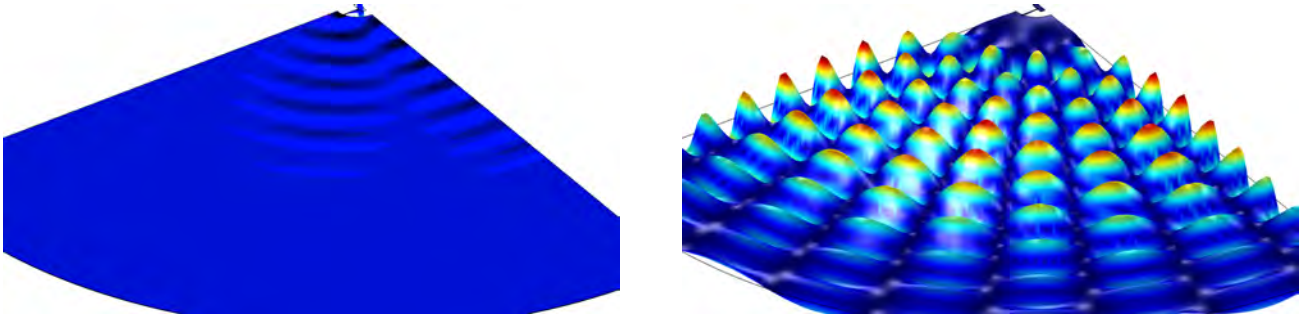

(a) Example of mechanical displacement with suitable η. The propagating wave is visible, but attenuated before reaching the edge of the surrounding structure.

(b) Example of mechanical displacement without enough absorption.

Figure 4.7.: Q_m estimate

Conclusions from the FEM

From the investigations of the tethered membrane structure it was found that the estimates of Q_m follows

- Q_m increases as the width of the tethers decreases
- Q_m increases as the length of the tethers increases
- Q_m increases to a maximum if the tether is placed slightly offset from the center of the membrane where there is a node in the displacement field

This is among the findings used for the design of the next generation micromembrane structures described in **chap. 8**.

4.4. Heat transfer and bending

Work have also been done on modeling the local heating of the different membrane structures due to a light beam. This of course mostly relevant for the direct band-gap semiconductor structures and thus no heating for the SiN membranes are taken into account. A local expansion due to heat in the FEM can be introduced by a local expansion following the intensity of the modeled light beam as a gaussian. By coupling the *structural mechanics* framework and the *heat transfer in solids* in Comsol, the bending due to local heating can be modeled. This was done for the "big" GaAs but as the conclusions was the same as the simple heat diffusion discussion in **sec. A.5**, no further work was done in this direction. If more was known about the current crop of nanomembranes, it would be obvious to study the bending do to radiation pressure and also local heating for an above-band probe light. However at the time of this writing the nanomembranes have only shown a few detectable mechanical modes and this modeling have not been done.

4.5. Applicability of FEM

The FEM method is invaluable for identifying the different mechanical modes that is available for structures more complicated than a simple membrane structure. For the simple structures an exact solution can be found as described in **sec. 3.1**, but when that is not applicable a FEM solution is desirable.

At the same time it has been realized that the frequencies of the FEM eigenmodes do not always fit with the measured mechanical modes. In the normal stretched membrane mode of an 'off the shelf' membrane from e.g. Norcada, the tensile stress is known from the fabrication. From this known T the eigenfrequencies can be estimated using the expressions from **sec. 3.1** and compared with the FEM solution.

For more complicated structures, such as tethered membranes as presented in [Cole10], the stretched membrane approximation is not valid anymore. Such a FEM is indicated in **fig. 4.8**. Unfortunately this means that the internal stress is no longer dominated by the tensile stress, and then the determination of the fundamental frequency becomes a different problem. The eigenmodes can be modeled by assuming a free-free model for a rectangular structure, but then the effect of the tethers are of course disregarded. This can be applicable for the modes where the nodes of the motion

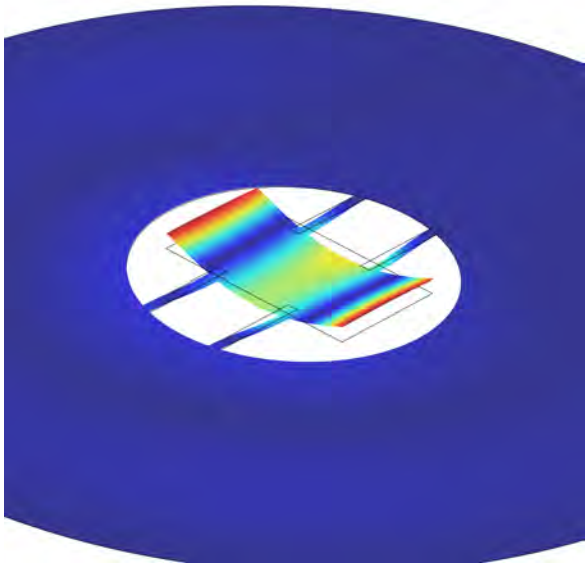

Figure 4.8.: Example FEM of a structure such as presented in [Cole10]. The color indicates the displacement. The displacement is grossly exaggerated for clarity. The underetched area around the tethered membrane itself extends far out with the edges being fixed by a boundary condition, thus affecting the membrane motion the least.

are at the tether points (assuming infinitely thin tethers), but to get the full list of modes a FEM is necessary. Without adding internal pressure in the FEM the values unfortunately do not fit with the experimental results, and this would not be easy to do in a systematic and accurate fashion. If the form is kept, even through the prefactor is much more complicated, the order of mechanical energy in the different eigenmodes are assumed to be unchanged. This is only true assuming the internal pressure distribution is isotropic which will not be the case. For a quick test for simple structures the FEM is very applicable to determine which mode is which.

Part III.

Cooling vibrations with light

5. Cooling with light

This chapter describes the implementation and investigation of cooling of vibrational modes for a GaAs membrane. The experimental setup is described and the different characterization methods are introduced. The evidence for strong cavity cooling is shown and the physical method that gives rise to this is investigated. It is proven that the cooling stems from a delay in the response of the membrane to a change in the cavity field. The delay is found to be due to the excitation of electron-hole pairs and the subsequent slow relaxation into heat is what governs the strong cooling effect.

What is remarkable is how strong the vibrational cooling is, which is found to be due to a strong photothermal cooling combined with the intrinsic bend of the membrane, and this is investigated and explained. It is shown how the vibrational cooling could be due in part to the so-called *deformation potential* cooling, and this is described as the next step in **chap. 6**.

5.1. The search for ground state cooling

It has been the goal of the optomechanics field to achieve vibrational groundstate cooling using the radiation pressure side-band cooling for a couple of years as described above. In this terminology the vibrational groundstate refer to the vibrational occupation being close to being equivalent of a quantum harmonic oscillator with a single phonon occupation. This have been achieved with three very different realizations being shown in '11 and '12. In fig. (5.1) is shown these 3 realizations [Verhagen12, Chan11, Teufel11] where a phonon population of the vibrational mode is cooled to less than 1. This is a remarkable statement and a milestone for physics.

The reason that these systems were the first was due to the very small size and the very clever engineering that has been put into designing them. The system in [Verhagen12] is a microtoroidal cavity where the ring of the torroid supports *whispering gallery modes* for the containment of both the light field and the vibrational degree of freedom. Additionally [O'Connell10] deserves an honourable mention as the first system showing this ground state cooling, but it was not vibrationally cooling with light, but rather via piezoelectric coupling. The system in [Chan11] is a highly engineered phononic cavity that localizes and decouples the vibrational mode at the point where a photonic crystal cavity is created, thus creating a very small, and highly isolated system. The system in [Teufel11] is a superconduction microwave circuit and thus the cooling field is a coherent microwave drive, but it is essentially the same type of system.

It should also be noted that even though these groups have shown an average phonon occupation of less that one, they are still in a thermal state but with a small probability of measuring more than one phonon occupation. The conclusion that this state is purely non-classical is thus a little bit of a stretch, but a lot of new avenues such as strong coupling allowing for coherent state transfer into the membrane motion and storing of quantum states in the vibrations, are possible now this milestone has been achieved [O'Connell10, Teufel11, Chan11].

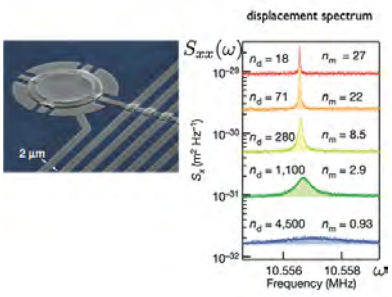

(a) System from the NIST/JILA groups [Teufel11].

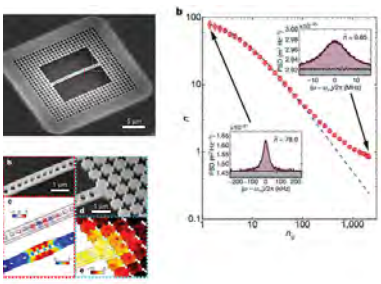

(b) System from the Painter group (Aspelmeyer) [Chan11].

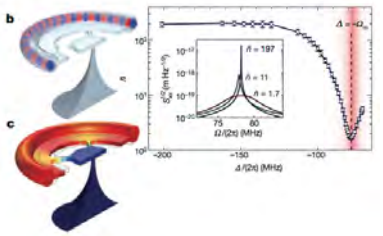

(c) System from the Kippenberg group [Verhagen12].

Figure 5.1.: Examples of cooling 3 very different micromechanical systems to the vibrational ground state.

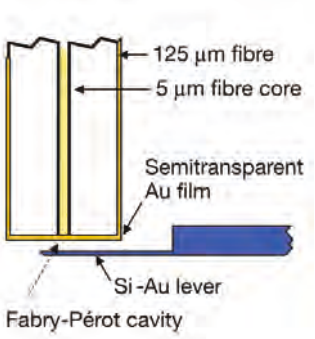

Figure 5.2.: System from [Metzger04]. A gold coated silicium cantilever creates a Fabry-Pèrot cavity with a gold coated fiber. Reproduced from [Metzger04].

Here the focus is on a different cooling method than the one employed in these setups. The experiment is performed at room temperature and the cooling process is due to heat induced by the impinging photons. This is the socalled photothermal cooling [Metzger04], where the local heating couple to the mechanical degree of freedom and leads to vibrational cooling.

The contributions of the author
While the original optomechanical setup was designed and implemented by Koji Usami, Bo Melholt Nielsen, Tolga Bagci and the author, the work presented in this chapter was done almost exclusively by Koji Usami and the author. Koji Usami made the realization that the strange chaotic behaviour that was witnessed was due to a strong photoinduced force, and the author and Koji Usami then embarked on a long investigation of the mechanism with the help and councel, as well as experimental assistance, from many sides. Thus the author has been heavily involved in the design, optimization and operation of experiments and analyzation of the results to investigate this effect in the GaAs membrane, with help from Tolga Bagci.

5.1.1. Examples of photothermal cooling

In [Metzger04] the cavity-induced photothermal cooling of a vibrational mode using a gold coated silicon micro cantilever was shown. The thermal motion of the cantilever was monitored by setting up a Fabry Pérot cavity between the cantilever and a gold coated fiber tip, and then measuring the reflection. By measuring the high frequency components (around the vibrational frequency) of the reflection signal, the motion of the cantilever can be deduced. In **fig. 5.2** the system in question is shown. They succeeded in cooling a vibrational mode from room temperature more than a factor of 16. In the language of effective vibrational temperature, T^{eff}, from **eqn.** (2.2.27) they achieved vibrational cooling to $T^{\text{eff}} = 18$ K. In this case the photothermal force is implemented through the different thermal expansion coefficients between the silicon cantilever, and the gold coating. When photons are absorbed in the gold film they heat locally and expand. This expansion then couples to the motion of the lever by bending, but as it does not instantaneously deform, there is a delay to the response. This enters into the equations of motion as the delay $h(t) = 1 - e^{-t/\tau}$ that was introduced in **chap. 2**.

Because of the time delay between the local heating and the feedback on the motion of the mechanical system, the coupling to the vibrational motion of the cantilever and vibrational heating and cooling is possible, as was described in **chap. 2**.

5.2. Functional devices

So why is it interesting to focus on systems where photothermal cooling is a strong effect rather than trying to achieve grounds state cooling in the same fashion as a lot of other groups? A major reason is the potential outlook for designing functional optomechanical systems, where the vibrating mirror/membrane itself includes a nonlinear feature such as a confined structure as a quantum dot as proposed in [Wilson-Rae04]. Some of the avenues of investigating structures made of GaAs that exhibit this photothermal cooling are described in **sec. 2.3**.

5.3. Experimental setup

In this seciton the experimental setup will be described.

5.3.1. Membrane fabrication

The GaAs membrane was fabricated by the group of Peter Lodahl. As described in [Liu11] it was fabricated using a GaAs/AlGaAs heterostructure with a GaAs substrate, a 1 μm AlGaAs etch stopping layer, and a GaAs capping layer of 160 nm that is being turned into the membrane. The configuration is sketched in **fig. 5.3a**. The substrate GaAs is removed from the projected membrane area by selective wet-etching that etches away until it hits the AlGaAs stopping layer. A so-called non-buffered acid then selectively wet-etches the AlGaAs layer away from the underside, and what is left is then the thin GaAs layer. The remarkable thing by this fabrication proceedure is that the membrane is optically accessible from both top and bottom, which is unusual for such semiconductor structures. This is a bonus for using the membrane in optomechanical systems where it could be placed in a membrane-in-the-middle configuration, to achieve high cavity finesse and thus higher photon numbers.

The sample was cleaned and ready for use. It is worth noting how in the SEM picture **fig. 5.3b** the irregular rounded rectangle shape is obvious. This is not a fancy design choice, but rather how the etching follows the axis of the GaAs crystal, and the result of a rectangular mask is then this shape. This is different than the equations derived in **chap. 3** for the rectangular membrane. The main difference is that the different modes that are degenerate in a perfectly rectangular membrane, shows up with as different modes. In order to identify modes the membrane was investigated in a Vibrometer, and modeled using FEM.

The fabricated membrane is very big compared to other optomechanical systems, with a width of 1.36 mm and a length of 1.91 mm. The thickness is 160 nm. This "big" GaAs system is the main sample used in **chap. 5**. The system is shown in **fig. 5.4** in microscope pictures.

5.3.2. Membrane characterization setup

The basic setup is illustrated in **fig. 5.5**. A dielectric concave $^1/_2$ inch mirror with 96 % reflectivity forms a poor cavity with a membrane with a reflectivity of about 62 %. The finesse of the Fabry-Pérot cavity is measured to be about 10 in the wavelength of interest from 810 nm to 884 nm. The mirror is mounted on a piezo crystal to ensure that the cavity length, which is $\approx$ 29 mm, can be swept accross the cavity resonance, and the sample membrane is mounted in a movable

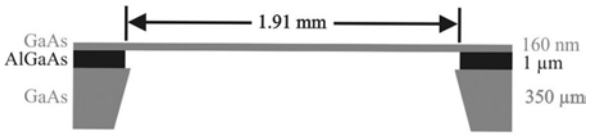

(a) Cross section sketch of the nanomembrane showing substrate, etch stopping layer and capping layer.

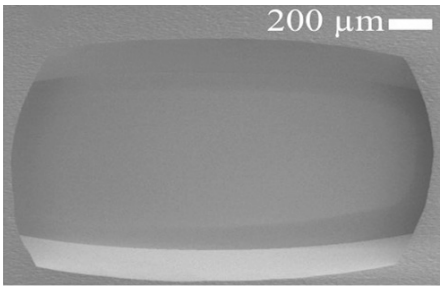

(b) Scanning electron micrograph of the cleaned membrane.

Figure 5.3.: GaAs membrane fabrication. Reproduced from [Liu11].

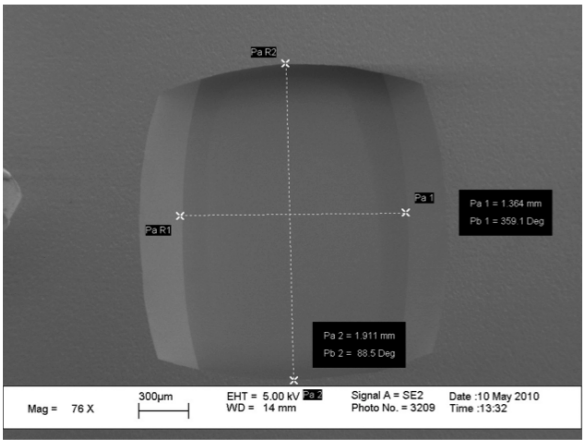

(a) Microscope picture of the backside of the GaAs membrane with dimensions.

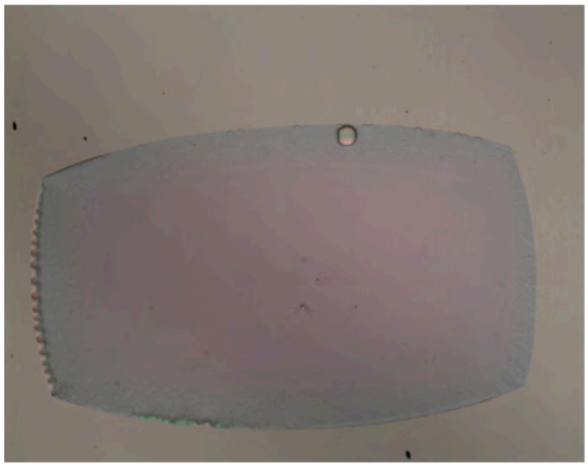

(b) Microscope picture of the backside of the GaAs membrane.

Figure 5.4.: GaAs membrane microscope pictures. Courtesy of the Lodahl group.

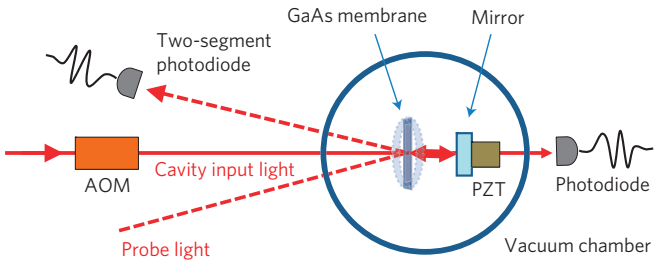

Figure 5.5.: Ringdown experimental setup. Reproduced from [Usami11].

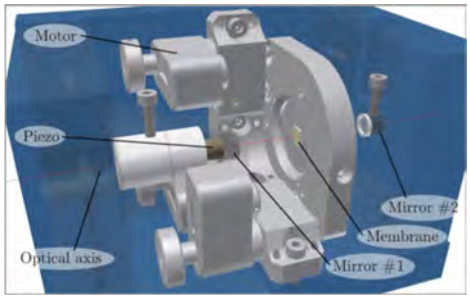

(a) Membrane mount with 3 degrees of freedom.

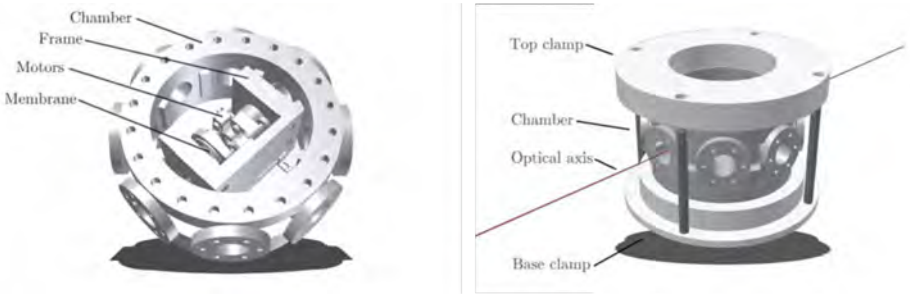

(b) Setup in the vacuum chamber. The transmission path for probe and pump light is indicated in purple.

Figure 5.6.: Fabricated setup pieces. Reproduced from [Nielsen10].

mount with 3 degrees of freedom in motion, see **fig. 5.6a**. The vacuum chamber is kept at 10^{-5} Pa with an initial pumping using a roughing/turbo pump combination, and is then kept at this pressure using a high voltage ion pump. The pressure is initially in the high range of ion pumps capabilities, but after a couple of days the leak current drops, indicating a lower particle number, and the system reaches a stable 10^{-5} Pa. Several lasers are used in the setup, the principal one being

Figure 5.7.: Cavity mirror mounted on a piezo prior to mounting. The piezo is glued to a cylinder made of teflon with the optical axis free and a channel for the external wire for the piezo. The internal wire is glued to the inside of the optical channel.

a Titanium:Sapphire laser capable of working in the 810 nm - 880 nm range. This is used for the cavity input beam achieving both cooling and agitating the mechanical oscillations. The beam from this laser is indicated with the full line in **fig. 5.5**. The membrane motion can be measured as a high frequency component of the transmission signal if the cavity length is kept on the slope of the transmission peak. This will be explained further. In order to control the power of this laser

light it is fed through an 800 MHz acousto-optical modulator crystal (AOM). This AOM enables a large degree of control of the cavity light and is used to stabilize the intensity of the laser. This is done by splitting the beam on a beamsplitter, and using an electronic photodetector-noiseeater combination to change the intensity of the RF signal that is driving the AOM. This is capable of fixing the optical power so that it is fixed to about 5% of the set power. The AOM also enables the modulation of the light intensity and is used for agitation of the vibrational modes, as is used for the so-called *Ringdown* measurement technique which is described in **sec. 5.4.2**.
Additionally a 975 nm diode laser is used as the probe light from an angle on the membrane. It is indicated with the dashed line in **fig. 5.5** and is used to measure the vibrations using a two-segment photodiode. The two main methods for determining the vibrational motion of the membranes are described later in **sec. 5.4**.

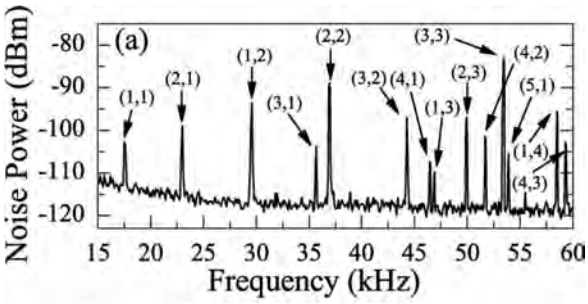

Figure 5.8.: Mechanical modes of the GaAs membrane. Measured using the transmission method and with the mode numbers indicated. Reproduced from [Liu11].

What is not shown in **fig. 5.5** is the stabilization electronics and the cavity lock. The length of the cavity is locked electronically on the slope of the cavity resonance. This is done by feeding the cavity transmission signal to the lock, which then puts feedback on the piezo controlling the cavity length. When the cavity length is locked at the middle slope position of the transmission signal, the measured voltage from the transmission detector contains information of the motion of the membrane. This is because a change in the cavity length due to the membrane motion modulates the cavity transmission, and if the length change is due to a mechanical vibration at frequency ν_m of the membrane, it will modulate the transmission intensity at this frequency.

An example of a measurement of the cavity transmission as it is being scanned by sweeping the mirror piezo is shown in **fig. 5.9**. The figure shows a measurement of the free spectral range (FSR) of the cavity, which is the shift in optical frequency from one transmission peak to the next. From the oscilloscope this shift can be related into the time it takes to sweep the cavity, 1.17 ms, and by measuring the FWHM of the transmission peak to 202 μs the finesse can be determined as, $\mathcal{F} \approx \mathrm{FSR}/\Delta\nu \approx 8.9$. The bandwidth was determined to be about 5.17 GHz by establishing the relationship between the time axis and the displacement of the mirror in the cavity.

In **fig. 5.10** the GaAs membrane with the cavity beam spot visible is indicated. The beam spot on the membrane is 80 μm in radius. Due to the geometry of the membrane and the mount it was only possible to achieve cavity coupling where the beam was hitting the upper right area of the membrane.

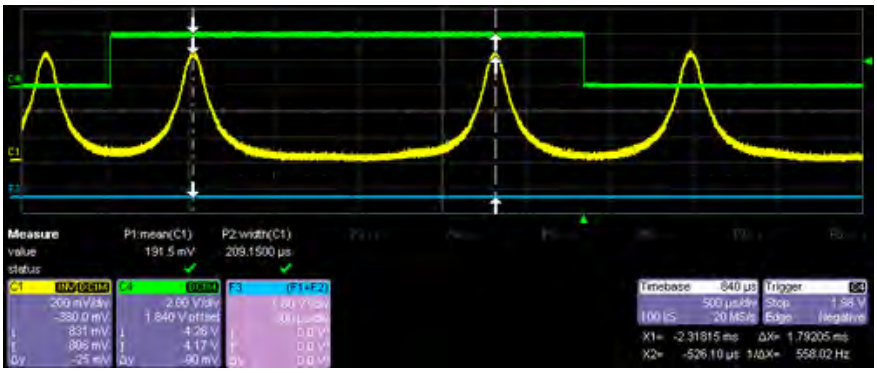

Figure 5.9.: Example of the measurement of the FSR by sweeping the cavity piezo accross the TEM_{00} cavity mode. The green trace of channel 4 indicates the sweep duration, but does not correspond to the actual sweep signal.

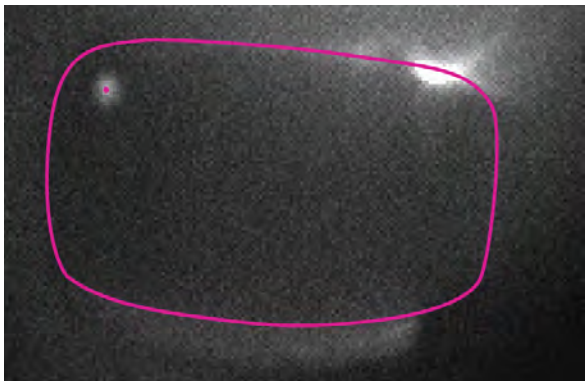

Figure 5.10.: Photo of GaAs membrane with the cavity beam spot visible. The beam spot is indicated with a dot, and the edges of the GaAs membrane is indicated with a line. The bright white spot in the top right is a reflection from the illumination provided from a side in order to produce the photo.

5.4. Mechanical characterization

Going back to the experimental methods the basic experimental methods for determining the fundamental properties of the membranes are described.

Determining the mechanical Q_m

Finding the Q_m value of the vibrational modes is not possible by determining the linewidth of the peaks in the displacement noise spectra as this is a harder problem than what would be expected. Because the mechanical modes of some of these samples exhibit very high Q_m they show sub Hz linewidth in the spectra, while unfortunately shifting in frequency ν_m over a time scale of seconds. Because a sampling time of 1 second is necessary to get a 1 Hz frequency resolution in frequency space, a shift of the frequency on the order of a couple of Hz will broaden the measured peak significantly.

Performing the Q_m measurement as a ringdown removes these problems. This can be implemented by the use of another laser beam that is intensity modulated with a frequency that is resonant with the mode that is to be excited. If the oscillation is enhanced due to the coherent excitation of the harmonic vibration it will decay with an exponential behaviour following the decay rate γ_m, when the intensity modulation is abruptly stopped. This is what is denoted a *ringdown* measurement. The Q_m is then found by $Q_m = \pi\tau\nu_m$ where τ is the ringdown time and ν_m is the mechanical eigenfrequency. This is the most reliable method that *Quantop* has identified so far, but it is a labourous process to characterize mechanical modes like this. This is again because of the high mechanical Q_m of the membranes which makes them hard to excite when as they are drifting. This makes it a game of 'cat and mouse', which takes a lot of time in order to get reliable results.

5.4.1. Reflection amplitude measurement

One of the simplest methods for characterizing which mechanical modes a given system is vibrating with is to shine a laser on it and detect the reflection on a split diode. If the probe laser is hitting a membrane in the center this method is very sensitive for changes in the angle of the membrane. The reflected light is led to a split diode detector as shown in **fig. 5.12a** and focused such that it takes up a large part of the split detector without 'clipping' on the edges of it. This makes it sensitive to changes in angle of the membrane in the plane of the split diode. The reflected beam is led trough a two mirror path to enable the alignment, and the position is optimized so that the difference signal from the two diodes is around zero. An example spectra measured with this method is shown in **fig. 5.12b**. In **fig. 5.11** a sketch of the setup is shown with the sample membrane in a vacuum chamger and the probe light coming in at an angle, and being reflected on a split diode. The advantage of being angle sensitive is unfortunately also a problem. Because it is an angle sensitive measurement at the probe position, vibrational modes of the membrane such as the fundamental drum mode (1,1) that only show displacement at the probe position, are not measurable with this method. Although the membrane displaces the path of the reflection beam by a couple of μm this only results in a very small change in the position on the detector while an angle change results in a much larger displacement from alignment. Thus this method is only sensitive to mechanical modes that have a node at the probe position and aligns with the orientation of the split diode. In the experiment the split diode was mounted horizontally, which means that the setup was sensitive to

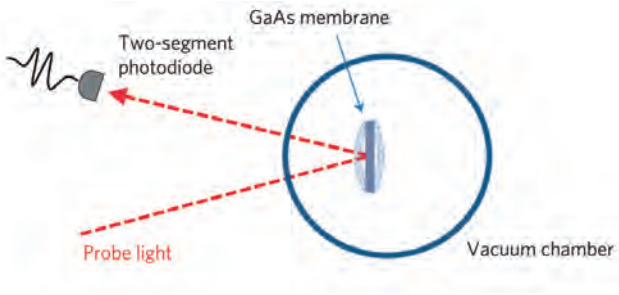

Figure 5.11.: Reflection amplitude measurement. Modified from [Usami11].

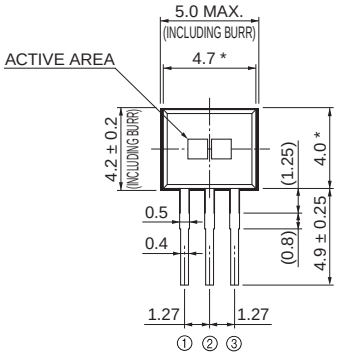

(a) Split diode S8703 from Hamamatsu.

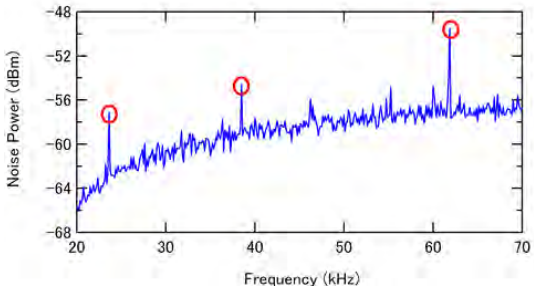

(b) Example of a spectrum derived using the reflection amplitude measurement. A couple of the very visible peaks are indicated with red, but several are not visible in this trace.

Figure 5.12.: Split diode for reflection amplitude measurement.

the modes with a node at the center and horizontal symmetry. It would be possible to manufacture a rotation mount for the split mount in order to achieve sensitivity to other angles. This could also be achieved by a split diode with 4 sensors, but it was deemed unneccessary as other methods are available.

In **fig. 5.13** is shown an illustration of the (2,1) vibrational mode of a rectangular membrane. This is the kind of mechanical mode that the reflection amplitude method is sensitive to.

5.4.2. Ringdown measurement

The procedure for performing a ringdown of the vibrational mode is as follows. The cavity input light is stabilized at a power $P_{ringdown}$ with a noise eater circuit. This low bandwidth stabilization keeps the cavity light stable where the fluctuations are on the order of maybe 5 % of the light power. In the signal path from the power stabilization, the noise eater is added an AM modulation, before the signal is fed to an amplifier driving the RF for the AOM. Thus the power is stabilized and the amplitude is modulated with a frequency ν_{mod} that is close to the mechanical frequency ν_m that is under investigation. The modulation amplitude is never so strong that the power P_{mod} is significantly changed from the set optical power $P_{ringdown}$, but can be on the order of $1/10$ of $P_{ringdown}$.

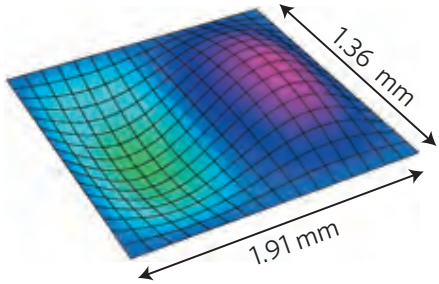

Figure 5.13.: Example of the (2,1) vibrational mode for GaAs membrane. Reproduced from [Usami11].

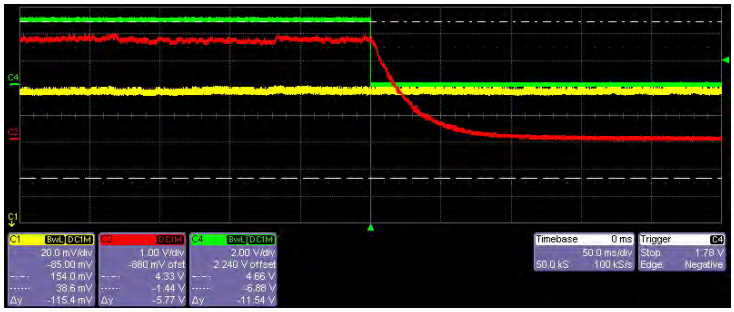

Figure 5.14.: Example *ringdown* measurement. The red trace is the lock-in signal amplitude and the green trace is the trigger signal for the AM. Thus when the green changes the AM is cut. The yellow is the tranmission intensity through the cavity, showing that the power does not change appreciably in this case with or without the AM. In this example a exponential fit [not shown] of the 651 kHz peak gives a $Q_m \approx 8 \times 10^4$.

If the AM frequency is close to the mechanical resonance[4] the drive excites the mechanical resonance strongly. This makes the membrane oscillate at a much higher amplitude at the resonance frequency and this is measured. When it has been established that the AM light is driving the membrane oscillating with high amplitude, the AM is stopped and the cavity light returns to being stable at $P_{ringdown}$. The excitation of the membrane then dies out with an exponential behaviour with a characteristic time that is $\tau_m = 1/\gamma_m$. Thus the decay rate γ_m can be established, and this is done by repeating the measurement 5 times to ensure repeatability.

Reproducing **eqn.** (2.2.22) it is noted how the effective decay rate is

$$\gamma_m^{\text{eff}} = \gamma_m \left(1 + Q_m \frac{\omega_0 \tau}{1 + \omega_m^2 \tau^2} \frac{\nabla F}{K}\right)$$

In **fig. 5.14** is shown an example of the measurement, with the red trace clearly showing the exponential decay of the amplitude of oscillations from the membrane as the AM is cut. The decay rate is changed to γ_m^{eff} when it is cooled following the discussion in **sec. 2.2**. By repeating this procedure for several cavity input power, most often 5, 10, 20, 30, 40, and 50 μW, a fit for the cooling factor $\gamma_m^{\text{eff}}/\gamma_m$ can be established. This is shown in **fig. 5.18**.

Technically an off angle laser is used for the detection of the vibrations. This laser is reflected by the membrane and led to an AC coupled split-diode for detection of the motion. Different lasers was used for this, but a 975 nm diode laser was used for a lot of the measurements. The amplitude from the ringdown measurement is gathered by use of a lock-in amplifier that is fed the frequency of the modulation and the signal from the photodiode measuring the reflection from the membrane. When the $\nu_{mod} \approx \nu_m^{\text{eff}}$ the amplitude of the membrane oscillation at ν_{mod} is measured by taking the square of the sine and cosine components of the lock-in signal. The bandwidth of the lock-in is kept at 100 Hz so that the measurement is sensitive to this frequency window around ν_{mod}.

The downside of using a off-angle laser for the detection of the motion, is that the reflection is off the membrane in the plane of the optical table, and thus the motion in the horizontal direction is mainly what is detected. This unfortunately means that the detection system for the *ringdown* measurement is more sensitive to modes like the (2,1) than the (1,1) because of the high dependence of the horizontal direction. In fact the (1,1) mode at around 17 kHz was hard to distinguish in the noise spectra from the off-angle beam.

5.4.3. Transmission measurement

In order to get the power spectra the power of the transmitted light is measured on a photodiode. This is done using the same detector that has the cavity lock built in and work was done to optimize the bandwidth of the lock versus the bandwidth of the detection. In the end a scheme with a differential measurement of the transmitted light with the input light subtracted resulted in a nice measurement for the mechanical modes of the membrane with some of the common mode noise subtracted. The input light is split on a PBS and a part of the light power is detected in order to stabilize the power. This detector monitor signal is subtracted from the detected transmitted light. The high frequency part of the signal contains the motion of the membrane. An example of a broad me-

[4] There is of course a situation where this is not the case. If the cavity beam is overlapping with a node of the mechanical mode, the AM of the light at that frequency will not couple to the vibration and drive it. This was never a problem in practice.

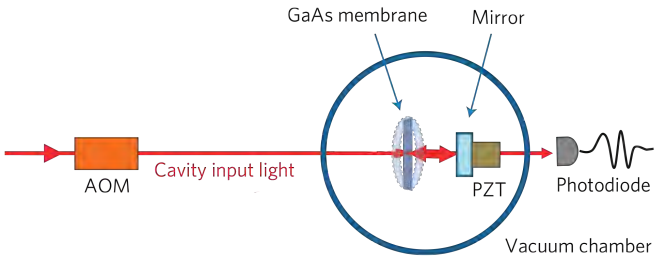

Figure 5.15.: Transmission experimental setup. Modified from [Usami11].

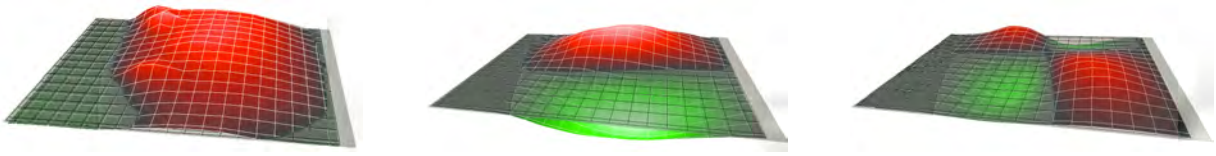

(a) (1,2) mode. 25.38 kHz (b) (1,3) mode. 44 kHz (c) (3,2) mode. 48 kHz

Figure 5.16.: Vibrational measurements of the GaAs membrane using the Vibrometer. Compare with the spectrum in **fig. 5.8**.

chanical spectrum measured using this method is shown in **fig. 5.8**. In order to calibrate the power spectra an additional calibration step is necessary as described in **sec. 5.5.1**. This makes a conversion into a calibrated displacement spectral density possible, as will be described in **sec. 5.5.1**. Examples of such calibrated spectra are shown in **fig. 5.17a**.

5.4.4. Vibrometer measurements

As mentioned *Quantop* has access to a Polytec Vibrometer and this device has been very useful for initial characterization. In **fig. 5.16** example measurements of three mechanical modes are shown. The microscope objective does not enable enough viewable area which unfortunately means the big GaAs membrane is not vieweable in one measurement. It is however still suitable for identifying modes as is obvious.

5.4.5. Topology measurements

In addition to the measurement technieques described above to characterize the vibrational characteristics of the membrane, visual inspection and topology measurements were done. As shown in **figs. 5.3b, 5.4** the samples were inspected under various microscopes. What is noticed by visual inspection is that the edges of the membrane structure show 'bubbles' or 'ridges', but that the surface itself is nice and clean after the cleaning procedure described in [Liu11]. An additional setup of measurements were performed in the Polytec Vibrometer to characterize the topology of the membrane. In **A.4** these topology measurements is shown. It should be noted that this was done using a different sample from the same fabrication batch than the one the vibrational measurements were performed with. As they are made at the same time, it is believed that the behaviour measured on one sample is transferable to another. What is found is that the GaAs

membranes have a high intrinsic bending due to stresses induced in the material during the fabrication as described in [Liu11, Usami11]. A bending on the order of μm is determined for the membrane, and this is a remarkable difference from e.g. the SiN membranes from Norcada. These are fabricated with high tensile stress around 800 MPa and subsequently behave like a tight drumskin with only a few nm of intrinsic bending. This reflects the difference between the shell behaviour for the GaAs membrane, and the membrane behaviour of the SiN system, as noted in **sec. 3.1**.

5.5. Experimental evidence of cavity cooling

Using the methods described in **sec. 5.4** it is possible to characterize the motional behaviour of the membrane sample. It was found that a cooling of the vibrational modes was measured, if the cavity length was fixed, and the light had energy larger than the bandgap energy of GaAs. This section details the search and proof of a very strong cooling effect in the GaAs membrane. It is found to follow the model described in **chap. 2**

In **fig. 5.17a** typical power spectra are shown for increasing cooling power of the Brownian motion peak for the (2,1) mechanical mode. These are gathered by measuring the cavity transmission for (13.7 μW, 20.1 μW, 26.2 μW) cavity light powers. The unorthodox choice of powers is due to technical reasons in the experiment[5]. The wavelength for this specific measurement is 870 nm. As the effective mode temperature, T_{eff}, is proportional to the area of the peak, [Metzger08b], it is clear how the vibrational motion of this mode is cooled for increasing cavity light power. Additionally the frequency ω_m decreases which also fits with a cooling effect as described in **sec. 2.2**.

In **fig. 5.17b** the result of the ringdown measurements done using the beam deflection method for the same mechanical mode is shown. The damping rate increases with increasing light power, and the frequency decreases as above.

The cooling is only observable for one detuning of the laser compared to the cavity resonance frequency. That is when the frequency of the cavity mode resonance $\omega_c/(2\pi)$ is detuned to the red from the frequency of the laser, $\omega_L/(2\pi)$. That is for $\omega_c < \omega_L$. This is the opposite detuning dependence that is associated with cavity cooling by radiation pressure [Kippenberg08, Favero09, Florian Marquardt09]. The system is unstable at the blue detuning side of the cavity transmisison peak, and mechanical instability behaviour set, in at just 5 μW of cavity light power. This is attribuated to the mechanical decay rate changing sign to negative as the system is heated, initiating chaotic behavior. The chaotic instability behaviour is also apparent for the $\omega_c < \omega_L$ detuning when the cavity power exceeds about 50 μW, and this limits the possible cooling. The reason for this is that the strong cooling effect introduces a high deformation of the membrane and as the effect gets stronger and stronger for increasing cavity power, at some point the power in the cavity becomes unstable, and the instability sets in. See **sec. A.3**.

As described in **chap. 2** the influence of a photoinduced force can lead to a change in the effective parameters describing the motion of a movable mirror in a Fabry-Pèrot cavity. In this setup the cavity is a mirror and membrane system. It was shown that if there is some time delay be-

[5]The technical reason was simply the need to keep the oscilloscope at the same dynamic range for all the measurements, and technical reasons with the intensity stabilization made the choice of these light powers a nice compromise.

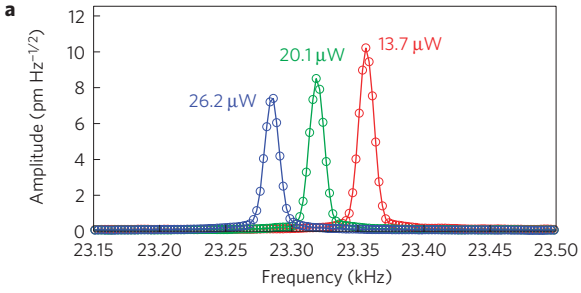

(a) Calibrated power spectra for the (2,1) mechanical mode. The resolution bandwidth was 10 Hz for these measurements.

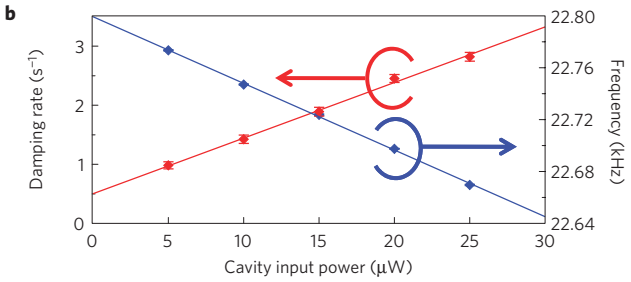

(b) Results of the mechanical ringdown measurements. The red measurements refer to the damping rate γ_m while the blue refer to the change in mode frequency ω_m as a function of cavity input power.

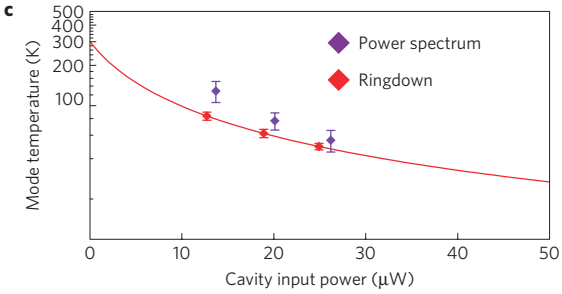

(c) Comparison between the effective mode temperature deduced using the calibrated power spectrum (purple) and the ringdown measurement (red). The error bars indicate the standard deviation over 5 identical measurements for each. The red line indicate a least-squares fit to the ringdown measurements.

Figure 5.17.: Measurements of the (2,1) mechanical mode temperature for increasing cooling power. Laser frequency wavelength of 870 nm. Reproduced from [Usami11].

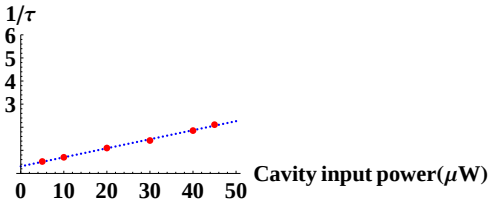

(a) Decay rate $\gamma_m = 1/\tau$ measurement.

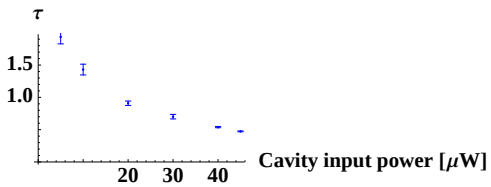

(b) Decay time τ measurement.

Figure 5.18.: Ringdown measurements of cooling for the (2,1) mechanical mode using 871.9 nm cavity input.

tween a mechanical perturbation of the membrane and the response of the photoinduced force, this can lead to a 'viscous' force on the mechanical motion of the membrane. It is then possible to remove mechanical motion from the vibrational mode of the membrane and this is denoted 'cooling' of the mechanical motion. The relevant time lag τ enters into the equations describing the cooling. The formula for the effective frequency due to the cooling is according to **eqn.** (2.2.24)

$$(\omega_m^{\text{eff}})^2 = \omega_m^2 \left(1 - \frac{1}{1+\omega^2\tau^2}\right)\left(\frac{\nabla F_{ph}}{m\omega_m^2}\right) \tag{5.5.1}$$

where m is the motional mass, γ_m is the intrinsic mechanical decay rate, and the intrinsic (without cooling) quality factor is $Q_m = \omega_m/\gamma_m$. $\nabla F_{ph}(x)$ is the spatial derivative of the photoinduced force F_{ph}. This corresponds to the induced rigidity, and is thus basically the effective induced spring constant. Correspondingly the decay rate of the mechanical vibration will be according to **eqn.** (2.2.22)

$$\gamma_m^{\text{eff}} = \gamma_m \left(1 + Q_m \frac{\omega_m\tau}{1+\omega^2\tau^2}\right)\left(\frac{\nabla F_{ph}}{m\omega_m^2}\right) \tag{5.5.2}$$

and the effective mode temperature can be found by **eqn.** (2.2.27) as

$$T^{\text{eff}} = \frac{\gamma_m}{\gamma_m^{\text{eff}}} T \tag{5.5.3}$$

In **fig. 5.17c** the comparison between the two methods for assessing the effective mode temperature for increasing cavity input power are shown. The ringdown and power spectrum methods were described above in sec. **sec. 5.4.2** and **5.4.3**. There is found a nice correspondence between the results of the two different methods. This is remarkable in that it is very different ways of deducing the decay rate of the mode, while one is actively driving the vibrational mode using amplitude modulation of the cavity light, and the other is measuring the brownian motion directly without significant excitation. The cooling factor, i.e. the ratio of the effective cooled mode temperature to room temperature, for a input power of 50 μW, is about 10 for this (2,1) mode. This can be compared to the the (4,3) mode which showed a mechanical Q_m of 2.3×10^6. This mode was cooled to an effective 4 K temperature, which corresponds to a cooling factor of about 75 which is rather impressive and a record for this kind of system[6].

Also worth noting is that the good correspondence in **fig. 5.17c** between the ringdown and the power spectrum measurements mean that the bulk temperature of the membrane is not changed significantly by the cavity light power. One could imagine that the actual bulk temperature of the membrane was changed significantly by the cavity light, which would mean that while the measurement of γ_m^{eff} using the ringdown method obviously yields a nice determination of γ_m^{eff} it is not possible to deduce the cooling factor, if the actual bulk temperature of the membrane is changed significantly. Using the power spectrum method, the actual mode temperature is measured and thus this is not the case for the low cavity input powers used (less than 50 μW).

5.5.1. Calibration scheme

In order to calibrate the spectral density gathered using the transmission measurement method, a frequency modulation is put on the cavity light beam as described in [Usami11, Tittonen99].

[6] Where 'this kind of system' refer to a semiconductor system such as this GaAs membrane and the cooling effect is photothermal rather than radiation pressure induced. Higher cooling powers have certainly been witnessed using high finesse cavity cooling using radiation pressure. [Kippenberg08, Aspelmeyer10]

When a frequency modulation is put on the cavity light by means of a AOM there is actually also a slight amplitude modulation. This is because the deflection angle is frequency dependent, and subsequently the coupling efficiency onwards to the membrane is slightly frequency dependent. This translates into an amplitude modulation by

$$\frac{\text{AM}}{\text{FM}} = \frac{\kappa}{\omega_m} \tag{5.5.4}$$

which makes the difference for low cavity finesse where the cavity decay rate κ is big. It is clear from this expression that in order not to have the AM dominate it needs to be suppressed an order of κ/ω_m. For this low finesse cavity, the bandwidth was determined to be 5.17 GHz at 870 nm. and for a $\omega_m/(2\pi) \approx 22$ kHz for the (2,1) mode, it is clear that this puts bounds on the amount of AM acceptable. The inability to eliminate the AM sufficiently for this low finesse cavity is probably a large part of the explanation for the discrepancy between the cavity transmission power spectrum measurement of the mode temperature versus the *ringdown* measurements as shown in **fig. 5.17c**.

Now the goal is to understand how the induced frequency modulation in the cavity light leads to a peak in the spectrum at the modulation frequency. With the wavelength of 870.1 nm and a FSR of 5.17 GHz it is possible, it can be shown that with a modulation depth of 100 kHz the effective RMS displacement of the calibration peak can be found as

$$\sqrt{\langle x^2 \rangle} = \frac{\lambda/2}{\text{FSR}} \frac{100\text{kHz}}{\sqrt{2}} \approx 6 \text{ pm} \tag{5.5.5}$$

This is then to be compared with the brownian motion peak in the transmission measurement. If the power in the vibrational peak is half that of the calibration peak, the vibrational motion is then half of these 6 pm.

In **fig. 5.19** the calibrated power spectrum showing the calibration peak and the brownian motion peak for the (2,1) mode for different cooling powers are shown. For this measurement the modulation depth was chosen to be 100 kHz around the RF signal that is driving the input AOM. The peak height that this modulation puts on the input light corresponds to a length difference of 1.91 pm. The frequency modulation is swept with a rate that is chosen to be near the brownian peak in frequency. In this case it was chosen as 23.5 kHz to be near the brownian peak as is seen in **fig. 5.19**. The 3 different traces show for increasing input light power that is stabilized to 10, 20, and 30 μW respectively. It is seen how the power in the calibration peak is a measure for the input power, and how the vibrational peak broadens and moves to lower frequency for increasing light power. This fits with the explanation that the increasing light power increases the photoinduced force, and cools the vibration. In order to prove that cooling happens it is necessary to show that the power in the peak decreases, and not only that the peak broadens due to damping **sec. 2.2.2**. By performing a numerical integration the power can be determined and if the experiment is repeated statistics can be obtained. This was the method used to produce the calibrated transmission measurements in **fig. 5.17c**. Clearly strong cooling has been proved using the ringdown measurement technique as well as the calibrated transmission measurement technique.

The GaAs spring constant of the (2,1) mode at 23 kHz was found to be 10.7 N/m by $K = m\omega_m^2$. The motional mass (1/4 of the total membrane mass) was 520 ng. By the same method the spring constant of the 17 kHz (1,1) mode was determined to be 11.3 N/m. From the equipartition theorem, the displacement due to Brownian motion at room temperature is given as (T=300 K)

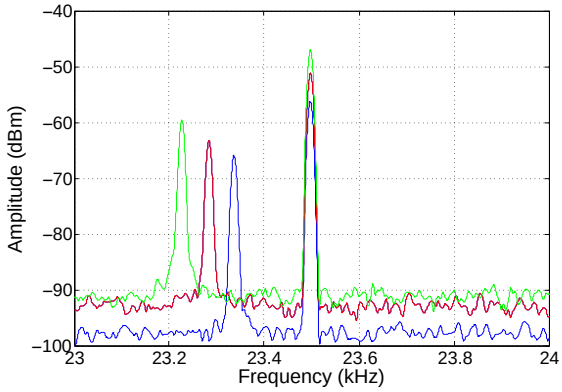

Figure 5.19.: Example calibration scheme measurement of cooling. Blue correspond to 10 μW, red to 20 μW, and green 30 μW.

$$\frac{1}{2}k\langle x^2\rangle = \frac{1}{2}k_B T \tag{5.5.6a}$$

$$\sqrt{\langle x^2\rangle} \approx 19.1 \text{ pm} \tag{5.5.6b}$$

and this can then be compared with the measured displacement. In **fig. 5.17a** it is shown how the calibrated displacement is found to be around 10 pm/$\sqrt{\text{Hz}}$ for the (2,1) mode. As the (2,1) mode has a node in the center, the maximum displacement is expected to be about half that of the (1,1) mode at maximum, and **eqn.** (5.5.6) is found to fit nicely. It should be noted that the measurement shown in **fig. 5.19** does not show exceptional cavity cooling, but shows a cooling of about a factor of 10 from the room temperature to the effective temperature of $T^{\text{eff}} \approx 30$ K. For the (4,3) mechanical mode around 59 kHz a cooling of 74 times down to a an effective $T^{\text{eff}} \approx 4$ K was measured. This was a record for mechanical Q_m of GaAs mechanical systems at the time of publication of [Liu11]. Usually high-Q_m is only possible in SiN structures but this was an example of a Q_m =2.3 $\times$ 10^6.

5.5.2. Wavelength dependence

In the beginning of the investigation of the GaAs nanomembrane it was not clear which process affected the vibrational modes. It turned out that the cooling efficiency is strongly dependent of the wavelength of the cavity laser, and thus of the photon energy. The measured cooling factors $\gamma_m^{\text{eff}}/\gamma_0$ for a cavity input power of 50 μW is shown in **fig. 5.20a** for cavity wavelength ranging from 810 nm to 884 nm. The data is gathered by the ringdown measurement of the (2,1) vibrational mode for 5 different cavity input powers up to 50 μW and from the behavoiur at 50 μW cavity input power, the effective cooling factor can be inferred. The cooling factor is again defined as the ratio of the room temperature to the effective vibrational temperature as T/T^{eff} with T being 300 K. The corresponding photon energies in eV are included and the band gap energy E_g of GaAs is indicated with a dashed line. Interestingly a strong dependence on the wavelength is obvious. For photon energies much higher than the bandgap energy E_g, the cooling factor is essentially constant at $\approx$12 but varies for energies closer to E_g. It drops dramatically off for energies lower than E_g and is not seen for $E < E_g - k_B T$ with $k_B T$ being the thermal broadening. The shape of this cooling

factor fits the excitonic absorption spectrum to a remarkable degree [Fox10]. In **fig. 5.21** is shown a more detailed investigation of this wavelength dependence.

In **fig. 5.20b** the transmission of the cavity as a function of wavelength is shown. This is essentially a measurement of the absorption (when taken the cavity finesse change with wavelength into account) of the membrane, and by comparing with **fig. 5.20a** it is seen how the cooling factor follows the absorption.

In **fig. 5.20a** it is seen how the cooling factor shows some 'bumpy' behaviour around E_g but for higher photon energies than E_g. In **fig. 5.21** a higher resolution scan is shown for the 850 nm to 885 nm wavelength range. Two distinguishable peaks in the cooling factor are obvious around the band gap energy. This is a fascinating discovery and a clear indication of some more advanced dynamics that would need to be investigated. As noted the behaviour of a peak in the cooling factor follows well with the measurement of such a peak in the optical absorption from GaAs samples [Blakemore82, Elliott57, Goi90]. While this is fascinating a measurement of the transmission does not show these bumps as shown in **fig. 5.20b**, indicating that the bumps in **fig. 5.20a** is not trivially the peaks in absorption that are measurable in GaAs samples. An explanation for the bumps in the cooling factor measurement is then still to be found.

5.5.3. Detuning dependence

In **fig. 5.23** is shown the dependence of the cavity detuning of the calculated power transmission, reflection and absorption probabilities, the cooling factor and the mechanical resonance.

As shown in **fig. 5.22** the 160 nm thick GaAs membrane presents itself as an etalon and such the cavity should be modeled as a coupled cavity. It is assumed that the mirror is infinitely thin and lossless and with a dielectric constant that is taken from the literature [Chuang09]. See **sec. A.1**. Introducing L as the distance from the membrane to the mirror, the intra-membrane fields are found to be

$$E_{mem}(L,x) = E_1(L)e^{ik\tilde{n}x} + E_1'(L)e^{ik\tilde{n}(l-x)} \tag{5.5.7}$$

with $\tilde{n}$ denoting the complex dielectric constant of GaAs, $k = 2\pi/\lambda$, and l=160 nm is the thickness of the membrane. If the photo-induced force F_{ph} is proportional to the number of electron-hole pairs in the membrane it should be proportional to the intra-membrane photon number, n_{mem}, as

$$F_{ph} \propto n_{mem} \propto \int_0^l |E_{mem}(L,x)|^2 dx \tag{5.5.8}$$

Interestingly the intra-membrane photon number n_{mem} shows a shifted asymmetric resonance in respect to the cavity detuning. This is shown as the red solid line in **fig. 5.23b**.

The cooling factor $\gamma_m^{\text{eff}}/\gamma_m$ is

$$\gamma_m^{\text{eff}}/\gamma_m = 1 + Q_0 \frac{\omega_m \tau}{1+\omega_m^2} \frac{\nabla F_{ph}}{m\omega_m^2} \tag{5.5.9}$$

and the second part is

$$\gamma_m^{\text{eff}}/\gamma_m - 1 \propto \nabla F_{ph} \propto \nabla n_{mem} = \frac{d}{dL} n_{mem} \propto \frac{d}{dL} \int_0^l |E_{mem}(L,x)|^2 dx \tag{5.5.10}$$

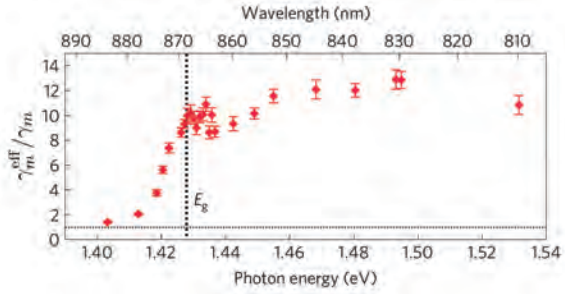

(a) Wavelength dependence of the cooling factor $\gamma_m^{\rm eff}/\gamma_m$. Each point correspond to an average cooling factor from five identical ringdown measurements, with the error bars indicating one standard deviation. The dotted horizontal line indicate a cooling factor of identity. Modified from [Usami11].

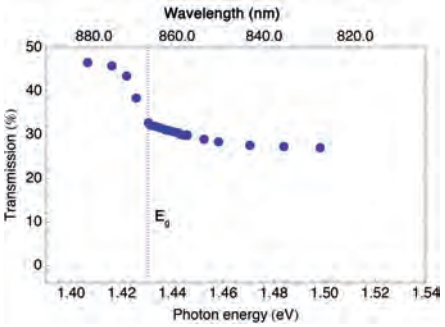

(b) Cavity transmission.

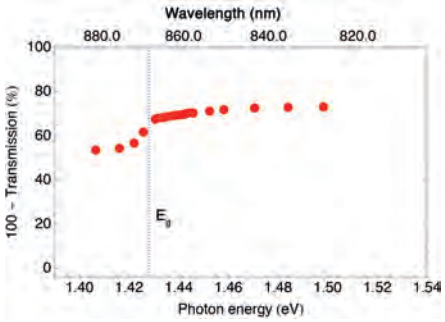

(c) 1-Transmission.

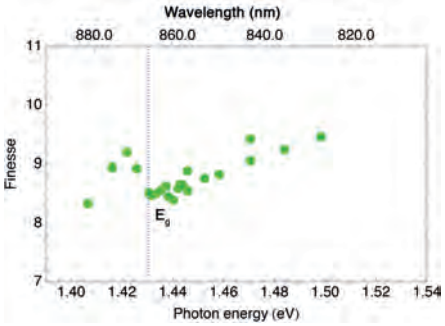

(d) Cavity finesse.

Figure 5.20.: Wavelength dependence. The measurements that are tightly spaced in wavelength are chosen to investigate the 'bumpy' behaviour found in **fig. 5.20a**. The bandgap energy, E_g, of GaAs is indicated.

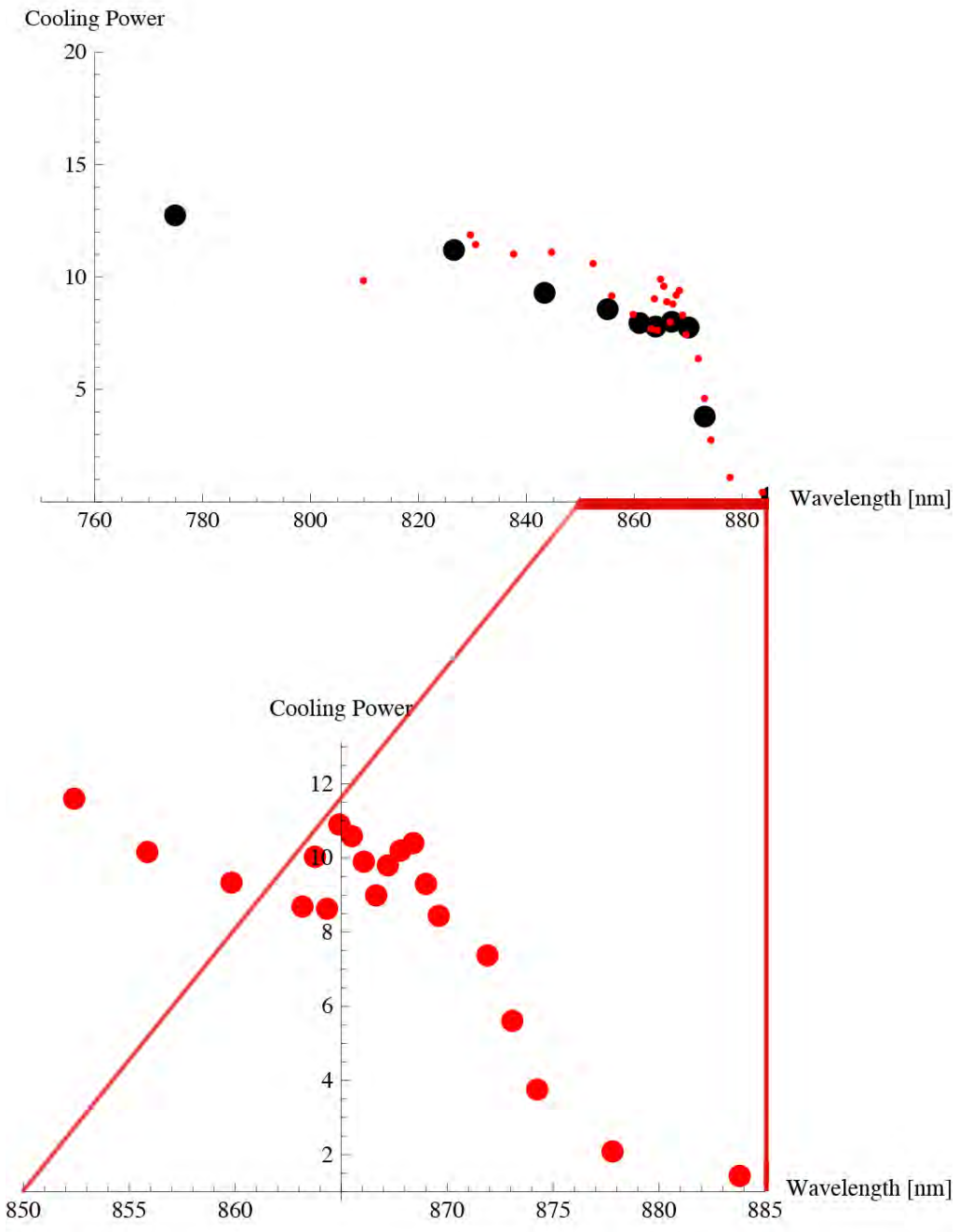

Figure 5.21.: Cooling power (factor) for different cavity input wavelengths. The black points correspond to one sweep of measurements, while the red points show a later and more thorough measurement series. The *zoom in* shows the same measurements for a smaller wavelength range for visual clarity.

This observed assymetry in the cavity detuning dependence in the cooling factor can be explained by this formula, and in **fig. 5.23b** $\gamma_m^{\text{eff}}/\gamma_0 - 1 = \alpha \nabla n_{mem}$, with α being a fitting parameter, is shown as the dashed line to fit the experimental results well. Thus the dependence on ∇n_{mem} of the cooling effect is established.

In **fig. 5.23c** the mechanical resonance ω_m^{eff} dependence on the cavity detuning is shown. Here it is immediately obvious that the experimental data for the frequency change do not follow ∇n_{mem} but rather the actual intra-membrane photon number n_{mem}. This is different than the the dynamic optomechanical back-action model [Metzger04, Metzger08b]. In the Karrai model described in **sec. 2.2** the shift in ω_m^{eff} is due to the dynamic part of the photoinduced force. However there is a static part of the photoinduced force that also leads to a static displacement (which can normally be disregarded as it does not enter the dynamics, but in this case results in the mechanical instability) and a change in the static spring constant. This is due to the change of tensile stress of the membrane due to a local temperature rise at the membrane due to the photon absorption [Larsen11]. This local heat absorption δT is proportional to the intra-membrane photon number n_{mem} and thus the frequency change is found to be dependent on n_{mem}.

This is again deemed to be an indication of the uniqueness of the 'big' GaAs membrane, as a small local heating lead to a large displacement, in contrast to the typical high tensile stress SiN membranes. This is attributed to the intrinsic bending of the membrane that is due to internal stress, that makes a small local expansion turn into a large displacement.

The change in bulk temperature of the membrane is not very high as the two different methods for measuring the mechanical decay rate shown in **fig. 5.17c** indicate, but apparently still strong enough that this correspondance is visibile in the cavity detuning experiment.

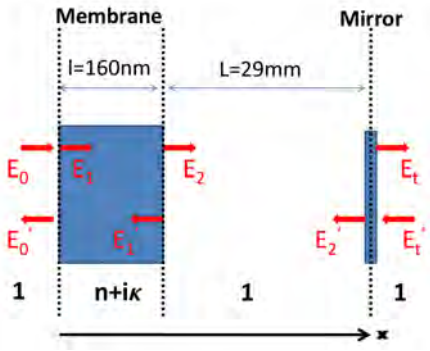

Figure 5.22.: Schematic of the coupled cavity of the membrane/mirror. Relevant field amplitudes and dielectric constants are shown.

5.5.4. Cooling mechanism identification

The wavelength dependence and cavity detuning experiments were done to identify the cooling mechanism involved. From the wavelength dependence in **fig. 5.20a** it is clear that radiation pressure cannot be the dominant effect, as this would not follow the absorption of the GaAs membrane. Another reason is that the low finesse cavity created between the membrane and mirror, leads to a very low photon number and this makes the radiation pressure effect negligible. From the wavelength dependence it is clear that the cooling effect follows the absorption and suggests an electron-hole generation effect. The generation of free carriers by the incoming photons leads

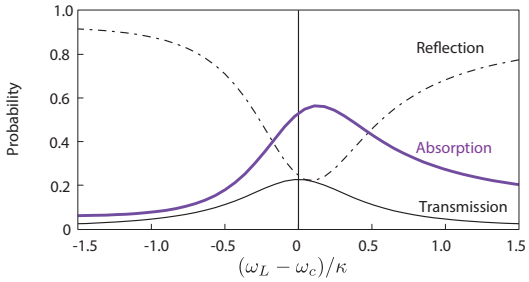

(a) Calculated power transmission, reflection and absorption probabilities.

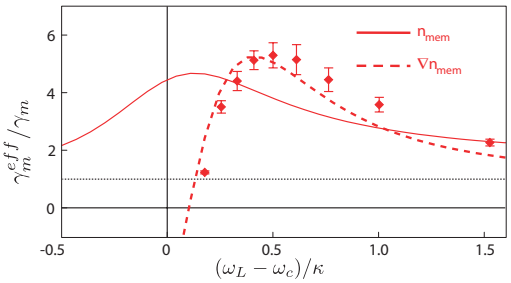

(b) Cooling factor measured using the ringdown method. The intra membrane photon number and spatial derivative of this is indicated.

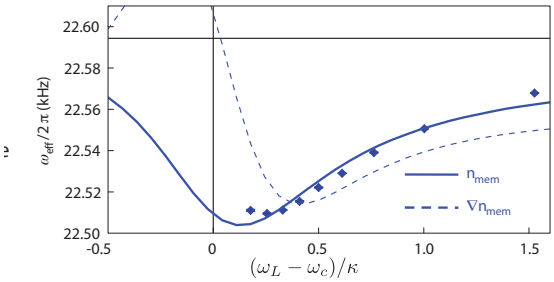

(c) Dependence of the mechanical resonance on cavity detuning. It should be noted that the measurement point at the 9/10 point closest to the resonance is slightly off the n_{mem} and that this is attribuated to the instability onset already setting in here, as it was problematic to keep the system at this detuning.

Figure 5.23.: Cavity detuning dependences for the (2,1) mechanical mode using 870 nm cavity light. Reproduced from [Usami11].

to both a electronic pressure via deformation potential cooling [Thomsen86, Matsuda05], simply imagined as the free carriers taking up more space in the material lattice, and thermal pressure due to the local heating — the so-called photothermal cooling.

The membrane was intrinsically bent due to high stress in the membrane in the etching process. Some topology measurements are shown in **A.4** but what is important to understand the effect is mainly that the membrane is intrinsically bent on the order of 10 μm which is about 0.1 % of the lateral dimension, and much more than the thickness of the membrane, l=160 nm. It was bend in the direction of the end mirror, and the oscillations that were studied are then of much lesser amplitude than this bend. Incoming photons are thought to excite electron-hole pairs in the lattice and because of the electronic and thermal stresses introduced, the lattice expands. As the local spot expands the whole membrane deforms due to the local deformation and it does this in the direction of the mirror, because of the intrinsic bend, which then leads to a change in cavity length. The cavity length is then getting smaller with higher intra-membrane photon number and as such the number of photons in the cavity changes, leading to the optomechanical coupling. The direction of the intrinsic bend is then absolutely related to whether a strong cooling effect is possible as the opposite configuration would lead to a local expansion making the cavity length longer. This explains the difference between the radiation pressure dependence of the cavity detuning, and for this setup.

The power of the electronic stress and thermal stress can be compared. The electronic stress is due to the excitation of an electron-hole pair, and the stress induced is given by $\sigma_{el} = -B(dE_g/dp)$ with B denoting the bulk modulus of GaAs, and dE_g/dp is the change in band gap energy due to the pressure p. The expression $-B(dE_g/dp)$ is then the hydrostatic deformation which is the strain introduced by the hydrostatic pressure p. For this sample $\sigma_{el} = -B(dE_g/dp) \approx 8$ eV per unit volume is estimated. The excited electron-hole pairs are shortlived as the excited carriers recombine when scattering on impurities or surfaces and releasing the energy into the lattice. See **7.1.2** about excitons in semiconductors. The stress due to the local heating is given by $\sigma_{th} = -3B\beta(\eta E_{ph}/C)$ where β, C denote the thermal expansion coefficient and the heat capacity, respectively. The η parameter represents the conversion efficiency from the absorbed photon energy, E_{ph}, to the local heating. In the case of $\eta = 1$ all absorbed energy is converted into heat through non-radiative decay, while for $(E_{ph} - E_g)/E_{ph}$ all the absorbed energy is reemitted (radiative perfect decay) and thus exits the lattice. The thermal stress is estimated to be $\sigma_{th} \approx 0.8\eta E_{ph}$ eV per unit volume for this sample. From the change in mechanical frequency shown in **fig. 5.23c** a conversion efficiency due to thermal expansion of $\eta \approx 0.9$ was determined for this sample.

The main mechanism is the thermal stress introduced by the absorption of photons and the subsequent non-radiative relaxation of the electron-hole pairs. In **fig. 5.24a** is shown the time resolved measurement of the transmission through the membrane-mirror cavity when an external pump light is turned on and off. A laser with the wavelength of 853 nm and thus above the bandgap energy of the GaAs is called the pump and is mounted so that the laser beam is hitting the membrane at an off-angle and thus not entering the transmission path. It is checked that no light is leaking into the measurement path. The pump is run with relatively high optical power of 3 mW. For the cavity light a laser with 884 nm, and thus below bandgap energy, is used running with 150 μW. The cavity length is locked so that the cavity light is on the slope of the cavity transmission peak, and thus the cavity light provides a probe of the membrane displacement. In **fig. 5.24a** the change in amplitude that follows when the above band laser is turned on or off is shown. The mechanical response is found to be 10 ms. The amplitude of the change is only a fraction of the

total transmitted power, as the membrane only moves slightly on the slope of the cavity transmission. A lot of experiments were done. See **sec. 5.5.5**, to investigate whether several time scales were involved and measurable in this experiment, but here it is just noted that the 10 ms that is clearly visible, fit very well with the thermal timescale. The thermal diffusivity of GaAs, $D \approx 0.25$ cm^2/s [Yao87], and the heat diffusion time is estimated to be $\tau_{th} = l^2/(2D) = 20$ ms with the size $l^2 \approx 1$ mm^2. This fits very well with a thermal process being the dominant force involved in the cooling.

To confirm this another experiment was performed where a modulation of the input light was introduced. In figs. 5.24b, 5.24c is shown the response when driving the cavity light as follows. Introducing an amplitude modulation on the cavity light introduces a sinusoidal component in the photoinduced force as [Metzger08a]

$$F_{ph}(t) = 1 + \epsilon \cos(\omega_{\mathrm{mod}} t) F_{ph} \tag{5.5.11}$$

where $\epsilon = \epsilon(\omega_{mod})$ is the modulation strength for the modulation frequency $2\pi\nu_{mod} = \omega_{mod}$. For low frequency modulations, i.e. $\omega_{mod} \ll \omega_m^{\mathrm{eff}}$, the imaginary part of the lock-in response of the membrane displacement x_ω is

$$\Im(\omega) \approx -\frac{F_{ph}\epsilon}{m\omega_m^{\mathrm{eff}}} \frac{1}{\omega_m^{\mathrm{eff}}\tau} \frac{\omega}{\omega^2 + (1/\tau)^2} \tag{5.5.12}$$

The minimum for $\Im(x_\omega)$ shows a minimum for $\tau = 1/\omega$ if there is a slow component. In **fig. 5.24b** is shown this for low frequency modulations and the τ is measured to be $\tau \approx 6.6$ ms. This fits well with the 10 ms found using the pump-probe experiment.

The full expression for the imaginary part of the lock in response is not shown here, and shows a more complex behaviour than **eqn.** (5.5.12). The full expression is shown in [Metzger08a, Usami11] and have a zero in the denominator at $\omega_{\mathrm{mod}} = \omega_m^{\mathrm{eff}}$. In **fig. 5.24c** the response when the modulation frequency is driven is shown in a range close to the mechanical resonance, $\omega_{\mathrm{mod}} \approx \omega_m^{\mathrm{eff}}$. A dispersion like behavior is found around the (2,1) mechanical mode. This measurements again fit with the expected behaviour derived from the full expression, and the magnitude and time response fit with the established.

Conclusion about the dominant effect

These findings confirms the thesis that the strong cooling effect is dominantly due to the thermal stress due to the excitation and subsequent relaxation of the electron-hole pairs into thermal expansion. The alternative method with electronic pressure via deformation potential coupling is negligible for the cooling process in this setup.

A time resolved measurement of the photoluminescence from a similar GaAs sample also found that the non-radiative decay into heat was the dominating effect. The radiative decay was determined to be very fast, $\tau_{el} < 50$ ps. This is what is expected for a bulk GaAs sample as the excited carriers, can recombine on surfaces of the membrane or impurities very quickly. This behaviour fits well with the interpretation that thermal stress dominates the cooling effect.

5.5.5. Search for a fast time constant

It was stipulated that maybe another effect was coupling to the behaviour and should show up as a 'fast timescale' in the cooling behaviour. This could be interesting in the search for the mechanism

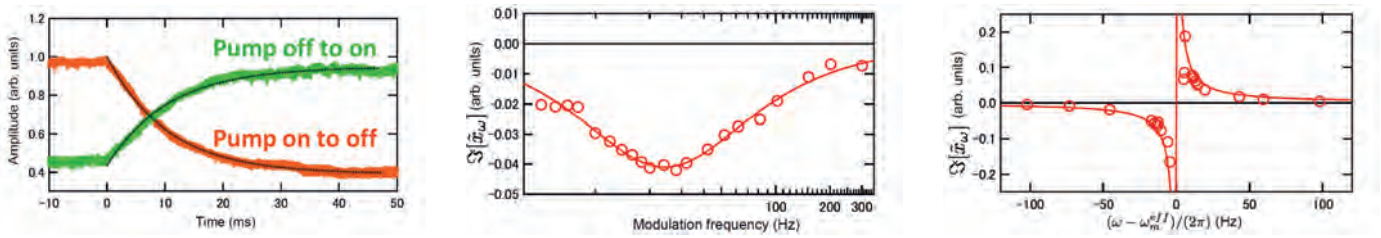

(a) Result of a pump-probe measurement. The response of the mem- brane displacement upon the illumination (green points) and blocking (orange points) of the pump light.

(b) Imaginary parts of the lock-in response of the membrane displacement x on the modulated cavity driving at low-frequencies. Note that this is denoted $\Im(\omega)$ in the text.

(c) The response on the driving around the mechanical resonance (the (2,1)-mode.

Figure 5.24.: Cooling mechanism identification. Reproduced from [Usami11].

behind the cooling, and potentially determine if some part of the behaviour should be attributed to electronic pressure via deformation potential cooling.

A lot of different experiments were performed in the search for the 'fast timescale'. It was established above that the slow timescale due to heating, τ_{th}, dominates the cooling of the vibrational modes. This was due to the quick non-radiative recombination of excited electron-hole pairs that is known to be quick due to recombination on surfaces of the membrane and impurities in the GaAs.

As described in **sec. 2.2** the vibrational cooling is due to the 'viscosity' of the photoinduced force, in that there is a time delay, τ, between a change of configuration and a change in the force. The delay then lead to work being done, and dependent on the detuning of the cavity, this can lead to energy being removed from the vibration. **eqn.** (2.2.22) describes the cooled decay rate, if a single τ describe the cooling effect

$$\gamma_m^{\text{eff}} = \gamma_m \left(1 + Q_0 \frac{\omega_0 \tau}{1 + \omega_0^2 \tau^2} \frac{\nabla F_{ph}}{m\omega_m^2}\right) \tag{5.5.13}$$

That is if the effective τ leads to the first fraction being close to unity the damping is the strongest. It is seen that this is the largest for $\tau = 1/\omega_0$. For resonances about $\omega_0/2\pi \approx 20$ kHz this yields an optimal $\tau \approx 8$ μs. From this it is clear why the thermal diffusion time leads to a strong cooling effect in this system.

An alternative hypothetical cooling process with a time scale of 100 ns, would lead to the fraction becoming about 0.01 for the same resonance frequency, and then this effect should be very small for these low frequency mechanical modes, but might be measurable for the higher frequency modes. However this is only the scaling for the $\omega_0\tau/(1 + \omega_m^2\tau^2)$ and there is also the strength of the photoinduced force to take into account.

As will be shown below, the local stress that electron pressure induce can be estimated to be about $\sigma_{el} \approx 8$ eV per electron-hole pair that is excited, per unit volume. This can compared with the thermal pressure which is roughly $\sigma_{th} \approx 0.7E_{Ph}$ eV, per unit volume per photon with energy E_{Ph}. As the above band light that is used to excite the carriers have wavelength shorter than about 865 nm, which correspond to 1.43 eV, the thermal pressure is estimate around $\sigma_{th} \approx 1.2eV$ per photon, per unit volume. Thus $\sigma_{el} > \sigma_{th}$ but the time scales are very different, with $\tau_{el} \ll \tau_{th}$. Another complexity is that the cavity lifetime enters as a delay of a hypothetical fast decay process. If the time is a combination of the cavity lifetime and the electron pressure delay time

the cavity will dominate as the processes cascade, and the cavity lifetime will be the limiting, as $\tau = \tau_{cav} + \tau_{el} \approx \tau_{cav}$. The cavity lifetime was established to be about $\tau_{cav} \approx 20$ ns, and this limits the effective τ.

Photoluminescence

The radiative recombination time is very fast in bulk GaAs, and experiments was performed by Søren Stobbe at DTU Fotonik to investigate this. Using a pulsed excitation scheme the timing of the photoluminescence was measured from the recombination of carriers, in a GaAs membrane similar to the one investigated here. The time of the radiative recombination was found to be faster than the response of the APD detectors. This put a bound on the radiative recombination time of less than 40 ns and it is expected that this is a sign that most of the excitations decay non-radiatively through coupling to the phonon bath and thus heat up the system. It is also known that the recombination processes in bulk GaAs is on the order of 100 ps [Harrison10] and this fits well with the measured.

Ripples due to heating

It might however be that other time constants are entering into the dynamics of the vibrational modes of the GaAs membrane. The speed of sound in bulk GaAs is on the order of 3-5 km/s at room temperature ([Blakemore61]) and introducing a kick to the membrane would introduce waves like ripples in a pond, although the magnitude of these waves is not clear. If the magnitude of this effect is big enough, it could potentially enter into the dynamics of the vibrations. This is the motivation for searching for ripples after an excitation of the membrane. An illustration of an example of these ripples is shown in **fig. 5.25** for a circular membrane.

Assuming a speed of sound of 4 km/s, a wave propagating in the membrane will take around 450 ns to travel largest dimension of 1.8 mm. Of course this will be dependent on the position of the kick and the probe position and thus 3 different positions were chosen.

The local heating due to the kick of an above-band laser pulse on the membrane can be estimated. Pulses of 50 ns length 827 nm light were used and monitored using a fast photodetector. A light power corresponding to 2 mW when running in CW mode was chosen. Approximating the pulse shape as a rectangle and using the pulse length of 50 ns yields an energy of about 10 mJ pr. pulse. This means that with 827 nm light with 1.499 eV of energy there is 10^9 photons per pulse. Assuming an absorption and conversion into heat of about 0.9 this gives an idea of the punch that is afflicted on the membrane by the pulse. Of course it is actually only the transient we are interested in, and the 50 ns pulses are chosen due to technical issues and a shorter would be preferable. However

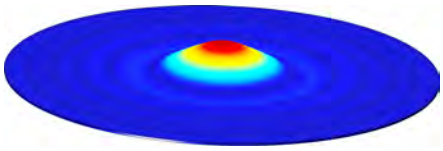

Figure 5.25.: Generic displacement model showing both the exaggerated displacement at the center due to the pulse and the reflection. The first reflection of the wave returns at the center about 0.5 μs after the initial *kick*.

again the time scales enters but this time it is different as a local heating of the size of the membrane is not the same timescale as the timescale τ_{th}. τ_{th} is estimated using the thermal diffusivity of GaAs, $D \approx 0.25$ cm$^2/s$ and using the lateral size of the membrane, $l^2 \approx 1mm^2$ the heat diffusion time is estimated to be $\tau_{th} = l^2/2D = 20$ ms. However the local heating on the size of the beam would be expected to be the non-radiative recombination time as no diffusion of hot carriers is included locally. Thus it is interesting to determine the local expansion at the pulse beam spot and whether this is detectable, and the time constant and magnitude of the ripples introduced in the membrane.

The local expansion due to heating can be estimated using the methods described in **sec. A.5**. By the formula for volumetric thermal stress

$$\sigma_{th} = -\beta \left(3B \frac{\eta_{abs} E_{ph}}{C} \right) \approx 0.8 \eta_{abs} E_{ph} \tag{5.5.14}$$

where for isotropic thermal expansion the volumetric expansion coefficient is equal to the linear coefficient $3\times\alpha_l$. By assuming small deformations due to the thermal stress and using the bulk modulus of 75.5 GPa[Adachi85]. The bulk modulus B is the defined as

$$B = -V \frac{\Delta P}{\Delta V} \tag{5.5.15}$$

where P is the pressure, V is the volume and $\Delta P/\Delta V$ is the change of pressure for a change of volume. From figs. **5.5.14, 5.5.15** the volume change is then

$$\frac{\Delta V}{V_0} = \frac{0.8 \eta_{abs} E_{ph}}{B} \tag{5.5.16}$$

where E_{ph} is the photon energy absorbed and η_{abs} specify the conversion efficiency from absorbed E_{ph} to heat energy, B is the bulk modulus. Likewise, for the deformation potential coupling it can be shown that the volumetric electronic stress per single electron-hole pair is

$$\sigma_{el} = -B \frac{\Delta E_g}{\Delta p} \approx 8\text{eV} \tag{5.5.17}$$

and that the volume change per absorbed photon follows **eqn.** (A.5.29)

$$\frac{\Delta V}{V} = \frac{(\sigma_{el}/V_{ill})}{B} \tag{5.5.18}$$

with V_{ill} being the volume that the force affects. σ_{el} is the deformation potential stress (in unit energy). In order to estimate the expansion, the parameters specified above is used and if the beam size is assumed on the order of 100 μm in diameter, this enables the volume change due to local heating to be

$$\frac{\Delta V}{V_0} \approx 4 \times 10^{-16} \tag{5.5.19}$$

The fractional volume expansion per photon will be

Thermal	Deformation potential
4×10^{-16}	3×10^{-15}

and for a photon number of 10^9 photons per pulse, the fractional expansion per pulse is then

Thermal	Deformation potential
4×10^{-7}	3×10^{-6}

Which for the ideal (100 μm diameter cylinder with height of 160 nm) cylinder will lead to at most an increase in height of $\Delta V/Vh = 0.5$ pm, with h being the thickness of the membrane. This is a very small change, but might be detectable using the cavity transmission measurement technique. This was the hope for the experiments in this section. If possible to detect, this could give hints as to other timescales governing, which might couple to the vibrations, and be part of the explanation for the strong vibrational cooling.

Comsol modeling

The setup was modeled in Comsol. This was done to try and estimate the timescales involved, and to gauge how realistic a measurement of the displacements are. As the FEM is done with the parameters from the experiment the governing time scale is the speed of sound in the material. Dependent on the lattice orientation the speed of sound is from about 2.5 km/s to 5.5 km/s [Blakemore61], and for a 1 mm diameter membrane a 'kick' at the center at time t_0 will result in a wave travelling with about 3.5 km/s to be reflected at the boundary and travel back in 1 mm/(3.5 km/s) ≈ 0.3 μs. This estimate is good for motivating the search for a μs timescale in this system, but more complex FEM models were implemented.

The position and timing of the pulses at and the expected travelling wave were modeled at three different positions. These correspond to the experimentally chosen setups as described in **sec. 5.5.6**. By comparing the different positions it was hoped to show proof of the displacement and the ripples, indicating a source for a fast timescale.

5.5.6. Time resolved experiment

Motivated by the above it was tried to implement a way to measure this quick timescale, with the ultimate goal of trying to correlate it with the timescale that enters into the cooling of these GaAs membranes.

The 'kick' was implemented using a pump laser that hit the membrane at an off angle with an above bandgap laser with 827 nm wavelength. In this way the force is both the radiation pressure kick as well as exciting carriers causing local heating and local expansion. The kick was established with 50 ns pulses with a repetition rate of 1 μs, and the optical power was about 10 mW when measured running in CW mode. As was estimated above, this should give a local expansion of about 0.5 pm. The cavity transmission was monitored using 50 μW 870 nm light, and measured using a fast photodetector. In this way it was hoped to time the triggering of the pulse with cable length and be able to detect the motion of the membrane in different spots as the pulse excited it.

After having solved problems with scattered 827 nm light going into the transmission detector, problems were obvious with ringing. The electrical pulse going into the control of the laser was resulting in ringing in the signal measured by the fast photodetector. Different cable lengths were tested but the ringing was still problematic. After some investigations it was concluded that the

ringing was in the LeCroy WP7100 Oscilloscope itself, and this made it harder to handle. As the ringing was exactly on the timescale after the pulse where a acoustic signal was expected to occur, this was a problem. As the ringing was electronic in nature and expected to be a leakthrough from one channel to the next in the oscilloscope, it should be present no matter whether the pump pulse hits the membrane or not. Thus a mechanical shutter was installed in the pump beam path, and driven at speeds up to 3 krpm. This enables a quick differential measurement where the electronics are unchanged but the light only hits the sample in some portion of the measured triggering events. A differential measurement scheme was developed. Here the transmission noise was measured with and without the pulse being blocked. As the mechanical chopper was running at about 3 krpm the two types of events where only seperated by milliseconds, which should render the setup robust against power fluctuations and so on. Unfortunately no systematic signal was found to fit with the arrival times estimated using the different models.

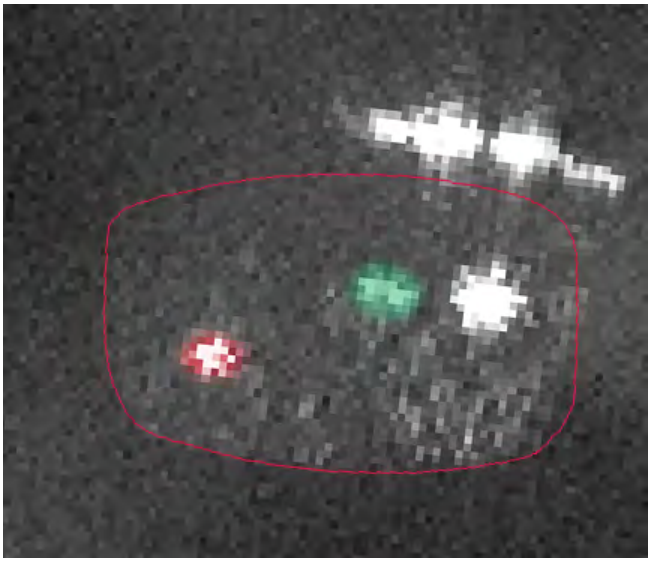

Figure 5.26.: Composite image of the membrane with probe and pump beams. The cavity probe beam is at the white beam spot at the rightmost position, while the three bright spots show the three pump positions tried.

Heterodyne detection

As a final test of the hypothesis of the rippling being measurable, a heterodyne detection scheme was implemented in order to overcome various electronic noise sources in the MHz range that were plaguing the experiment.

Heterodyne detection work by mixing the light carrying the signal to be detected with a strong *local oscillator*. The *LO* is traditionally a strong laser field with an angular frequency ω_{LO}. The signal is in the electric field $E_S(t) = E_S \cos(\omega_S + \phi_S)t$ and the *LO* in $E_{LO}(t) = E_{LO} \cos(\omega_{LO} + \phi_{LO})t$ [Milonni88]. Here ω_S is the angular frequency of the signal carrying field, and ϕ_S and ϕ_{LO} are the phase terms. The electric current of the photodetector that measures the resulting light is denoted

I_D, and it will be proportional to the intensity at the detector as

$$I_D \propto [E_S \cos(\omega_s t + \phi_S) + E_{LO} \cos(\omega_{LO} t + \phi_{LO})]^2 \tag{5.5.20}$$

$$\propto \frac{1}{2}E_S^2 + \frac{1}{2}E_{LO}^2 + E_S E_{LO} \cos\left((\omega_S - \omega_{LO})t + (\phi_S - \phi_{LO})\right) \tag{5.5.21}$$

where going from **eqn.** (5.5.20) to **eqn.** (5.5.21) fast terms with $2\omega_S$, $2\omega_{LO}$ and $\omega_S + \omega_{LO}$ are dropped as these are assumed to be averaged out. This means that the fast oscillation about zero is averaged to a zero intensity. The two first terms in **eqn.** (5.5.21) have no frequency dependence and the interesting term is clearly the third interference term. The detected current will oscillate (beat) at the difference frequency $\omega_S - \omega_{LO}$. What is more interesting is how this term is proportional to $E_S E_{LO}$ as this enables directly an enhancement of the ω_S that is to be detected. As the local oscillator is increased in power $|E_{LO}|^2$ the measured signal at $\omega_S - \omega_{LO}$ will increase in the same order, and thus having a much stronger LO enables detection of weak signals.

By a combination of the differential scheme from above and a heterodyne mixing it was hoped that the weak signature of the rippling could be measured. By using a very strong local oscillator, the signal should be amplified significantly. It was implemented by mixing the cavity transmission light with the input light from the Ti:S laser. As the the cavity input was power stabilized using the first deflected beam of an AOM being driven with a 815 MHz drive, the transmitted and undeflected light from the AOM was an obvious choice. The Ti:S light was mixed with the 815 MHz shifted cavity transmission light, and as the intensity of the cavity transmission was in the μW range, a strong LO was needed. A couple of hundred μW LO was used and the mixed light was coupled to a fiber and fed to the fast photodetector. Technically a Thorlabs 9.5 GHz Amplified fibercoupled photodetector PDA8GS was used and after being bandpassed around 800 MHz with a passive filter, the signal was amplified using a ZX60-2534MS 500-2500 MHz amplifier. As both the lasers and the electronics show much better and less noisy behaviour at 800 MHz than around 1 MHz this is a much more sensitive setup than the simple transmission measurement.

Results

In **fig. 5.26** a composite image of the three different chosen pump positions on the GaAs membrane is shown as well as the probe beam for the cavity transmission beam. In **fig. 5.27** representable traces for data from the 3 positions are shown. The setup was optimized to result in the pulse hitting the membrane at the time $t = 0$ in **fig. 5.27** and thus a peak was expected around 400-600 ns after this. The black scatter is the intensity of light averaged over many triggering events, and the red is then a smoothing of this. It was found impossible to prove any systematic signal of a travelling wave using this setup.

This means that the effect is smaller than what was detectable using this setup, and as time scales about 10 ms was found due to heating in **sec. 5.5.4** this is concluded to be the dominating time scale for the vibrational behaviour of the membrane.

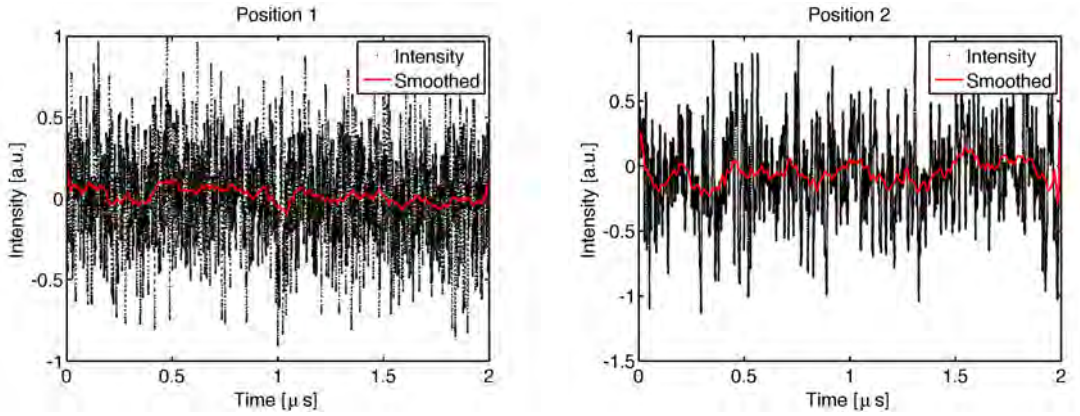

(a) Position 1

(b) Position 2

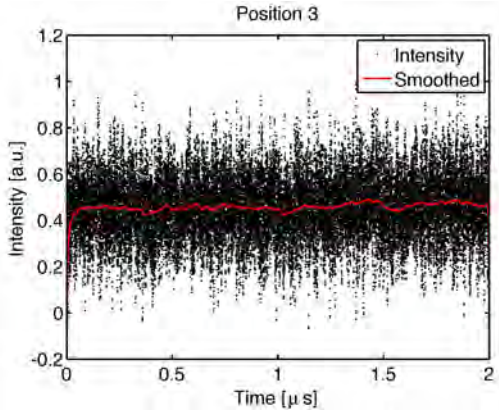

(c) Position 3

Figure 5.27.: Measured fast response signal intensity at 3 different positions.

5.6. The photothermal cooling in the GaAs membrane

In conclusion it has been established that the strong vibrational cooling that was shown in this membrane was primarily due to a strong photothermal coupling in the membrane. The cooling power was found to be completely dependent on the wavelength of the cooling light being high enough energy per photon, to excite carriers in the material and heat it. Very strong cooling down to effective vibrational temperature of 4 K was found for the (4,3) mode, but the effect was limited due to mechanical instability setting in for about 50 μW of cooling power. It was found that the very strong effect, as well as this onset of instability for relatively low power, was due to a strong intrinsic bend in the membrane. This led to the local heating always making the membrane bending in the same direction, and this changes the effective spring constant by making another deformation.

The intrinsic bending was shown to be a general feature as a consequence of the fabrication proceedure, and probably include a lot of stress at the boundaries and as a consequency the membranes are dramatically bend. This is very different than the case for the SiN Norcada membranes, where the tensile stress dominates the behaviour completely.

5.6.1. Shell / Membrane description

At this point it is interesting to point out the difference between these GaAs membranes compared to the typical SiN membranes from Norcada. As the GaAs membrane is intrinsically bent, any absorbed light leads to a expansion and displacement in the same direction no matter the position in the cavity. This is in contrast to the standard SiN membrane where the high tensile stress is dominating the behaviour. This is the difference described in **sec. 3.1** where the difference between systems, where the plate equation is a good approximation such as this GaAs membrane, in contrast to systems where the membrane equation is a good description, as is the case for the drumskin SiN membrane.

5.6.2. Conclusion about mechanical coupling

As was obvious from **fig. 5.27** no clear signature of a fast time scale was detectable in a micro second time range. From this experiment and the experiment described in **sec. 5.5.4**, it is clear that the fast time scale that would be due to the quicker coupling through deformation potential coupling, that was proposed to explain the cooling phenomena, is not detectable. It is then an explanation of a dominating cooling mechanism, in this system and the photothermal cooling is concluded to dominate the behaviour.

6. Next steps for vibrational cooling

An obvious next step is also to cool the GaAs structure to a cryogenic temperature. Several advantages are thought to follow with lower bulk temperature, the most obvious being that the thermal noise will be lower, and thermal damping processes [Okamoto08, Lifshitz00] will be dampened resulting in higher mechanical Q_m's. A special case for studying the interplay between thermally induced cooling witnessed in this system and electronic pressure cooling, is that GaAs shows a strong temperature dependence of the thermal expansion coefficient. The thermal expansion coefficient is shown measured in **fig. 6.1** [Okamoto08, Sparks67] and a clear zero is witnessed at around 12 K and 50 K. This is not a special property of GaAs but it could be used fortuitously for studying the photo thermally induced cooling, as the vibrational cooling efficiency would vary dramatically in the temperature range around 12 K or 50 K. Also a change to these temperature ranges would eliminate the instability due to the thermal deformation, thus enabling a broader range of parameters where the system could be studied.

Because the photothermal deformation put a limit to how much light power can be used to cool the vibrational modes, there is a limit to how much cooling can be achieved in this system. That is not to say that cooling with photothermal cooling in general is insufficient to reach the ground state of vibrations, as [Restrepo11] argues, but it will be limiting for this configuration of membranes. Thus the supposed electronic stress becomes interesting to utilize. The total electronic stress $\sigma_{el} n_{mem} \tau_{el}$ is smaller than the total thermal stress $\sigma_{th} n_{mem} \tau_{th}$, with n_{mem} signifying the photon number absorbed per unit time. This is beecause the lifetime, τ_{el}, of the electronic pressure is related to the recombination of the excited electron-hole pairs, which is a very fast process in this system, while the thermal lifetime τ_{th} is much longer. This is why the thermal stress overwhelms the electronic stress. In this situation $\tau_{el}/\tau_{th} \leq 5 \times 10^{-9}$ so it is clear that the electronic pressure effect is neglible.

It is also possible to engineer the different time scales entering to make the electronic stress dominate. By setting up the membrane in a cavity generated by two mirrors, in the membrane-in-the-middle approach [Thompson08, Wilson09], a higher finesse cavity is possible. If the wavelength of the laser is optimized so that the loss in the cavity due to absorption in the membrane is minimized, but keeping a finite absorption for electron-hole pair generation. If this combination of cavity wavelength and laser could be achieved the time scale of the cooling processes could be dominated by

$$\tau = \tau_{cav} + \tau_{el} \approx \tau_{cav} \tag{6.0.1}$$

where $\tau_{cav} = 1/\kappa$ is the lifetime of the cavity. This would mean the process were dominated by the slower cavity lifetime than the electronic pressure timescale τ_{el} and this would again make the electronic pressure effect noticeable while including high enough photon numbers to make radiation pressure cooling also enter the dynamics.

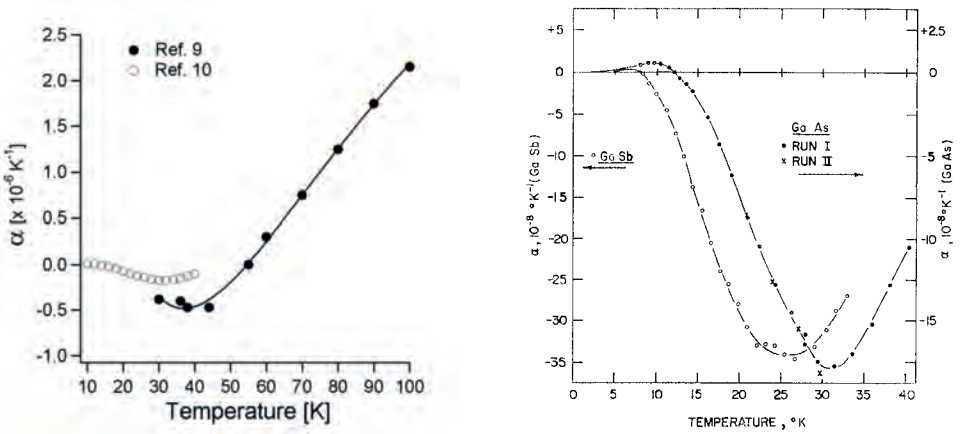

(a) Reproduced from [Okamoto08]. (b) Reproduced from [Sparks67].

Figure 6.1.: Thermal Expansion coefficient for GaAs. The zero crossings are visible and are at 12 K and around 50 K.

6.1. Status quo

The big GaAs membranes have been retired as they were found to show a strong degrading in the mechanical properties. This is due to the aging due to the change in environments with different air pressures, temperature and being subjected to light in many different experiments. The strong photo induced electron-hole thermal relaxation process leads to a strong derformation of the systems, and with high strain deformations are introduced in the lattice of the membranes. This results in loss of mechanical Q due to many damping effects. Also a deposition of oxide on the surfaces of the membranes should also degrade the samples. Thus the focus is on the next generation GaAs systems, such as the nanomembranes with a single Quantum Well, and the indirect exciton systems. Such a system is described in the following in **6.2**.

6.2. Deformation potential cooling

As described in **sec. 5.5.4** the identification of the cooling processes led to the revalation that photothermally induced cooling dominates the cooling process for the big GaAs membrane. However it is envisioned that the electronic pressure induced cooling process could lead to a lot of advantages when going to lower temperatures. This effect is due to the local expansion due to the disassociation of electrons and holes from the lattice, and is also called deformation potential cooling, as this is the formal name for the bandshift due to deformation of lattice cells. The photothermal effect is limited in effectiveness as the bulk temperature goes lower, as the thermal time constant τ_{th} is entering the expression for the effective Q_m as shown in **eqn.** (2.2.22). The instability that sets in due to the thermal deformations at strong light power sets a natural limit to how much cooling is achievable in the current setup.

In the appendix **sec. A.5.1** is described how the local absorption leads to a local expansion due to electron pressure. This can then couple back to the motion of the membrane if the structure is optimized, and a cavity is created to establish the resonance effect.

There are several optimization possibilities to show electron pressure cooling. An obvious method would be to place the membrane system in between two mirrors in the membrane-in-the-middle approach [Thompson08, Wilson09] and thus create a cavity with high finesse. The wavelength of the laser should be chosen to be the right compromise between enough absorption, that efficient cooling of a mechanical mode due to electronic pressure can be realized but not too much so that no cavity mode is sustained. If this is realized the effective delay time can be dominated by the cavity lifetime τ_{cav} instead of the short carrier lifetime τ_{el} because of the cascade nature of the decay processes as $\tau = \tau_{cav} + \tau_{el} \approx \tau_{cav}$.

Coherent deformation potential coupling

The electron pressure effect can be modeled by considering the simplification that there is only a single available exciton mode to couple to, and not a continuum. In this case a Hamiltonian for the interaction between a mechanical eigenmode with operators b, $b^\dagger$ and a exciton mode with operators d, $d^\dagger$ becomes

$$H = \hbar g_0 d^\dagger d \left(b + b^\dagger \right) \tag{6.2.1}$$

Following [Wilson-Rae] the coupling due to deformation potential coupling in a free oscilator can be written

$$|g_0| \approx \frac{(1-2\gamma)|D_c - D_v||z|}{(\rho E)^{1/4}\sqrt{\hbar w} t L^{3/2}} \tag{6.2.2}$$

This expression contains a lot of parameters but the main point is that the excitonic optomechanical coupling scales with the deformation potential difference $|D_c - D_v|$ where D_c is the deformation potential for the conduction band and D_v is for the valence band. Values for GaAs are $D_c = 9.36$ eV and $D_v = -1.21$ eV so that $|D_c - D_v| = 9$ eV. Here γ, ρ and E denote the density, Poisson ratio and Young's modulus and w, t and L denote the width, thickness and length of the resonator. z is the longitudinal coordinate and it is assumed that the optical beam is hitting an antinode of the oscillator and that the beam is of a size where it only samples the antinode. In this case the z value denotes the difference from the midline of the oscillator and this is due to the intensity of the light assumed to be highest here. In a more realistic implementation the coupling of a cavity field to the internal field amplitude should be included in the model.

Conclusion

In the following **chap. 7** the experimental work towards getting this (possibly) coherent cooling mechanism working experimentally is presented. With a lot of theoretical work describing the possibilities for the deformation potential coupling in regards to vibrational cooling, [Wilson-Rae, Xuereb12], it seems that what is needed is some experimental results. This will probably lead to some surprise or other, and this will influence the design of the next generation of experiment to investigate the possibilities that have been presented above.

7. Engineering devices towards deformation potential cooling

In this chapter the next step towards realizing deformation potential cooling is described. This is done by designing advanced heterostructures that will show a different time dependence than the system investigated in previous chapters. Additionally a degree of freedom is created by tuning the heterostructure through external electrical means, and it is the hope to get these devices to perform in a regime where the deformation potential effect dominates over e.g. photothermal cooling effect.

First the states of electrons and holes that are excited by the light field are described, and how these can be confined by designing thin structures called Quantum Wells. A system utilizing these confinement principles were manufactured courtesy of Ataç İmamoğlu at the Quantum Photonics group at ETH Zürich, and these *nanomembranes* were studied in collaboration with members of this group. This was done first in Switzerland and then brought to *Quantop* for investigation. The characterization is described and the future possibilities for these systems are discussed. It was not possible to show the deformation potential cooling with these samples, and the next generation is underway.

Secondly a description of how the knowledge gathered from these *nanomembranes* were used to design the next generation of heterostructure membranes follows. It is theorized that creating a so-called indirect confined state would lead to even longer delay times, as well as allowing for greater tunability. The systems were modeled in Comsol and designed in collaboration with the Lodahl group which has done initial testing of the systems.

The current status of these systems is described and how the outlook for showing the deformation potential cooling looks very bright indeed.

7.1. Many body phenomena

By the discussion of the various processes that is happening in the GaAs semiconductor membrane discussed in **chap. 5**, it was shown how other effects than photothermal and radiation pressure forces could also enter into the dynamics of the mechanical systems. The dynamics due to electron pressure is thus interesting and a natural extension of the work presented there.

In this process a single photon excites an electron from the lattice of the membrane, and the local expansion due to this excited carrier can in turn couple to the mechanical dynamics of the membrane. This has various advantages over the traditional optomechanical effects of radiation pressure and photothermal forces. Mainly the effect can be implemented in semiconductor structures that show a so-called direct bandgap such as 3-5 materials where a photon can excite a carrier. These are used in photoelectric devices already such as photodiodes and LEDs. Thus it seems obvious that a stronger control of the dynamics of excitation in this kind of system is interesting from an engineering standpoint. Another important point is that the coupling to the mechanical motion can in principle be done in a coherent fashion if a resonant excitation in the semiconductor is possible. Work has been done to model this[7], and the possibilities from a fundamental standpoint with a coherent cooling process are interesting. Quantum information purposes seem obvious if such a coherent coupling between light and mechanical motion is possible.

Another strong point for utilizing this effect is that the semiconductors offer a much more tunable framework, i.e. the properties of the excitations could in turn be tuned by applying electrical bias and this would potentially lead to new technological and scientific possibilities.

7.1.1. Quantum Wells

It is well known how the dynamics of the electron states in semiconductures can be described by a band structure theory. Two distinct bands are discussed where the lower energy band is mostly full of electrons and can conduct by the movement of vacancies. This band is denoted the valence band as it is formed due to the valence electronic states of the atoms in the lattice. The vacancies, that is the empty states where no electron is present, are similarly denoted *holes*. The valence band is then the band describing the available states of these holes. The upper band is mostly empty of electrons and is a description of the available states into which electrons can be excited. These states are a combination of delocalized excited states of the electrons in the lattice, and because of the high movability of these, they are easily accelerated and make up a current flow. This band is thus denoted the *conduction* band. What is important for a semiconductor is the apperance of a *bandgap* between the two bands, i.e. a regime of energy where no states are available in contrast to a metal where no such gap is found. Of course this model is a simplification and in reality at least a distinction between so-called *heavy*- and *light*-hole valence bands are often necessary, where 'weight' refers to the effective mass of the hole state.

The confinement of an electron state in a potential will change the available states, and an example of this can be found in heterostructures where e.g. a layer of one material is built in the bulk of another material. As the materials are chosen to have different dielectric constants, a range of electron states can be confined. In **fig. 7.1** the resulting potential $V(z)$ for such a structure is

[7] Unpublished work by Ignacio Wilson-Rae has been done to model the coherent deformation potential vibrational cooling. The model reduces the exciton reservoir to a single exciton level and includes the various decay processes and couplings necessary for understanding the deformation potential coupling to vibrations. There has been a lot of work on the various details of this model, but further experimental work is necessary.

shown. An example of such a structure is a quantum well (QW) where the thickness of the structure is chosen to be small 'enough', say 10 nm, to yield a considerable confinement and show quantum properties [Butov01b, Butov01a].

An excitation by optical means excite carriers from the valence band to the conduction band while leaving a hole in the valence band. Any excitation of carriers in the system will try minimize the energy and does this by relaxation by coupling to the vibrational modes of the crystal lattice, the phonons. Thus after losing some energy to heat and phonons in the lattice, electrons and holes will collect in the quantum well. Because of this confinement of the carriers it is clear how a recombination of the electron and hole will happen quickly once the excitation has 'fallen' down in energy into the QW. The example of a single QW of one material in a big wafer of GaAs is a so-called type *type*

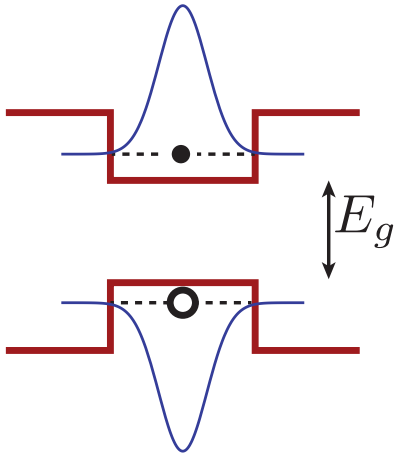

Figure 7.1.: Confined state in a semiconductor QW structure. E_g indicates the bandgap energy of the semiconductor.

1 QW. The QW could be made of InGaAs. The bandgap of the InGaAs is then nestled within the wider bandgap GaAs, and both the electrons and the holes congreate to the QW [Harrison10]. An alternative approach is to implement a *type 2* system where the bandgap of the materials are aligned so that the quantum wells formed in the conduction and valence bands reside in different materials, such that e.g. the electrons are in one material while the holes are in a different material. This spatial confinement in different layers mean that the coupling is lower than in the type 1 QW and consequently the recombination times are longer. It is possible to engineer this kind of structure with a lot of different combinations of materials and dimensions.

7.1.2. Excitons in semiconductors

If an electron is excited from the bound state in the lattice by e.g. an optical excitation, with enough energy to move around in the lattice, a free electron is created and an empty state of a hole is left in the valence band. The hole has the dynamics of an air bubble in a glass and behaves positively charged. As such it rises to the top of the valence band and it is energetically favourable for an electron and hole to form a bond. A bound electron-hole pair is described as a quasiparticle denoted an exciton. If the light photon has energy just below the band gap of the material a resonant excitation can form an exciton directly. As the exciton is made of a an electron and a hole it is clear that it is bound to recombine after some time (pun intended), but the lifetime is

still relatively long compared to free carrier recombination time, and up to a nanosecond lifetime is normal. This is of course at cryogenic temperatures where exciton states are quickly thermally dissociated.

In bulk an exciton has the same energy as the band gap plus an exciton binding energy that is e.g. -4.7 meV for bulk GaAs [Harrison10], and this small value also hints why these excitons are not long lived. In a heterostructure such as a a QW there is also the confinement energy of the electron and hole separately, as well as the binding energy.

A QW is thus a useful structure for relatively long time confinement of excited carriers in semiconductors, and this is important for the consideration of the mechanical structures considered in this work. An important point is also that the excitation of a QW excitation can be made to be close to resonant by a slight detuning of the pump laser from the band gap energy of the state in the QW, and thus a coherent excitation is possible. This opens up the avenue of coherent coupling between the dynamics of the internal many-body properties in semiconductor structures and mechanical motion of a macroscopic device with the QW embedded.

Decay dynamics

In reality the decay dynamics of excitations in semiconductors is much more complicated than what is hinted above, and several effects enter the process. An obvious distinction is the difference between the recombination of electrons and holes in either a radiative or non-radiative recombination. That is a recombination results in the emission of a photon or a coupling to the phonon modes of the lattice and converted into heat.

If the electron density n is equivalent to the hole density, which is accurate for high excitation powers, [Shen07] describes how it is possible to describe the total recombination rate of electron-hole pairs as

$$\frac{dn}{dt} = -An - Bn^2 - C^3n^3 + G \tag{7.1.1}$$

where A is the so-called Shockley-Read-Hall nonradiative recombination where the exciton relaxes by coupling to an impurity, B is the radiative recombination and C is the Auger nonradiative recombination which couples to a third carrier. G denotes the generation and is proporptional to the absorption laser field, and inversely to the thickness of the excited QW layer.

The easiest to measure of these effects is the radiative recombination rate as this can be measured using a pulsed excitation laser and a time resolved measurement scheme of the radiated luminescence. This is often done using avelanche photodiodes (APDs) where a histogram of the radiative decay rate can be established. It is possible to fit the total recombination rate equation **eqn.** (7.1.1) by the quantum efficiency

$$\eta = \frac{Bn^2}{G} \tag{7.1.2}$$

which is the proportion of light that recombines radiatively compared to the absorbed light.

The coefficients are determined with an iterative procedure. The radiative decay coefficient is found by fitting a decay curve to find the carrier density n. This requires that the quantum efficiency η and absorbed laser excitation q is known. In [Shen07] this is achieved by probing a sample without QW structures and comparing with the PL from a sample with a QW. When n, η and G is

determined the radiative coefficient follows from $B = \eta G/n^2$ which makes it possible to fit A and C.

The nonradiative recombination is a very quick process if the carriers can relax through other processes than the recombination of an electron and a hole. This can e.g. be done if the electron hits and impurity in the lattice, or it can hit a surface with so-called dangling bonds. This is the case for surfaces of e.g. GaAs if it is not coated with another material that passivates the surface by binding to these free bonds on the surface. Likewise a poor constructured QW with a varying material composition could also work like local defects and change the recombination time.

The dynamics of excitons in QWs is a complicated topic, and it is well beyond the interest in coupling with optomechanics for this work. For an example of these dynamics the reader is referred to e.g. [Sivalertporn12].

Strained Quantum Wells

The choice of materials in use for fabricating QWs are varied and a lot of different properties can be chosen and designed to optimize the chosen behaviour. Obvious parameters are the thickness of the QW and the material composition, where different content of e.g. indium and aluminum change the properties of GaAs. The different materials have slightly different size of the unit cell in the lattice because of the different atoms. Of course the different lattices have to match up in the boundary between one material and the other, and this limits which materials can 'work' together. If there is too much of a mismatch between the lattice sizes, the sites tend to 'jump' a space when deposited and this results in dislocations and defects in the crystal.

In most cases one of the materials will be either compressed or expanded compared to the equilibrium bulk case for the material, and this means that the lattice of the QW will be strained. The strain is a result of the stress introduced because of the lattice mismatch and the strain is then defined through Hooke's law. Certain engineering methods exist for compensating for this strain by e.g. compensating for the change in lattice constant gradually over a larger distance.

The reason strain is important is that it changes the band structure available in the structure because the lattice has a different size. Thus a strained QW has a different band structure. Since the strain is small for the possible QW configurations, first order perturbation theory can predict the change in energy. The Hamiltonian can be expressed as the unstrained Hamiltonian, H_0, and the contribution due to strain, H_ϵ. Thus the Hamiltonian is $H = H_0 + H_\epsilon$. According to [Harrison10] the dependence of strain is

$$H_\epsilon = \sum_{i,j} \frac{\partial V}{\partial \epsilon_{i,j}} \epsilon_{i,j} \tag{7.1.3}$$

where V is potential without strain. The critical point is now that the so-called deformation potential can be used to describe the energy shift due to strain. Defining D_{ij} as a tensor describing the deformation potential as $D_{ij} = \frac{\partial V}{\partial \epsilon_{ij}}$ in the different symmetry directions of the crystal. From this the energy shift of a band, at a specific point in k space, is then identified as

$$\delta E = \sum_{i,j} D_{i,j} \epsilon_{i,j} \tag{7.1.4}$$

It is thus clear that the deformation potential is a description for the band shift due to strain. While an *ab-initio* calculation of these deformation potentials are possible to some extent, it is customary to measure these deformation potentials [Gorczyca92, Mair98]. There is quite a large dependence on the specific system in regards to the values listed in the literature, and as such the values should not be taken to be too precise for this setup.

7.2. ETH System

The design and fabrication of the nanomembranes[8] was done by Javier Sánchez. The design is shown in **fig. 7.2** where the various structures are indicated. The parameters a, b and d are varied accross a lot of samples in one production. These parameters are also indicated. In **fig. 7.4** is shown a microscope picture of the entire sample of nanomembranes. The whole structure is split into two fields (left and right) which are idential. Then the parameters are varied for the different samples to account for fabrication problems, and perhaps to deduce some dependence of the geometry of the physical properties. Due to the low survival rate of the nanomembranes it is also necessary to have a lot of samples with varying properties.

A 11 nm (up to 30-35 atoms thick), InGaAs QW is grown as the center of the GaAS nanomembranes. Specifically the composition of the QW is $In_{0.12}Ga_0.88As$. The membrane is grown to be 110 nm.

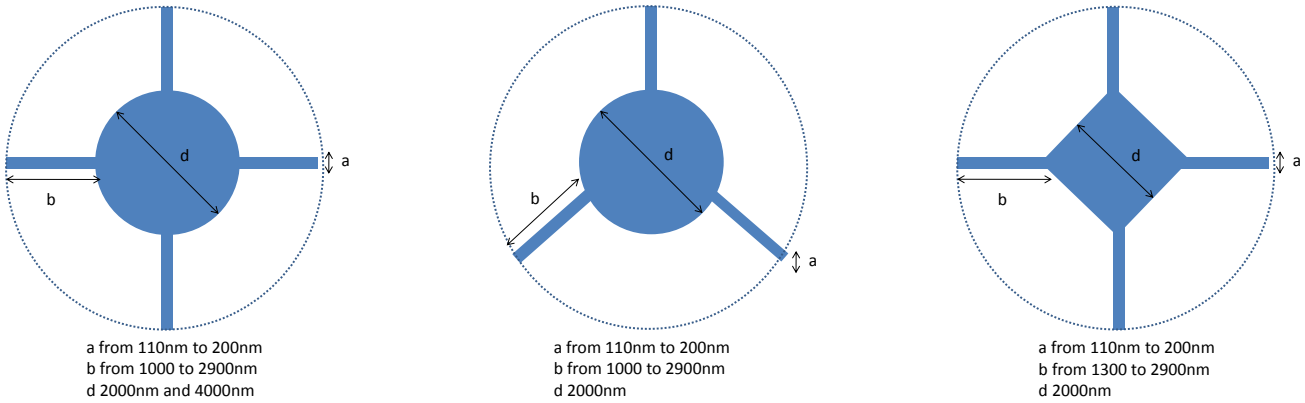

Figure 7.2.: Designed membrane structures width the various dimensions indicated. The structures were etched with a thickness of 110 or 120 nm.

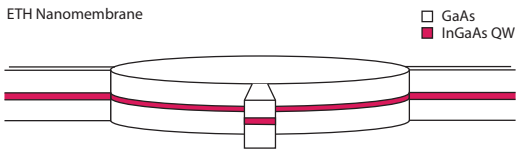

Figure 7.3.: Schematic of the nanomembranes with the QW visible. The width of the QW is exaggerated for clarity. The QW is about 11 nm thick while the entire structure is 110 nm or 120 nm depending on the sample.

7.2.1. Fabrication details

The structure is made by molecular beam epitaxy where a substrate of GaAs is grown as the basis. A QW structure is made by growing a thick 1 nm layer of InGaAs before growing the

[8] So named after the thickness and the length of the tethers, as it is clear that calling a 2 μm structure a nano is a slight stretch.

rest of the GaAs structure. A selective etching is then performed by masking out the nanomembranes and etching below the membranes. This underetching procedure leads to different distances to the substrate below the free standing membrane and to different sizes of the socalled underetched area. This area is part of the vibrational structure of the nanomembranes and is also varied.

Fabricated examples of the 3 different designs are shown in **fig. 7.5** and **fig. 7.6**. A lot of the samples do not look as pretty and well defined as these, with many being bent and stuck to the bottom beneath the membrane leaving them useless for experiments. The GaAs structure also oxidizes if subjected to air, so a minimum of exposure to the atmosphere has been an objective. The structure has been kept in vacuum for almost all its time at NBI, and was stored in a nitrogen flowbox in Zürich.

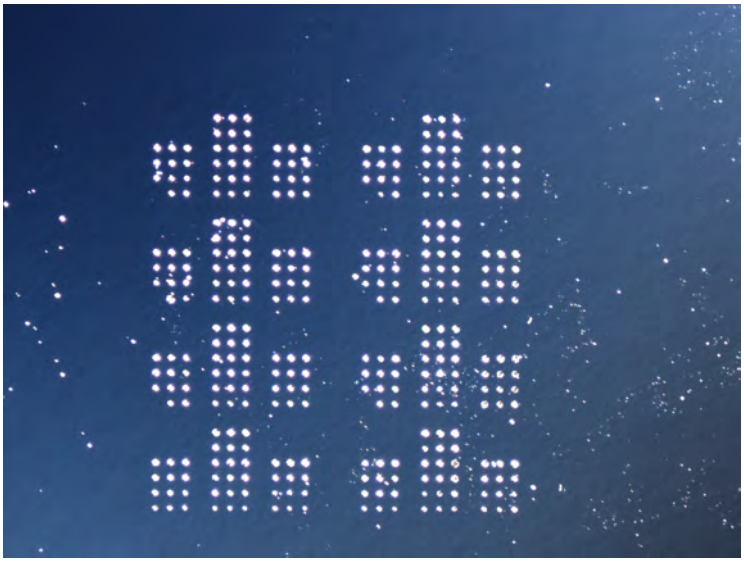

Figure 7.4.: Microscope picture of the entire sample showing the duplicate fields of nanomembranes.

7.2.2. Design parameters

The goal with the design was to minimize the thermal coupling to the reservoir and still get a good Q_m. Thus the choice of really small nanomembranes where the ratio of volume to surface are low, and the choice of narrow tethers to couple to the reservoir. This is a very different approach than what has been done with the big GaAs membrane described in part 2, where the high mechanical Q_m was due to the high induced stress, but for these nanomembranes the stress is relieved due to a relaxation that is allowed by the tethers. The inbuilt QW structure induces a stress due to lattice mismatch between GaAs and InGaAs as the structure is grown. When the nanomembranes are etched out this stress is released to some extent as the nanomembrane can move in the tethers. As such quite a few of the nanomembranes do not really follow the horizontal plane of the structure. It is also very obvious from the inherent bending of the underetched region where some samples bend downwards toward the substrate and some bend upwards.

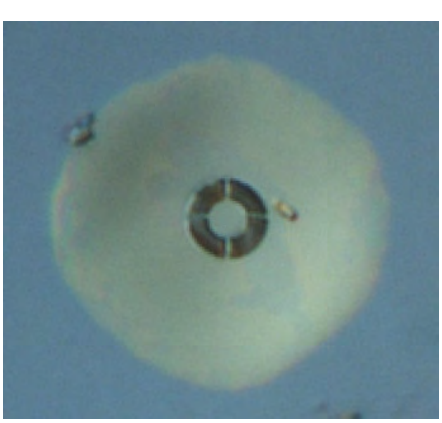

(a) Example of good circular nanomembrane with 4 tethers.

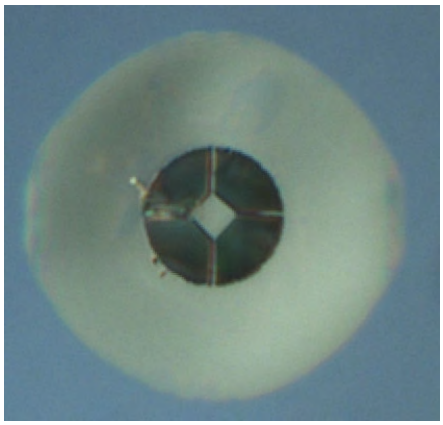

(b) Example of good square nanomembrane with 4 tethers.

Figure 7.5.: Examples of nanomembrane structure measured using a differential interference contrast microscope.

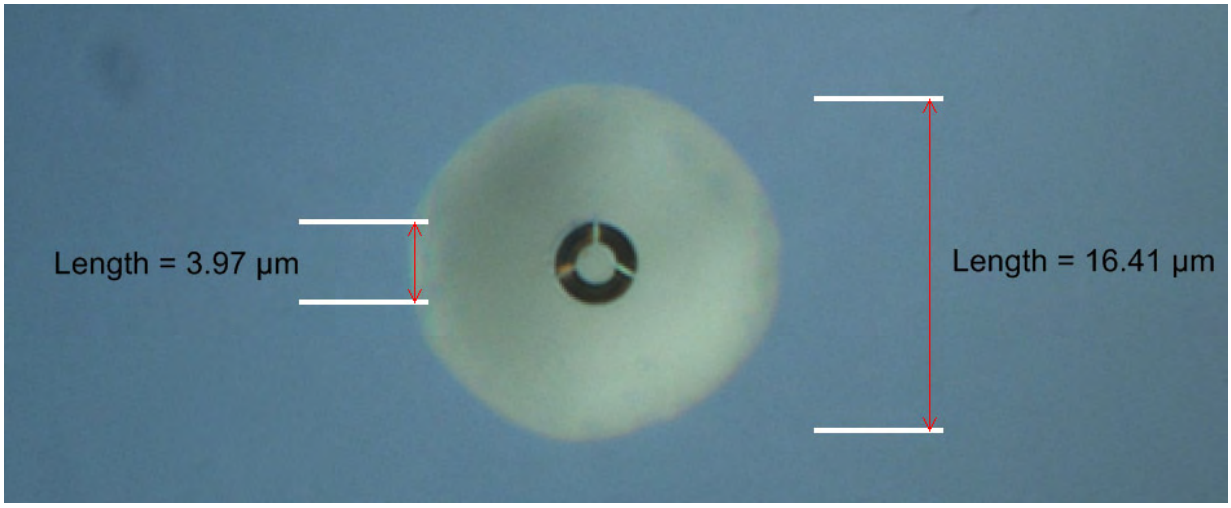

Figure 7.6.: Example of triangle nanomembrane structure measured using a differential interference contrast microscope. Dimensions are indicated.

7.2.3. Numerical Simulation of system

Numerical modeling of the vibrational modes of the nanomembranes have been done, and examples of the vibrational modes are shown in **fig. 7.7**. Shown is a typical sample with a round nanomembrane mounted with 4 comparatively long tethers. The characterizations of the different mechanical modes in experiment is hard due to the very small displacement of these small nanomembranes vibrate. Unfortunately calibrated measurements of the displacement have not been successfull, and the estimate using the method described in **sec. 2.2.3** for the brownian motion is unreliable for tethered structures such as these.

The FEM modeling enables the identification of the different mechanical modes, and it was found that the interesting range for the nanomembranes is roughly in the 4 MHz to 8 MHz regime for the varying sizes of samples. In **sec. B.2.1** a FEM investigation of the lowest energy vibrational modes of one of these typical nanomembranes is shown.

Figure 7.7.: FEM of two vibrations.

Additionally heat conductance simulations were performed with the thermal properties of the GaAs/InGaAs heterostructure included in the model. An instantaneous change in local heating with a gaussian intensity profile modeling the incidence of a heating laser was included and the timescale for heat diffusion accross the tethers and reaching equilibrium was investigated. No new conclusions were drawn from this modeling.

7.3. Experimental setup

Several different experiments were performed at ETH Zürich with the nanomembranes. As well as the vibrational properties of the system, the internal properties could also be investigated. Photoluminescence (PL) experiments were performed to this end. A pulsed laser was exciting carriers in the QW and the resulting luminescence from the recombination of these carriers was measured. This was done in a time resolved manner using a configuration of avalance photodiodes (APDs) or spectrally by feeding the PL to a spectrometer. Additionally it was tried to probe the vibrational motion of the nanomembranes by building a Michelson Interferometer, but the high frequency requirements unfortunately made this impossible in the short time frame of the project.

Pictures of the humble setup in the danish lab[9] is shown in **fig. 7.9**. The lab is at ETH in the Imamoglu group. The cryogenic fascillities at ETH made it possible to routinely cool the sample to 4.3 K, which is necessary in order to have well defined PL from the QW for a long time. The linewidth of the PL is thermally broadened at higher temperatures and impossible to distinguish at e.g. 150 K. The cooling system was a dewar with liquid helium flowing through a Oxford Instru-

[9]Sometimes called G13.

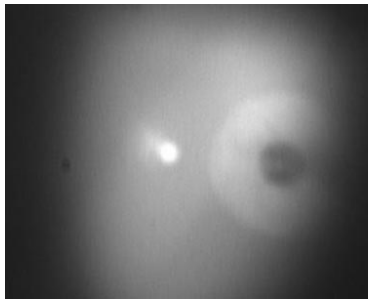

(a) Probe to the left of the membrane.

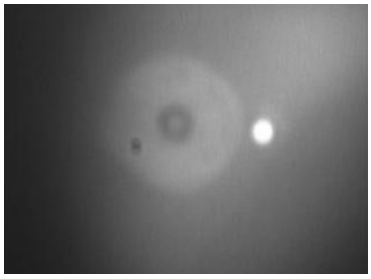

(b) Probe to the right of the membrane.

Figure 7.8.: Picture of the probing setup during the experiment run.

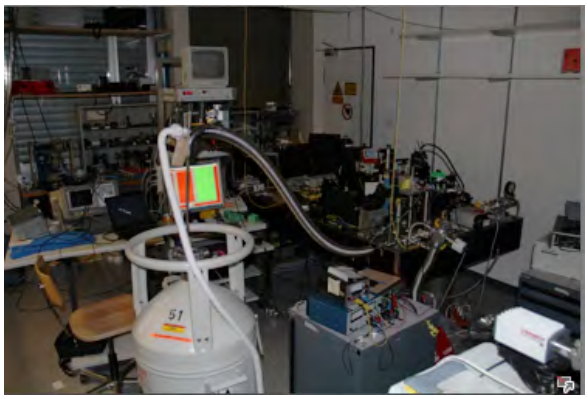

(a) Setup with liquid helium dewar shown

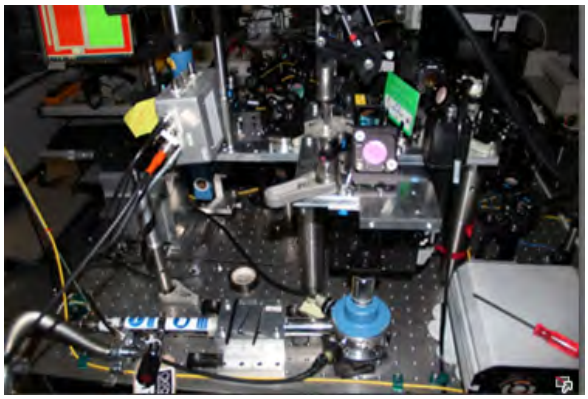

(b) Close up of the interferometer/photoluminescence setup

Figure 7.9.: The cryogenic interferometer and PL setup at ETH Zürich.

ments flow cryostat with temperature control. The GaAs structure was mounted in the cryostat and investigated using a microscope objective mounted on translation stage. A white light source as well as a camera for visualization was placed in the optical path of the laser source. Two pictures of the setup running with the nanomembrane visible and the probe laser hitting the bulk part of the sample for visual clarity are shown in **fig. 7.8**. A number of beam splitters on flip mounts made the setup very dynamic, and the fibercoupling of different labs in the Imamoglu group made the quick combination of various equipment possible. For example the change to probing the sample with a pulsed laser required only that the Ti:S laser in one lab is quickly fiber coupled to the danish lab avoiding having to move any equipment.

7.3.1. Characterization

Spectral characterization

The photoluminescence from the samples are led through a long wavelength filter with a cutoff e.g. at 870 nm depending on the exact conditions for the experiment. The free carriers in the samples are generated using an above band gap laser and most often a 780 nm Ti:S are used for pumping well above the band gap which creates high energy carriers that are then subsequently relaxed though the coupling to phonons in the lattice before existing in the QW. Test were made

with exciting the system with a pump laser with an energy closer to the band gap energy of the QW states (around 840 nm), but there was not a qualitative difference in the spectral features or the time resolved measurement.

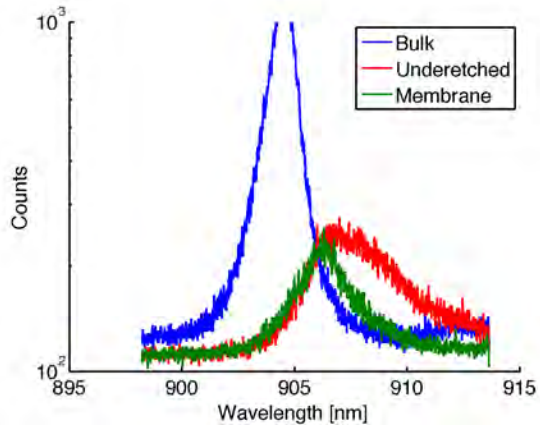

Figure 7.10.: Comparison of PL from membrane, underetched and bulk. More light is emitted from the bulk and the underetched and membrane structures emit at longer wavelength due to the release of stress in the QW for these.

In **fig. 7.10** a non-normalized spectrum of the PL is shown from a nanomembrane, the underetched area and the bulk system. They are all excited using a 780 nm laser with a couple of hundred μW power. However the data is not normalized to counts per second, so it should be noted that the bulk PL is indeed found to be very much brighter than the emission from the underetched and the membrane, but should not be compared directly. The reason that the bulk should emit a lot more PL is that the system is excited with a 780 nm laser, which is above bandgap for GaAs at 4 K, and thus it will excite a lot of carriers in the whole structure and not just in the QW. Specifically for bulk the excitation simply reach a larger volume of GaAs, that what is the case when the the membrane is illuminated, and this results in more carriers relaxing into the state of the QW subsequently.

The spectral features of the PL is also interesting. The PL from the bulk system shows a slightly assymetric lorentzian at about 904.5 nm peak emission. Note that it is the emission wavelength from the QW that is measured, and thus the higher energy emissions from recombinations with higher energy, e.g. in the bulk lattice, are filtered out. The emission from the underetched and membrane are clearly at longer wavelength than the bulk, with the underetched emission being broader in wavelength than for the membrane. The interpretation for this difference between bulk and the others are exactly the noted relaxation of the stress induced by the inclusion of the QW in the lattice. In bulk the stress is inherent [Harrison10] while for the underetched and the membrane some of the stress is released during the etching process while it is reconfigured in some way. The release of stress has then changed the energy of the confined carriers in the QW and this is reflected in the emission wavelengths. It could be interesting to gather more information about this release and about whether a correlation with apparent strain in the samples could be established, but unfortunately too few of the samples survived the fabrication to be able to conclude much, and a separate investigation would be necessary. From these measurements it is not clear why the underetched emission shows a broader feature than the membrane.

In **fig. 7.11** two systematic probings of the PL is shown as the excitation and probing path is swept

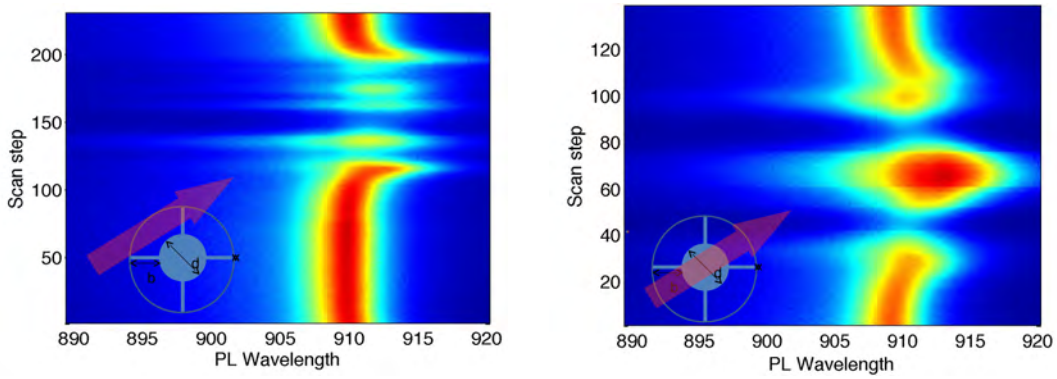

(a) Photoluminescence as the excitation and probing is swept across the underetched area.

(b) Photoluminescence as the excitation and probing is swept across the underetched area and the membrane.

Figure 7.11.: Photoluminescence as the probe and excitation is swept across the sample. The Scan step axis denote the number of steps from the beginning, and the inset figure illustrate the scan direction across the sample.

accross the sample. In practice this was implemented by moving the sample using Attocube position stages accross the optical path. In **fig. 7.11a** the path is chosen so that the luminescence is collected from the bulk, then into the underetched, then nothing as the path is in the gap and then to the underetched again. In **fig. 7.11b** the path is chosen to cross from the underetched, to the gap, to the membrane, to the gap, and then back to the underetched. It is noted that the experiment time were quite a few minutes in these experiments, and thus thermal effects should be considered for the explanation.

From the measurements shown in **fig. 7.11**, is is seen how the PL shifts to longer wavelengths as the pump light move closer to the membrane and tethers. By comparison between **fig. 7.11a** and **fig. 7.11b** it is again seen how the membrane emit at longer wavelength than the underetched and bulk GaAs. This is due the stress that is induced in the fabrication process, leads to higher energy confined states in the QW [Harrison10], but that when the membrane is etched away the tethers allow for the nanomembrane to release some of this stress by reconfiguring. The relatively more stress released nanomembranes then show PL at longer wavelength as the QW in them are under less stress.

Another interesting feature is the very slow broadening of the PL peak from the QW in the nanomembrane itself when the pump beam is fixed on a membrane and left there. This is visible in **fig. 7.11b** where the PL from the nanomembrane is on the order of 5 nm wide spectrally, which is much borader than in **fig. 7.10**. This is thought to be due to thermal broadening. A measurement of the PL from the membrane after the pump is turned on is shown in **fig. 7.12**. It is seen how a strong broadening happens over a long timescale of seconds. Here 30 seconds of measurements are shown. The very slow time scale indicate that a thermal process is happening as the pump beam at 780 nm excites carriers everywhere where it is absorbed and this couples to phonon modes in the lattice. Due to the thin tethers between the membrane and the underetched thermal reservoir, it takes quite some time for the heat to diffuse and for the system to reach equilibrium. It is theorized that as the local heat builds up, the membrane expands, which leads to a broadening of the emission from the QW. A FEM model of the the nanomembrane was found to fit well with the hypothesis

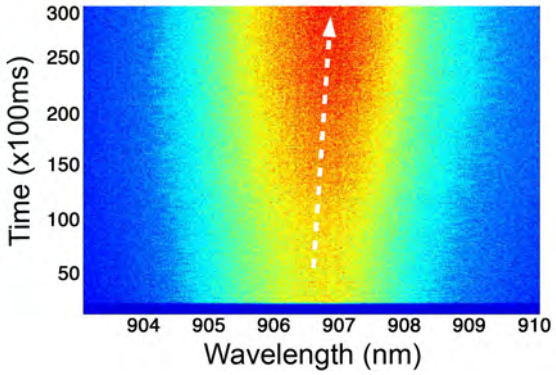

Figure 7.12.: Example of the photoluminescence from the membrane widening over a very long time scale of 30 seconds, indicating a thermal process.

that the thermal conduction through the thin tethers limits the thermal equilibration, but this is not included in this work.

The measurement shown in **fig. 7.12** was done over a timescale of 100 ms per measurement, but another feature is not visible with this setting. By visually investigating the PL over a long timescale, an oscillating behaviour can be witnessed. It was not possible to get a good measurement showing the oscillation, but a time dependent oscillation in the wavelength of the PL from the membrane was present. In one second measurement the emission would be mainly at 909 nm with a width of about a nm, and in the next second it would consist of mainly two peaks spread around this center emission wavelength, with e.g. 906 nm and 911 nm peaks. This could be due to the nanomembrane readjusting to the local heating and emitting at different wavelengths depending on the configuration that released the stress the most. Over longer time scale these oscillations lead to the overall broadening of the PL peak. The tethers are very narrow compared to the volume of the nanomembrane itself, and the heat flow are very slow, which explains the time scale of seconds.

Time resolved

A different kind of measurement was done to investigate the time resolved properties of the nanomembranes. A Coherent Ti:S was run in pulsed mode with a repetition rate of 80 MHz and the pulsed 780 nm light was sent to the samples as above. The spectrally filtered PL was sent to a set of two correlated APDs which was set to trigger on the repetition signal of the Ti:S. By recording the timing of the 'clicks' in the APD signal in a histogram, decay curves such as shown in **fig. 7.14** were obtained. Again the most light were emitted from the bulk of the samples, as more carriers were excited and thus more carriers couples to excitation of the QW. The decay processes are modeled by an exponential decay [Narukawa97, Harrison10]

$$N(t) = ae^{\frac{t}{\tau}} + C \tag{7.3.1}$$

where τ is the inverse of the decay rate, and C is the background. It turned out to not fit very well with the measured behaviour however. The fitting were then performed by a double exponential (biexponential) with a fast and a slow decay rate. Thus the amount of 'clicks' per time $N(t)$ follow as

$$N(t) = ae^{\frac{t}{\tau_a}} + be^{\frac{t}{\tau_b}} + C \tag{7.3.2}$$

with τ_a and τ_b then being the decay times, and τ_a^{-1} and τ_b^{-1} are then the decay rates in units ns^{-1}. This was found to fit the measured decay curves better.

In the experiment the excitation was done with a 780 nm laser running at a 80 MHz repetition rate. Time resolved measurements were performed for a lot of different samples with a lot of different settings. An example is a measurement as shown **fig. 7.13**. Here the pump power was 50 μW on a nanomembrane. It is seen how the decay of the emission from the QW follows a biexponential to a large extend.

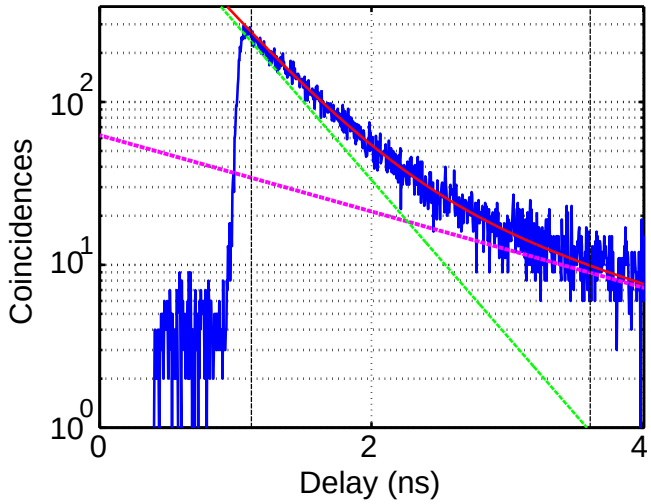

Figure 7.13.: Example biexponential fitting of time resolved measurement for a 50 uW power on a nanomembrane. The time range chosen for fitting is shown with vertical dashed lines. The fit is shown with a red trace, while the purple and green indicate the two exponential timescales, $\tau_a = 1.86$ ns and $\tau_b = 0.45$ ns.

Additional time resolved measurements performed for different power on bulk, underetched, and on a membrane itself is shown in **fig. 7.14**. For pump powers smaller than about 200 μW the decay curves fit nicely with a biexponential, but for high power a dip is obvious at the peak value of the decay histogram. The explanation of the strange dip at the beginning of the decay curve is beyond the scope of this work to investigate in depth, but is attributed to complicated many-body effects when the excitation of carriers in the QW is strong enough.

A collection of the decay rates found by time resolved measurements at different pump powers is shown in **fig. 7.15** and in **fig. 7.14**. The decay rate is determined by the same method as done in **fig. 7.13**, and both the fast and the slow part of the decay is included. Measurements for a membrane is collected along with measurements from the underetched area around it, as well as bulk. There is quite a large spread for the decay rates determined in this fashion, with the bulk measurements being most spread out. It is not clear why this is. For the membrane and the underetched it is more obvious that two timescales have been dominating the decay, and dashed lines are included in **fig. 7.15** as guides for the eye. Some of the outlier values in **fig. 7.15** can be attributed to the biexponential simply not fitting as well as a single expontial fit, and a more thorough investigation would be necessary to understand this.

In general it has then been established that biexponential behaviour is describing the decay of PL from the QW in the bulk, underetched, and membrane structures, but what is the dominating factors into the lifetime is not known. The pumping is thought to create a combination of electron-

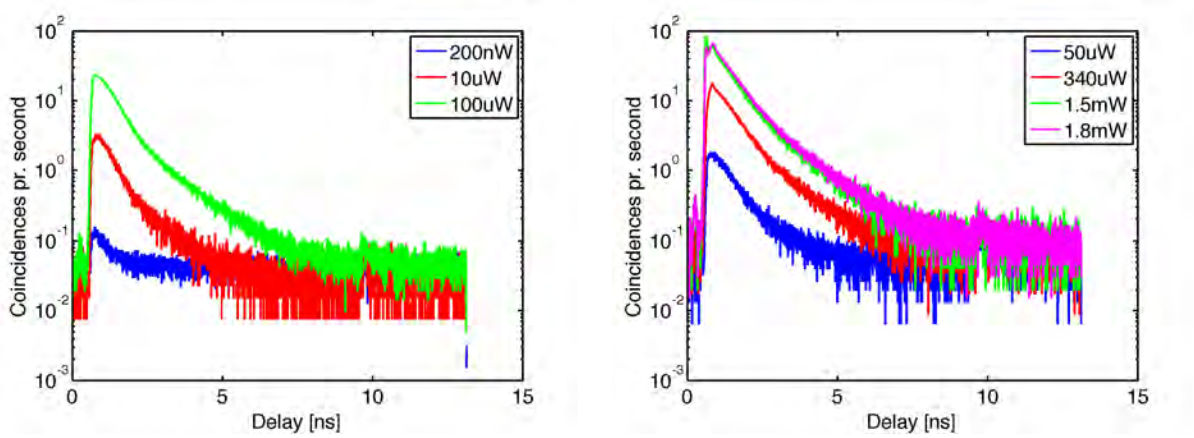

(a) Bulk

(b) Underetched

(c) Membrane

Figure 7.14.: Examples of time resolved ringdown measurements. Excitation with 780 nm pulsed laser.

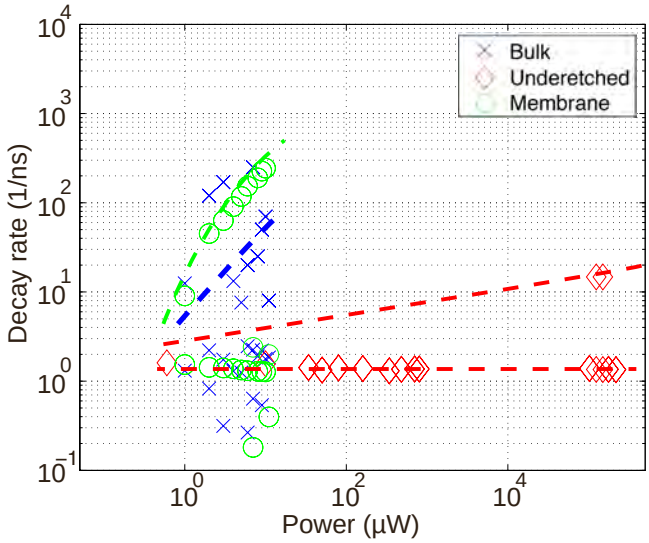

Figure 7.15.: The two timescales involved in the time resolved measurements of the QW structure for bulk, underetched and membrane.

hole pairs in a combination of free carriers trapped in the QW, and more bound exciton like states. By varying the wavelength it could be possible to investigate this by exciting close to the bandgap energy in the QW, and then investigate the effect this would have on the decay behaviour. Unfortunately a lower pump energy also mean less photoluminescence from the sample, as fewer decay trajectories in the GaAs are available for an excitation, and less carriers then decay to the QW states.

Experiments were performed with the pump laser around 840 nm, but this was abandoned as no discernable difference was seen in the spectrum. With the PL intensity it was deemed infeasible to continue with thorough time resolved measurement with the setup as it were. By optimization of the pickup from the sample and the fiber coupling to the APD setup, an increase of orders of magnitude in light power could have been achieved, but this was not pursued. Possibly a semi-resonant excitation scheme could also have been used, where the excitation wavelength is as close as possible to the absorption line of the QW mode, but this would have required that the absorption spectrum was mapped out, and thus this was not implemented.

Time scales

In the end it can be concluded that the time resolved measurements have complimented the spectral measurements nicely, and it has been established that fast and slow timescales around 1 ns were dominating in these samples. So what can these timescales be attributed? It can be shown that if the exciton state in the QW is allowed to tunnel to e.g. a surface state the decay will follow two timescales [Stobbe09], and the decay will be bi-exponential, and consist of τ_{rad}^{-1} and τ_{nonrad}^{-1}.

7.3.2. Mechanical motion

In ETH Zürich was also implemented a Michelson interferometer as described in **chap. 9** for the mechanical characterization of the nanomembranes. Historically this was done first, and with the knowledge gathered from the trials in Zürich, the Michelson in **chap. 9** was designed.

The mechanical modes of the nanomembranes themselves are not well understood. FEM modeling of the mechanical modes of typical samples of these nanomembranes are presented in **sec. B.2.1**. There is a lot of mechanical modes due to freedom of the tethers and the underetched area, but in order to make use of the decoupling due to the tethers, modes which do not include the motion of the tether or underetched area are preferred for optomechanics. The identification of the vibration frequency is a nontrivial problem because of the intrinsic stress in the structures, and the values in **sec. B.2.1** is based on low stress. Experiments are needed to confidently identify which vibrational peak correspond to which mode.

It was not possible to reliably detect the vibrations of the nanomembranes with the interferometer in Zürich, with the problem primarily being the displacement of the membranes being smaller than the detection limit. The author then brought one of the samples to the Vibrometer at DTU, where it was characterized. It turned out to be a really hard measurement, as the nanomembranes absorb the probe laser to a large extend and this local heating couple to the vibrations as described before. Examples of two vibrational measurement are shown in **fig. 7.16**, where the velocity of the membrane is measured. The sample was mounted on a piezo and driven with a chirp from 3 MHz and up. Vibrational modes were found at 4.5 MHz and above, but the SNR was too low to be able to discern the mode shape of the motion. The estimated mechanical Q_m is added in **fig. 7.16**, but since the probe laser is known to heat up the nanomembranes considerably, the spring constant will change and the Q_m lowered. This was again the motivation for fabricating the interferometer shown above in **chap. 9**.

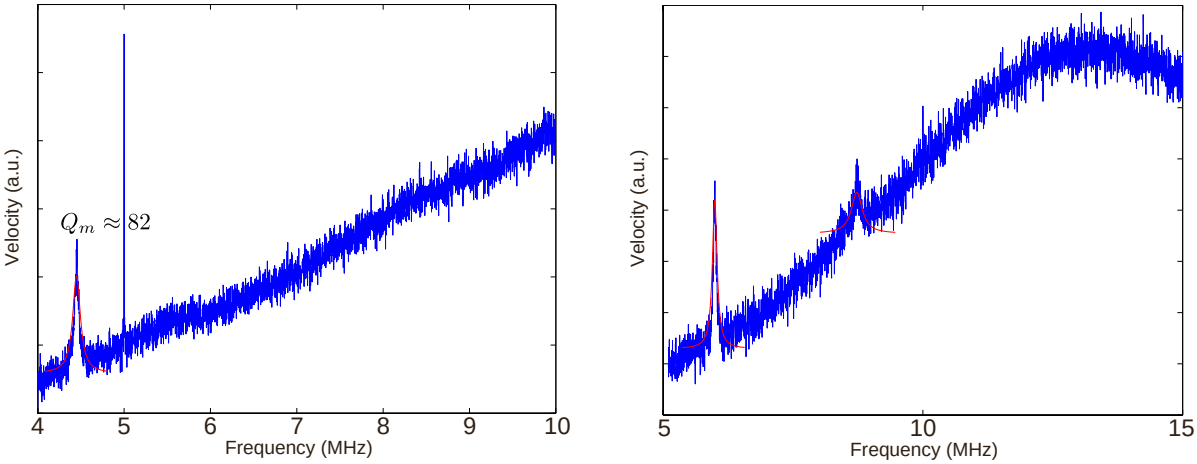

(a) Sample **f1-4ba-1,1**. Mechanical peak with $Q_m \approx 82$. The bright peak at 5 MHz is electronic noise.

(b) Sample **f1-4ba-1,2**. Mechanical peaks with $Q_m \approx 109$ and $Q_m \approx 68$

Figure 7.16.: Examples of nanomembrane Vibrometer measurements. The peculiar shape of the noise floor is due to different agitation signals to a piezo element, different lightpower and different amplification settings between the two measurements. Averaging over 1000 sweeps. Measured using 250 μW of red HeNe laser at room temperature.

7.4. Thermometry

If the vibrational measurements could be done with more sensitivity without affecting the nanomembranes as much this setup entails some interesting possibilites.

It could be possible to deduce more knowledge of the internal processes involved in the nanomembranes by measuring the temperature in various ways. Because of the vibrational degree of freedom of the nanomembranes, it is possible to estimate the bulk temperature of the nanomembrane, T_{nano}, in contrast to the effective mode temperature T_{eff}, by measuring the brownian motion of these vibrational modes. With knowledge of which mode correspond to which frequency, it should be possible to determine the bulk temperature some of the mechanical modes. Specifically the modes where most of the motion is the vibration of the nanomembrane independent of the tethers and underetched should follow the form expected in **sec. 2.2.3**. If the temperature of the whole sample is controlled by the cryostat temperature, this temperature can be used as reference for sufficiently low probe power. In an experiment such as the Michelson implemented in **chap. 9** the 1064 nm laser should not affect the nanomembranes a lot, and a large signal to noise can be achieved using very little light on the sample by using a homodyne scheme with a strong reference arm. Thus a reference measurement of the vibrational displacement and how this follow with the cryostat temperature, enable the calibration and measurement of the bulk temperature of the nanomembrane. Another possibility is to introduce a pump laser with above bandgap light in the setup and thus heat the nanomembrane, to study how the heat flow is in the system, and how well isolated the nanomembrane is from the reservoir.

Establishing the T_{nano} from vibrations would be interesting in itself, but could also be combined with the internal dynanamics of the nanomembranes. It is an open question how T_{nano} can be estimate using the PL, but work has been done to try an estimate this. For example the method of

so-called *differential luminescence thermometry* is a possibility [Patterson10]. As temperature is changed the lattice expands and the emission from the QW change to lower energy emission. This could be calibrated using the same kind of method as above, and combining the two methods could lead to insights into how the internal behaviour couples to the temperature and the vibrations.

7.5. Deformation potential cooling of vibrations

One of the motivations for designing and investigating these nanomembranes was of course to try and prove the thesis of strong deformation potential cooling [Mahan90, Stroscio05] of the vibrational modes of the nanomembranes, inspired by the strong cooling by photothermal effects found in the big GaAs membrane described in **chap. 5**. A requirement for witnessing a strong cooling of the vibrational modes by a process with a time delay, i.e. photothermal or electron pressure induced deformation potention cooling, is set by the time scale of the delay, τ. As described in **chap. 5** it is the order of $\omega_m\tau$ that is important, and thus the deformation potential cooling could be witnessed if $\omega_m\tau \approx 1$. For vibrational modes in the 4-6 MHz range this would require a time scale of $\omega_m\tau = 1$ and thus $\tau \approx 30$ ns for a $\omega_m/(2\pi) = 5$ MHz. As was shown in **sec. 7.3.1** the time scales measured for the excitation of the QW in the nanomembrane was in the 0.1 ns to 0.5 ns range so it is quite different. For the GaAs membrane studied in **chap. 5**, photoluminescence ringdown measurements were performed [Usami11] and found that the decay time was shorter than the limit of the experiment, 50 ps. Thus it is found that confined states in the QW in the nanomembranes indeed have a longer lifetime, and thus the deformation potential cooling is more likely. As the measured lifetimes which could be attributed to radiative and non-radiative lifetimes, was 2 orders of magnitude off from the optimal, it is not deemed a feasible experiment to try to prove deformation potential cooling using these structures.

If it was possible to place the nanomembranes in an experimental configuration where the vibrational motion could be monitored while the carriers could be excited using above band-gap light, it should be possible to witness this deformation potential cooling. As the thermal expansion coefficient is negligible around 12 K or 50 K for GaAs, as shown in **chap. 6**, the photothermal effect is believed to be minimized, and as cryogenic temperatures are needed for the QW to be well resolved, maybe deformation potential cooling of vibrations is possible to prove. Of course the vibrational energy also follows the bulk temperature and thus the measurement will be hard.

7.6. Conclusion and outlook

As mentioned above a lot of characterization have been done on the nanomembrane systems, but the conclusion is that the lifetime of excitations is too short to couple efficiently to the vibrations. This does not rule out that the samples can be used for studying other effects, and work is still going on with the samples, but in regards to the deformation potential coupling a more involved approach will be necessary. The manner that have been chosen is to confine the excitations for longer in a 2 QW heterostructure, and this idea is described in **chap. 8**.

8. Indirect exciton membranes

After the realization that the nanomembranes described in **sec. 7.2** have a very quick recombination time and show very little mechanical motion, the search for deformation potential cooling using these structures was halted. Instead work begun on the next generation of device where this among other effects will be possible to investigate.

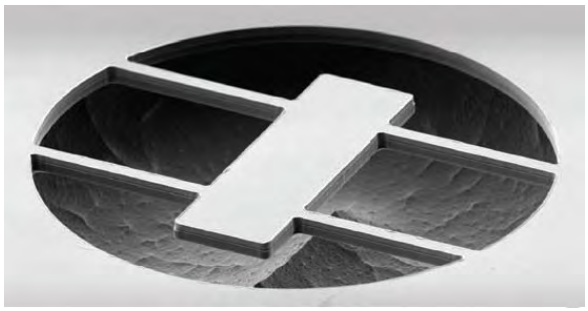

Figure 8.1.: The structure used for inspiration for the next generation design. The 2 MHz GaAs resonator by [Cole11], with dimensions of about 40 μm $\times$ 130 μm. Reproduced from [Cole11].

A lot of work was put into the design of the next generation of the GaAs membrane structures as these have shown a lot of potential for showing deformation potential cooling of vibrational modes, along with a lot of other possible advantages if designed and fabricated well. The realization from the nanomembranes was that it definitely is a lot harder to measure the mechanics of structures at the nanometer to a few micrometer scale and also that these structures have shown a low mechanical Q_m due to fabrication issues. A lot of changes was then put into effect for the next generation of these devices. The design has been a collaborative effort between *Quantop* from the optomechanical point of view, and the Lodahl group at NBI which also has other experiments planned with this setup. Additionally meetings have been held with the İmamoğlu group at ETH.

In **fig. 8.2** the structure design is shown. The design consist of a double QW structure with 2 InGaAs layers pancaked between GaAs buffer layers. Additionally the membrane structure has added regions that is doped with p+ or n+ concentrations of ions. These regions enable a control of the internal electric field by applying a bias voltage accross electrodes. The membrane is designed to be of the type as shown in **fig. 8.1** by [Cole11], where the membrane is suspended on thin tethers. The system is supposed to be put in a Membrane-in-the-middle configuration with a manufactured Bragg mirror beneath and a conventional mirror mounted at the top. In this cavity configuration the thickness of the whole sample is chosen, so that the optimal field strength at the QWs can be achieved. Additionally another set of electrodes enable application of a field from the membrane to the substrate beneath, which will enable the tuning of the position of the membrane in the cavity.

A lot of consideration went into this design, but the main motivation from the optomechanical

point of view, is getting a longer confinement time of the excitation. This in turn will lead to a longer τ. It is the hope that the additional control of the mechanical and internal dynamics and the position of the membrane, will enable a systematic mapping of a broad parameter space, and the investigation of both the photothermal, deformation potential and radiation pressure cooling in this setup.

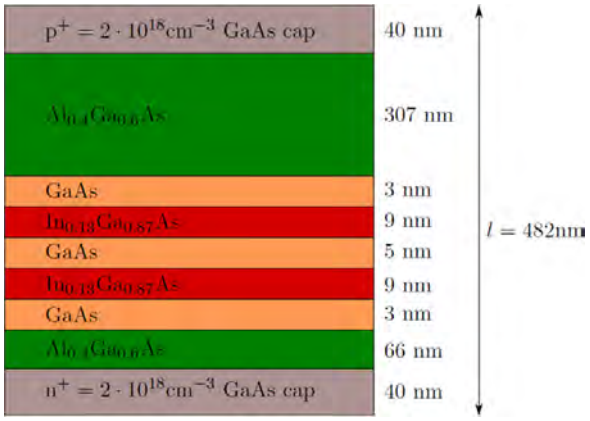

Figure 8.2.: Next generation Heterostructure. Reproduced courtesy of Petru Tighineanu.

The motivation for going to a double QW (DQW) structure comes from the realization that a long delay time is necessary in order to achieve considerable deformation potential cooling. This was not found to be possible in a bulk GaAs structure because of the quick decay processes with the surfaces. It is known that confined states in DQWs can have long lifetimes [Butov99]. Additionally the DQW design with added electrodes introduces the added control that the coupling between the states between the DQW coupled can be tuned. The excitation of a DQW structure can be engineered so a so-called indirect exciton state is possible where the excited electron and hole are spatially seperated in the two QWs, and because of the lessened coupling this entails, the time constant for recombination is longer than it is for a single QW structure [Butov99, Harrison10]. It should be noted that all discussions about the luminescence and in general the confinement of excitations in these QW should be performed at cryogenic temperatures as the thermal broadening of the states otherwise will change the overlap considerably. This is also taking into account in the modeling where a cryogenic temperature has been included.

In **fig. 8.3** a sketch of the band structure for the heterostructure is shown. The lowest energy hole state is indicated with a black circle, and its confinement is sketched using a blue trace. Similarly the lowest energy confined electron state is indicated with a filled black cirle and its confinement is sketched with a blue trace. The thick red lines indicate the energy landscape in the conductance and valence band due to the different materials. This shows how the energy landscape is tilted due to the intrinsic bias applied by the dopant introduced in the structure to form the electrodes. The lowest energy state is designed to be the case where a hole is confined in one QW while an electron is confined in the other. This is the situation indicated, and the electron and hole form an so-called indirect exciton. This is preferable as this enables a strong tuning of the coupling, and thus the lifetime, by applying an external bias on the electrodes which then shifts the slant on the energy landscape.

In **fig. 8.4** calculations of the wavefunctions for the 3 lowest energy states of the electron and hole states in the DQW as a function of the field accross the p+ and n+ electrodes are shown. The

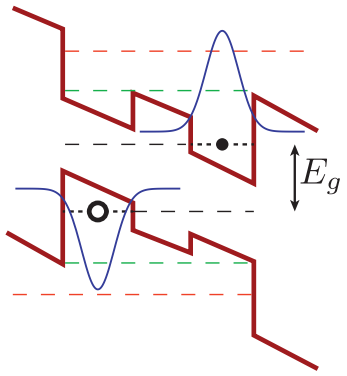

Figure 8.3.: The ground state indirect exciton with an applied electrical bias. The lowest energy hole is indicated with a ring, while ground electron state is indicated with a full circle. The first excited state is direct exciton formed by e.g. the hole ground level coupling to the first excited state of the electron states indicated with green.

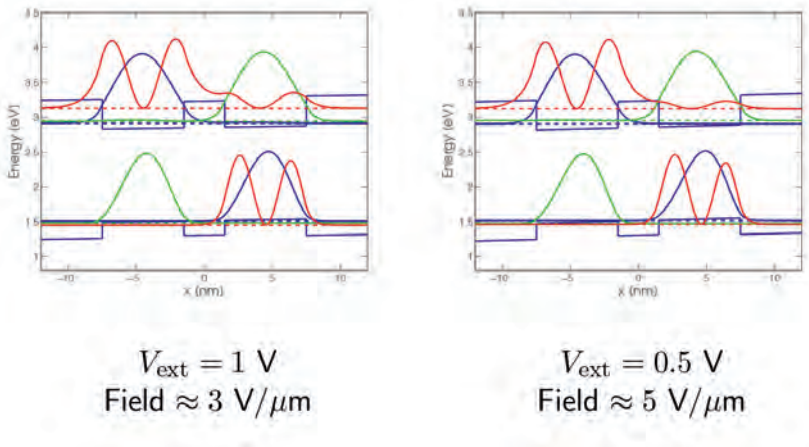

Figure 8.4.: The lowest energy wavefunctions for the electron and hole states in the DQW. Shown with an external field of $V_{ext} = 1$ V and $V_{ext} = 0.5$ which results in slightly different overlap. Reproduced courtesy of Petru Tighineanu.

calculations are reproduced courtesy of Petru Tighineanu from the Lodahl group. It is seeen how a higher field accross the electrodes, V_{ext}, puts a slant on the confinement energies and in conjunction with the internal field produced by the different alloys and dopings, the overlap between the electron and hole wavefunctions can be increased and decreased. As the probability of the recombination is proportional to the mode overlap, this means that the decay time is controllable using V_{ext}.

Calculations by Petru Tighineanu of the proposed structure shows that this control of the field in the proposed structure will lead the decay lifetime of an excitation of the DQW to be tuned from μs to ps by a change of 3 V over the elecrodes. This remarkable control would lead to the different effects in the structure being investigated in a systematic way, as e.g. the photothermal cooling effect can be changed with temperature, while the deformation potential cooling could then be changed by changing the applied voltage.

Cavity configuration

The design of the cavity configuration for the setup has been done in tandem with the design of the membrane structure. The design is shown in **fig. 8.5** and shows how a cavity is created with the membrane in the center, above a Bragg mirror that is part of the fabricated structure. A traditional mirror is then positioned far above the sample. In this context 'far' means on the order of a mm, while the distance between the membrane and the Bragg mirror is 1 or 2 μm, depending on the configuration.

This scheme allows for a lot of tuning, as electrical contacts (not shown) enable the tuning of the position of the membrane, as well as inducing a stationary bending of the membrane.

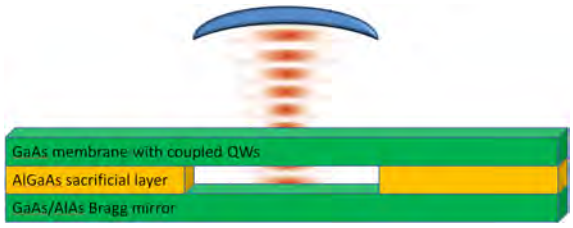

Figure 8.5.: Next generation cavity configuration, with a fabricated Bragg mirror beneath, and a traditional mirror on top of the double QW membrane in the center.

8.1. The bulk system

8.1.1. Fabrication

At the time of this writing the bulk systems have been grown using electron beam epitaxy at ETH and these samples have been characterized by the Lodahl group. The mechanical side of the design has not been perfected yet. While the nanomembranes were etched at ETH Zürich using a technique involving dry etching as described in **sec. 7.2.1**, this is not available at NBI yet. Initial wet etching procedures have made it clear that equipment and knowledge has to be gathered before

the etching of optomechanical systems can be undertaken, and this has postponed the realization of optomechanical systems with DQW.

8.1.2. Experimental results

Quite a lot of experiments have already been done by the Lodahl group on this bulk system. As an example the photoluminescence has been measured with above bandgap pumping, in the spectrum and timeresolved domain. As the work is to be published later it is not included here. It has been established that indeed the electrical contacts enable a tuning of the available states. The overlap between excited states in the distributed QWs has been shown to change with this tuning, which is promising. The same kind of experiments as was done with the nanomembranes in **sec. 7.3** has been done on the DQW system, in order to investigate the complex behaviour of the confined states. Using these methods it has been established that indeed trapped confined states are created in the DQW. The kind of bound indirect exciton that can be bound between the two QWs is called a Wannier exciton [Wannier37, Harrison10], and for these the relative motion of the indirect excitons is locked, while the motional mass of the exciton is delocalized. As was modeled in **fig. 8.4** a change in the bias voltage changes the overlap between the electron and hole in the indirect exciton. As an example a measurement of the PL spectrum is shown in **fig. 8.6**. The emision from the DQW is in the double peak around 915-930 nm at cryogenic temperatures. A lot can be found by tuning parameters such as temperature, pump power and wavelength, and the electrical bias. It is established how the confined states can be tuned, as expected, and follow the model that has been developed for the system. This will be published elsewhere, but for the outlook of this project, it is very promising for the realization of deformation potential cooling as a dominant effect.

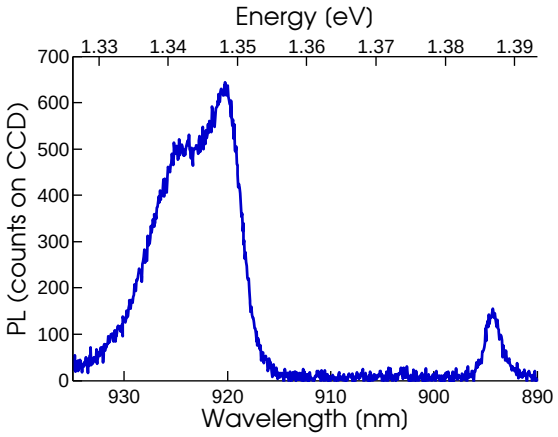

Figure 8.6.: PL of the DQWs for a pumping power of 32 nW. Integration time of 30s was used. Reproduced courtesy of Gabija Kirsanske and Petru Tighineanu.

8.1.3. Lifetime

Specifically regarding the lifetime of the exciton states, the tuning should lead to very different lifetimes for the confined states in the DQW, and indeed this has been shown experimentally. Pre-

liminary measurements have shown a large tuning in lifetime of 3 orders of magnitude, but experimental difficulties with focusing have meant that good reproducible measurements have only been done for one electrical bias. It is expected that better data will be available soon, but it is very encouraging to be able to achieve a tuning of the timescale from nanoseconds to microseconds. This makes it possible to realize the situation where deformation potential cooling is the dominating effect for the behavoiur of mechanical modes.

8.1.4. Towards optomechanical structures

In order to realize the deformation potential cooling of vibrations, a suitable mechanical resonator has to be fabricated from this heterostructure. At the time of writing fabrication issues are being worked on, but due to the requirements of thin tethers and dimensions on the micrometer scale, as stipulated by the design by [Cole11], work is still in progress. Additionally the best possible design will be a compromise of strong optomechanical coupling and high Q_m so the design of every dimension of the resonator and the resulting cavity field from the resonator and two mirros have to be taken into account.

The position of the tether of these structures are essential for the coupling of the different mechanical modes to the reservoir of the underetched surroundings as was investigated by [Cole10]. Using a series of FEM simulations Emre Togan from ETH and the author, with a test design of $40 \times 80\mu$ m, several conclusions have been made for a good design taking notes from the design presented in [Cole10]. The FEM method for estimating the Q_m was described in **sec. 4.3**.

- Q_m increases as the width of the tethers decreases.
- Q_m increases as the length of the tethers increases.
- Q_m increases to a maximum if the tether is placed a couple of μ m offset from the center of the membrane where there is a node in the displacement field.
- There is an optimum (and short) size of the underetched area that the tether is attached to.

These conclusions from the FEM follow with the expected from experience except for the third one, that seems to contradict the discussion in [Cole10], where the node should be placed closer to the node of the mechanical mode. Luckily in the experiment the tether position can be varied by manufacturing a lot of membranes on the same chip, to find the optimal position for the highest Q_m. This is the plan.

8.1.5. FEM of the proposed structure

In order to investigate the possibility of achieving strong deformation potential coupling in this proposed system, a 3D FEM implementation has been created. The proposed dimensions used here are 40 μm $\times$ 80 μm with a thickness of 480 nm. A calculation of the displacement using this model is illustrated in **fig. 8.7** where the displacement is grossly exaggerated for visual clarity.

The derivation of the force estimate due to the deformation potential coupling is included in **sec. A.5.3** as well as the implementation details for the *Comsol* model. It is shown that with realistic parameters, a change on the order of 1 μm displacement at the beam spot, can be achieved with around 1 μW of above band light hitting with a 10 μm beam size. This seems quite large

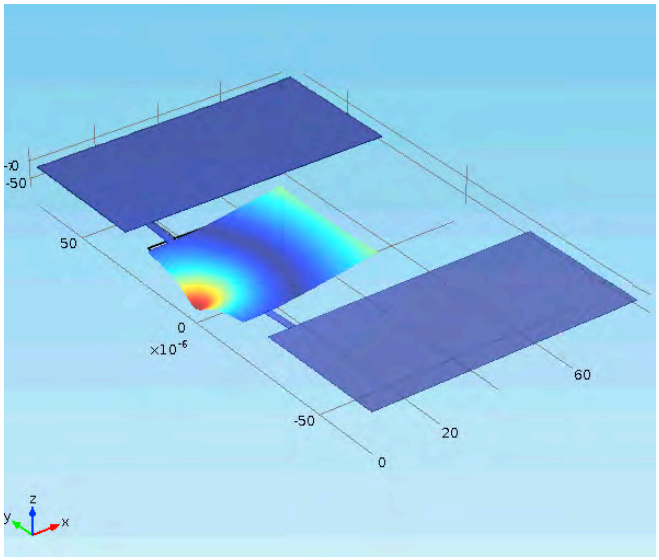

Figure 8.7.: FEM of displacement for the next generation membrane model with two quantum wells (not visible). The model is assumed symmetric and thus only half the modeled system is shown. The coupling to the optical field can be estimated due to the displacement. The displacement is grossly exaggerated for visual clarity.

but is thought to be due to the freedom that the tethers allow for. This large displacement at the beam position seems very promising for the prospect of seeing the deformation potential expansion having a strong effect on the vibrations of the system. Without including the deformation potential coupling in the FEM a load on the QW layer is included as a simple point force, and as a gaussian force following the modeled laser beam. In this manner it is estimated in **sec. A.5.3** that the equivalent force is on the order of 10^{-18} N per photon.

The way this force is modeled is for the stationary change of the system, with the inclusion of the expansion due to deformation potential coupling. It is entered as a isotropic and constant strain in the FEM, which has the implication that the time response is not included in the model. Thus the model does not include the coupling to the various mechanical modes of the membrane, nor does it include coupling to other time scales of the structure.

8.1.6. Deformation potential coupling

In order to estimate the coupling to the vibrations the cavity feedback have to be taken into account. A model made by Petru Tighineanu have estimated the cavity coupling strength, $g = \partial\omega_c/\partial\delta x$, to be

$$\frac{g}{2\pi} \approx 2\text{GHz}\,\text{nm}^{-1} \tag{8.1.1}$$

for the structure here modeled included in a cavity. Using this it is possible to estimate the supposed ratio of the different forces. A force such as the photothermal effect of the coupling to the vibrational modes via the deformation potential coupling, is dependent on the number of photons absorbed in the membrane, denoted $\langle n_{\text{membrane}} \rangle$. Then for a general force F, which could be F_{th} or F_{el}, the

mean value $\langle F \rangle$, will be

$$\langle F \rangle = \beta \langle n_{\text{membrane}} \rangle \tag{8.1.2}$$

where β here denotes the magnitude of the force per absorbed photon. The same could be written as

$$\langle F \rangle = \beta \alpha \langle n_{\text{cav}} \rangle \tag{8.1.3}$$

where α is the optical absorption in the membrane, and $\langle n_{\text{cav}} \rangle$ is the mean number of photons in the cavity. α is dependent on the cavity configuration as well as the absorption in the QWs in the membrane and can then easily be determined. The FEM is needed for the estimate of β though.

The photothermal/deformation potential force can be shown [Wilson12] to follow $\nabla F_{\text{th/dp}} \approx \beta \alpha \nabla n_{\text{cav}}$ with ∇n_{cav} being the spatial derivative of the intracavity photon number around equillibrium. For the radiation pressure force the pressure force gradient sales as $\nabla F_{\text{rad}} \approx \hbar g \nabla n_{\text{cav}}$. The comparison between these forces then enable the comparison between radiation pressure and photothermal/deformation potential forces, reveals the important factor

$$\nabla F_{\text{rad}} / \nabla F_{th/dp} = \frac{\beta \alpha}{\hbar g} \tag{8.1.4}$$

As $\beta \approx 1 \times 10^{-18}$N per absorbed photon, and assuming $\alpha = 0.1$ as a start, and a light power of 1 μW, which leads to a photon number of 1×10^{12}, the factor in **eqn.** (8.1.4) is on the order of 0.1, with the strange unit [K s]. This hints that low optical power, it should indeed be possible to achieve a regime where the deformation potential cooling will be measurable. And this rough estimate has not at all included the tunable strength of the deformation potential coupling in the proposed cavity setup.

Outlook

The samples are grown and characterized and soon etched to form mechanical oscillators. Thus the work in this group of mechanical investigation and design of the final cavity setup can soon be started and the cryogenic setup built.

The cavity has to be designed in a fashion where two different light fields can be sustained. There will be the probe light for determing the membrane vibrational properties and the cooling light for deformation potential cooling. The cavity should exhibit a relatively low finesse for the probe wavelength, such that the mechanical motion can be detected using the transmission measurement, while achieving high cavity finesse with a wavelength where the absorption in the QWs can be strong. It is the hope that all of this can be achieved in 2013.

8.2. Conclusions

A lot of things have been going on for the next step for vibrational cooling after the big GaAs membranes were retired. The next step is minimizing the photothermal cooling and showing the deformation potential cooling of vibrations. A lot of research has been done on the GaAs nanomembranes with a single QW embedded as described in **chap. 10**, but these have shown not

to be good enough systems for studying potential deformation potential cooling due to the short lifetime of excitations. The design and fabrication is underway for the next generation GaAs mechanical oscillator with two QWs to confine excitons for a longer time scale. In 2013 it is the hope that the two groups at NBI will have a working sample where deformation potential cooling can be tuned to be the dominant vibrational cooling process.

Part IV.

Next generation mechanical characterization

The nanomembranes manufactured at ETH Zürich turned out to be difficult to vibrationally characterize, as they simply do not move a lot and have relatively high frequencies. This was one of the motivations for considering how a better characterization setup could be designed which would be beneficial for the whole group. The task of the author then became the design and implementation of the proposed setup and this is discussed in **chap. 9**.

9. Characterization of mechanical modes with an interferometer

There has been a lot of use for a quick method for characterizing membranes in the group. The prevalent method have been to build a cavity with the membrane as one of the mirrors, and then the methods described in **sec. 5.4** enables the characterization of the mechanical modes of the sample. An alternative (and quicker) method have been to travel to DTU and borrow a *Polytec Vibrometer* (shown in **fig. 9.1a**), that the Anja Boisen group have generously granted access to. This device is a doppler interferometer with a high sensitivity with a microscope objective and advanced software for analysis. As such it is of course a coveted machine, and in use most of the time. Thus it would be optimal to be able to characterize several membranes over a short timespan, without sacrificing the sensitivity that is attainable with the cavity or Vibrometer approach.

The first method of building a cavity with the membrane as a mirror, is very sensitive, and the basis for most of the work that has been done. However it is a very time consuming process to create, align, and optimize a cavity, before measuring the mechanical motion by the transmission. The problem with the cavity approach is also that the mounting of the membrane in a vacuum chamber will limit the mechanical degrees of freedom for the membrane, and thus make it hard to sample different points on the membrane, as cavity coupling will have to be regained at every point. This is not impossible and has indeed been done a number of times in the various cavity setups in the group, but as it is cumbersome and time consuming an approach such as the Vibrometer would be better. This paves the way for designing a new setup for this characterization.

Another important problem with the Vibrometer at DTU is that there is no possibility of cooling the temperature of the sample to lower temperatures than achievable with a Peltier element. This is because it is built around a standard vacuum chamber, which rules out the possiblity of characterizing the mechanical motion at temperatures lower than maybe -50 °C. This was not a big problem for the characterization of samples at room temperature but as it could be interesting to push towards functional semiconductor devices and these require lower temperature to function, the need for lower temperatures arises. Examples of such functional devices would be heterostructures designed to show the deformation potential cooling process as described in **chap. 6**. Because of thermal broadening at room temperature the confinement of the excited states in the structure is much lower at room temperature, and cryogenic temperatures are necessary. Such systems and the work on realising new phenomena in these are described in **chap. 7**. With the above motivations the work on building a Michelson Interferometer [Michelson87] begun.

The contributions of the author
The Interferometer was designed and built by the author in collaboration with Andi Barg as a master student. The work was shared with the author doing a large part of the designing and Andi Barg performing a lot of the implementation with a lot of discussion and development with helpful members of the rest of *Quantop*.

(a) A commercial Doppler interferometer. *Polytec Vibrometer*. [Pol]

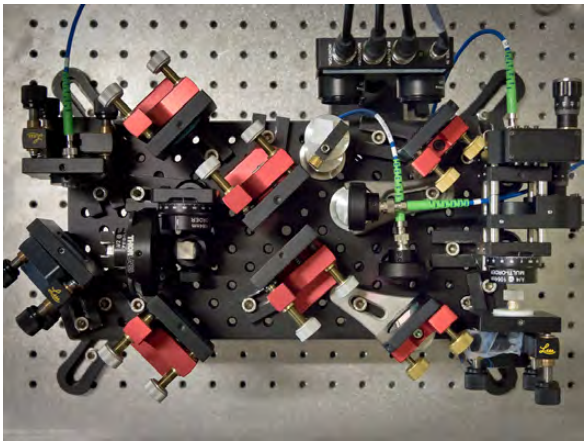

(b) The interferometer seen from above.

Figure 9.1.: The Polytec Vibrometer, and the homebuilt Michelson interferometer.

9.1. Interferometer requirements

The design criteria for the interferometer was simply that it should be able to detect very small displacement with a bandwidth suitable for the samples the group is working with. More specifically

- Microscope objective with high magnification, able to achieve a small probe spot size, capable of focusing through a cryostat window.
- Ability to detect the motion of the membrane with displacements of pm range.
- Mount and setup compatible with Cryostat.
- Illumination and degrees of freedom capable of scanning and visualizing samples ranging from μm size to mm size.

All of this should be achieved while not subjecting the sample to high optical power, which would change the characteristics by heating, and potentially destroy sensitive samples.

9.1.1. Expected vibration

The interferometer should be able to detect the brownian motion of the mechanical samples, and this motion should therefore be estimated for the various samples that is of interest to the group. The main mechanical system that have been used are the SiN thin membranes with thicknesses of 50, 100, 200 nm and lateral dimensions of 500 μm and 1 mm. It was shown in **sec. 2.2.3** how the expected RMS displacement Brownian motion are on the order of 4 pm, so this is what the interferometer should be able to detect with an appreciable signal-to-noise.

For ideal mode overlap between the two interferometer arms and balanced power it turns out that

the output field power will be $\cos^2 k\Delta l$, with k being the wavenumber and Δl is the difference in path length between the two arms. This is derived below. By operating at the $\Delta l = \lambda/8$ position, a small displacement around this position lead to a linear change in the signal. This would follow as a linearization of $\cos^2 kx \approx \frac{1}{2} - \frac{2\pi x}{\lambda}$. So with a probing wavelength of $\lambda = 1064$ nm, the displacement of 10 pm would yield about 6×10^{-5} out of 1 of the signal strength for moving a full wavelength. This is then what should at minimum be detectable which is attainable in an interferometer. If the interference signal from the interferometer can be cast into a -15 to 15 Volt range, then the brownian motion of the membrane in the probe arm would correspond to 6×10^{-5} parts of the 30 Volt signal amplitude, corresponding to a signal of about 2 mV. This is then the requirement for the interferometer to be able to measure.

9.2. Interferometer model

In **fig. 9.2** the chosen Michelson interferometer scheme is shown.

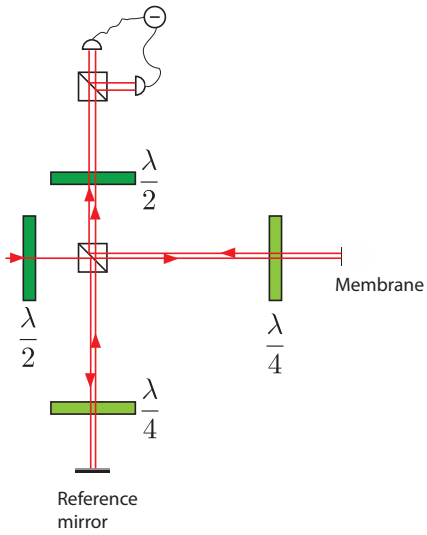

Figure 9.2.: Interferometer scheme. The green rectangles signify waveplates. Also illustrated is polarizing beam splitters, and a differential photodetector setup. The sample membrane is in the *probe* arm, while the arm with the reference mirror is denoted the *reference* arm. Two detectors are used to measure the signal, in a scheme called balanced detection.

9.2.1. Interferometer equations

The equations for a Michelson interferometer as indicated in **fig. 9.2**, is to be derived. It is assumed that the interferometer is perfectly balanced, which is to say that the powers are the same in the reference arm as in the probe/membrane arm. Additionally the overlap between the two beams from the arms are assumed perfectly overlapped.

The input electric field that enters the interferometer is denoted

$$E_0 e^{i(\omega t - kx)} \tag{9.2.1}$$

with E_0 being the amplitude, ω the angular frequency, t the time, k the wavevector and x here denoting the position. If the beamsplitter is assumed a perfect 50:50 beamsplitter the amplitude reflection coefficient can be denoted as $r = 1/\sqrt{2}$ and likewise for the transmission, $t = i/\sqrt{2}$. Thus the light that is transmitted through the beam splitter in the probe arm will be $i(E_0/\sqrt{2})e^{i(\omega t - kx)}$, while for the reflected light in the reference arm the field will be $(E_0/\sqrt{2})e^{i(\omega t - kx)}$. As the light is reflected from the sample in the probe arm and the reference mirror in the reference arm they are multiplied with a factor -1. The returning beams are transmitted and reflected with the same t, r amplitudes as the first go and the output field will be [Saulson94]

$$E_{out} = \frac{i}{2}E_0 e^{i(\omega t)-2kL_R} + \frac{i}{2}E_0 e^{i(\omega t)-2kL_P} \tag{9.2.2}$$

with L_R now identified as the length of the reference arm, and L_P denoting the probe arm length. Rewriting **eqn.** (9.2.2) as

$$E_{out} = \frac{1}{2}ie^{i\omega t}\left(E_0 e^{-i2kL_R} + E_0 e^{-i2kL_P}\right) \tag{9.2.3}$$

$$= iE_0 e^{i(\omega t - kL_R - kL_P)}\cos(kL_R - kL_P) \tag{9.2.4}$$

and identifying the path length difference as $\Delta l = L_R - L_P$, the output field can be written

$$E_{out} = iE_0 e^{i(\omega t - k\Delta l)}\cos(k\Delta l) \tag{9.2.5}$$

where Δl then is related to the motion of the sample that is to be measured. From **eqn.** (9.2.5) the detected output power can be found to be

$$P_{out} = |E_{out}|^2 \tag{9.2.6}$$

$$= P_{in}\cos^2(kL_R - kL_P) \tag{9.2.7}$$

$$= \frac{P_{in}}{2}(1 + \cos\left[2(kL_R - kL_P)\right]) \tag{9.2.8}$$

and by identifying $\Delta l = L_R - L_P$ this can be written

$$P_{out} = \frac{1}{2}P_{in}\left(1 + \cos[2k\Delta l]\right) \tag{9.2.9}$$

and thus it is clear how the interferometer is sensitive to the modulations of the length of the two arms, e.g. when the membrane vibrates. A dependence of the displacement Δl of the interferometer in P_{out} indicated in **fig. 9.3**. This is the basis for the function of the interferometer as a vibration sensitive instrument.

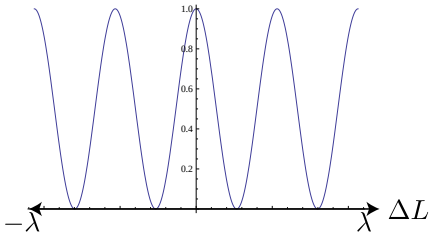

Figure 9.3.: Interferometer output $(1 + \cos[2k\Delta l])$ by **eqn.** (9.2.9) for a balanced interferometer.

A number of choices were made for the interferometer setup. A conventional flow cryostat was chosen as the main vacuum chamber, but the setup was designed with flexibility in mind, and the probe fiber is easily movable to another probe 'head'. The reason for working with fibers is also for easier extension into a more advanced scheme were e.g. a fiber coupled EOM could be put in the reference arm for a heterodyning scheme, and this could be installed without a major restructuring. At the same time the Michelson was designed to be as compact as possible to minimize the acoustic vibration pickup.

9.2.2. Interferometer scheme

Here the scheme will be described in more detail. The scheme is indicated in **fig. 9.4** with the polarization degree of freedom indicated with red arrows. It is described as

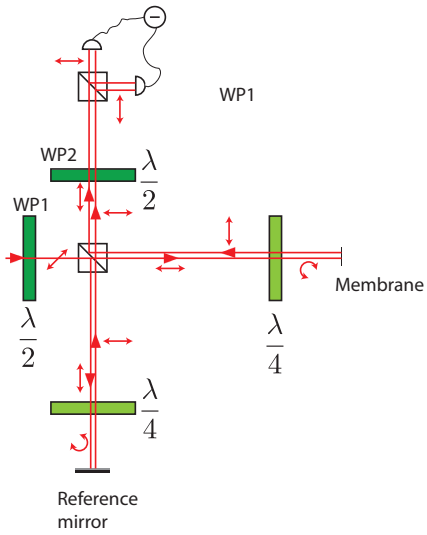

Figure 9.4.: Michelson interferometer scheme in detail. The polarization degree of freedom is indicated with red arrows.

1. Light enters the interferometer. The polarization has been cleaned by a beamsplitter before entering.
2. The first $\lambda/2$ WP is controlling the balancing of powers in the interferometer. The light hits the main PBS and is split between the probe arm and the reference arm.
3. **The probe arm**
   a) A small amount of the light is transmitted in the PBS and with horizontal polarization it is fed to the probe fiber. The power should be on the μW scale to not affect the micromembranes.
   b) The horizontally polarized light travels through the fiber and is fed through a $\lambda/4$ WP before it reflects off the membrane, (disregarding microscope objective and fiber coupling optics which is presumed to only introduce losses).
   c) The reflected light is retarded by the $\lambda/4$ WP and returns to the main PBS.

d) As the reflected light now has vertical polarization the main PBS reflects and the probe light is fed to $\lambda/2$ WP in the interference arm.

e) The WP is set to balance the power coming from the two arms of the interferometer.

f) In order to not throw away half of the signal the balanced light is fed to another PBS and both arms are fed to an amplified differential photodetector. This removes common mode noise from the table and the laser. If the interferometer is balanced when no membrane is hit it should function as a "null instrument" and thus only the membrane motion enters as a signal.

4. **The reference arm**

a) A beam is reflected with vertical polarization through the main PBS.

b) It is chosen to be much larger in intensity by adjusting WP1 so that the SNR can be improved by the ratio of the intensities in a heterodyne fashion.

c) It is fed through a fiber and through a $\lambda/4$ WP.

d) It is reflected off the PZT mounted mirror.

e) The strong reference beam is balanced with the probe beam using WP2. Thus increasing the SNR by the ratio of the intensities of the two arms.

5. A differential measurement is performed after balancing the powers of the two arms on the two photodiodes, thus cancelling out common intensity fluctuations.

6. The signal from the differential measurement is split. A part is fed to a locking circuit used for controlling the PZT in the reference arm, stabilizing the interferometer. A connection to a fast oscilloscope or spectrum analyzer with a measurement load of 50 Ω is made and the noise from the probe arm can then be measured and from this the vibrations of the sample system can be deduced.

The interferometer is designed to work in a unbalanced scheme where the probe light power can be much less than the power in the reference arm. This is done by working with different polarizations in the two arms, and then mixing them on the second PBS and measuring both outputs. Thus no light is wasted and the signal from the membrane can be increased $\sqrt{P_{ref}/P_{probe}}$ where P_{ref} and P_{probe} is the optical power stemming from the two arms. This is the basis for*homodyne* detection and will be described in **sec. 9.6.2**. Another benefit is that both of the detectors can be fed a suffiently strong light power so that they are running in a shotnoise limited regime. For realistic powers this ratio is 10 mW/50 μW$\sim$200, and thus a large increase in signal to noise is achievable by having large power in the reference arm.

The output signal is measured using a *balanced detection* scheme where the output is split on a beamsplitter and measured on two photodiodes. This has the advantage that a differential amplifier immediately removes the common mode noise from the two photodetectors, and this makes the system insensitive too intensity fluctuations and other noise sources.

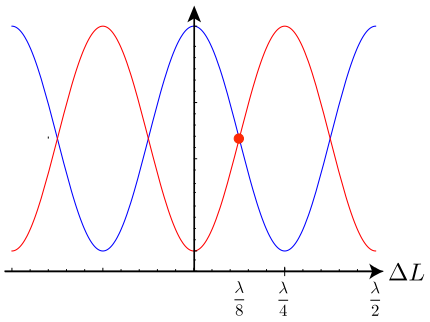

(a) Output field.

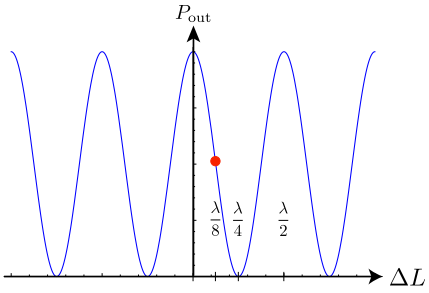

(b) Output power P_{out}.

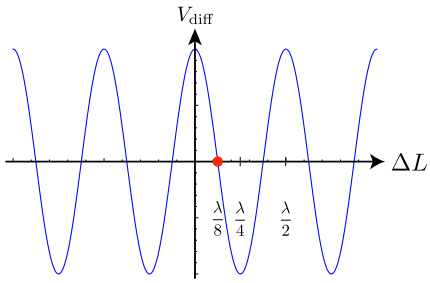

(c) The differential signal V_{diff}.

Figure 9.5.: The interference of the probe arm and reference arm in the interferometer. The interferometer is locked such that a phase difference between the arms are fixed at $\Delta L = \lambda/8$. The lock position is indicated with a red dot.

9.2.3. Interferometer locking

From the interference term in **eqn.** (9.2.9) the output power as a function of arm length difference, ΔL, will be

$$P_{out} = P_{in}\frac{1}{2}\left(1+\cos(2k\Delta L)\right) = P_{in}\frac{1}{2}\left(1+\cos(2\frac{2\pi}{\lambda}\Delta L)\right) \tag{9.2.10}$$

and this is illustrated as the blue trace in **fig. 9.5a**.

It is convenient to lock the reference arm of the interferometer so that the interference signal is at a chosen position at all times. It would be possible to let the interferometer "free run" where the two arms drift due to temperature fluctuations and vibrations, but this would result in varying intensity of the interference signal, and thus would lead to a lower SNR. In **fig. 9.5** the chosen locking point is indicated .

In the experiment the interference signal is measured using a differential measurement scheme, where the voltage from one photodiode is subtracted from the voltage from the second detector and these results in a shifted interference signal as indicated in **fig. 9.5c**. The interferometer lock is built using an operational amplifier configured in a integrator circuit, and with a chosen characteristic frequency of 76 kHz.

When the lock is engaged the fluctuations due to the sample moving will then produce a high frequency component. These will not be cancelled out by the differential measurement, while e.g. the common mode noise due to acoustic noise on the interferometer table, will be cancelled to a large extend. This is the motivation for the homodyne detection scheme used and described in **sec. 9.6.2**. The differential signal is measured using an instrument amplifier working with gain 1 with a bandwidth of 6 MHz, and measured using a high speed oscilloscope.

Piezoelectric element

To take the whole transfer function of the setup into account, the piezo in the reference arm must be calibrated. This can be done by taking the sample in the probe arm out of the system and just replace it with a mirror. By driving the piezo in the reference arm the effect on the interference signal can be determined. If the piezo is driven with a sinusoidal voltage, the motion of the piezo is expected to follow as $x(t) = x_0 + A_d\cos(\omega_d t)$ where x_0 is the equilibrium position of the piezo, $\omega_d/(2\pi) = \nu_d$ is the driving frequency and A_d is the amplitude of the driven piezo motion. For simplicity the x_0 can be set to zero as it will not affect the conclusion as seen below.

An additional complication enters with the piezo having different response at different modulation frequencies, and this needs to be taken into account. This can be done by calibrating the piezo response at different frequencies driving frequencies. The response of the piezo crystal is expected to follow the frequency behaviour indicated in **fig. 9.6**. For low modulation frequencies the response will be pretty independent of frequency, while it gets a much larger 'stroke' around the resonance frequency of the piezo crystal. This is indicated as a peak in **fig. 9.6**, and the response is expected to drop off as $1/\nu_{mod}$ for higher frequencies. The crystal is also expected to show the harmonics of the resonance, and these can be used to create a larger signal even at relatively high modulation frequencies.

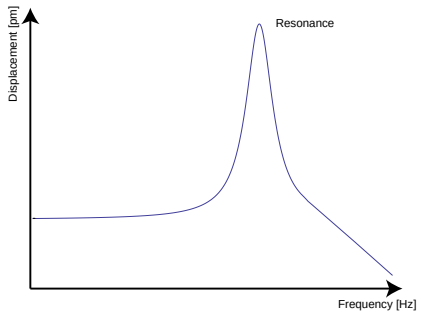

Figure 9.6.: Theoretical frequency response of piezo crystal. The displacement is much enhanced around the resonance of the crystal, and then decays as $1/\nu$ for higher frequencies. What is not indicated is that the harmonics also show a higher displacement than the $1/\nu_{mod}$ dependence.

The change in length Δl_{pzt} is linear in applied voltage as

$$\Delta l_{pzt} \approx \pm E d_{ij} L_0 \tag{9.2.11}$$

with E being the electric field strength at the piezo crystal {V/m}, d_{ij} being the piezoelectric coefficient of the material {m/V}.

9.3. Displacement calibration

A scheme for calibration is needed. A single interference fringe strictly speaking corresponds to $\lambda/2$ of the light, but that means that the transfer function of the locking circuit/piezo driver needs to be measured. Additionally the laser intensity should be contant so that the voltage between maximum and minimum of the sweeping signal is constant and a change in voltage corresponds to a change in path length. This is not a trivial characterization.

Instead the form of the interference signal is utilized.

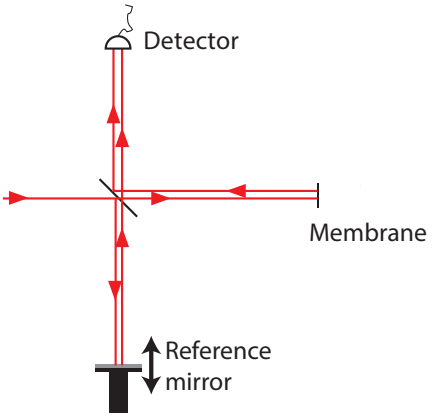

Figure 9.7.: Calibration scheme. The reference mirror is mounted on a piezo crystal.

9.3.1. Relation between δv and δx

It is necessary to be able to determine the displacement that a certain measured voltage correspond to. The interferometer is chosen to operate around the locking point at $\Delta L = \lambda/8$, with the motion of the sample adding a small shift δx as $\Delta L = \lambda/8 + \delta x$. This is illustrated in **fig. 9.5**. The output power at this point is

$$P_{out} = P_{in}\frac{1}{2}\left(1+\cos(\frac{2\pi}{\lambda}\lambda/4)\right) = P_{in}\frac{1}{2}\left(1+\cos\left(\frac{\pi}{2}+\frac{4\pi}{\lambda}\delta x\right)\right) = P_{in}\frac{1}{2}\left(1-\sin\left(\frac{4\pi}{\lambda}\delta x\right)\right) \tag{9.3.1}$$

If the sample in the probe arm moves a small distance δx in the direction of the light beam, it introduces a small shift δl between the two arms. If the interferometer is locked at the $\Delta L = \lambda/8$ point the change in power will to first order be proportional to the shift in arm length δx. Then by linearizing **eqn.** (9.3.1) to first order in the displacement δx

$$P_{out} \approx P_{in}\frac{1}{2}\left(1-\frac{4\pi}{\lambda}\delta x\right) \tag{9.3.2}$$

and the measured photocurrent will then be assumed proportional to this power, when the interferometer is kept locked around the $\Delta l = \lambda/8$ position. The optical power is however measured using a differential setup between two detectors, and the differential voltage can be written

$$V_{\text{diff}}(\Delta L) = \frac{V_{FF}}{2}\cos(2k\Delta L) \tag{9.3.3}$$

where V_{FF} is the peak-to-peak measurement of the 'full fringe' measurement of the amplitude of the interference signal. This is measured independently by sweeping the reference arm length over several wavelengths. It is noted that the first term in **eqn.** (9.3.2) is cancelled by doing a differential measurement and thus the stationary term is not entering in **eqn.** (9.3.3). Insertion of $\Delta L = \lambda/8 + \delta x$ in **eqn.** (9.3.3) yields

$$V_{\text{diff}}(\lambda/8+\delta x) = -\frac{V_{FF}}{2}\sin\left(\frac{4\pi}{\lambda}\delta x\right) \tag{9.3.4}$$

where the same trigonometric identity as above was used. The minus sign reflects that the locking position is on a negative slope of the interferometer signal. If the interferometer is kept around the so-called *white light* position, this would be the optimal place to lock the interferometer. The white light condition is described later in **sec. 9.6.1**. Again this can be linearized for small δx around the $\Delta L = \lambda/8$ point as

$$V_{\text{diff}} \approx -\frac{V_{\text{FF}}}{2}\frac{4\pi}{\lambda}\delta x = -V_{\text{FF}}\frac{2\pi}{\lambda}\delta x \tag{9.3.5}$$

From this expression it is now possible to translate from a change in measured voltage into a small misalignment of the interferometer. The size of the displacement δx for a given voltage V_{diff} will be

$$|\delta x| \approx \left|\frac{V_{\text{diff}}}{V_{\text{FF}}}\right|\frac{\lambda}{2\pi} \tag{9.3.6}$$

Thus a small measured voltage can be related to a small displacement of the membrane in the probe arm. But this is only true in the case where V_{FF} has been determined reliably.

This is the 'full fringe' measurement which is basically a measurement of the interference overlap as it is changing from one position to the next on a sample. The reflection will be slightly different and the focusing will be slightly different as the probe beam is moved across a big sample, due to it not being perfectly horizontal. To remedy this, a measurement of V_{FF} could be doneat every sample point, but this would be impractical for a lot of sampling points. More pressing though, is that because the configuration changes from the vibrational measurement setup where the interferometer is locked, to the 'full fringe' measurement where it is not locked, there might be fluctuations of V_{FF} that are not measured. This is because the measurement is not done in parallel with the vibrational measurement. To solve this, a calibration scheme was deviced.

Calibration signal

A calibration signal is created by applying a reference modulation on the piezo of the mirror in the reference arm, which will show up as a calibration peak in the vibrational spectrum. The magnitude of this reference peak is then used to reference the 'actual' V_{FF} taken into account the changes in the conditions of the experiments since the independent measurement of V_{FF}. In the experiment this means that V_{FF} is measured at the initial position, as well as the calibration peak, and this measurement is then the reference for all the next sample points.

The reference piezo can be driven to relatively high frequency while still introducing a large displacement that is strong enough to be measured as a modulation of the interference signal on an oscilloscope. The comparison between the two different ways of measuring the same modulation is shown in**fig. 9.8a**. First in the time domain on the fast oscilloscope, and then compared with the peak height at the modulation frequency in the FFT derived spectrum, measured with the same settings as when the actual measurements are performed. Firstly it is interesting how more amplitude is transferred with frequencies about 230 kHz. The piezo is specified to have a fundamental resonance frequency at 63 kHz, and as this changes slightly when the piezo is subjected to stress in the mount, it is thought that the peak can be ascribed to a harmonic of the fundamental resonance of the piezo. As these measurements are done with the interferometer lock engaged, lower frequency modulations do not make sense to measure, as the lock will counteract the motion of the reference arm mirror that is introduced. The lock was designed to have a characteristic frequency of 76 kHz. In this context this means that the gain of the locking circuit is 0 dB for 76 kHz and then drops off for higher frequencies. This is designed as such exactly to not interfere with a calibration modulation around 250 kHz, which is also one of the reasons for choosing 250 kHz as beeing the calibration frequency. This is also around the highest frequency where the piezo response is such that a calibration peak could be measured with a high signal-to-noise ratio while being driven with a 10 V ramp signal from a signal generator.

Regarding the interferometer lock it should be noted that although the 0 dB gain operation is with signals at 76 kHz, the response of the piezo effectively works as a low pass filter so the effect of the lock should be completely negligible at the calibration frequency. It can then be assumed that the calibration peak is independent of the locking circuit.

It is worth noting that at a modulation of 250 kHz the displacement of the reference arm piezo is so small that the modulation of the interference signal is only a few mV from the locking level on the oscilloscope. At this low level the noise due to different sources is starting to become a significant factor, and it was clear that the measured RMS did not reflect the actual displacement. This explains the 250 kHz measurement in **fig. 9.8a**.

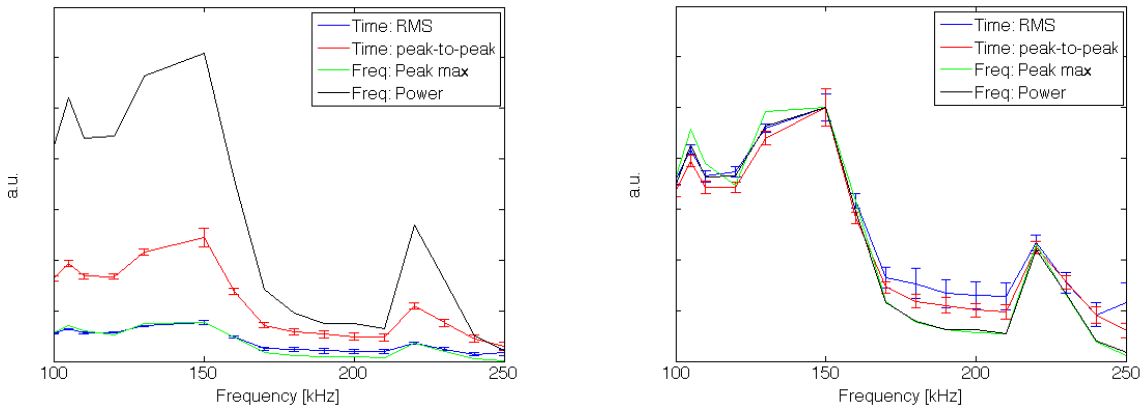

(a) Unnormalized reference piezo response.

(b) Normalized reference piezo response.

Figure 9.8.: Response of the piezo in the reference arm when driven with increasing frequency. The response is measured both as the interference signal modulation compared to the full fringe amplitude V_{FF}, and as the peak power in the Fourier space. There is a good correlation up until 250 kHz where the reponse of the PZT gets very low and difficult to measure precisely. Error bars not shown for power in frequency space, as the spectrum was the result of a long measurement in time.

If the reference piezo is swept a distance longer than an interference fringe, the amplitude V_{FF} can be determined. As the displacement range of the PZT decreases with higher driving frequencies, this is not possible at the frequencies where the reference modulation needs to be perfomed. However if the 'full fringe' voltage is determined at low modulation frequencies (say 100 Hz) a given amplitude that is measured with a higher ν_{mod} can be compared to this. This is only true under the assumption that the response of the detector system and amplifiers do not change from the low frequency regime to the frequency range of the vibrational mode frequency that is under investigation. For mechanical systems with less than 1 MHz vibrational modes this is deemed a good approximation using the current 10 MHz detector scheme, but this is not obvious for e.g. the nanomembranes with 4 MHz mechanical modes and higher.

As an example the relation between a peak height in the spectrum and the amplitude measured in the time domain is roughly a V^{-1} in the example shown in **fig. 9.8a**. As the displacement in absolute units can be infered directly from the time domain measurement, this calibration meakes the conversion of the peak power to a displacement possible. But for this the A and V_{offset} needs to be determined at low frequency.

9.3.2. Measurement of *full fringe* amplitude

The reference arm piezo can be driven by a signal generator at low frequency in order to measure the full fringe amplitude. A frequency of about 100 Hz is found to present a good compromise between speed and acquisition. The voltage amplitude of the differential signal is then measured and V_{FF} can be determined. This full fringe measurement is then measured once during an acquisition run, and if the interferometer is locked and a calibration peak is added, the power in the calibration peak is compared with the reference measurement.

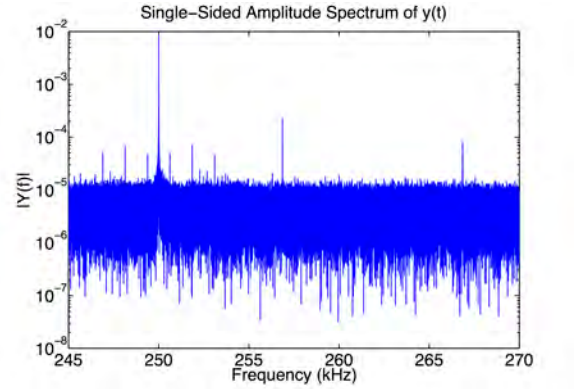

(a) Spectrum around calibration and fundamental frequency.

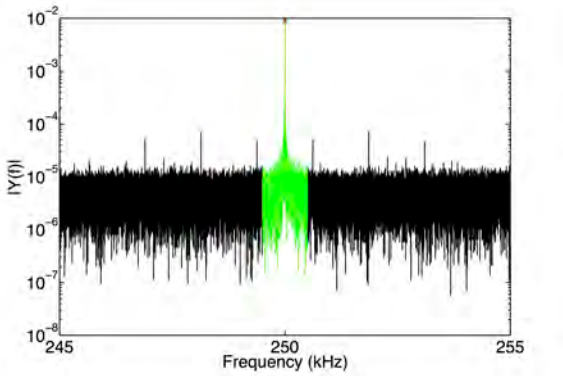

(b) Calibration peak with integration interval indicated.

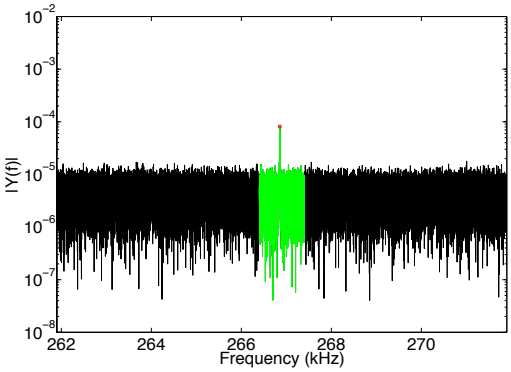

(c) Brownian motion peak with integration interval indicated.

Figure 9.9.: Example spectrum with no agitation of the mechanical modes. Clear sidebands are visible due to the agitation repetition. The sample was a 1 × 1 mm SiN membrane coated with aluminum. The green indicate the area of integration.

9.3.3. Example calibration spectrum

In **fig. 9.9** an example spectrum is shown. The system investigated was a 1 × 1 mm SiN membrane coated with aluminum with a fundamental frequency of about 266 kHz. The measurements were done with a sample rate of 2 MS/sec for 5 seconds with a 500 mV/div gain and a timebase of 500 ms/div on the oscilloscope. The calibration peak was added using a Tektronix signal generator that added a 250 kHz sine function to the lock output.

The ratio of the measured power in the calibration peak in **fig. 9.9b** and the brownian motion peak in **fig. 9.9c** is needed in order to calibrate the displacement in the brownian motion peak. The integration range is chosen to be as narrow around the peaks as possible in order to not include the sidebands. In this case sidebands of 700 Hz are very prevalent, hinting a modulation source of unknown origin.

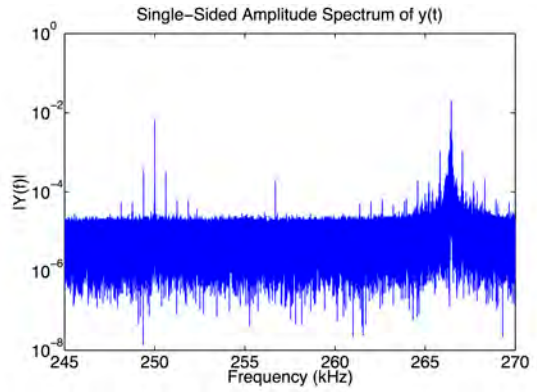

(a) Spectrum around calibration and fundamental frequency.

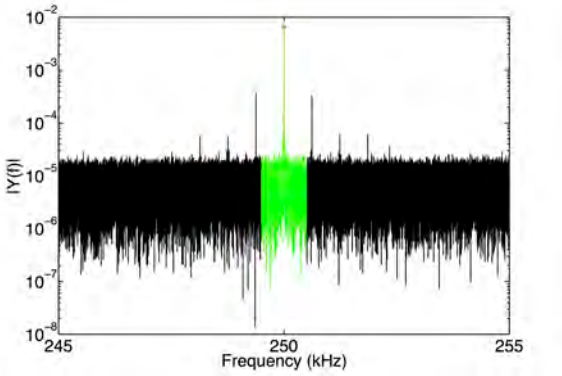

(b) Calibration peak with integration interval indicated.

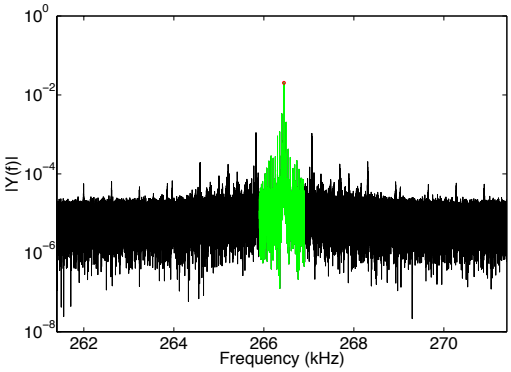

(c) Brownian motion peak with integration interval indicated.

Figure 9.10.: Example spectrum with agitation of the mechanical modes. The sample was a 1 × 1 mm SiN membrane coated with aluminum. The green indicate the area of integration.

9.4. Interferometer setup

In **fig. 9.11** parts of the interferometer setup is shown. The interferometer itself is mounted on a small table to minimize the size and the coupling to other mechanical noise sources on the optical table. Thick 1.5 inch poles are used for mounting the small table. In order to make the setup as dynamic as possible both the probe arm and the reference arm are fiber coupled to enable the coupling to different probe heads. Additionally it could be possible to extend the setup with fiber coupled devices such as an electrooptic modulator or an acoustooptic modulator in a later iteration. Future possibilities are described in **9.7**. The probe head is shown in **fig. 9.11b** and consists of an ultra stable 3 dimensional moving mount with a fiber coupler and microscope objective mounted. The modular design means that the probe head can be moved to different positions without affecting the rest of the interferometer.

9.4.1. Imaging

The imaging is done with a CMOS camera mounted on a stand by itself. In **fig. 9.12** a picture of the setup is shown. The camera is connected with a number of lenses for magnification and image the light returned from the cryostat reflected by the beamsplitter. The beamsplitter is a 92:8 ratio beamsplitter (i.e. 92 % transmission) and is indicated as BS in **fig. 9.12**. The sample is mounted in the cryostat and the microscope objective is chosen such that the probe beam becomes small, while realizing a good compromise of working distance, magnification and compatibility with the cryostat. The objective is described in **chap. 9.4.2**. The illumination of the sample with visible light is made with a ring of green miniature SMD LEDs around the input of the probe laser. This method of illumination is practical for freeing up space at the objective – cryostat interface. However the illumination is not perfect as the center of the imaged area is not visible. This is not a big problem as the probe laser of course can be chosen to be in this area and this provides some hint as to the position of the sample. Dependent on the need an alternative configuration is with the LED ring mounted on the objective at the very interface between the objective and the cryostat. This provides excellent illumination of the sample, but reduces the travelling distance available without scratching the cryostat top glass with the LEDs.

What has not been described is the quarter waveplate that is indicated as WP in **fig. 9.12**. The need for this in the probe arm is described in **chap. 9.2.2**.

9.4.2. Optics

The specific microscope objective bought is indicated *in situ* in **figs. 9.12,9.13** and is the type

Nikon objective MRP05422
CFI Achromat LWD 40X C
N.A. 0.55, W.D. 2.7-1.7 mm
Cover glass correction: 0-2.0 mm

The choice was a compromise between the requirements of cover glass correction to achieve a gaussian beam on the sample, a high numerical aperture (N.A.) which results in a very small diffraction limited spot in the focus, and a large working distance (W.D.) because of the relatively thick

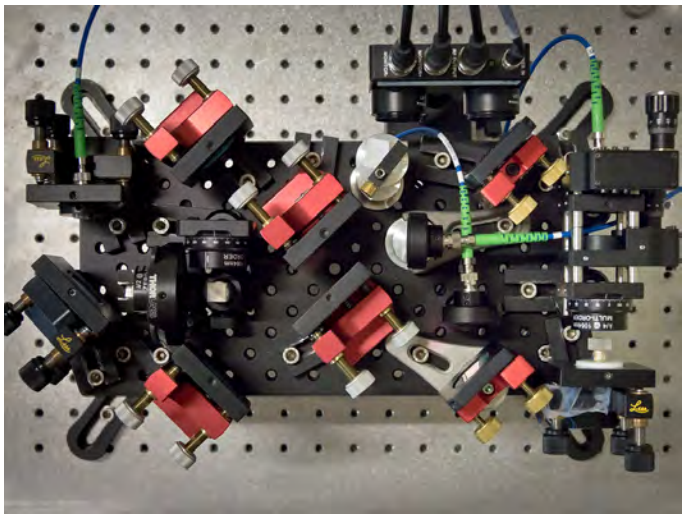

(a) The interferometer seen from above. The detector in this image is a 1 MHz balanced detector used for priliminary testing.

(b) The probe "head" with optics mounted on a translation stage with 3 degrees of freedom.

Figure 9.11.: Interferometer parts.

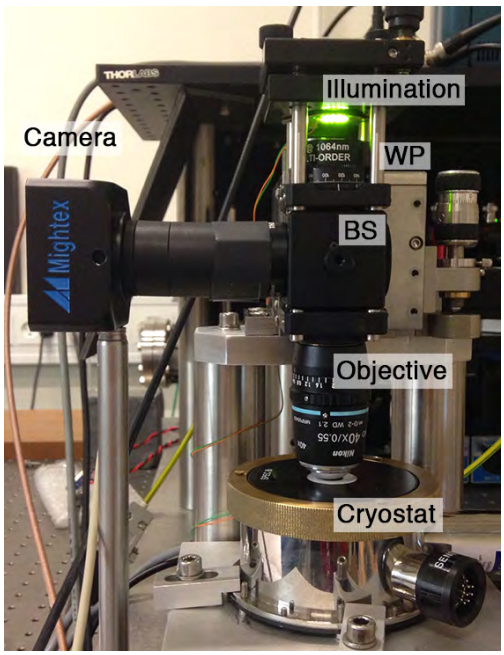

Figure 9.12.: Illumination setup. The probe arm and the imaging setup. A ring of green LEDs is placed around the fiber collimator for illumination.

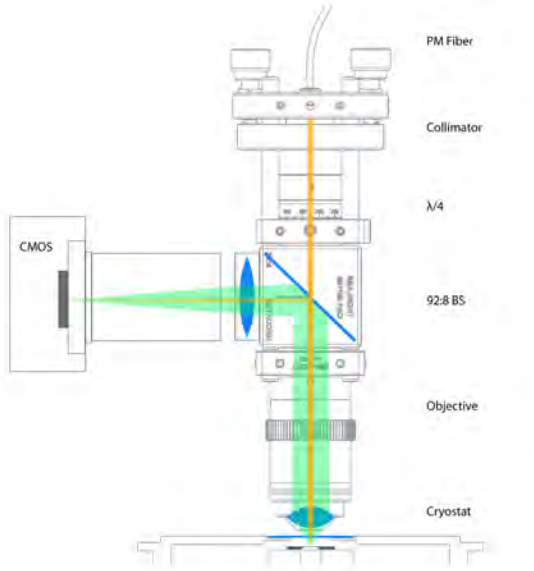

(a) Schematic of the imaging for the alternative illumination scheme. The green area indicate the imaging path while the orange line indicate the probe beam.

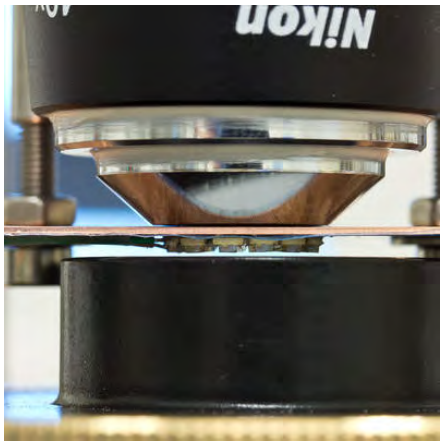

(b) Alternative illumination system with LEDs mounted on the microscope objective.

(c) Alternative illumination system with LEDs mounted on the microscope objective.

Figure 9.13.: The alternative illumination scheme. The LED is mounted right on the microscope objective.

cover glass through the cryostat. The glass for the cover is specified by Oxford Instruments as: *QOVC05HR2 Cryostat top plate with 0.5 mm thick, 10 mm diameter optical access, Spectrosil-B fused quartz window*. With this objective the plane of focus i about 0.5 mm into the cryostat depending on the configuration and achieves a small beamspot. It seems that the choice of objecive was adequate.

9.4.3. Agitation

It is possible to agitate the vibrations of the sample with an external source and this is achieved by an externally mounted PZT crystal that is mechanically clamped to the setup mount. It is then in direct mechanical contact with the sample. A periodic chirp is applied in the frequency range around the mechanical resonance, and a rise in signal of up to 40 dBm was witnessed when turning on this agitation. Of course this is not the optimum configuration and the group has had success with mounting a PZT inside the cryostat in close proximity to the sample. This yields a much stronger response, and enables the agitation of higher frequencies.

In **fig. 9.14** an example of the possible agitation of a mechanical peak is shown. The fundamental resonance of a 1 $\times$ 1 mm aluminum coated SiN membrane measured using no agitation in **fig. 9.14a** and then a agitation was applied in **fig. 9.14b**. In this example an increase in peak power of about 4 times was achieved. The rise in spectral energy at the peak position with the agitation confirms that the peak is mechanical in origin. It is possible to overlap a peak of unknown origin with the agitation frequency and be fooled into believing that the peak is enhanced, while it actually is just the combined energy of the two noise sources that is measured. Thus it is only sure that it is mechanical in origin if it can be agitated, so that it is driven at its resonance frequency. It is also possible to get hints of the origin of a peak by how it drifts with changes in temperature or light power.

In **fig. 9.14** it is noted how the agitation proceedure has added a lot of sidebands to the mechanical peak. This was due to the way the agitation signal was made with a periodic chirp with a repetition rate of 20 ms, resulting in effectively a low frequency component to the agitation. To avoid this it is possible to mix a single frequency sine with a gaussian function and thus introduce some spectral width to the agitation signal, which results in less problems with sidebands, but it was found sufficient for the time being to just agitate with a single frequency. This was also the case because of the large SNR for the mechanical peaks for the testmembrane, which rendered the agitation more a nuisance than a plus. Thus the agitation was mainly used as a hint to prove that the peaks were indeed mechanical, and not to measure anything specific while agitating.

9.4.4. Hysteresis and creep of piezo crystal

It is well known [PI] that piezoes exhibit a hysteresis in displacement when driven with a periodic, e.g. sinusoidal, voltage. This means that the first excitation period result in a larger displacement than the subsequent periods. The amount of hysteresis increase with increasing voltage but is not expected to exceed 15% [PI] under maximal driving signal. However this should be expected to reach a equilibrium displacement amplitude quickly after a small number of periods, and thus should not influence an average measurement of the displacement fourier component at the driving frequency. Another effect is called creep where a fixed position of the piezo can change displacement slowly. This is however expected to be over times on the hour scale, and anyway only less

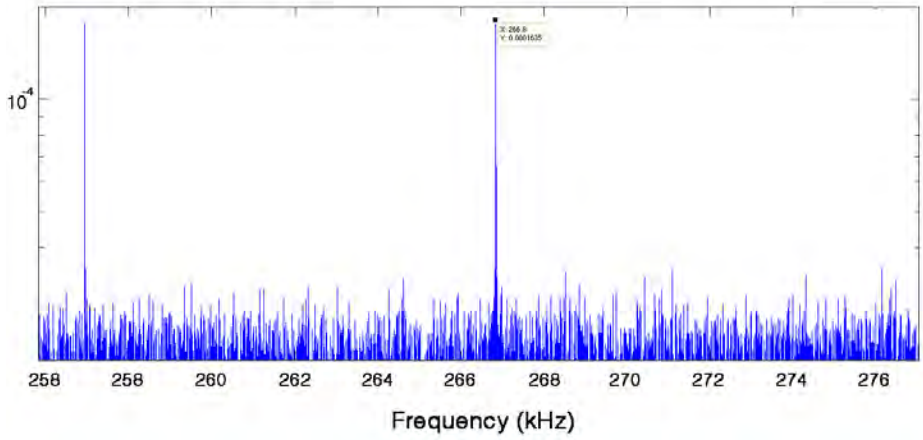

(a) No agitation.

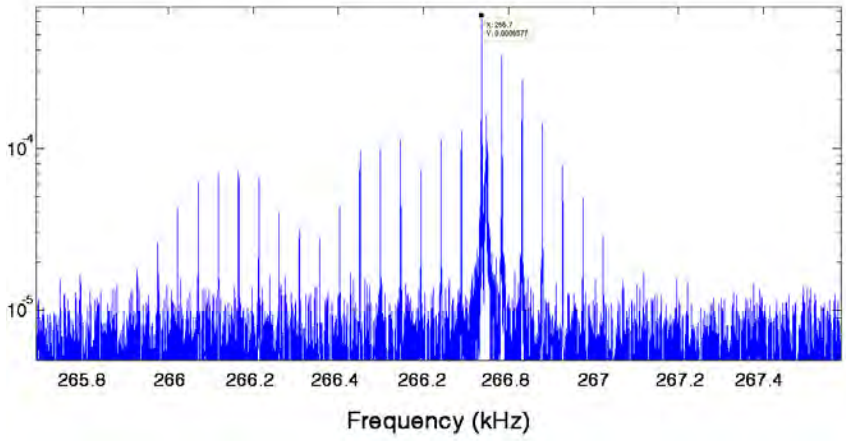

(b) With agitation.

Figure 9.14.: Agitation of mechanical peak. The agitation was done with a 2 ms repetition rate resulting in sidebands.

than a % in length, and is thus then not really influencing the considerations for a periodic motion setup.

There is also the consideration of whether a change in the displacement is perfectly linear in the applied field strength, which is of course not the case. One talks about Stroke vs. Electric Field Strength nonlinearity [Nol]. This would change the transduction signal to include a nonlinearity in the amplitude of the drive A_d. Because the PZT in the reference arm is controlled with a lock built using an operational amplifier with a $\pm$ 15 V output, and the calibration signal is generated using a 10 V_{pp} sinusoidal signal, this is les than 10 % of the maximum driving voltage of the specific PZT, and it is then a fair approximation to assume the response to be linear.

9.5. Measurements

In this section examples of measurements will be described and the performance of the interferometer will be evaluated.

9.5.1. Examples of measurements

In **fig. 9.15** a test system for the verification of the interferometer performance is shown. It is a 1 mm $\times$ 1mm and 50 nm thick stoichiometric SiN membrane, selectively coated with a 200 nm thick aluminium layer, so that only SiN is in the center. A thorough measurement of the power in the fundamental vibrational mode with a $\nu_m \approx 270$ kHz was performed over a dense grid.

A calibration peak at 250 kHz was introduced through a phase modulation as described in **sec. 9.3** and the measured spectral density power in the calibration peak, can then be compared to the thermal noise peak. In this case the fundamental vibrational mode was agitated using an external piezo crystal driven with a frequency sweep around the mode, and thus it was not limited to brownian motion. In **fig. 9.16** the example measurement for this system is shown, with **fig. 9.16** representing the resulting vibrational profile. Interestingly the center point shows a dip both in the mechanical peak power in **fig. 9.16a** directly and in the calibration peak power in **fig. 9.16b**, but in the ratio of these two in **fig. 9.16c** it is not visible.

Example measurements of three lowest energy modes of an aluminum coated membrane such as shown in **fig. 9.15** are shown in **fig. 9.17**.

9.5.2. Calibrated measurements

Using the methods described above it was possible to map out the different mechanical modes of the sample systems. The next step is then to create a calibrated displacement map of the membrane motion. An example of such a calibrated measurement is shown in **fig. 9.18**. The full membrane is scanned with a 5 MHz sample rate and the power in the peak is established.

The displacement was determined using **eqn.** (9.3.6)

$$|\delta x| = \left|\frac{V_{\text{diff}}}{V_{\text{FF}}}\right| \frac{\lambda}{2\pi} \tag{9.5.1}$$

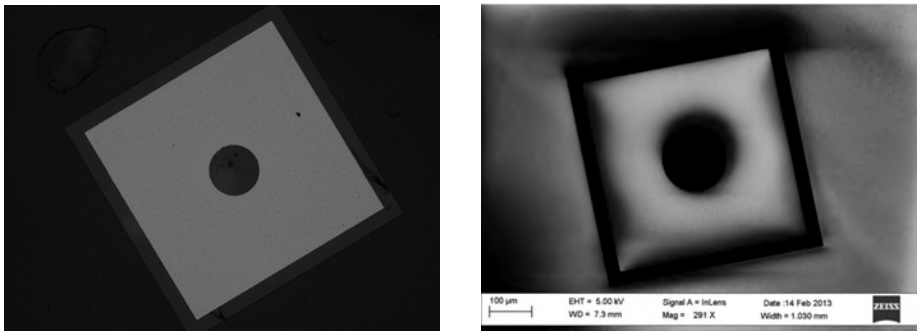

(a) Example microscope picture of SiN membrane coated with aluminium.

(b) SEM picture of a similarly aluminum coated SiN membrane.

Figure 9.15.: Two interferometer example system.

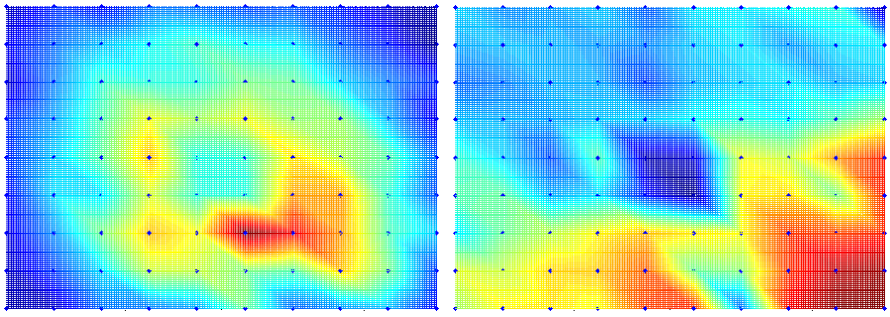

(a) Mechanical peak power.

(b) Calibration peak power.

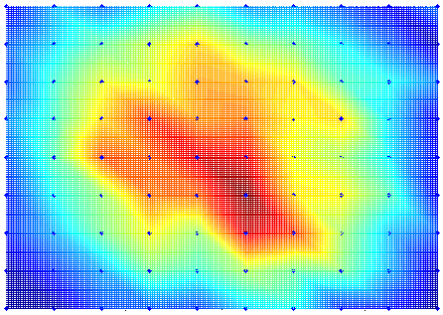

(c) Displacement field given as the ratio of the power in the mechanical peak vs. the calibration peak.

Figure 9.16.: Example interferometer measurement. The main shape of the fundamental resonance is visible. The black points indicate measurement positions, while the triangular shape is due to the chosen interpolation algorithm, and as such is not physical.

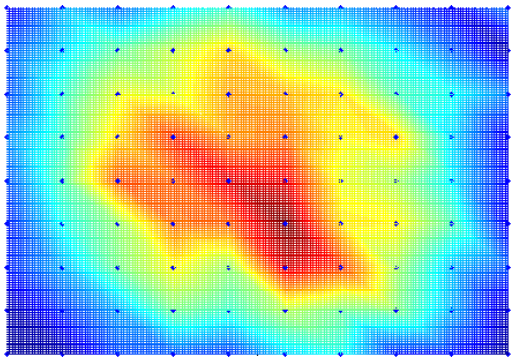

(a) (1,1) 266 kHz Mechanical/Calibration

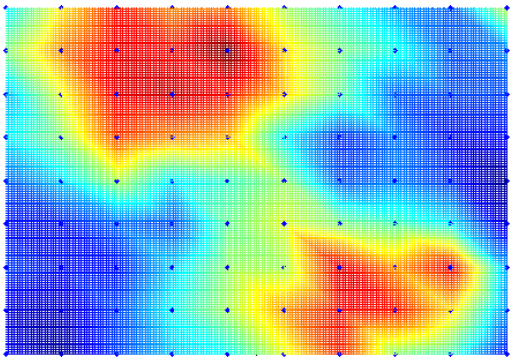

(b) (1,2) 407 kHz Mechanical/Calibration

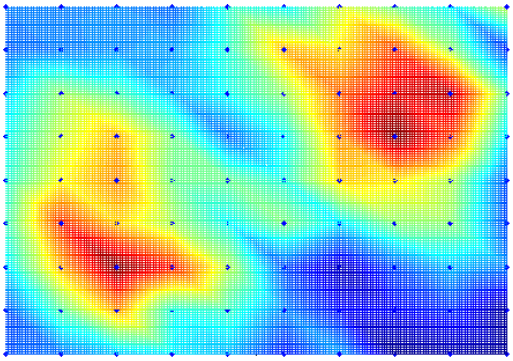

(c) (2,1) 408 kHz Mechanical/Calibration

Figure 9.17.: Interferometer mappings of the alumembrane. The black points indicate measurement positions, while the triangular shape is due to the chosen interpolation algorithm, and as such is not physical.

where the full fringe measurement of V_{FF} was done at an initial reference measurement. It is then denoted V_{FF}^R to make this clear. Because of the added calibration peak at 250 kHz, it is possible to refer subsequent measurements back to the reference measurements. If the variance in voltage in an interval around the calibration peak is denoted $\langle V_{\mathrm{cal}}^2 \rangle$ at a measurement point on the sample it can be referred back to the value that was in the calibration peak at the reference position, $\langle (V_{\mathrm{cal}}^R)^2 \rangle$. Then the effective full fringe measurement at a measurement point can be determined by

$$V_{\mathrm{FF}} = \sqrt{\frac{\langle V_{\mathrm{cal}}^2 \rangle}{\langle (V_{\mathrm{cal}}^R)^2 \rangle}} V_{\mathrm{FF}}^R \tag{9.5.2}$$

where the squareroot comes from the relation between light power and voltage. **eqn.** (9.3.6) can be rewritten in terms of the variations in displacement $|\delta x| = \sqrt{\langle x^2 \rangle}$ and $V_{\mathrm{diff}} = \sqrt{\langle V_{\mathrm{diff}}^2 \rangle}$ by realizing that this is what will be determined in the experiment. Insertion of V_{FF} in **eqn.** (9.3.6) leads to

$$\sqrt{\langle x^2 \rangle} = \frac{\sqrt{\langle V_{\mathrm{diff}}^2 \rangle}}{\sqrt{\frac{\langle (V_{\mathrm{cal}}^2 \rangle}{\langle (V_{\mathrm{cal}}^R)^2 \rangle}} V_{\mathrm{FF}}^R} \frac{\lambda}{2\pi} = \frac{\sqrt{\langle V_{\mathrm{diff}}^2 \rangle}}{V_{\mathrm{FF}}^R} \sqrt{\frac{\langle (V_{\mathrm{cal}}^R)^2 \rangle}{\langle V_{cal}^2 \rangle}} \frac{\lambda}{2\pi} \tag{9.5.3}$$

For the measurements presented in **fig. 9.18** the reference full fringe measurement was determined as $V_{FF}^R \approx 12.6$ V. This measurement was done simply by sweeping the interferometer, and measuring a timetrace of a second to determine the peak to peak voltage. In future experiments this measurement will be repeated a couple of times in order to prove that the value does not change as the interferometer is locked and then swept again. Additionally the variation of V_{FF}^R should be measured as a deviation on this reference measurement propagate to the displacement amplitudes.

It is noted how the displacement measurement shown in **fig. 9.18a** show a definite shape of the (1,1) vibrational mode, and also that the frame around the membrane is seen to be discernable. As the frame is stationary at this frequency, this is essentially a measurement of the noise floor for this measurement, and it is determined to be on the order of 3 pm in this measurement. This is then the limit of the displacement that is detectable. The (1,1) mode is very visible with the highest displacement in the center of the mode as expected, but a large variation in displacement is found between neighboring sample points on the membrane. Comparing with the measurement of the aluminium coated membrane shown in **fig. 9.17**, the mode shape look much more noisy. The spatial sampling density is much higher for this calibrated measurement. The sampling time of 2 seconds per spot was the same for both measurement, so it is not due to a difference in this.

Several possibilities are now available for presenting the calibrated displacement amplitude in **fig. 9.18a**. A spatial average of the data gathered makes the measured mode shape look more as expected, but this introduce the variable of how many sampling points to average, and this has not been done here. Alternatively it can be used that the mode shape is known in advance for this specific (1,1) mode. Indeed the sample was characterized using the Vibrometer first, so it was established that it was moving as expected. If it is assumed that the (1,1) is measured and the mode function then follow the standard form of **eqn.** (3.2.17), it is easy to fit the measured data with this mode shape. A fit with this mode shape is shown in **fig. 9.18b** where the displacement is subtracted the displacement of the stationary frame. The maximum displacement for this fitted mode shape

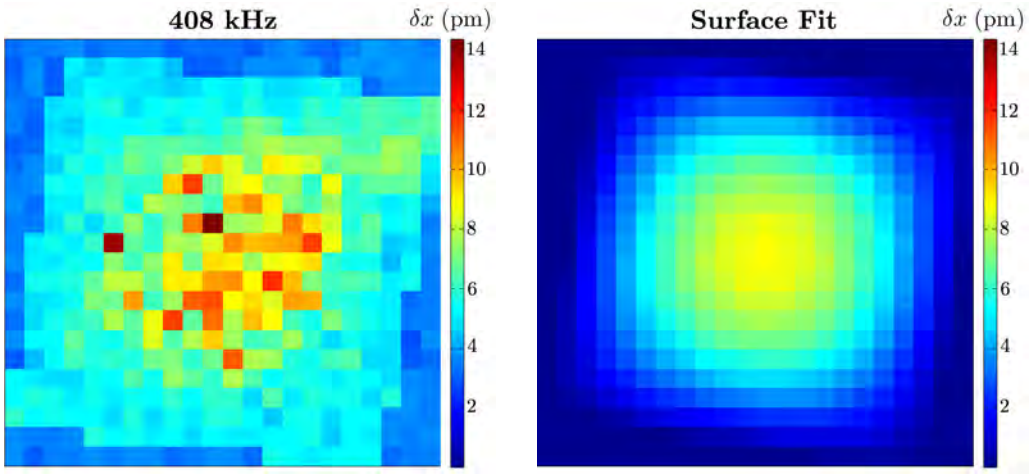

(a) Measured displacement amplitude.

(b) Renormalized fit, with the frame normalized to $\delta x = 0$

Figure 9.18.: Calibrated spatial map of the (1,1) mode for SiN membrane and the fit of the vibrational mode with a 2D sine function. Each pixel corresponds to a measurement position. It is noted how the frame is visible at the sides.

is then found to be 8.5 pm, which fits very well with the values measured in the Vibrometer for the same membrane. It has then been established that interferometer calibration scheme works and can be used for characterizing more interesting systems.

For a general structure where the mode shape cannot be taken to be known in advance, a spatial average is thought to be a better method. What is essentially done by spatially averaging is to measure longer at the same area of the membrane, and in this way the change in motional amplitude over long timescales are taken into account. This is more practical than measuring for a longer time at every point, as slow drifts of the system would then start to affect the results.

9.5.3. Signal

In this section the steps necessary to consider going from the motion of the membrane to a measurement of the displacement is discussed. It starts out from the motion of the membrane that is driven by thermal noise and light noise power on the membrane. If the displacement from equilibrium x_0 is described as x, the spectral density for the membrane motion is denoted as $S_{xx}(\omega)$. This is introduced in **sec. C.1**, but for now it is just stated as the Fourier transform of a two time auto-correlation function of the displacement. The power spectral density in displacement is

$$S_{xx}(\omega) = \int_{-\infty}^{\infty} \langle x(t)x(t+\tau)\rangle e^{-i\omega\tau} d\tau \tag{9.5.4}$$

As have been stated before back in **chap. 3** in **sec. 2.2.3** the RMS displacement of a typical system can be related to the effective mechanical mass, and the thermal energy of the heat bath it is con-

nected to. From this the typical motion is related as [Saulson90, Kippenberg07]

$$x_{rms}^2 = \frac{k_B T}{m\omega_m^2} = \int S_{xx}(x)dx \tag{9.5.5}$$

For a system such as an aluminum coated membrane the effective mass can be calculated. The system have dimensions 1×1 mm and a thickness of 50 nm SiN which is then coated with 200 nm of aluminum. The motional mass is then

$$\frac{1}{4}\left(\rho_{SiN} \times 50 \text{ nm} \times 1 \text{ mm} \times 1 \text{ mm} + \rho_{Alu} \times 200 \text{ um} \times 1 \text{ mm} \times 1 \text{ mm}\right) \approx 156 \text{ ng} \tag{9.5.6}$$

As stated in **sec. 9.1.1** such a system has a fundamental frequency of about 270 kHz and from this the RMS displacement is found to be

$$\sqrt{\langle x^2 \rangle} \approx 3.0 \text{ pm} \tag{9.5.7}$$

Now this displacement can be detected interferometely by the change in phase of the probe light that a displacement would introduce. The relation between the displacement x and the phase change ϕ is just

$$\frac{\partial \phi}{\partial x} = \frac{2\pi}{2\lambda} \tag{9.5.8}$$

where λ is the wavelength of the probe light. This can be understood as the transduction function converting from the displacement spectral density to the phase spectral density as

$$S_{xx}(\omega) \rightarrow S_{\phi\phi}(\omega) \tag{9.5.9}$$

It is customary to write this up as a linear transformation $G(\omega)$ so that $S_{\phi\phi}(\omega) = |G_{x\phi}(\omega)|^2 S_{\phi\phi}$ as noted in [Wilson11] and **sec. C.1**.

With the displacement information transferred into phase information it is possible to detect this difference. Through the interference between the probe and the reference arm of the interferometer the phase information is transferred into a change in photocurrent, ΔI. This can be written as

$$S_{\phi\phi}(\omega) \rightarrow S_{\Delta I \Delta I}(\omega) \tag{9.5.10}$$

with $S_{\Delta I \Delta I}(\omega)$ being the photocurrent spectral density for the detector. The transfer function for this will be dependent on the interference contrast and the balancing of the interferometer as well as the responsivity of the chosen detector. While the interference contrast can be made almost perfect, the choice of the reference power is a more tricky question. See **sec. 9.6.2**.

In order to measure the generated signal the induced photocurrent is transferred into a voltage

$$S_{\Delta I \Delta I}(\omega) \rightarrow S_{VV}(\omega) \tag{9.5.11}$$

and this transfer is going to be dependent on the quantum efficiency of the detector, η, as well as the gain and noise profile of the detector. $S_{VV}(\omega)$ is then the spectral voltage density. The chain of detection is then

$$S_{xx}(\omega) \rightarrow S_{\phi\phi}(\omega) \rightarrow S_{\Delta I \Delta I}(\omega) \rightarrow S_{VV}(\omega) \tag{9.5.12}$$

It is clear from this chain of transformations that a lot of calibration is necessary in order to establish all the transfer functions to fully understand the processes, and in **eqn.** (9.5.12) the chain is only written up for the steps from displacement to the voltage density on one detector.

In the experiment the voltage signal is actually stemming from two detectors each measuring a part of the signal and then fed to a difference amplifier, further increasing the number of steps that need to be characterized. Additionally the response of the measurement equipment, e.g. an oscilloscope should also be included. In the experiment the calibration was done in a more ad-hoc fashion as described in **sec. 9.3**.

What is measured in the experiment is the variance of the voltage in a sampled time. This is transformed to frequency space and into the units of V^2/Hz. The variance of the voltage squared in a frequency window around the resonance frequency is then found $\langle V^2 \rangle = \int S_{\text{VV}}(\omega) \frac{d\omega}{2\pi}$. This is what is determined by integrating the frequency domain spectrum around the resonance peak.

Electronic detector noise

The noise due to the displacement of the sample is then be compared with the expected noise from the detector electronics and the shot noise of the probe light. The current spectral density due to electronic noise can be denoted $S_{II}^{noise}(\omega)$.

For photodetectors a commonly denoted metric for the electronic noise level is called the noise equivalent power, *NEP*. The detectors used in the interferometer setup are 2 standard Thorlabs PDA36A-EC, which have a nominated NEP Range (W^2/Hz) of $2.1 \times 10^{-12} - 7.7 \times 10^{-11}$ depending on the gain. For the specific gain setting of 0 dB used to get a 10.0 MHz bandwidth, the noise is rated to have a 280 μV RMS, and the NEP to be 2.91×10^{-11} W/$\sqrt{\text{Hz}}$ at the tested wavelength of 970 nm. The responsivity is rated as $\mathcal{R} = 0.35$ A/W for 1050 nm. The responsivity can also be written as [Hobbs09]

$$\mathcal{R} = \frac{\eta e}{\hbar \omega} \tag{9.5.13}$$

with e being the elementary charge, and η specifying the quantum efficiency. From this the quantum efficiency can be found as $\eta = \mathcal{R}\frac{hc}{e} \approx 0.4$ at 1064 nm. The NEP is equal to the noise spectral density [Richards94], which is the power spectral density of the electronic noise, divided by the responsivity, NEP = $S_{VV}(\omega)/\mathcal{R}$.

$$\text{NEP} = \frac{\sqrt{S_{VV}(\omega, \Delta\omega)}}{\mathcal{R}} \tag{9.5.14}$$

in W/$\sqrt{\text{Hz}}$. The NEP is basically the signal power required to obtain a signal to noise ratio of 1 in a 1 Hz bandwidth. The 2.91×10^{-11} W/$\sqrt{\text{Hz}}$ rating is then optical power needed to obtain a SNR of 1 in a 1 Hz bandwidth. Another way of approaching it is to say that 2.91×10^{-11} W/$\sqrt{\text{Hz}}$ is the optical power on the detector at which the light noise and electronic noise are equal.

Another way to see it is that the optical power, needed to measure light shot noise would be

$$\frac{\text{NEP}^2}{\eta \omega \hbar} \approx 15 \text{ mW} \tag{9.5.15}$$

which is rather a high power. The detectors saturate with an optical power around 20 mW so this gives a nice power interval where it is possible to measure light noise. In the experiment it is unfortunately not a good idea to have a strong power in the probe arm, as a large power will heat the sample. The laser is chosen to be 1064 nm wavelength which makes the aborption smaller than it would be for a shorter wavelength, but as there still is an effect it which can be measured as a frequency change on the order of 100 Hz for e.g. a 412 kHz resonance frequency. The change is very small (less than a promille), but detectable. Since the frequency change is explained with local heating changing the effective spring constant, it is undesirable to measure with strong probe power. Thus the power is adjusted so that the total power on detectors are close to saturation power, and this is achieved by having a large power in the reference arm. This turns out to still increase the signal from the membrane in a scheme described as *homodyne detection*. It is described below in **sec. 9.6.2** why this works.

The next question is then what is measured, and with what sensitivity. Even though the optical power on the detector is more powerful than the denoted NEP it still needs to be investigated how much signal comes from the light. This is shown below in **sec. 9.5.3**.

In the experiment the electronic noise power in the interesting frequency range is established in a simpler fashion. The noise level in the interesting frequency range is first measured with no illumination. The interesting frequency range will be in some frequency range around where the signal to be measured is expected. If the detector is illuminated the measured noise will increase depending on the frequency range, and the properties of the detector. If the noise level in the interesting frequency is increasing with light power it can be claimed to be limited by the light noise. Thus as long as the light power is much higher than the noise level where the light power is the same as the dark noise level the measurement can be said to be limited by shot noise. See **sec. 9.6.2**. If the light is modulated in power with a frequency ν_{mod} that is in the interesting frequency range, a peak will appear in the measured frequency range, and be measurable.

Light noise

For such a balanced homodyne detection scheme the light is split on a perfect beam splitter and two photodiodes are used to measure the photocurrents and a difference signal is generated electronically from these. If the probe arm is blocked the difference photocurrent is a measure of the light noise level of the reference arm. [Hobbs09, Bachor04, Saulson90]. Thus the balanced detection scheme makes the detection of the light noise limit compared to the actual noise easy. The sum of the two photocurrents from the detectors have the same noise as e.g. the reference arm directly on a detector.

A measurements of this is shown in **fig. 9.19** using the optical power settings used for the experiments. The interference from the interferometer is measured with the locking circuit actively keeping the $\Delta L = \lambda/8$. A calibration signal is added to the reference arm with a frequency of 250 kHz, and the measured peak is obvious in the figure in the blue trace. The blue trace is a measure of the noise in with the interferometer locked in the normal operation state. The yellow trace denote the same with the probe arm blocked, showing the contribution due to the probe arm. The purple trace shows the noise when no light is impending on the photodiodes. The noise due to light noise is apparent as the blue and yellow trace are about 3 dB higher in measured power than the case with no light. This is verified up to about 3 MHz for this configuration with the electronic noise following the same curve as the light noise for higher frequencies. As no apparent difference is found between the blue and the yellow trace, the setup was then not limited by light noise for

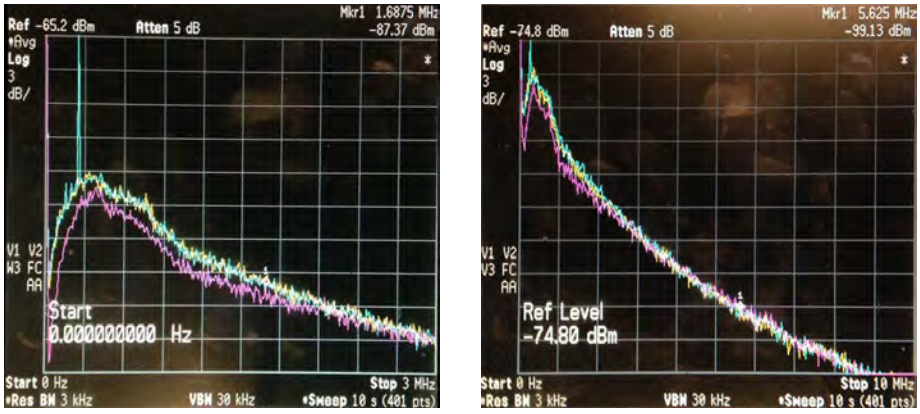

(a) Light noise measurement from 100 kHz up to 3 MHz

(b) Light noise measurement up 100 kHz to 10 MHz

Figure 9.19.: Performance of the interferometer. The blue trace denotes the normal running performance with the probe arm hitting a mirror. The calibration peak is obvious. The yellow is with the probe arm blocked and it is seen how the calibration peak is gone as now interference between the arms are allowed. The noise is the same as with the probe arm open, indicating that a lot less power is in the probe arm than in the reference man. With no light hitting the detectors the purple trace is measured. It is measured that at most the interferometer can detect about 3 dB of light noise for frequencies less than 3 MHz.

higher than 3 MHz.

In order to make a claim about being shot noise limited, an investigation of the light power dependence on the scaling of the measured light noise is needed [Bachor04, Hobbs09]. Unfortunately such an investigation has not been done meticulously, and as such this cannot be claimed. From the noise measurement in **fig. 9.19a** it looks like there is several peaks in the light noise compared with the purple electronic noise. The laser used for the setup is a Nd:YAG laser [Innolight] and the relaxation oscillation in these lasers have a strong contribution of classical noise at around 800 kHz, depending on the injection current. The balanced detection of the setup removes a large part of the classical input noise, but maybe what is measured here is what is not removed. As most noise sources are not flat in $1/\nu$ it seems likely that at least some of the 3 dB of light noise shown in **fig. 9.19a** is due to shot noise. This is also backed by that the light power was higher than the 15 mW that was estimated to be the limit for being shot noise limited in **eqn.** (9.5.15). In order to more fully be able to understand the sensitivity of the instrument, it is need to determine the exact origin of the noise floor in the interesting bandwidth. This will be done for the next generation of balanced detector, which is already installed at the time of this writing.

9.6. Optimization

A number of techniques have been employed to improve the sensitivity of the instrument and the resistance to noise from various sources.

9.6.1. White light position

An optimization technique that has been employed in the setup is to try and find the so-called *white light position*. As will be shown the interferometer is much less sensitive to noise in the phase and frequency of the input laser at this position, and thus it is worth thriving for. As noted before the output power from the interferometer will be

$$P_{out} = |E_{out}|^2 = 2|trE_0|^2(1 - \cos(2k\Delta l)) \tag{9.6.1}$$

with Δl denoting the path length difference between the two arms. The condition for the wavelength fluctuation is sought in terms of the membrane motion.

By identifying the fringe pattern as a function of the path length difference Δl from this expression, it is clear that the condition for destructive interference and thus a dark fringe is that the path length difference is an integer multiple of the wavelength as

$$\Delta l = n\lambda_n/2 \tag{9.6.2}$$

where n is an integer, and λ_n denotes the wavelength corresponding to the nth dark fringe. By defining the nth wavelength $\lambda_n = 1064\,\text{nm}$, it is possible to find the wavelength corresponding to the adjacent fringes. Thus it is possible to find the laser wavelength noise that would lead to a "jump" from one dark fringe to the next. This noise is what is sought to be minimized to go to the white light position. The difference in wavelength for two fringes is denoted $\Delta\lambda = \lambda_n - \lambda_{n-1}$. A change in wavelength due to laser fluctuations is denoted $\delta\lambda$ and can be required to be much less than

$$\delta\lambda \ll \Delta\lambda\frac{\delta\phi}{2\pi} \tag{9.6.3}$$

where $\delta\phi$ is the phase fluctuations, and 2π comes from the phase change from one dark fringe to the next. If this was not true, the laser wavelength fluctuations would be bigger than the fringes.

The principle is indictated in **fig. 9.20**. Laser frequency/phase noise is shown as waves with slightly different wavelength. At exactly $\delta l = 0$ all different wavelengths overlap perfectly at the bright fringe indicated at origo of the coordinate system. From this figure it should be clear why it is called the white light condition, as it is the only configuration where spectrally white light will interfere.

The linear spectral density of the 1064 nm Innolight Mephisto laser is rated at about 10 $\text{Hz}/\sqrt{\text{Hz}}$ at a kHz [Innolight]. Unfortunately the frequency noise is not specified for higher frequencies, because these lasers are traditionally sold to groups with setups such as for the gravitational wave community, where a lower frequency is interesting. The linear spectral density of the frequency of the output from the laser should be much smaller than the difference between two fringes (here leniently just stated as the variance of the frequency, $\delta\nu$)

$$\delta\nu \ll \Delta x\frac{c}{\lambda^2}\frac{1}{n+1} \tag{9.6.4}$$

which can be rewritten as

$$(n+1) \ll \frac{\Delta x}{\delta\nu}\frac{c}{\lambda^2} \tag{9.6.5}$$

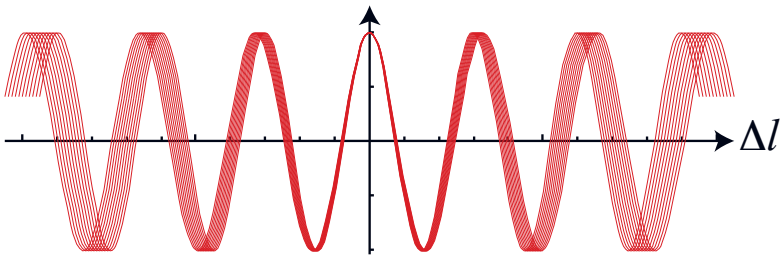

Figure 9.20.: The white light condition. Waves with different wavelengths correspond to phase noise in the laser, and they all overlap at the whitelight condition. If the arm length difference Δl is zero the intererometer is then neglecting the phase noise.

which can be shown to yield a criterion of

$$\delta L \ll 2650 \times \lambda_n \approx 2.8\,\mathrm{mm} \tag{9.6.6}$$

This rough estimate makes it seem possible, albeit optimistic, that the interferometer is built with the arm length difference being close to the white-light condition. The path length difference was measured as precisely as possible, but attemps to prove interference using a spectrally wide light source was discontinued due to technical problems.

For a good description of the various methods employed to minimize different noise sources the reader is referred to [Oblak09].

9.6.2. Homodyne detection

A *homodyne* detection is a method for enhancing a signal buried in noise. The term homodyne refers to that the reference signal is derived from the same source as the probe signal, and is defined in contrast to *heterodyne* detection where the reference signal is derived from another source. In the case for am interferometer homodyne refers to that reference arm and the probe arm stem from the same laser and neither is frequency shifted afterwards. The reference arm then functions as a *local oscillator* [Saulson94, Bachor04].

As shown in **sec. 9.2.1** the detection is actually designed using *balanced detection* where two photodetectors each measure part of the signal, and the difference between the two photocurrrents is then what is measured. The difference between a balanced interferometer and balanced detection should be noted. Balancing in regards to the interferometer as a whole refer to the power ratio in the interferometer arms, and the interferometer is said to be balanced for $E_R = E_P$. Balanced detection is implemented using the polarization degree of freedom in the interferometer and the balancing can thus be controlled easily by the manipulation of a $\lambda/2$ waveplate before a PBS before the 2 detectors. The output of the detectors is connected to a differential amplifier and the balancing is then performed to minimize the difference signal.

In the case where the interferometer is not *balanced* the amplitude of the fields in the reference arm and the probe arm are different. These are introduced as E_R and E_P for the reference arm and

probe arm respectively in **sec. 9.2.1**. Now from **eqn.** (9.2.2) the field at the output can be written

$$E_R(t) = \frac{i}{2} E_R e^{i(\omega t - 2kL_R)} \tag{9.6.7a}$$

$$E_P(t) = \frac{i}{2} E_P e^{i(\omega t - 2kL_P)} \tag{9.6.7b}$$

or by combining these in a single field E_{out} this could be described

$$E_{out} = \frac{1}{2} i e^{i\omega t} \left(E_R e^{-i2kL_R} + E_P e^{-i2kL_P} \right) \tag{9.6.8}$$

$$= i e^{i(\omega t - kL_R - kL_P)} \cos(kL_R - kL_P)(E_R + E_P) \tag{9.6.9}$$

The output power will be $P_{out} = |E_{out}|^2$ which from **eqn.** (9.6.9) becomes

$$P_{out} = \left| i e^{i(\omega t - kL_R - kL_P)} \cos(kL_R - kL_P)(E_R + E_P) \right|^2$$

$$= \cos^2(k\Delta l)(E_P^2 + E_R^2 + 2E_P E_R) \tag{9.6.10}$$

where again $\Delta l = L_R - L_L$. If the output field was detected using a photodetector the induced photocurrent would be proportional to P_{out} from **eqn.** (9.6.10).

If the output signal is measured using balanced detection instead the situation changes. The output field E_{out} is led through a $\lambda/2$ waveplate and is split on a PBS before the photodetectors. The waveplate is optimized to a fixed 45 degree angle to optimally interfere the light from one arm with the light from the other. As one arm is chosen to be horizontally polarized and the other vertically polarized this means that the field amplitudes at the photodetectors, $D1$ and $D2$, are

$$E_{D1} = \frac{1}{\sqrt{2}} E_R(t) + \frac{1}{\sqrt{2}} E_P(t) \tag{9.6.11a}$$

$$E_{D2} = \frac{1}{\sqrt{2}} E_R(t) - \frac{1}{\sqrt{2}} E_P(t) \tag{9.6.11b}$$

where the phase shift due to the PBS has been included. The photocurrent from the detectors will then be proportional to the optical power as

$$I_{D1} \propto |E_{D1}|^2 = \frac{1}{2} \left(|E_R(t)|^2 + E_R(t)E_P(t)^* + E_P(t)E_R(t)^* + |E_P(t)|^2 \right) \tag{9.6.12a}$$

$$I_{D2} \propto |E_{D2}|^2 = \frac{1}{2} \left(|E_R(t)|^2 - E_R(t)E_P(t)^* - E_P(t)E_R(t)^* + |E_P(t)|^2 \right) \tag{9.6.12b}$$

So far so good. Assuming that these photocurrents can be fed to a piece of equipment that outputs the difference between the photocurrents[10] the differential photocurrent, I_D, can be defined as

$$I_D = I_{D1} - I_{D2}$$

$$\propto E_P(t)E_R(t)^* + E_R(t)E_P(t)^* = 2|E_P(t)E_R(t)| \tag{9.6.13}$$

[10] The actual implementation with the conversion from the induced photocurrent to the voltage measured on a differential ampflier is not included here. In the experiment the detectors are switchable gain Thorlabs Si photodetectors that use a transimpendance amplifier to convert the signal.

where the subtraction removed the offset powers $|E_R(t)|^2$ and $|E_P(t)|^2$. By insertion of the full field expressions from **eqn.** (9.6.7) the difference signal will then reduce to

$$I_D \propto 2E_P E_R \cos^2(k\Delta l) \tag{9.6.14}$$

This is a remarkable result that shows how the difference signal from a balanced detection scheme scales with E_P and E_R. An increase in the field strength in the reference arm, $|E_R|^2$ will enhance the signal from the motion of the sample, and enable the detection of the motion of a mechanical system without having to use a high power probe beam as the reference beam can be made relatively strong to compensate. This is one of the advantages of the homodyne balanced detection system.

Another advantage is inherent in the balanced detection in that it cancels out the intensity fluctuations that the input light might have. These enter the interferometer as common mode noise and are thus subtracted by the differential measurement. Additionally the phase noise of the input laser is reduced significantly as the same phase noise enters both arms and thus also is dampened by the differential measurement.

In the experiment the alignment of the polarization degree of freedom is optimized using the waveplate before the PBS at the detectors. However it is necessary to correct this balancing when changing the configuration of e.g. the power balancing in the two arms, or the total power. This imperfection is probably due to a small misalignment of the polarization of the fibers in the two arms, as well as slightly different quantum efficiencies and gain profiles for the two detectors. The balancing is optimized by turning the waveplate until the difference signal is measured to be about zero.

9.7. Interferometer outlook

The working interferometer has been built and used to characterize different samples. The quick change from one sample to another is an obvious benefit for the interferometer, instead of having to couple the sample to a mirror and use the cavity transmission scheme as was the custom before. It is the easiest way to work with samples such as the nanomembrane or other samples that have no transmission path, and would be harder to couple a cavity to. The interferometer will indeed be useful in the future, and can be combined with new projects such as the search for the deformation potential cooling in the next generation of GaAs membrane heterostructures as described in **chap. 7**, and for systems made for optical refrigeration, **chap. 10**, as well as the other optomechanical investigations going on in *Quantop*.

An obvious extension of the present interferometer setup would be to introduce a phase modulation scheme in the reference arm of the interferometer. Different schemes are possible. For a phase modulation device (e.g. an EOM) in both arms it would be prudent to introduce a phase shift of ϕ_m in one arm and $-\phi_m$ in the other. The scheme that is used in the Polytec MSA-500 Vibrometer is the same as we have implemented but with a an AOM that introduces a shift to high frequencies [Pol]. This is useful as a lot of the electronic noise is a lower frequencies and such a heterodyning scheme transfers the information into a higher frequency range. Aditionally the phase information gathered can be used to They use it to determine which way the vibration goes, by shifting to 40 MHz and detecting the shift.

In the more immediate future, it is the plan to replace the photodiodes with a more sensitive configuration. A device containing 2 fast photodiodes and embedded AC coupled differential amplifier

has been purchased to achieve higher sensitivity. It is a Thorlabs PDB420C-AC InGaAs balanced photodetector package with a bandwidth of 75 MHz. With the specifications provided the NEP is equal to the light shot noise at around 100 μW of optical power. This is a much better sensitivity than the detector combination noted above.

The interferometer has proved to be working well with the calibrated mapping of the Brownian motion for sample systems. Now the time is to use this setup for characterizing more difficult samples such as the nanomembranes, as well as the next generation of optomechanical systems in *Quantop*.

Part V.

Outlook

The pursuit of cooling with light

While the optomechanics community has been fighting over the quest for the cooling to the ground state of the vibrational modes, there is another less famous push towards trying to cool the bulk temperature of materials using laser light. The method is called *optical refrigeration* and is theorized as utilization of a slightly red-detuned laser that is absorbed by the emission of phonons in the material, and subsequent emission of blue-shifted light that then removed thermal energy from the material. This had been shown in rare-earth doped metal doped glasses and crystals [Sheik-Bahae04, Epstein09] but at the time of this project it had not been shown in semiconductors. This was a natural pursuit as the need for new methods of cooling electronics is always needed, and an optical way could enable the aplication in optoelectronic devices and in devices where e.g. convection cooling is impossible. An often cited example is on board of satelites traveling in the vacuum of space.

Below is outlined how optical refrigeration might be possible in these nano- and microstructures shown in this thesis. Interestingly it was shown very recently in [Zhang13] that net cooling was possible in a semiconductor nanostructure by a group from Singapore. Their work is using 2-6 group materials CdS and is thus different than the 3-5 materials of GaAs, but very much corroborate that a structured nanosample is a good approach to show net cooling.

This is good news for the field as a whole. With added focus and research that will come new possibilities will be available.

It is also a good indicator for the possibilities that an active material and a coherent interaction process give, and once again motivate the pursuit towards utilizing the processes that e.g. QW embedded GaAs structures enable.

10. Optical refrigeration

As described above optical refrigeration in semiconductors is a fascinating possibility. Here the idea, as would be realized in QW heterostructures are presented.

10.1. Optical refrigeration / bulk effects

An example of the optical refrigeration scheme is illustrated in **fig. 10.1**. It is described in [Hoyt03, Sheik-Bahae07, Epstein09] and is an ambitious goal to realize in semiconductor devices.

The cooling cycle is illustrated in **fig. 10.1**. The goal is to achieve so-called *anti-Stokes fluorescence*, where the pump light creates an excitation that ultimately lead to emission of light with slightly higher energy. Electrons in the top of the valence band are excited optically to the bottom of the conduction band where they thermalize by coupling to phonons. If the energy of the pump light is slightly less than the band gap energy of the semiconductor the structure can only absorb photons by the coupling to phonons. The energy of the pump photons determine the amount of energy removed from the system by coupling to phonons, and in the ideal case the excitation decay through spontaneous emission with an energy lower than the energy of the pump photons. Say the pump photons have the energy $h\nu$ and the emitted photons have a mean energy of $h\nu_f$ (floures-cence), then the energy removed is $h\nu - h\nu_f$. The cooling power is then assumed to scale with the absorbed power. This is however not the case in a simple semiconductor as the excited carriers couple back to phonons and then heats the structure. If it was possible to make these excitations exit as photons it would remove thermal energy from the system. The emission is hampered by total internal reflection for high refractive index semiconductors as well as simple non-radiative decay.

Very strong optical refrigeration have been shown in glass materials doped with rare-earth donors [Hoyt03, Epstein09]. Recently in [Seletskiy12] cooling to 155 K was achieved in ytterbium-doped fluoride crystal (Yb3+:YLiF4), while 110 K was presented in [Seletskiy10]. While fascinating in itself, the potential applications for achieving bulk cooling in semiconductors are obvious and motivates the search for this effect in GaAs. As optical refrigeration of CdS by 40 K was shown in [Zhang13] for nanowire structures, this is a fascinating time.

Cooling power

By defining the absorbed power as P_{abs} the cooling power can be found as

$$P_{cool} = P_{abs}\frac{h\nu_f - h\nu}{h\nu} \tag{10.1.1}$$

and the efficiency is then $\eta = P_{cool}/P_{abs}$. From **eqn.** (10.1.1) it would be expected that lower photon energies would would be more efficient but as the absorption also decrease a compromise have to be made.

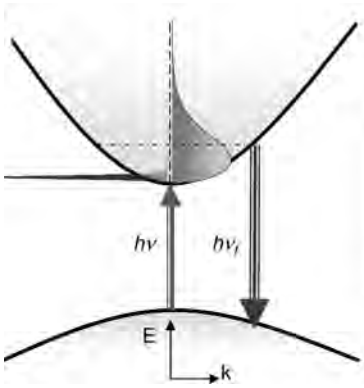

Figure 10.1.: Cooling cycle with the pumping laser with energy $h\nu$ being absorbed by the absorption of a phonon mode and the upconverted carriers are emitted with energy $h\nu_f$. The electron distribution in the valence band is shown with gray. Reproduced from [Epstein09].

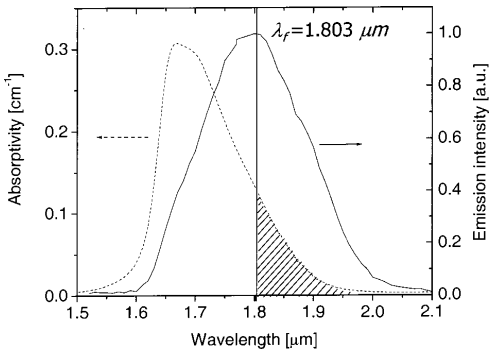

Figure 10.2.: Absorptivity and fluorescence spectra from [Hoyt03]. The dashed area is where pumping should lead to cooling. The mean flourescence wavelength is indicated with λ_f.

The practical energy range is on the order of thermal energy (k_BT) because of the ground-state Boltzmann distribution. The energy-gap law states that multiphonon emission rate is inversely proportional to the exponential of the energy difference between the initial energy state and the state that the excitation decay into [Harrison10].

As shown in **chaps. 5, 7, 8** the carrier lifetime in GaAs is very short, and most of the excitation couple directly to heat in the lattice. However tricks can be played by creating a more complicated heterostructure with QWs, and with the right design it might be possible to achieve optical bulk cooling.

Quantum Well structures

A possibility for making sure the excitations in the lattice do not turn into heat by the recombination on surfaces or impurities, is to excite the system in a confined QW structure. This was proposed in [Rupper08, Epstein09] and elsewhere. Non-radiative recombination is a combination of defect trapping and surface recombination. With no surfaces available for the excitations, the non-radiative decay should be less using QWs if it was possible to excite these semi-resonantly, but if the surfaces are not passivated they will dominate the non-radiative decay and QWs will not help significantly.

Unfortunately the conclusion presented in [Epstein09] is that because the radiative recombination is greatly reduced in QW structures compared to bulk, netto cooling of the whole structure is impossible, as there is simply not enough light removing energy. This is of course only based on an estimate, and hopefully the problems of parasitic absorption can be mitigated by designing the structure. The first demonstration of netto cooling in a semicondcutor by optical refrigeration in [Zhang13] was achievable by using thin nanoribbons of a few micrometers in with. This small structure made the coupling between the excited excitons and optical phonon modes of the ribbon strong enough that energy could be removed.

While optical refrigeration is a hard problem, and not immediately possible to achieve in the GaAs structures investigated in this thesis, it is very possible that the knowledge gained from the design of the 2 QW heterostructure described in **chap. 8**, and the tunability of the design will make the next step towards optical refrigeration GaAs clear.

Possibilities for enhancement of the radiative decay of the blueshifted light have been discussed. It might be possible to fabricate a heterostructure with a cavity embedded. This could be done via fabrication of a Bragg mirror, or alternatively a small mirror could be placed above the sample. As the main problem is to get the blueshifted light out of the system without decaying non-radiatively, a cavity designed with a narrow bandwidth at the proper wavelength would help to Purcell enhance [Purcell46, Hansen09] the radiative decay out of the system. If this was possible yet another improvement could be by the design of another cavity to aid in the absorption in the QWs, which would enhanced by the cavity finesse.

Another approach would be to limit the available states in the material by fabricating a photonic crystal band gap structure. This could be designed to force the excitation to exit the system as light, as it cannot propagate in the photonic crystal [Joannopoulos08].

Consequences for optomechanical systems

The coupling of the scheme for optical refrigeration with the possibilities of optomechanical systems might enable new avenues for cooling semiconductors. Some different approaches for estimating the temperature were discussed in **sec. 7.4**, and and understanding of the interplay between the vibrational degrees of freedom and the bulk temperature could lead to the combination of optical refrigeration for bulk cooling, and simultaneous vibrational cooling through deformation potential coupling. The ultimate goal is then to reach the mechanical groundstate using all optical cooling in a designed heterostructure.

11. Conclusion and outlook

In this thesis the work on optomechanical coupling in semiconductor vibrational systems have been described.

Initially a setup was built for characterizing mechanical samples and venture towards realising a membrane-in-the-middle setup inspired by [Thompson08]. By a nice chance the Lodahl group fabricated 160 nm GaAs membranes while making photonic crystal structures, and while trying to characterize these some very chaotic behaviour was witnessed when the probe power was more than 50 μW. With this discovery the project moved from a 'trival' characterization to a hunt for the explanation of this behaviour, and it was found that not only did the GaAs membrane show instability behaviour, but some of the vibrational modes had an exceptional high mechanical Q_m with the largest of more than a million. This was published in [Liu11]. After a lot of research the optomechanical coupling was proven to be due to strong photothermal cooling in the GaAs membrane due to absorption, excitations of carriers from the lattice resulting in local heating and feedback from the cavity field. At the same time it was found that a coupling due to electron pressure in the membrane should also contribute to the coupling. The work on the identification of the coupling and cooling process was published in [Usami11, Xuereb12].

It became an interesting goal to try and find this electron pressure vibrational cooling and the author went to Zürich to study nanomembranes with a quantum well embedded. A lot of knowledge about these were gathered, but the main takeaway is that the confinement of excitations in the quantum well was still not strong enough. Thus the next generation of membrane structure has been designed, and hopefully experiments will soon show the many advantages of working with optically active and tunable functional structures in the field of optomechanics.

Finally the design and implementation of an interferometer for characterization of these kinds of optomechanical system were described. The system has been shown sensitive to the brownian motion of typical membrane structures and upgrades are underway that will make characterization of more difficult samples, such as the nanomembranes, possible.

It is fascinating to work with the design of systems combining the advantages of different systems such as embedded low dimensional structures as in quantum dots and quantum wells, with very different degrees of freedom, such as the vibrations of micromechanical systems. With the added tunability that heterostructures introduce by attaching biasing electrodes, the future is indeed very bright and interesting.

12. Timeline

This is not meant to be a complete list of all that has been going on in the membrane group, but rather give an idea about the activities during the experiments relevant to this thesis.

2008 Members: *Koji*, *Bo* and *Eugene*.

- Initial scheme
- Test setup with FP and membrane on table

2009

Tolga joins the project.

- **January** Transmission tests of mirrors.
- **February** Absorption test at Brewster angle.
- **March** Absorption test at Brewster angle. Cavity test.
- **April** Fiber coupling cavity.
- **May** Noise characterization of Ti:S. Trouble with Verdi.
- **June** Noise characterization of Ti:S. Vacuum chamber setup. Baking and Ion pump testing.
- **July** NewFocus iPico motors installed and setup.
- **August** Verdi trouble. Lock circuits for the brewster and tweeter improved.
- **September** *Andreas* joins the project. Characterization of the membrane mount with CCD camera and split-diode detector. Initial double pass AOM scheme for two colour setup.
- **October** Cavity mirrors characterized.
- **November** EOM characterized. Vacuum chamber setup. Trying to couple to cavity made of two mirrors.
- **December** Cavity implemented with 100 kHz linewidth and a finesse around 1200. Characterization.

2010

- **January** Characterisation of two-color setup
- **February** Transmission, Rebuilding of setup, Initial Ringdown measurements with membrane-mirror setup
- **March** Ringdown measurements using slope-locking. Found surprising frequencies for the vibrational modes compared to the literature. Unfortunately with too low SNR for the Pound-Drever-Hall locking. Attended the GRC conference on optomechanics in Galveston, Texas. Did not present any results but got to meet and talk to a lot of the prominent people

in the field, as well as refresh the memory of our optomechanical push at NBI.

- **April** Tried to perform ringdown measurements with Ti:S laser from Light table. Have to reestablish Lasing.
- **May** Did ringdown measurements with pump laser at 852 nm modulated with EOM. Found Q factors on the 10^6 scale for membrane number 2.
- **May** Ringdown measurements for the second SiN membrane. Problems with sending a necessary spectrum analyzer out for repair. Realization of a new deflection method with a sensitive split-diode for determining the vibrational modes.
- **June** First measurements on GaAs membrane from DTU Fotonik. Witnessed strange chaotic behaviour in the mechanical vibrations. It was found that this behaviour was due to the 852 nm laser pumping electrons above the band-gap in the GaAs and leading to violent chaotic vibrations at the different eigenmodes. Initial trials to determine the absorption of the GaAs at different wavelengths. Performed ringdown and spectral characterization of the vibrational modes.
- **July** Concluded that more precise method for determining the absorption was needed and started to construct cavity with 1064 nm laser. The GaAs sample should then be placed in the cavity. Unfortunately the laser from Clock lab proved not to be single-mode and thus this project was postponed. Showed signs of multimode cooling for increasing 852 nm pump light. Implemented frequency and intensity lock to the cavity.
- **August** Redid spectral and ringdown for a range of vibrational modes. Showing the cooling being most effective at the fundamental frequency and then less effective for higher modes.
- **September** Cooling of mechanical modes.
- **October** Nothing to report.
- **November** Cooling of mechanical modes. Wavelength dependence. Time resolved measurements.
- **December** Time resolved measurements. Chirp of modulations. Assymetry in cavity peak is detected.

2011

- **January** Time response after light cutoff. DC deflection measurement of the membrane.
- **February** Dependence of cavity resonance asymmetry on the membrane orientation. DC membrane deformation test. Temperature dependence of resonance frequencies. Absorption of GaAs 160 nm sample was measured, but only possible to put bounds on.
- **March** Cooling characterization. Detuning and detuning dependence. Position dependence.
- **April** Topographic characterization of GaAs and SiN membranes at DTU. Brownian motion calibaration and calibrated cooling measurement for paper.
- **May** New Vacuum chamber prepared. Position dependence of cooling with calibrated spectral method.
- **June** Decalcified the cooling sink of the Verdi pump laser. Probed membrane at different

positions.

- **July** Redone vibrational mode characterization. Shows a lower Q than earlier due to aging. Recognized 17 kHz mode as the (1,1) mode in contrast to the 23 kHz (1,2) mode.
- **August** Hunting for the 'elusive' time constant.
- **September** Lock-in response measurements of the membrane displacement on the modulated cavity driving at low-frequencies..
- **October** Time resolved 'kick' measurements on GaAs membrane. Reestablishing ringdown configuration.
- **November** *Dominik Vogel* visits the group.
- **December** *Andreas* goes to ETH Zürich to study GaAs micromembranes.

2012

- **January** *Dal Wilson* visits the group. Initial building of the monolithic SiN cavity. Andreas at ETH Zürich, building interferometer for GaAs micromembrane project.
- **February**
- **March** *Andreas* brings one of the micromembranes back to NBI. Initial charactization at DTU. *William* joins the group.
- **April** Cryogenic system implemented.
- **May** Ti:S in Cell lab coupled to the Dungeon.
- **June** Ti:S locked to cavity. *Dal* moves on to the Kippenberg group.
- **July** Design of interferometer finished. Ordering parts. New cryostat for next generation experiment ordered. *Andi* joins the lab as a master student.
- **August** Interferometer for mechanical characterization build. Microscopic setup build. New cryostat characterized and pumped. Moving toward PDH locking of monolithic cavity.
- **September** Continue to search for Q vibrational mode. Interferometer working but not with high enough visibility. *Anders* joins the group.
- **Oktober** Reason for interferometer trouble found to be different radial profile of the overlapping beam, which unfortunately required a rather big redesign.
- **November** Interferometer calibration scheme introduced. Change of piezo and characterization of aluminium coated SiN membrane with the interferometer.
- **December** Preparation for higher frequency measurements for going to the nanomembranes. *Albert* joins the group.

2013

- **January** Interferometer improvements. New turbopumps ordered for the interferometer setup.
- **February** Nanomembrane characterization in interferometer. Improvements towards high frequency setup.

- **March** *Koji* leaves the group.
- **April** Next generation of balanced detector for the interferometer purchased.

13. Appendix

A. The *big* GaAs membrane

In this chapter parameters and models for the "big" GaAs membrane are shown, that was the main study for **chap. 5**.

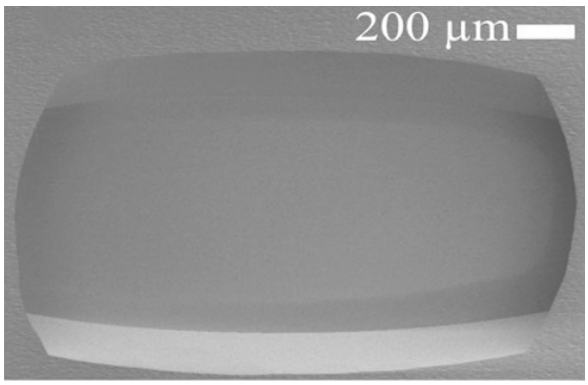

Figure A.1.: The "big" GaAs membrane

A.1. Material parameters of GaAs

Parameters from [Adachi85].

Density	ρ	5316 [kg m^{-3}]
Young's modulus	E	85.9 [GPa]
Bulk modulus	B	75.5 [GPa]
Poisson's ratio	ν	0.31
Coefficient of thermal expansion	α	5.7 $\times 10^{-}6$ [K^{-1}]
Heat capactity at constant pressure	C_p	550 [J kg^{-1} K^{-1}]
Dielectric constant[Strzalkowski76]	ϵ	13.08

A.2. Modeled mechanical modes

Using **eqn.** (3.2.16) the mechanical modes, ν_m, of the GaAs membrane is modeled to be (in unit [Hz])

(n,m)	**1**	**2**	**3**	**4**	**5**	**6**
1	16649.1	28792.3	41817.2	55102.	68495.6	81944.7
2	23600.	33298.2	45038.3	57584.7	70508.3	83634.4
3	31988.1	39686.9	49947.2	61500.2	73740.7	86377
4	40939.4	47200.	56102.7	66596.3	78041.6	90076.5
5	50153.1	55381.8	63141.3	72624.9	83245.4	94620.8
6	59507.6	63976.3	70800.	79373.7	89194.2	99894.5

Simple model of GaAs membrane mechanical modes.

A.3. Instability due to static thermal deformation

Following the supplementary material in [Usami11] and [Metzger04, Metzger08a] the static and dynamic behaviour for the GaAs membrane is studied. The photo induced for F_{ph} can be seperated as a static and dynamic part.

$$F_{ph}(t) = F_{ph}^{(0)} + \int_0^t \frac{dF_{ph}(t')}{dt'} h(t-t')dt' \tag{A.3.1}$$

with the time delay $h(t-t')$ being the response time between a change in cavity length, and the subsequent change in photoinduced force. The static part is denoted $F_{ph}^{(0)}$. It is assumed that the static deformation of the membrane due to $F_{ph}^{(0)}$ is proportional to the photon energy in the cavity as

$$\int_l^{l+L} \frac{1}{c}|E_{cav}(L,x)|^2 dx = \hbar\omega_l n_{cav} \equiv P_{cav}\tau_{rt} \tag{A.3.2}$$

with c denoting the speed of light, $E_{cav}(L,x) = E_2(L)e^{ikx} + E_2'(L)e^{ik(L-x)}$ is the field amplitude at position x in the cavity, P_{cav} is the optical power in the cavity, and $\tau \equiv 2L/c$ is the cavity roundtrip time for a photon.

The cavity detuning is the difference between the laser frequency $\omega_l/(2\pi)$ and the cavity frequency $\omega_c/(2\pi)$, is $\Delta = \omega_l - \omega_c$

$$P_{cav}(\omega_c) = \frac{(\kappa/2)^2}{(\omega_l-\omega_c)^2 + (\kappa/2)^2}\tilde{P}_{cav} \tag{A.3.3}$$

with the power in the cavity at the resonance with $\kappa/(2\pi)$

$$\tilde{P}_{cav} \equiv \frac{4|E_0|^2/\kappa}{\tau_{rt}} = \frac{2\mathcal{F}|E_0|^2}{\pi} \tag{A.3.4}$$

with $\mathcal{F}$ is the cavity finesse. The membrane deforms as a result of $F_{ph}^0 \propto n_{mem}$ and thus the cavity length L is indeed a function of the cavity power as

$$L(P_{cav}) = L + \delta L(P_{cav}) \simeq L - gP_{cav} \tag{A.3.5}$$

with g being the constant between the contraction of the cavity length, δL, and the power in the cavity, P_{cav}. Here it is assumed that L decrease with the power as the membrane deformas towards

the mirror, which is the case for the used orientation of the membrane with inherent bending. Now the spatial derivative of $L(P_{cav})$ is

$$\frac{\partial L(P_{cav})}{\partial L} = 1 - g\frac{\partial P_{cav}}{\partial L} \tag{A.3.6}$$

and this can be used to find the slope at the detuning used for the experiments. In the experiments the detuning is kept at $L - \tilde{L} = \lambda/(4\mathcal{F})$ where the cavity transmission is at half the maximum as at resonance of the cavity. Here $\tilde{L}$ is the cavity length when the cavity is at resonance.

$$-\frac{\partial P_{cav}(L)}{\partial L}|_{\text{cooling}} = \frac{\frac{\tilde{P}_{cav}}{\lambda/(2\mathcal{F})}}{1 - g\frac{\tilde{P}_{cav}}{\lambda/(2\mathcal{F})}} \tag{A.3.7}$$

The slope $-\partial P_{cav}/\partial L$ on the cooling side gets steeper and diverges as $\tilde{P}_{cav}$ approaches $\lambda/(2\mathcal{F}g)$ and this leads the cavity to be unstable. At the opposite detuning point $L - \tilde{L} = -\lambda/(4\mathcal{F})$ the dynamic instability (mechanical parametric oscillations) sets in. The slope here will be

$$-\frac{\partial P_{cav}(L)}{\partial L}|_{\text{heating}} = -\frac{\frac{\tilde{P}_{cav}}{\lambda/(2\mathcal{F})}}{1 - g\frac{\tilde{P}_{cav}}{\lambda/(2\mathcal{F})}} \tag{A.3.8}$$

and for this it is seen how the slope $-\partial P_{cav}/\partial L$ on the heating side becomes smaller as $\tilde{P}_{cav}$ aproaches $\lambda/(2\mathcal{F}g)$.

The steepening and softening of the slope on the heating and on the cooling side is the reason for the observed asymmetric cavity resonance shown in **fig. A.2**. When the speed of the scan of the cavity length is faster than the thermal timescale, $\tau_{th} \approx 10$ ms, the cavity transmission peak is measured as being symmetric as expected. When the speed of the scan is decreased so that the scan is slower than τ_{th} the effect of this steepening and softening of the slope is obvious in *b* in **fig. A.2**.

The mechanical instability onset is for $\tilde{P}_{cav} = \lambda/(2\mathcal{F}g)$ and for the case of $\lambda = 870$ nm and $\mathcal{F} = 10$ the instability sets in around 200 μW following [Usami11]. However experimentally it was found that the cavity input power has to be less than 50 μW. This discrepancy is attributed to the cavity lock not compensating perfectly for the instabilities in the system and thus introducing changes in the cavity mode as it moves back and forth on the slope. This introduces a change in the field intensity at the membrane, and the mechanical instability sets in for lower optical power than would be needed in the 'perfect' cavity lock case.

The found behaviour confirms that the instability mechanism is due to the static deformation of the membrane.

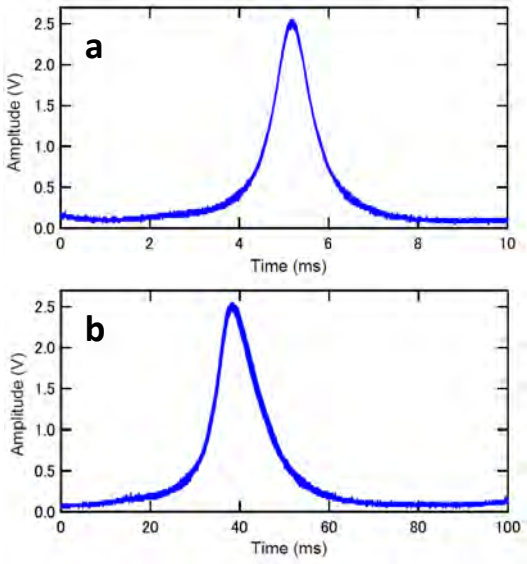

Figure A.2.: Cavity transmission signal with 200 μW input power (852 nm) measured while the cavity length is swept. In *a* the scan speed is fast compared to the thermal timescale, while in *b* the scan speed is slow compared to this timescale. The transmission signal is symmetric for high scan speed while for slow speed it is asymmetric. Reproduced from [Usami11].

A.4. GaAs membrane topology measurements

Topology measurements were done on a similar membrane from the same fabrication batch. The membrane was placed on a mount and situated beneath the microscope in the MSA-500 Micro System Analyzer available at DTU Nanotech. White light interferometry method was used [Pol]. The principle is that a very spectrally wide light source illuminates the sample and interferometry is done by moving a reference mirror. Computer software then analyzes the ripples in the captured images and combine these to a 3D model of the topography of the system. The light is a green LED so wavelength of about 530 nm but with a spectral width of many nm, i.e. 'white' light.

The objective for the interferometry was unfortunately not of appropriate magnification, which meant it was impossible to get the absolute strain of the whole structure. This problem means that although the height values are in principle absolute and could be compared, it is dangerous as there is no overlap between the measurement areas, and as the interferometry is optimized each time.

The light power of the probe light was characterized using a power meter set to 532 nm. It was found that the power was in small steps from below a single μW up to 325 μW. However as the beam of the LED was of the size of the so-called 'area-of-interest' of 776μm $\times$ 662μm, this still result in a small W/m^2. A quick estimate shows that the light power is 30 times less for this LED than for a typical 10 μ beam. The displacement was measured for many different powers and it was concluded that no significant dependence on light power was found, for the available light

powers.

Three characteristic measurements are overlaid on a micrscope image of the membrane. The measurement areas are chosen because they could be related to the microscope image by the characteristic 'pimple' defects that are on the sample. The red line indicates the line were the height is measured and shown in the graphs. The Y values indicated in the graphs are absolute distance, and as such it is shown that the membrane bends 700 nm over the 600 μm from the left edge towards the center. This is truly remarkable and a sign of the high tensile stress around the edges of the membrane. The right side of the membrane showns much more the behaviour that was expected with a minimum height at the edge and then a slight monotonic bending upwards. This bending is seen to be on the order of 80 nm which is still very high.

It is expected that the regions with the bubbles have the highest tensile stress as these are results of the etching process and form due to these energies. In **fig. A.3** is shown the 3D model for the topography of the left edge and the lower left corner.

It is clear from the strain in **fig. A.3** that the ripples signify a highly stressed region. It is also noted how the lower left corner without ripples show much smaller height than the rest.

From the combined measurements it is concluded that the left side is much more stressed than the rest and show a significant strain. Unfortunately it was not possible to judge the overall strain of the membrane as a measurement in the center just shows a bending of $\approx$ 10 nm but this is not to be trusted too much without reference to the frame.
Definitely the membrane is bending upward due to the tensile stress around the edges and not in a trival way. The one edge is much stressed than the other. The surprising feature is how strong this strain is.

It is assumed that the slight strain that is shown at the top and bottom is characteristic for all of the membrane, and that the left side with the ripples is then much more stressed and more displaced from the frame. Thus the there is an overall upward bending, with a local downward bending around the rippled left edge. This follows what was expected from our own measurements.

There was also performed measurements from the back side but these just confirmed the upward bending as found from the front.

As a detour the broken membrane on the same chip as the sample was also investigated. In **fig. A.5** is shown a 3D view of the shards on the edge of the broken membrane. It is truly remarkable how high the displacement of the shards is compared to the frame. Note that the 3D displacement is not to scale, but the color coding clearly shows how the edge of the small shard is more than 4μm above the frame. This is very extreme and again shows how much stress is around the edge of the membrane.

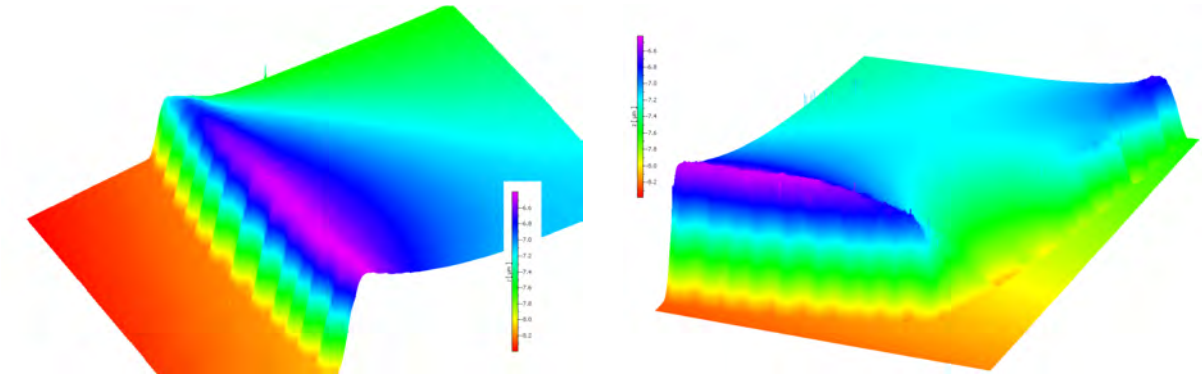

(a) Left edge (b) Lower left corner

Figure A.3.: Absolute topology measurements of the edge of the GaAs membrane. The colorbar is the calibrated height in μm.

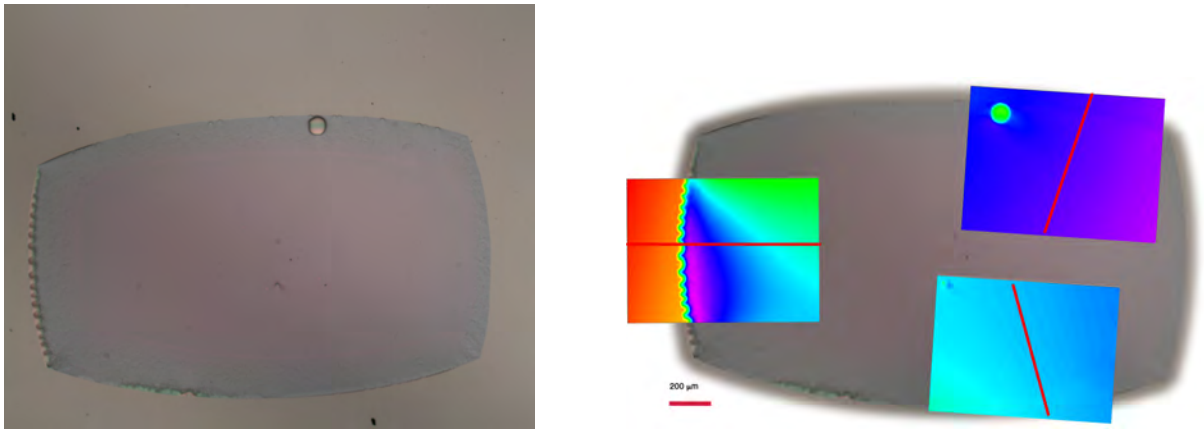

(a) Microscope picture (b)

Figure A.4.: Absolute topology measurements of the edge of the GaAs membrane. 200 μm indicated.

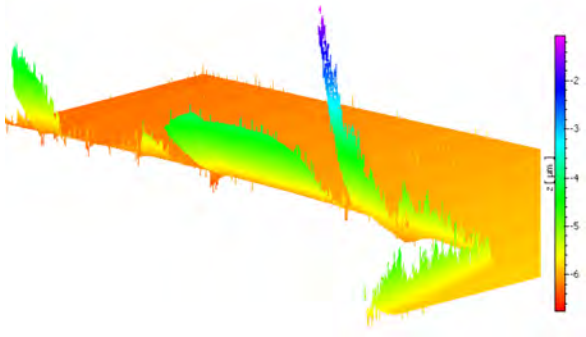

Figure A.5.: Broken membrane parts. A displacement of more than 4 μm is measured for one of the shards. This shows how strong a stress the membrane was under before it broke.

A.5. Estimates of local expansion

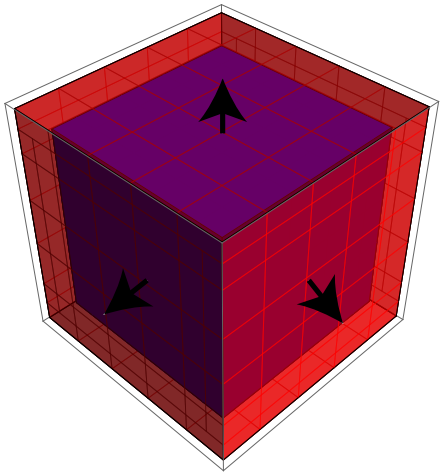

Figure A.6.: Thermal expansion. The blue box is assumed to expand homogenously in all directions.

The local thermal expansion can be estimated by assuming all the photon energy goes into heat through the non-radiative decay process at the surfaces or in defects in the bulk. Modeling the beam spot volume as a cubic box lead to a thermal expansion of

$$\frac{\Delta V}{V_0} = 3\alpha_L \Delta T \tag{A.5.1}$$

where V_0 is the initial volume, α_L is the linear thermal expansion (which for small deformations lead to the volume thermal expansion being 3 times α_L) and ΔT is the temperature change. The α_L parameter is on the order of 10^{-6} K^{-1} for most metals/semiconductors. Volumetric thermal stress (in units of energy) is given by [Thomsen86, Matsuda05]

$$\sigma_{th} = -3\alpha_L \left(B \frac{\eta_{abs} E_{ph}}{C_v} \right) \tag{A.5.2}$$

where B is the bulk modulus, η_{abs} is the absorption conversion factor, E_{ph} is the photon energy, and C_v is the heat capacity per unit volume. The expression for thermal stress can be approximated[11] as

$$\sigma_{th} \approx 0.8 \eta_{abs} E_{ph} \tag{A.5.5}$$

[11] The approximation done is $3\alpha_L B \approx C_v$ which holds for sufficiently small deformations. Using the bulk modulus of 75.5 GPa [Adachi85] and $\alpha_L = 6 \cdot 10^{-6}$ K, $C_{mass} = 350\mathrm{J}/(\mathrm{kg} \times \mathrm{K})$, the heat capacity per unit volume can be written

$$C_v = \rho C_m = 5.36\mathrm{g/cm}^3 \cdot 350 \times \mathrm{J}/(\mathrm{kg} \cdot \ \mathrm{K}) = 1.72 \times 10^6 \mathrm{J\ m}^{-3}\ \mathrm{K}^{-1} \tag{A.5.3}$$

with $C_m = \frac{C_v}{\rho}$ being the mass specific heat capacity. Using these parameters it is shown that the relation between $\alpha_L B$ and C_v is such that

$$\frac{3\alpha_L B}{C_v} = \frac{1.4 \times 10^6 \mathrm{K}^{-1}\mathrm{Pa}}{1.72 \times 10^6 \mathrm{Jm}^{-3}\mathrm{K}^{-1}} \approx 1 \tag{A.5.4}$$

where the fraction is indeed unitless. Thus it is shown how **eqn.** (A.5.2) can be approximated as **eqn.** (A.5.5).

by assuming small deformations due to the thermal stress. Again the unit is noted to be in energy. Expressing the bulk modulus through a pressure change ΔP, for a volume V and $\Delta P/\Delta V$ is the change of pressure for a change of volume, as

$$B = -V\frac{\Delta P}{\Delta V} \tag{A.5.6}$$

this can be used to relate the photon energy into thermal expansion. Following [Thomsen86] where E_{ph} is the photon energy absorbed and η_{abs} specify the conversion efficiency from absorbed E_{ph} to heat energy, the volume change

$$\frac{\Delta V}{V_0} = \frac{0.8\eta_{abs}E_{ph}}{B} \tag{A.5.7}$$

and thus for a given photon number the volume expansion by thermal expansion can be estimated. This can then later be used to describe the bending of a given membrane.

A.5.1. Estimate of the local expansion by electronic pressure

In regards to the deformation potential accompanied stress, the electronic stress is given by [Thomsen86, Matsuda05]

$$\sigma_{el} = -B\frac{dE_g}{dp} \tag{A.5.8}$$

with

$$\frac{dE_g}{dp} = -\frac{1}{B}\frac{dE_g}{d\eta} \tag{A.5.9}$$

where $dE_g/d\eta$ is the energy change of the energy band gap with the strain introduced by the deformation potential of the electron and hole. Note that η is not the same as in **sec. A.5**.

$$\frac{dE_g}{d\eta} = \frac{dE_c}{d\eta_{zz}} - \frac{dE_v}{d\eta_{zz}} \tag{A.5.10}$$

where v and c denote the valence, and conduction band. The terms $dE_c/d\eta_{zz}$ and $dE_v/d\eta_{zz}$ are found in the literature to be -5.3 eV and 2.7 eV[12]. This yields

$$\frac{dE_g}{dp} = -\frac{1}{B}\frac{dE_g}{d\eta} - \frac{1}{75.5\text{GPa}}(-8.0eV) = 1.06\times10^{-10}\text{eV}\cdot\text{Pa}^{-1} \tag{A.5.11}$$

The electronic stress can then be found in the same way as for above by knowing the absorbtion of photons generating the electron-hole pairs. As

$$\sigma_{el} = -B\frac{dE_g}{dp} \rightarrow 8.0\,\text{eV} \tag{A.5.12}$$

pr. unit volume, pr. photon. The $\rightarrow$ indicate that the magnitude is taken. For the test case of a r =5 μm radius spot with homogenous illumination the area is then $\pi r^2 d = 2\times10^{-17}\text{m}^3$ with d = 480 nm. For a lightpower of 50 μW and a 1 second illumination with photons of ~1.4 eV

[12] Courtesy of Petru Tighineanu.

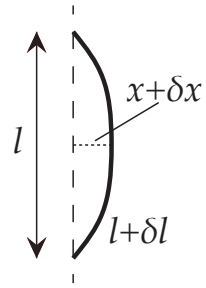

Figure A.7.: A membrane of width and height l has an initial displacement x from being perfectly flat. The small displacements introduced by a local expansion is denoted.

this yields a photon number of $\sim 2 \times 10^{14}$ photons pr. second. The introduced stress is then

$$\sigma_{el} \times N_{photons} \tag{A.5.13}$$

and this would lead to a volume increase as for the thermal expansion. With a volumetric electronic stress per photon being $\sigma_{el} \approx 8$ eV, the fractional volume expansion induced by deformation potential coupling can be written as

$$\frac{\Delta V}{V_0} = \frac{\sigma_{el}/V_{ill}}{B} \tag{A.5.14}$$

pr. photon, with V_{ill} being the illuminated volume. Comparing this with with the thermal stress **eqn.** (A.5.5) it is seen that this effect would be about 10 times stronger than the thermal effect, pr. photon.

A.5.2. Bending estimate for nanomembrane

Let us start with a very simple estimate of the bending of a membrane. The membrane is modeled simply as a slab with thickness of 50 nm and transverse dimensions of 100 μm $\times$ 100 μm. It is assumed fixed at the edges. With a photon energy of roughly 1 eV we can write the fractional volume expansion as

$$\frac{\Delta V}{V_0} = \frac{E_{ph}/V_{ill}}{B} \tag{A.5.15}$$

with E_{ph} being the photon energy, V_{ill} being the illuminated volume and V_0 is the initial volume of the whole membrane. Here an absorption efficiency of unity is assumed Going to a 1D model can be done by setting a small local expansion $l + \delta l$ to lead to a small displacement $x + \delta x$ with x being the displacement in the direction of the cavity mode.

$$\frac{3\delta l}{l_0} = \frac{1\text{eV}/(5\mu\text{m} \times 5\mu\text{m} \times \pi \times 50\text{nm})}{75.5\text{GPa}} \tag{A.5.16}$$

x is the initial displacement and is set to be 1 μm. This follow in line with the intrinsic bending of the GaAs membranes. It is necessary to have this intrinsic bending in order to make a local

expansion lead to a displacement and not just a bulging at the beam spot. In the above expression it can be seen that $l \times \delta l = x \times \delta x \Leftrightarrow \delta l = \frac{x}{l} dx$ and this enables sthe identification of

$$\frac{3\delta l}{l_0} = \frac{3x \times \delta x}{l_0^2} \tag{A.5.17}$$

which can be inserted in **eqn.** (A.5.16) to yield

$$\frac{3x \times \delta x}{l_0^2} = \frac{1\text{eV}/(5\mu\text{m} \times 5\mu\text{m} \times \pi \times 50\text{nm})}{75.5\text{GPa}} \tag{A.5.18}$$

which leads to an extension on the order of

$$\delta x/x \approx 10^{-11} \tag{A.5.19}$$

This means that 1 photon aborbed in the nanomembrane, there will be a displacement of $10^{-11}x$ and for a cooling light beam of realistic intensity, the flux of 10^9 photons hitting per second, which yields a displacement of about 10 nm. This is very large, and hints at why the photothermal effect is so strong. For a nanomembrane system with dimensions

$$10\mu\text{m} \times 10\mu\text{m} \times \pi \times 110\text{nm} \tag{A.5.20}$$

the length difference is estimated to be

$$\delta x/x \approx 10^{-13} \tag{A.5.21}$$

which for 10^9 photons yields a 0.1 nm displacement.

A.5.3. Comsol modeling of the bending

For the real bending of the proposed QW nanomembrane this estimate is of course too simple. For example the it is the hope to implement the effect in a nanomembrane with assymetrically placed QWs and then the estimates used above does not hold. A Comsol model have also been developed where the stress introduced by the electronic force by deformation potential coupling can be implemented. Here the 3D structure and the gaussian beam of the light can be included, as well as the absorption only in the QWs. Unfortunately the complexity of the model makes the problem computationally hard but some initial conclusions can be made.

Implementation

As it is not possible to implement af directionless strain directly in the Comsol software, a workaround was implemented where the local expansion due to heating was modified to include the electron pressure stress discussed. It was possible to include a local expansion in a way consistent with the electron pressure following the field intensity at the QWs and from this the displacement could be modeled. This is of course dependent on parameters such as the beam size on the membrane and the membrane dimensions, dimensions and position of the tethers, as well as the construction of the cavity. However assuming a strong but unchanging field strength in the direction of field propagation at the position of the QWs are consistent with the design choices, but a gaussian profile of the beam is implemented. The displacement per photon can be deduced by relating the

total displacement to the corresponding number of photons needed to introduce this local strain. In order to achieve this a FEM model have also been developed where the stress introduced by the electronic force by deformation potential coupling can be implemented. Here the 3D structure and the gaussian beam of the light can be included, as well as the absorption only in the QWs. Unfortunately the complexity of the model makes the problem computationally hard, and a conclusion have not been reached yet. In Comsol the strain due to absorption cannot be directly implemented as the nature of FEM requires a direction on the stress. However the volume expansion due to a hydrostatic pressure increase can be implemented in a bit of a cumbersome fashion, but might be sufficient for intial test. Comsol solves the mechanical problem of the gradient of the displacement tensor $\mathbf{u}$

$$\nabla \mathbf{u} \tag{A.5.22}$$

The total strain tensor is written in terms of this gradient as

$$\epsilon = \frac{1}{2}(\nabla \mathbf{u} + \nabla \mathbf{u}^T) \tag{A.5.23}$$

where $()^T$ denotes the transposed. This can also be written in of components as

$$\epsilon_{mn} = \frac{1}{2}\left(\frac{\partial u_m}{\partial x_n} + \frac{\partial u_n}{\partial x_m}\right) \tag{A.5.24}$$

The so-called Duhamel-Hooke law[13] relates the stress tensor as

$$\boldsymbol{s} = \boldsymbol{s}_0 + \mathrm{C} : (\boldsymbol{\epsilon} - \boldsymbol{\epsilon_0} - \alpha_T(T - T_{\mathrm{ref}})) \tag{A.5.25}$$

where s is the stress tensor, s_0 and ϵ_0 is the initial stress and strain tensors, C is the 4th order elasticity tensor and the ":" sign communcates the double-dot tensor product. The last term describe thermal expansion and for this T and T_{ref} stands for the temperature and the reference temperature, while α_T is the thermal expansion coefficient. The equation that is solved is Newton's second law formulated as

$$\rho\frac{\partial^2 \mathbf{u}}{\partial t^2} - \nabla \cdot \sigma = \mathbf{F}v \tag{A.5.26}$$

A way of forcing a volume expansion is to redefine the tensor α_T to not be the thermal expansion coefficient, but rather an expression for the local expansion due to the deformation potential coupling and the resulted volume expansion due to this. Redefining

$$\alpha_T \propto \exp\left(-\frac{(x - x_0)^2}{2\sigma_b^2} - \frac{(y - y_0)^2}{2\sigma_b^2}\right) \tag{A.5.27}$$

where x_0 and y_0 denote the beam center and σ_b denote the width of the beam. It is then possible to force the $T - T_{ref} = 1$ and by making sure that this temperature increase do not couple back to thermally induced stress, the volume expansion can be defined explicitly, and for isotropic expansion coefficients the strain is given as

$$3\frac{\Delta L}{L} = \frac{\Delta V}{V} \tag{A.5.28}$$

[13] See the Structural Mechanics Documentation for Comsol 4.2, and[Atanackovic00]

and since the strain in Comsol is defined as $\epsilon_{mn} = \alpha_{mn}(T - T_{ref})$ there is a factor of 3 that enters. Now again the expression for the volume expansion due to the deformation potential coupling can be written

$$\frac{\Delta V}{V} = \frac{(\sigma_{el}/V_{ill}) \times N_{ph}}{B} \tag{A.5.29}$$

σ_{el} being the electronic stress in energy and N_{ph} being the photon number.

A relation is needed between **eqn.** (A.5.27), and the excitation of electron-hole pairs. **eqn.** (A.5.27) states that the volume expansion is proportional to the light field intensity, and writing up the Gaussian function from **eqn.** (A.5.27), as exp , the α_T can be written

$$\alpha_T = \eta_{abs} \frac{\sigma_{el}/V_{ill}) \times N_{ph}}{B} \exp() \tag{A.5.30}$$

with η_{abs} being the ratio of the illuminated photons that is absorbed and leads to an excited e-h pair, compared to the illuminated number of photons. Initially this can be set to unity.

Bending of nanomembranes

For the specific case of the next generation GaAs membranes with 2 QWs this bending should be estimated. This is the system described in **chap. 8**. Using FEM implementation as sketched above, the displacement was found to be 4.9 μm at the beam center with just a unity prefactor. The implementation is shown in **fig. A.8**.

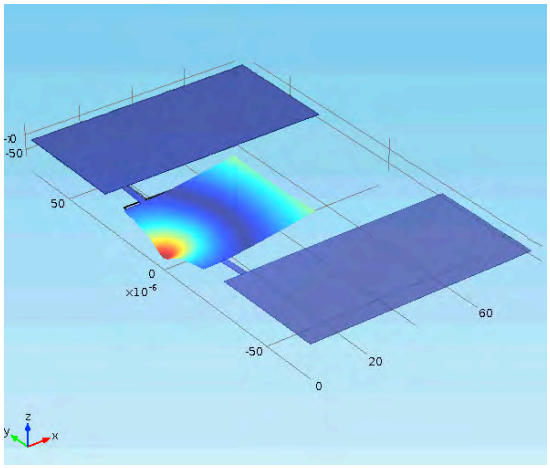

Figure A.8.: FEM of displacement for the next generation membrane model with two quantum wells (not visible). The model is assumed symmetric and thus only half the modeled system is shown. The coupling to the optical field can be estimated due to the displacement. The displacement is grossly exaggerated for visual clarity.

The illuminated area is $2\pi\sigma_b^2$ and thus the illuminated volume is $V_{ill} = 2w_{qw} \times 2\pi\sigma_b^2$, with w_{qw} being the thickness of the Quantum Wells. The value of $V_{ill} \approx 7 \times 10^{-18}\mathrm{m}^{-3}$ is then found with $w_{qw} = 6$ nm and a beam size with $\sigma_b = 10\mu$ m. As shown above the electron energy is around 8 eV and the prefactor to α_T is found to be

$$\frac{8\mathrm{eV}/\left(7 \times 10^{-18}\mathrm{m}^3\right)}{75.5\mathrm{GPa}} \approx 2 \times 10^{-12} \tag{A.5.31}$$

per photon absorbed. Setting $\eta_{abs} = 1$ the displacement of the proposed structure can be found. With the spoke placed at $0.1 \times l$ the displacements at the beam center due to deformation potential coupling is found to be

α_T	Max displacement [m]	Displacement by 1μW illumination
10^{-15}	10^{-21}	1 nm
10^{-12}	10^{-18}	1 μm

and this then gives the maximum displacement per photon. A view of the modeled structure showing the displacement in exagerated form is shown in **fig. A.8**. And thus with 1μW of light power, leading to a photon number of $N_{ph} = 10^{12}$ every second, this leads to a displacement on the order of about a μm. This is for photons with energy of 1.4 eV, which for an optical power of 1 μW is about 2×10^{12} photons pr. second.

Additional modeling was done with different spoke positions and thicknesses, but these are not included here.

A.5.4. Comsol force

Using the same kind of gaussian dependence for the force as was used above for the deformation potential coupling, a force on the QW layer was implemented in Comsol to establish the force that the deformation potential cooling would lead to. The force field intensity is illustrated in **fig. A.9** where again the symmetry of the problem has been used to minimize the memory requirements, and only a quarter of the modeled field is then shown. The force field on the QW section is modeled using the gaussian dependence in **eqn.** (A.5.27) with a prefactor A.

Gaussian Force distribution as shown in **fig. A.9**

A (N/m^2)	Displacement (m)
1×10^{-12}	4.3×10^{-25}
1×10^{-11}	5.7×10^{-24}
1×10^{-10}	5.7×10^{-23}
1×10^{-9}	5.7×10^{-22}

Point force at the center of the membrane

A (N)	Displacement (m)
1×10^{-12}	5.7×10^{-12}
1×10^{-11}	5.7×10^{-11}
1×10^{-10}	5.7×10^{-10}
1×10^{-9}	5.7×10^{-9}

When these displacements are compared with the displacement determined using the deformation potential modeling as shown above, the force is estimated to be $F \approx 10^{-18}$ N per absorbed photon.

This is done by seeing that a $\alpha_T = 10^{-12}$ leads to a displacement at the center of 10^{-18} m, and then comparing with the fictious force from above a force of $F \approx 10^{-18}$ N per absorbed photon is equivalent.

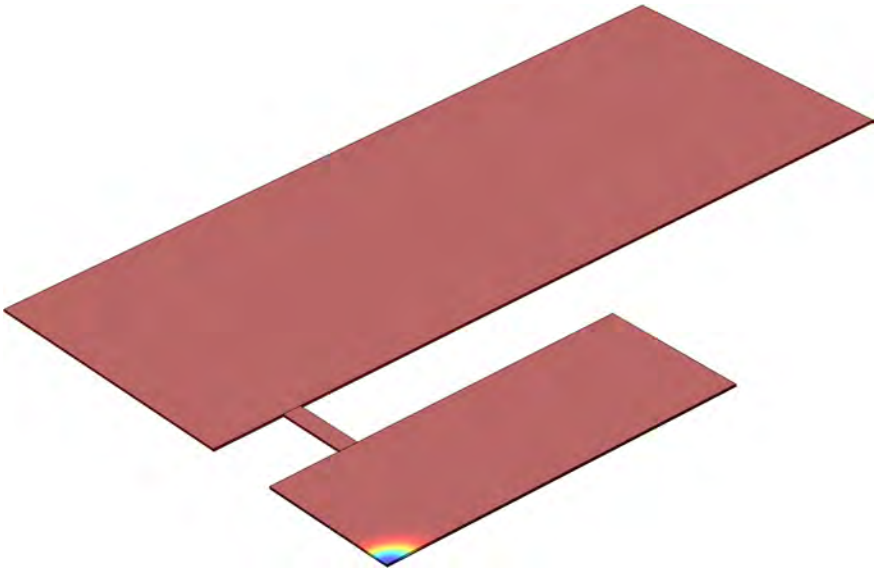

Figure A.9.: Field intensity used for modeling the beam of cooling light. The same gaussian distribution is used for finding the equivalent force of the deformation potential coupling expansion.

B. Optomechanics

B.1. Quantum noise approach to sideband cooling

The classical description of cooling ceases to be applicable if shot noise affects the system in a meaningful way. Under certain conditions, such as low light power or high cavity finesse, the shot noise heats the motion of the resonator in a appreciable magnitude and thus needs to be included in the model. This is the motivation for a quantum model of the side band cooling, and is due to [Wilson-Rae07, Marquardt07]. Here the resonator angular frequency ω_R is used instead of shifting the cavity resonance as in **chap. 2**. It is basically a description of weak coupling of the environment to the resonator, and if the coupling is weak enough a description of the spectrum of the light-induced force on the system is enough to fully describe the coupled system. At weak coupling the force spectrum can be determined as

$$\hat{H}_{int} = -\hat{F}\hat{x}$$

which is obviously just Hooke's law. The force is $\hat{F} = \frac{\omega_R}{L}\hat{a}^\dagger\hat{a}$ and the force spectrum is then given as

$$S_{FF}(\omega) = \int dt e^{i\omega t}\langle\hat{F}(t)\hat{F}(0)\rangle$$

where ω is the Fourier frequency component corresponding to t. Fermi's Golden Rule then enables the estimation of the population rates as

$$\Gamma^{\downarrow}_{opt} = \frac{x^2_{zpf}}{\hbar^2}S_{FF}(\omega_m), \quad \Gamma^{\uparrow}_{opt} = \frac{x^2_{zpf}}{\hbar^2}S_{FF}(-\omega_m)$$

with $\Gamma^{\downarrow}_{opt}$ then being the rate of a photon incidence that removes one phonon, and $\Gamma^{\uparrow}_{opt}$ being the opposite proces where a phonon is created by the incident photon. The choice of ω_m and $-\omega_m$ is because these are the frequencies where the influence of light is strongest (assuming $\omega_m \gg \Gamma_{opt}$). The optomechanical damping rate is the difference of noise spectra at the two sidebands at $\pm\omega_m$

$$\Gamma_{opt} = \frac{x^2_{zpf}}{\hbar^2}\left(S_{FF}(\omega_m) - S_{FF}(-\omega_m)\right) \tag{B.1.1}$$

The rates enters the master equation for the resonator coupled to a equilibrium heat bath and light induced field. The master equation is written up in the standard way for the density matrix $\hat{\rho}$ with Lindblad operators describing the population transitions of the resonator. In [Marquardt08] is derived the equation for the steady state phonon occupation number $\langle\hat{n}\rangle = \sum_n n\rho_{nm}$ as

$$\frac{\partial n}{\partial t} = \gamma_m\langle\hat{n}\rangle_{th} + \Gamma^{opt}_{\uparrow} - (\gamma_m + \Gamma_{opt})\langle\hat{n}\rangle \tag{B.1.2}$$

where $\langle\hat{n}\rangle_{th}$ denote the thermal equilibrium population. Following [Clerk10, Wilson-Rae07] and [Marquardt07] it is possible to find the force spectrum as a Lorentzian that is shifted due to the detuning $\Delta = \omega_L - \omega_R$ as

$$S_{FF}(\omega) = \int dt e^{i\omega t}\langle F(t)F(0)\rangle \tag{B.1.3}$$

$$= \left(\frac{\hbar\omega_R}{L}\right)^2 \langle\hat{n}_{photon}\rangle \frac{\Gamma_{opt}}{(\omega+\Delta)^2 + \left(\frac{\Gamma_{opt}}{2}\right)^2} \tag{B.1.4}$$

with $\langle\hat{n}_{photon}\rangle$ being the average photon number in the cavity and

$$\langle\hat{n}\rangle = \frac{\gamma_M\langle\hat{n}\rangle_{th} + \Gamma_{opt}\langle\hat{n}\rangle^{opt}_{th.M}}{\gamma_M + \Gamma_{opt}} \tag{B.1.5}$$

where again γ_M is the mechanical damping rate and, Γ_{opt} is the optical damping $\Gamma_{opt} = \Gamma^{\downarrow}_{opt} - \Gamma^{\uparrow}_{opt}$ and $\langle\hat{n}\rangle^{opt}_m$ is the minimal phonon number optained for $\langle\hat{n}\rangle^{opt}_m = \Gamma^{\uparrow}_{opt}/\Gamma^{\downarrow}_{opt}$.

Now choosing the laser frequency in a way where it fits with the parameters of the system, it is possible to cool the vibrational mode of the system significantly. As is seen from eqn. (B.1.5) the final phonon number will depend on the ratio of the decay rates. It is also required that the mechanical quality factor of the vibration $\omega_m/\gamma_m = Q_m \gg 1$. In this case $\gg 1$ is an understatement as there is a long range of work on achieving higher mechanical Q_m and values of 10^6 is commonplace, but this will not be discussed here.

Regimes

Several regimes are relevant for this discussion. For $\omega_m \ll \kappa$ the $\langle n^O_m\rangle \gg 1$ and thus ground-state cooling is not possible. In the so-called sideband resolved regime of $\kappa \ll \omega_m$ the minimum occupation can be found to be [Marquardt08]

$$\min\overline{n}_m \approx \left(\frac{\kappa}{4\omega_m}\right)^2 \tag{B.1.6}$$

and as illustrated in **fig. B.1** this goes well below a phonon occupation of 1. Thus ground state cooling is possible if the system can be brought in the resolved sideband regime.

Following [Schliesser08], when the decay rate κ of the cavity system is much larger than the mechanical frequency $\omega_m/(2\pi)$ ground state cooling is impossible in this picture. In **fig. B.2** it is seen how the sidebands are not discernable and thus it can be denoted as unresolved sideband regime. Another term for this would be to call it working in the bad cavity limit as $\kappa \ll \omega_m, \gamma_m$, and thus an excitation of the cavity is transferred out of the system quickly and before it can affect the internal elements. In the opposite case of $\omega_m \gg \kappa$ the motional sidebands are clearly discernable at $\omega_c \pm \omega_m$ as shown in **fig. B.2** and the ground state cooling is possible. For obvious reasons the resolved sideband regime is also termed the good cavity limit.

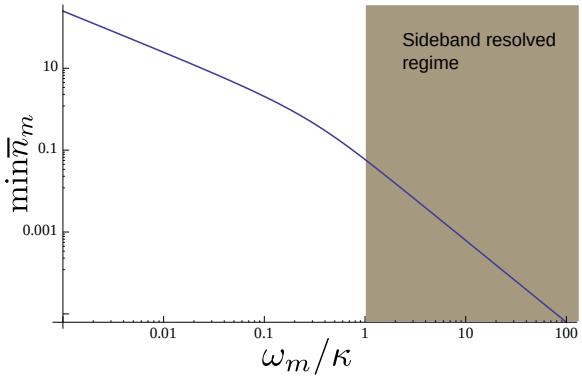

Figure B.1.: Minimal obtained phonon number $\min\overline{n}_m$ as a function of ω_m/κ. For $\omega_m/\kappa > 1$ the sideband resolved regime can be achieved with a minimum phonon number of less than one. [Marquardt08]

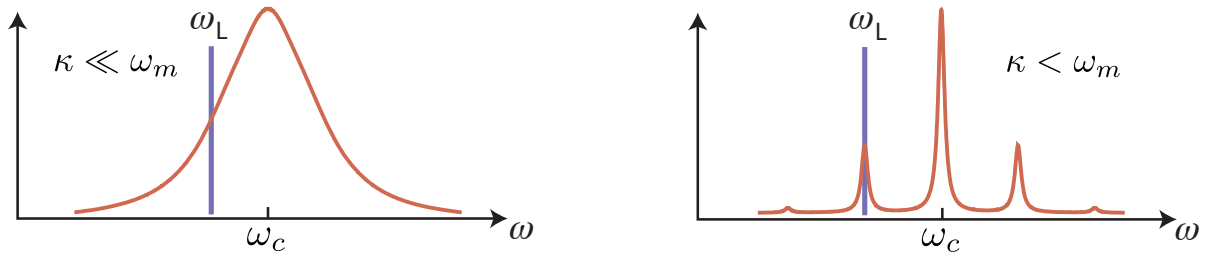

(a) Bad cavity (unresolved sideband) regime $\min\overline{n}_m \approx \kappa/(4\omega_m) \ll 1$

(b) Resolved sideband regime $\min\overline{n}_m \approx \kappa^2/(16\omega_m^2) < 1$.

Figure B.2.: Unresolved sideband and the resolved sideband regime. The red line shows the cavity systems resonance while the blue is the frequency of the input laser with frequency $\omega_L/(2\pi)$.

B.2. Aluminium membrane measurements

A microscope picture is shown in **fig. B.3** of an aluminum coated membrane.

Some of the FEM modeled mechanical modes of the aluminum coated membrane is shown in **fig. B.4**.

Measurements in the Polytec Vibrometer shows a vibrational spectrum as shown in **fig. B.5**. The measured mechanical modes are illustrated in **fig. B.6**.

B.2.1. FEM of nanomembranes

The spoked nanomembranes studied in **sec. 7.2** have a lot more available vibrational modes. Some of the lowest energy mechanical modes, as found by FEM, is illustrated in **fig. B.7**.

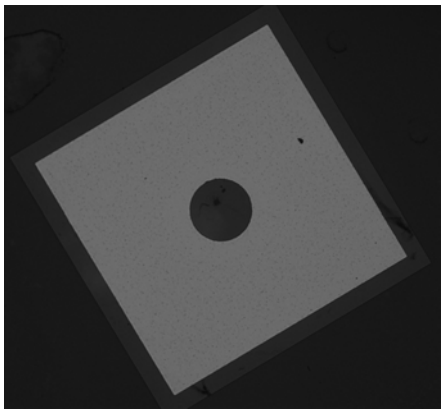

Figure B.3.: Aluminium coated membrane

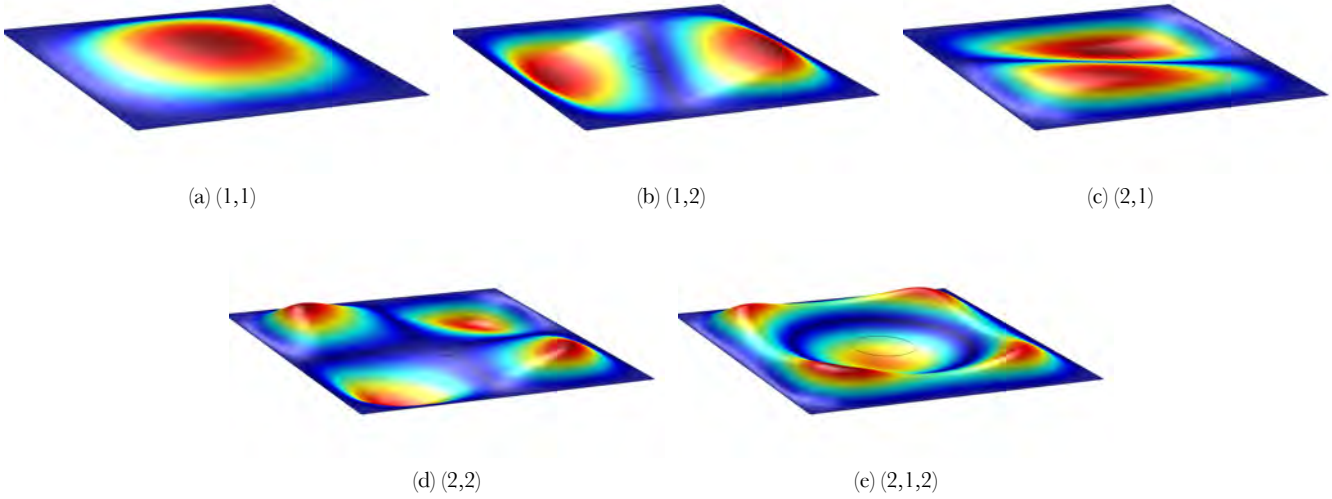

(a) (1,1) (b) (1,2) (c) (2,1)

(d) (2,2) (e) (2,1,2)

Figure B.4.: FEM of Aluminium coated membrane. The modes are different for higher order modes, due to the layer of aluminium with a hole in the center.

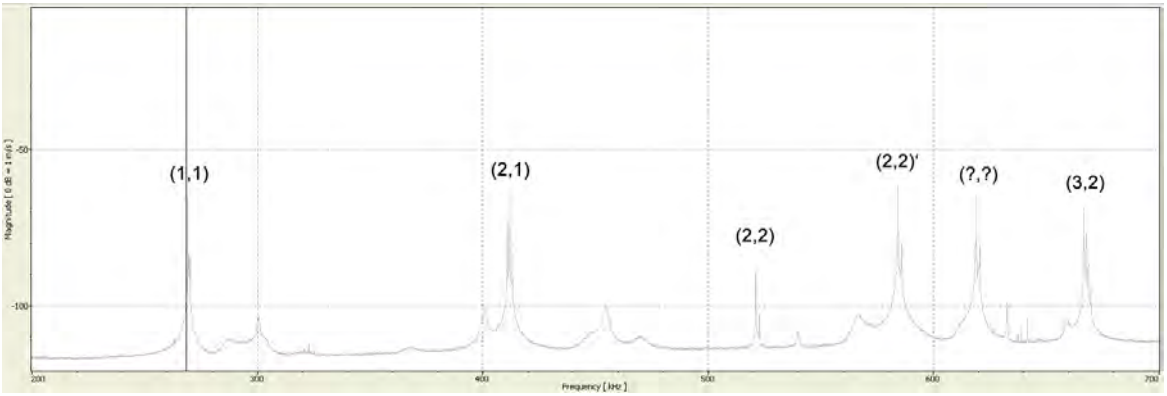

Figure B.5.: Vibrometer spectrum

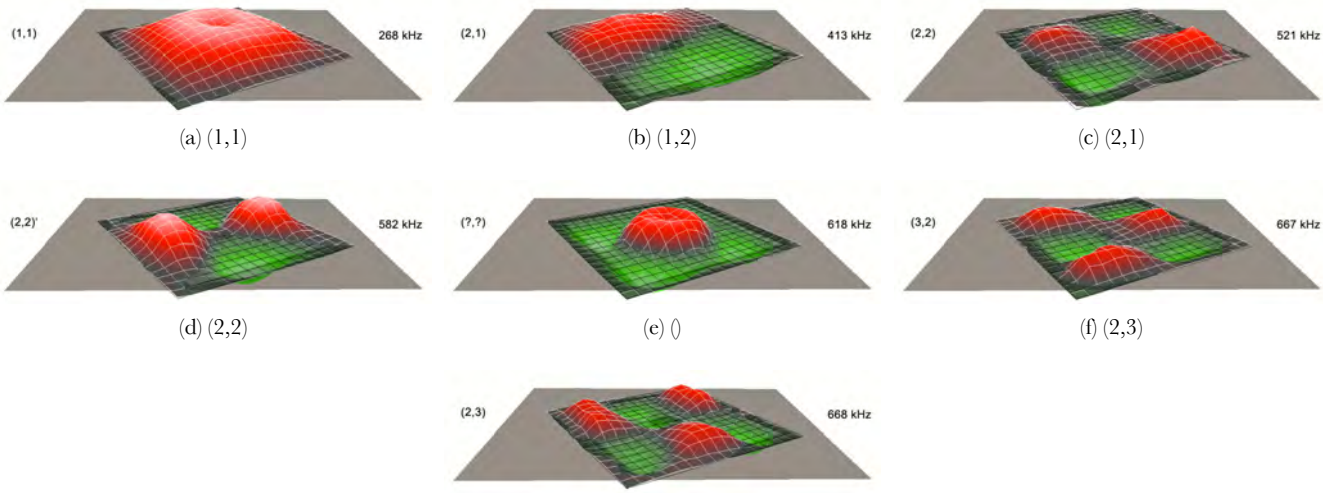

(a) (1,1) (b) (1,2) (c) (2,1)

(d) (2,2) (e) () (f) (2,3)

(g) (3,2)

Figure B.6.: Vibrometer measurement of Aluminium coated membrane

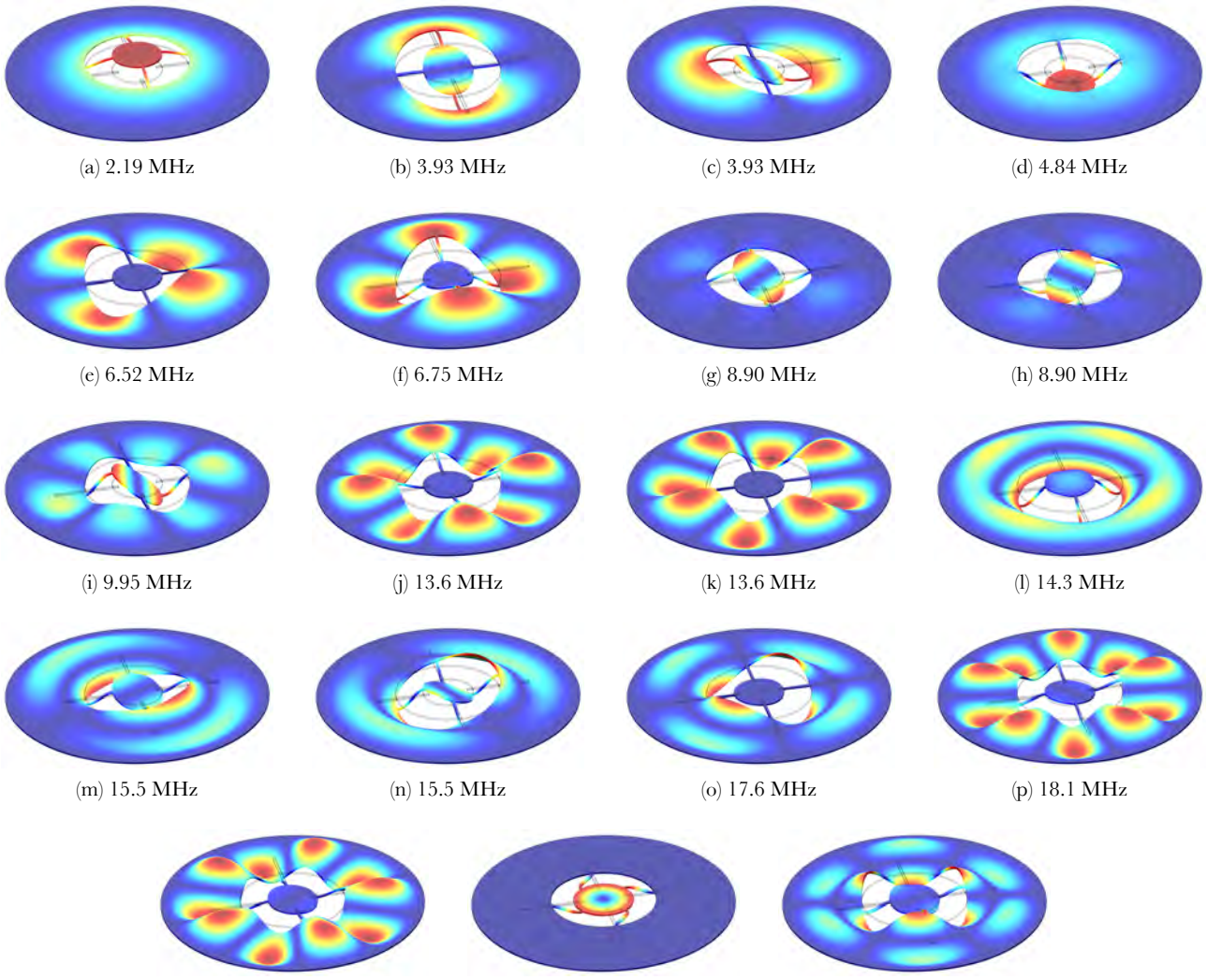

(a) 2.19 MHz (b) 3.93 MHz (c) 3.93 MHz (d) 4.84 MHz

(e) 6.52 MHz (f) 6.75 MHz (g) 8.90 MHz (h) 8.90 MHz

(i) 9.95 MHz (j) 13.6 MHz (k) 13.6 MHz (l) 14.3 MHz

(m) 15.5 MHz (n) 15.5 MHz (o) 17.6 MHz (p) 18.1 MHz

(q) 18.1 MHz (r) 20.2 MHz (s) 21.8 MHz

Figure B.7.: FEM of the mechanical modes for a typical nanomembrane.

C. Signals

C.1. Spectral density

Energy spectral density describe how the energy of a given signal is distributed in frequency. The energy of a signal $x(t)$ is

$$E_s = \int_{-\infty}^{\infty} |x(t)|^2 dt \tag{C.1.1}$$

Now this of course requires that $x(t)$ be absolutely integrable so that the energy is not infinite. Through Parselval's theorem [Kampen07] the energy of the signal can be written by the Fourier transform, $\tilde{x}(\omega)$, as

$$E_s = \int_{-\infty}^{\infty} |x(t)|^2 dt = \sqrt{\frac{1}{2\pi}} \int_{-\infty}^{\infty} |\tilde{x}(\omega)|^2 d\omega \tag{C.1.2}$$

In this expression the integrand $|\tilde{x}(\omega)|^2$ can be interpreted as a density function for the energy per frequency ω. From this the energy spectral density is then defined by

$$S_{xx}(\omega) = |\tilde{x}(\omega)|^2 = |\int_{-\infty}^{\infty} x(t) e^{-i\omega t} dt|^2 \tag{C.1.3}$$

For periodic signals it makes more sense to use the power spectral density, PSD, which describes the distribution of power over frequencies. The power in a signal over a time T will be given as

$$P = \langle x(t)^2 \rangle = \frac{1}{2T} \int_{-T}^{T} x(t)^2 dt \tag{C.1.4}$$

From this it is clear that for $T < \infty$ the power will be finite even though the energy might be infinite.

Suppose a random "stationary" function $x(t)$ describe a noisy physical process such as a mechanical oscillator with Brownian motion. The spectral properties can then be defined as above. The autocorrelation of $x(t)$ is defined as [Kampen07]

$$\langle x(t)x(t+\tau) \rangle = \lim_{T\to\infty} \frac{1}{2T} \int_{-T/2}^{T/2} x(t)x(t+\tau) d\tau \tag{C.1.5}$$

and then the Wiener-Khinchin theorem states that the Fourier transform of the autocorrelation function is the power spectral density as

$$S_{xx}(\omega) = \frac{1}{2T} \int_{-\infty}^{\infty} \langle x(t)x(t+\tau) \rangle e^{-i\omega\tau} d\tau \tag{C.1.6}$$

This is then the power spectrum density for the signal $x(t)$. Experimentally it would be easier to work with a single time component and not an autocorrelation, and it is easier to use as above that normalizing the energy spectral density of a measurement interval T can be shown to approximate the power spectral density for increasing T as

$$S_{xx,T}(\omega) = \lim_{T\to\infty} \frac{1}{T} |\int_{-T/2}^{T/2} x(t)e^{-i\omega t}dt|^2 = \lim_{T\to\infty} \frac{1}{T}|x_T(\omega)|^2 \tag{C.1.7}$$

where $x_T(t)$ is introduced with the value of $x(t)$ in the interval T and zero otherwise.

The power spectral densities can be used to write up the reponse of a system if it can be assumed to be a linear reponse. If $x(t)$ is a input signal and $y(t)$ is assumed the output signal, then the reponse of the system can be described by a linear transformation G. Thus $y(t) = G(x(t))$. It can be shown [Kampen07] that under certain assumptions about the transformation that it can be written as a convolution of $x(t)$ as

$$y(t) = \int_{-\infty}^{\infty} x(t)g(t-t')dt' \tag{C.1.8}$$

and that $g(t)$ has a Fourier transform, $g(\omega)$ that allow

$$y(\omega) = g(\omega)x(\omega) \tag{C.1.9}$$

which then enables the transformation of the power spectral densities as

$$S_{yy}(\omega) = |g(\omega)|^2 S_{xx}(\omega) \tag{C.1.10}$$

with $|g(\omega)|^2$ then being identified as the transfer function. From this it has then been established how the response of a linear system is to a input with some spectral density.

D. Miscellaneous

D.1. Mephisto data

Some specified properties of the Mephisto laser is illustrated in **fig. D.1**. The figure is reproduced from [Innolight]. This laser was used for the interferometer setup.

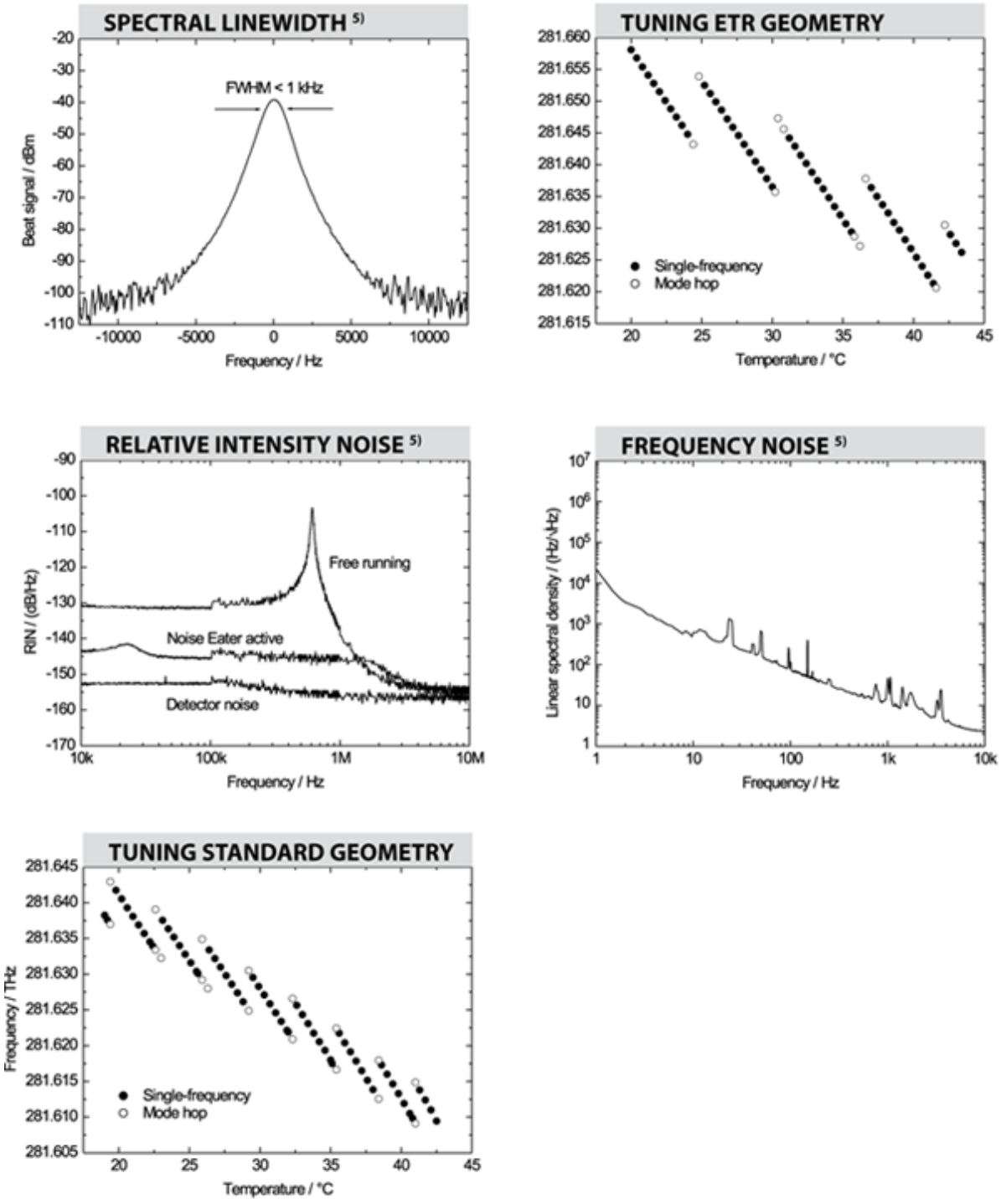

Figure D.1.: Mephisto data [Innolight].

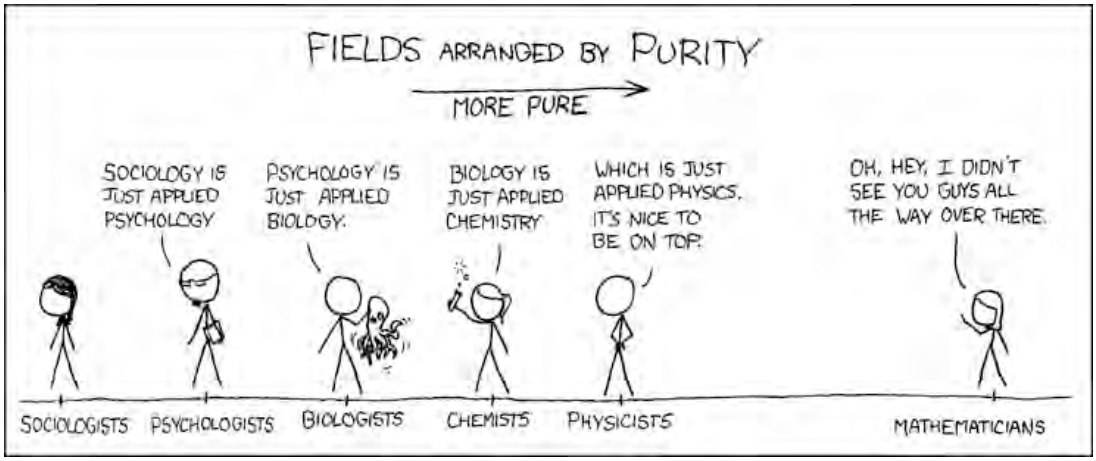

Fields arranged by purity. http://xkcd.com/435/

$\sim$

Bibliography

[Adachi85] Sadao Adachi, *GaAs, AlAs, and Al[sub x]Ga[sub 1 - x]As@B: Material parameters for use in research and device applications*, Journal of Applied Physics, **58**(3), R1 (1985)

[Arcizet06] O. Arcizet, P.-F. Cohadon, T. Briant, M. Pinard, A. Heidmann, *Radiation-pressure cooling and optomechanical instability of a micromirror*, Nature, **444**(7115), 71 (2006)

[Aspelmeyer10] Markus Aspelmeyer, Simon Groeblacher, Klemens Hammerer, Nikolai Kiesel, *Quantum Optomechanics - throwing a glance* (2010), `1005.5518v1`

[Atanackovic00] Teodor M. Atanackovic Ardeshir Guran, *Theory of Elasticity for Scientists and Engineers*, Birkhauser (2000)

[Bachor04] Hans-A. Bachor Timothy C. Ralph, *A Guide to Experiments in Quantum Optics*, Wyley (2004)

[Ballentine98] Leslie E. Ballentine, *Quantum Mechanics: A Modern Development*, World Scientific Publishing Company (1998)

[Bennett10] Steven D. Bennett, Lynda Cockins, Yoichi Miyahara, Peter Grütter, Aashish A. Clerk, *Strong Electromechanical Coupling of an Atomic Force Microscope Cantilever to a Quantum Dot*, Phys. Rev. Lett., **104**(1), 017203 (2010)

[Blakemore61] John Sydney Blakemore, *Gallium arsenide*, Springer (1961)

[Blakemore82] J. S. Blakemore, *Semiconducting and other major properties of gallium arsenide*, Journal of Applied Physics, **53**(10), R123 (1982)

[Butov99] L. Butov, *Photoluminescence kinetics of indirect excitons in GaAs/Al(x)Ga(1-x)As coupled quantum wells*, Phys. Rev. B; Physical Review B, **59**(3), 1625 (1999)

[Butov01a] L. V. Butov, A. Imamoglu, K. L. Campman, A. C. Gossard, *Coulomb effects in spatially separated electron and hole layers in coupled quantum wells*, Journal of Experimental and Theoretical Physics, **92**(2), 260 (2001)

[Butov01b] L. V. Butov, A. L. Ivanov, A. Imamoglu, P. B. Littlewood, A. A. Shashkin, V. T. Dolgopolov, K. L. Campman, A. C. Gossard, *Stimulated Scattering of Indirect Excitons in Coupled Quantum Wells: Signature of a Degenerate Bose-Gas of Excitons*, Phys. Rev. Lett., **86**, 5608 (2001)

[Chan11] Jasper Chan, T. P. Mayer Alegre, Amir H. Safavi-Naeini, Jeff T. Hill, Alex Krause, Simon Groblacher, Markus Aspelmeyer, Oskar Painter, *Laser cooling of a nanomechanical oscillator into its quantum ground state*, Nature, **478**(7367), 89 (2011)

[Chuang09] Shun Lien Chuang, *Physics of Photonic Devices*, Wiley, 2 (2009)

[Clerk10] A. A. Clerk, M. H. Devoret, S. M. Girvin, Florian Marquardt, R. J. Schoelkopf, *Introduction to quantum noise, measurement, and amplification*, Rev. Mod. Phys., **82**, 1155 (2010)

[Coffey96] William T. Coffey, Yu P. Kalmykov, J. T. Waldron, *The Langevin Equation: With Applications in Physics, Chemistry and Electrical Engineering*, World Scientific Pub Co Inc (1996)

[Cole10] Garrett D. Cole, Yu Bai, Markus Aspelmeyer, Eugene A. Fitzgerald, *Free-standing*

Al[sub x]Ga[sub 1 - x]As heterostructures by gas-phase etching of germanium, Applied Physics Letters, **96**(26), 261102 (2010)

[Cole11] Garrett D. Cole, Ignacio Wilson-Rae, Katharina Werbach, Michael R. Vanner, Markus Aspelmeyer, *Phonon-tunnelling dissipation in mechanical resonators*, Nat Commun, **2**, 231 (2011)

[Com] *Comsol Multiphysics: Reference Guide*

[Courtya01] J.-M. Courtya, A. Heidmannb, M. Pinardc, *Quantum limits of cold damping with optomechanical coupling*, The european physical journal D (2001)

[Eichenfield09] Matt Eichenfield, Jasper Chan, Ryan M. Camacho, Kerry J. Vahala, Oskar Painter, *Optomechanical crystals*, Nature, **462**(7269), 78 (2009)

[Elliott57] R. J. Elliott, *Intensity of Optical Absorption by Excitons*, Phys. Rev., **108**(6), 1384 (1957)

[Epstein09] Richard Epstein Mansoor Sheik–Bahae, *Optical Refrigeration in Solids: Fundamentals and Overview*, Wiley-Interscience (2009)

[Favero09] Ivan Favero Khaled Karrai, *Optomechanics of deformable optical cavities*, Nat Photon, **3**(4), 201 (2009)

[Florian Marquardt09] Steve M. Girvin Florian Marquardt, *Optomechanics*, Physics, **2**, 40 (2009)

[Fox10] Mark Fox, *Optical Properties of Solids*, Oxford University Press, USA, 2 (2010)

[Gillespie95] A. Gillespie F. Raab, *Thermally excited vibrations of the mirrors of laser interferometer gravitational-wave detectors*, Phys. Rev. D, **52**(2), 577 (1995)

[Goi90] A. R. Goi, A. Cantarero, K. Syassen, M. Cardona, *Effect of pressure on the low-temperature exciton absorption in GaAs*, Phys. Rev. B, **41**(14), 10111 (1990)

[Gorczyca92] I. Gorczyca, T. Suski, E. Litwin-Staszewska, L. Dmowski, J. Krupski, B. Etienne, *Deformation potential in a high-electron-mobility GaAs/*$Ga_{0.7}Al_{0.3}$*As heterostructure: Hydrostatic-pressure studies*, Phys. Rev. B, **46**, 4328 (1992)

[Grassia00] F. Grassia, J.-M. Courty, S. Reynaud, P. Touboul, *Quantum theory of fluctuations in a cold damped accelerometer*, The European Physical Journal D, **8**, 101 (2000)

[Greiner95] Walter Greiner, Ludwig Neise, Horst Stöcker, *Thermodynamics and Statistical Mechanics*, Springer (1995)

[Hansen09] Toke Lund Hansen, Henri Thyrrestrup, S. Reitzenstein, Peter Lodahl, *Purcell enhancement of a single quantum dot tuned through the resonance of a micropillar cavity* (2009), preprint

[Harrison10] Paul Harrison, *Quantum Wells, Wires and Dots: Theoretical and Computational Physics of Semiconductor Nanostructures*, Wiley, 3 (2010)

[Hobbs09] Philip C. D. Hobbs, *Building Electro-Optical Systems: Making It all Work*, Wiley, 2 (2009)

[Hoyt03] C. W. Hoyt, M. P. Hasselbeck, M. Sheik-Bahae, R. I. Epstein, S. Greenfield, J. Thiede, J. Distel, J. Valencia, *Advances in laser cooling of thulium-doped glass*, J. Opt. Soc. Am. B, **20**(5), 1066 (2003)

[Innolight] Innolight, *Mephisto, Technical information. Ultra-stable single-frequency cw laser.*

[Joannopoulos08] John D. Joannopoulos, Steven G. Johnson, Joshua N. Winn, Robert D. Meade, *Photonic Crystals: Molding the Flow of Light (Second Edition)*, Princeton University Press (2008)

[Kampen07] N. G. Van Kampen, *Stochastic Processes in Physics, Chemistry, and Biology*, Elsevier Science Technology Books (2007)

[Kippenberg07] Tobias J. Kippenberg Kerry J. Vahala, *Cavity Opto-Mechanics*, Opt. Express, **15**(25), 17172 (2007)

[Kippenberg08] T. J. Kippenberg K. J. Vahala, *Cavity Optomechanics: Back-Action at the Mesoscale*, Science, **321**(5893), 1172 (2008), `http://www.sciencemag.org/cgi/reprint/321/5893/1172.pdf`

[Landau86] L. D. Landau, L. P. Pitaevskii, E. M. Lifshitz, A. M. Kosevich, *Theory of Elasticity, Third Edition: Volume 7*, Butterworth-Heinemann, 3 (1986)

[Larsen11] T. Larsen, S. Schmid, L. Gronberg, A. O. Niskanen, J. Hassel, S. Dohn, A. Boisen, *Ultrasensitive string-based temperature sensors*, Applied Physics Letters, **98**(12), 121901 (2011)

[Law95] C. K. Law, *Interaction between a moving mirror and radiation pressure: A Hamiltonian formulation*, Physical Review A, **51**(3), 2537 (1995)

[Lifshitz00] Ron Lifshitz M. L. Roukes, *Thermoelastic damping in micro- and nanomechanical systems*, Phys. Rev. B, **61**, 5600 (2000)

[Liu11] J. Liu, K. Usami, A. Naesby, T. Bagci, E. S. Polzik, P. Lodahl, S. Stobbe, *High-Q optomechanical GaAs nanomembranes*, Applied Physics Letters, **99**(24), 243102 (2011)

[Loudon00] Rodney Loudon, *The Quantum Theory of Light*, Oxford University Press, USA, 3rd (2000)

[Mahan90] Gerald D. Mahan, *Many-particle physics*, -: Plenum Press, 2nd ed. (1990)

[Mair98] R.A. Mair, R. Prepost, E.L. Garwin, T. Maruyama, *Measurement of the deformation potentials for GaAs using polarized photoluminescence*, Physics Letters A, **239**(4â€“5), 277 (1998)

[Marquardt07] Florian Marquardt, Joe P. Chen, A. A. Clerk, S. M. Girvin, *Quantum Theory of Cavity-Assisted Sideband Cooling of Mechanical Motion*, Physical Review Letters, **99**(9), 093902 (2007)

[Marquardt08] Florian Marquardt, A. A. Clerk, S. M. Girvin, *Quantum theory of optomechanical cooling*, Journal of Modern Optics, **55**(19), 3329 (2008)

[Matsuda05] O. Matsuda, T. Tachizaki, T. Fukui, J. J. Baumberg, O. B. Wright, *Acoustic phonon generation and detection in $GaAs?Al_{0.3}Ga_{0.7}As$ quantum wells with picosecond laser pulses*, Phys. Rev. B, **71**(11), 115330 (2005)

[Mertz93] J. Mertz, O. Marti, J. Mlynek, *Regulation of a microcantilever response by force feedback*, Applied Physics Letters, **62**(19), 2344 (1993)

[Metzger04] Constanze Hohberger Metzger Khaled Karrai, *Cavity cooling of a microlever*, Nature, **432**(7020), 1002 (2004)

[Metzger08a] Constanze Metzger, Ivan Favero, Alexander Ortlieb, Khaled Karrai, *Optical self cooling of a deformable Fabry-Perot cavity in the classical limit*, Phys. Rev. B, **78**(3), 035309 (2008)

[Metzger08b] Constanze Metzger, Max Ludwig, Clemens Neuenhahn, Alexander Ortlieb, Ivan Favero, Khaled Karrai, Florian Marquardt, *Self-Induced Oscillations in an Optomechanical System Driven by Bolometric Backaction*, Physical Review Letters, **101**(13), 133903 (2008)

[Michelson87] A. A. Michelson E. W. Morley, Am. J. Sci., (34), 333 (1887)

[Miguel-Sánchez12] J. Miguel-Sánchez, A. Naesby, E. Togan, D. Pinotsi, A. Reinhard, T. Volz, A. Imamoglu, B. Besga, J. Esteve, J. Reichel, I. Wilson-Rae, K. Usami, E. Polzik, *Semiconductor quantum well based nanomembranes: From mechanical cooling towards polariton*

optomechanics, *ICPS* (2012)

[Milonni88] Peter W. Milonni Joseph H. Eberly, *Lasers*, Wiley-Interscience, 1 (1988)

[Naesby10] Andreas Naesby, Koji Usami, Tolga Bacgi, Bo Melholt, Eugene Polzik, *Quantum Opto-Nanomechanics*, *CONT* (2010)

[Naesby11] A. Naesby, K. Usami, T. Bagci, Bo Melholt Nielsen, Jin Liu, Søren Stobbe, Peter Lodahl, Eugene S. Polzik, *Optoelectronic cooling of mechanical modes in a semiconductor nanomembrane*, *CLEO Europe* (2011)

[Naesby12] A. Naesby, *Optical cavity cooling of mechanical modes and possibility of bulk cooling of a semiconductor nanomembrane*, *QNLO Summerschool* (2012)

[Narukawa97] Yukio Narukawa, Yoichi Kawakami, Shizuo Fujita, Shigeo Fujita, Shuji Nakamura, *Recombination dynamics of localized excitons in* $In_{0.20}Ga_{0.80}N$-$In_{0.05}Ga_{0.95}N$ *multiple quantum wells*, Phys. Rev. B, **55**, R1938 (1997)

[Nielsen10] Bo Melholt Nielsen, *A non-classical light source for light-matter interfaces*, , University of Copenhagen (2010)

[Nol] *http://www.noliac.com/Material_characteristics_-143.aspx*

[Oblak09] Daniel Oblak, *Quantum State Engineering in Cold Caesium Atoms*, , Danish National Research Foundation Centre for Quantum Optics (QUANTOP) (2009)

[O/'Connell10] A. D. O/'Connell, M. Hofheinz, M. Ansmann, Radoslaw C. Bialczak, M. Lenander, Erik Lucero, M. Neeley, D. Sank, H. Wang, M. Weides, J. Wenner, John M. Martinis, A. N. Cleland, *Quantum ground state and single-phonon control of a mechanical resonator*, Nature, **advance online publication**, (2010)

[Okamoto08] Hajime Okamoto, Daisuke Ito, Koji Onomitsu, Hiroshi Yamaguchi, *Thermoelastic damping in GaAs micromechanical resonators*, physica status solidi (c), **5**(9), 2920 (2008)

[Patterson10] W. M. Patterson, D. V. Seletskiy, M. Sheik-Bahae, R. I. Epstein, M. P. Hehlen, *Measurement of solid-state optical refrigeration by two-band differential luminescence thermometry*, J. Opt. Soc. Am. B, **27**(3), 611 (2010)

[PI] *http://www.physikinstrumente.com*

[Pinard99] M. Pinard, Y. Hadjar, A. Heidmann, *Effective mass in quantum effects of radiation pressure*, Eur. Phys. J. D, **7**(1), 107 (1999)

[Pinard00] M. Pinard, P. F. Cohadon, T. Briant, A. Heidmann, *Full mechanical characterization of a cold damped mirror*, Phys. Rev. A, **63**, 013808 (2000)

[Pol] *MSA-500 Micro System Analyzer*

[Purcell46] E. M. Purcell, H. C. Torrey, R. V. Pound, *Resonance Absorption by Nuclear Magnetic Moments in a Solid*, Phys. Rev., **69**(1-2), 37 (1946)

[Restrepo11] Juan Restrepo, Julien Gabelli, Cristiano Ciuti, Ivan Favero, *Classical and quantum theory of photothermal cavity cooling of a mechanical oscillator*, Comptes Rendus Physique, – (2011)

[Richards94] P. L. Richards, *Bolometers for infrared and millimeter waves*, Journal of Applied Physics, **76**(1), 1 (1994)

[Rupper08] G. Rupper, N. H. Kwong, B. Gu, R. Binder, *Theory of laser cooling of semiconductor quantum wells*, physica status solidi (b), **245**(6), 1049 (2008)

[Saulson90] Peter R. Saulson, *Thermal noise in mechanical experiments*, Phys. Rev. D, **42**, 2437 (1990)

[Saulson94] —, *Fundamentals of Interferometric Gravitational Wave Detectors*, World Scientific (1994)

[Schliesser08] A. Schliesser, R. Riviere, G. Anetsberger, O. Arcizet, T. J. Kippenberg, *Resolved-sideband cooling of a micromechanical oscillator*, Nat Phys, **4**(5), 415 (2008)

[Schließer09] Albert Schließer, *Cavity Optomechanics and Optical Frequency Comb Generation with Silica Whispering-Gallery-Mode Microresonators*, , Ludwig–Maximilians–Universität (2009)

[Scully97] Marlan O. Scully M. Suhail Zubairy, *Quantum Optics*, Cambridge: Cambridge University Press (1997)

[Seletskiy10] Denis V. Seletskiy, Seth D. Melgaard, Stefano Bigotta, Alberto Di Lieto, Mauro Tonelli, Mansoor Sheik-Bahae, *Laser cooling of solids to cryogenic temperatures*, Nat Photon, **4**(3), 161 (2010)

[Seletskiy12] Denis V. Seletskiy, Markus P. Hehlen, Richard I. Epstein, Mansoor Sheik-Bahae, *Cryogenic optical refrigeration*, Adv. Opt. Photon., **4**(1), 78 (2012)

[Sheik-Bahae04] Mansoor Sheik-Bahae Richard I. Epstein, *Can Laser Light Cool Semiconductors?*, Phys. Rev. Lett., **92**(24), 247403 (2004)

[Sheik-Bahae07] —, *Optical refrigeration*, Nat Photon, **1**(12), 693 (2007)

[Shen07] Y. C. Shen, G. O. Mueller, S. Watanabe, N. F. Gardner, A. Munkholm, M. R. Krames, *Auger recombination in InGaN measured by photoluminescence*, Applied Physics Letters, **91**(14), 141101 (2007)

[Siegman86] A. E. Siegman, *Lasers*, University Science Books (1986)

[Sivalertporn12] K. Sivalertporn, *Direct and indirect excitons in semiconductor coupled quantum wells in an applied electric field"*, Phys. Rev. B; Physical Review B, **85**(4) (2012)

[Soedel04] Werner Soedel, *Vibrations of Shells and Plates, Third Edition*, CRC Press, 3 (2004)

[Sparks67] P. W. Sparks C. A. Swenson, *Thermal Expansions from 2 to 40°K of Ge, Si, and Four III-V Compounds*, Phys. Rev., **163**, 779 (1967)

[Stobbe09] Søren Stobbe, *Enhancement of Light-Matter Interaction in Semiconductor Nanostructures*, , DTU Fotonik (2009)

[Stroscio05] Michael A. Stroscio Mitra Dutta, *Phonons in Nanostructures*, Cambridge University Press (2005)

[Strzalkowski76] Ireneusz Strzalkowski, Sharad Joshi, C. R. Crowell, *Dielectric constant and its temperature dependence for GaAs, CdTe, and ZnSe*, Applied Physics Letters, **28**(6), 350 (1976)

[Taflove05] Allen Taflove Susan C. Hagness, *Computational Electrodynamics: The Finite-Difference Time-Domain Method, Third Edition*, Artech House, 3 (2005)

[Taylor11] J. M. Taylor, A. S. Sørensen, C. M. Marcus, E. S. Polzik, *Laser Cooling and Optical Detection of Excitations in a LC Electrical Circuit*, Phys. Rev. Lett., **107**, 273601 (2011)

[Teufel11] J. D. Teufel, T. Donner, Dale Li, J. W. Harlow, M. S. Allman, K. Cicak, A. J. Sirois, J. D. Whittaker, K. W. Lehnert, R. W. Simmonds, *Sideband cooling of micromechanical motion to the quantum ground state*, Nature, **475**(7356), 359 (2011)

[Thompson08] J. D. Thompson, B. M. Zwickl, A. M. Jayich, Florian Marquardt, S. M. Girvin, J. G. E. Harris, *Strong dispersive coupling of a high-finesse cavity to a micromechanical membrane*, Nature, **452**(7183), 72 (2008)

[Thomsen86] C. Thomsen, H. T. Grahn, H. J. Maris, J. Tauc, *Surface generation and detection of phonons by picosecond light pulses*, Phys. Rev. B, **34**, 4129 (1986)

[Timoshenko08] S. Timoshenko, *Vibration Problems In Engineering, 2nd Edition*, Wolfenden Press, 2nd (2008)

[Tittonen99] I. Tittonen, G. Breitenbach, T. Kalkbrenner, T. Müller, R. Conradt, S. Schiller,

E. Steinsland, N. Blanc, N. F. de Rooij, *Interferometric measurements of the position of a macroscopic body: Towards observation of quantum limits*, Phys. Rev. A, **59**, 1038 (1999)

[Treutlein12] Philipp Treutlein, Claudiu Genes, Klemens Hammerer, Martino Poggio, Peter Rabl, *Hybrid Mechanical Systems*, arXiv:1210.4151 (2012)

[Usami11] Koji Usami, Andreas Naesby, Bo Melholt Nielsen, Jin Liu, Søren Stobbe, Peter Lodahl, Eugene S. Polzik, *Optical cavity cooling of mechanical modes of a semiconductor nanomembrane*, Nature Physics (2011)

[Verhagen12] E. Verhagen, S. Deleglise, S. Weis, A. Schliesser, T. J. Kippenberg, *Quantum-coherent coupling of a mechanical oscillator to an optical cavity mode*, Nature, **482**(7383), 63 (2012)

[Wannier37] Gregory H. Wannier, *The Structure of Electronic Excitation Levels in Insulating Crystals*, Phys. Rev., **52**, 191 (1937)

[Wilson-Rae] Ignacio Wilson-Rae, *Figures of merit and suggested design for "deformation-potential optomechanics"*, correspondance.

[Wilson-Rae04] I. Wilson-Rae, P. Zoller, A. Imamoğlu, *Laser Cooling of a Nanomechanical Resonator Mode to its Quantum Ground State*, Phys. Rev. Lett., **92**(7), 075507 (2004)

[Wilson-Rae07] I. Wilson-Rae, N. Nooshi, W. Zwerger, T. J. Kippenberg, *Theory of Ground State Cooling of a Mechanical Oscillator Using Dynamical Backaction*, Physical Review Letters, **99**(9), 093901 (2007)

[Wilson09] D. J. Wilson, C. A. Regal, S. B. Papp, H. J. Kimble, *Cavity optomechanics with stoichiometric SiN films* (2009), `0909.0970v1`

[Wilson11] Dalziel Wilson, *Cavity Optomechanics with High Stress Silicon Nitride Films*, , California Institute of Technology (2011)

[Wilson12] Dal Wilson, *GaAs Cavity Parameters* (2012), cavity Parameters

[Xuereb12] André Xuereb, Koji Usami, Andreas Naesby, Eugene S Polzik, Klemens Hammerer, *Exciton-mediated photothermal cooling in GaAs membranes*, New Journal of Physics, **14**(8), 085024 (2012)

[Yao87] T. Yao, *Thermal properties of AlAs/GaAs superlattices.*, Applied Physics Letters, **51**, 1798 (1987)

[Zhang13] Jun Zhang, Dehui Li, Renjie Chen, Qihua Xiong, *Laser cooling of a semiconductor by 40 kelvin*, Nature, **493**(7433), 504 (2013)